

‘Single-Entity’ Electrochemistry at Carbon Nanotubes

A thesis submitted for the degree of

Doctor of Philosophy

in Physical and Theoretical Chemistry

Archana Kaliyaraj Selva Kumar

Pembroke College

Trinity Term 2022

Contents

Acknowledgements……...vii

Abstract ……viii

Glossary…….…...x

Chapter 1 Introduction to Electrochemistry

1.1 Electrochemical Equilibrium…….....1

1.2 Electrode Kinetics…….....8

1.2.1 Butler – Volmer Theory: One Electron Transfer…….....8

1.2.2 Multistep Electron Transfer Process…….14

1.3 Mass Transport……..... 17

1.3.1 Diffusion…….....18

1.3.2 Convection……..... 20

1.3.3 Migration…….....21

1.4 Electrochemical Cells……..... 23

1.5 Electrochemical Techniques…….....24

1.5.1 Cyclic Voltammetry…….....24

1.5.2 Chronoamperometry…….....25

1.5.3 Nano-Impacts…….....26

References…….....29

Chapter 2 Experimental

2.1 Chemicals and Reagents…….....33

2.1.1 Bamboo-like Multiwalled Carbon Nanotubes……34

2.2 Cyclic Voltammetry Experiments…….....35

2.3 Preparation of Macro/Micro-disc Electrodes…….35

2.4 Fabrication of Microwire Carbon Fibre Electrodes……35

2.5 Optical Microscopy Imaging…….....36

2.6 Scanning Electron Microscopy Imaging……36

2.7 Simulation Software…….....36

References…….....38

Chapter 3 Introduction to Carbon Nanotubes and Diffusion at Nanotube and other Modified Electrodes

3.1 Introduction…….....37

3.2 Theory: Diffusion at Planar and Modified Electrode……..41

3.2.1 Cyclic Voltammetry at Planar Electrodes……..42

3.2.2 Thin-layer Voltammetry……... 46

3.2.3 Diffusion at CNTs Modified Electrodes……48

3.3 Conclusion…… 55

References……... 56

Chapter 4 Surface Heterogeneity of Drop-Casted Electrode Surfaces: Impact on Voltammetry

4.1 Introduction……61

4.2 Experimental……..64

4.2.1 Preparation of Bare GC Electrode and b-MWCNTs Modified GC Electrodes……...64

4.3 Results and Discussion……...65

4.4 Conclusions……72

Appendix……. 73

References……... 77

Chapter 5 The Oxidation of Bromide at Pt Macro Electrode: Measurement of the Formal Potential of a Non-Unity Stoichiometric Electrode Reaction

5.1 Introduction……80

5.2 Theory……81

5.3 Simulations…… 84

5.4 Experimental……..86

5.4.1 Preparation of Pt Macro Electrode…….86

5.5 Results and Discussion……...86

5.6 Conclusion……. 91

Appendix…….92

References……...94

Chapter 6 Do Carbon Nanotubes Catalyse Bromine/Bromide Redox Chemistry?

6.1 Introduction……96

6.2 Experimental……..99

6.2.1 Preparation of Electrodes for Cyclic Voltammetry Studies……..96

6.2.2 Nano-Impacts at Carbon Microwire Electrode – Chronoamperometry studies……..99

6.3 Results and Discussion……100

6.4 Conclusion……...111

Appendix……... 112

References……. 114

Chapter 7 Single Entity 'Nano-Catalysis': Carbon Nanotubes and the VO_2^+/VO^{2+} Redox Reaction

7.1 Introduction……..117

7.2 Experimental……117

7.2.1 Electrode Preparation for Cyclic Voltammetric Studies…….121

7.2.2 Microscopy Imaging……...122

7.2.3 'Nano-Impacts' Experiments on Single b-MWCNT – Chronoamperometric Studies…… 122

7.3 Results and Discussion……122

7.4 Conclusions…….147

Appendix……...148

References…….150

Chapter 8 Understanding Carbon Nanotube Voltammetry: Distinguishing Adsorptive and Thin Layer Effects Via 'Single-Entity' Electrochemistry

8.1 Introduction…….155

8.2 Experimental……157

8.2.1 Preparation of Bare GC Electrode and b-MWCNTs Modified GC Electrode…… 157

8.2.2 'Nano-Impact' Experiments at Single b-MWCNTs – Chronoamperometry Studies……..158

8.3 Results and Discussion…….158

8.4 Conclusions……..172

References……. 173

Chapter 9 Conclusions……...176

Acknowledgements

First of all, this thesis wouldn't have been possible without the unconditional support and encouragement from my beloved supervisor Prof. Richard Guy Compton. He is the Best Supervisor any student can get in life. I am taking with me a lot of lessons he taught, both in electrochemistry and beyond. My most favourite of all is "one at a time". Thank you for responding to my email and accepting me as your student, I am glad and honoured. Coming from a rural government school this degree at Oxford was something I didn't even think I deserve to apply but ONLY YOU made it possible. I am spell bound when I have to express my gratitude to you. Thanks for making my dream into reality. I am blessed to have you as my supervisor and shall cherish the bonding forever.

I would like to thank Commonwealth Scholarships Commission, UK, and University of Oxford for funding my DPhil.

Next, I would like to express my deepest gratitude to Dr. Ruiyang Miao, Dr. Danlei Li and Dr. Minjun Yang for helping me with experiments in the early stages of my research.

I am very pleased to have joined PhD in Compton group with optimistic minds like Miss Yuanyuan Lu, Mr. Yifei Zhang and Mr. Haotian Chen. I have co-authored papers with them and many other friendly events like introducing me to the Chinese hot pot delicacy. I am grateful for having an amazing group of colleagues turned friends Yanjun, Pranati, Joe, Yuqi, Bertold, Chris, Collin, Yuanzhe, and Haonan.

I would like to thank my dear mentors from India Dr. Ditty Dixon, Dr Ulaganathan, Dr. Ragupathy, Dr. Angeline Vedha, Dr. Anitha Varghese, and Dr. Maheshwaran Shanmugam for always supporting me and inspiring me to choose research as my career.

Finally, I thank my mother who is my pillar of support in all walks of life and have helped me in achieving who I am today. I would like to dedicate this thesis to her for her 50^{th} birthday which she shall be celebrating soon. HAPPY 50^{th} BIRTHDAY AMMA! I also thank my father and sister for their moral support and for being my cheer leaders. Love you.

I have made great friends from school, undergraduate, at Bengaluru, at Oxford and Ludo gang, at CECRI, thanks to them for putting up with me during the isolated COVID times. I am happy to have to you all in my life. Thanks to everyone mentioned here and others for their visible and invisible support, without all your love and support this thesis is impossible.

Abstract

In this thesis the electrocatalytic properties of carbon nanotubes was studied at both ensemble and single entity levels. For the former CNTs modified electrodes are characterised using cyclic voltammetry and for the latter the 'nano-impacts' method is used. This thesis develops a better understanding of diffusion at modified electrodes. Further, the electro-catalytic behaviour of CNTs was evaluated for the Br_2/Br^- and VO_2^+/VO^{2+} redox couples using the aforementioned techniques. These redox couples are used as catholytes in redox flow battery technology and are identified to undergo sluggish kinetics at carbon surfaces.

Chapter 1 introduces the fundamental principles of electrochemistry and the electrochemical techniques used in this thesis. Chapter 2 gives general information regarding the chemicals and instrumentation. Chapter 3 briefly summarises the use of CNTs in various electrochemical fields as a catalyst and introduces the role of diffusion under different electrode geometries - semi-infinite at planar electrodes and thin-layer at modified electrodes in evaluating the electrocatalytic property at modified electrodes. Further in Chapter 4 the effect of the heterogeneous distribution of CNTs on a substrate electrode as a result of drop-casting was studied. It was concluded that imaging techniques should be used in parallel with voltammetry techniques to interpret voltammetric data.

Next, the possible electrocatalysis of the Br_2/Br^- redox couple was studied at CNTs. As a pre-requisite, Chapter 5 determines the formal potential of the redox couple using the correct form of Randles-Ševčík equation which reflects on the non-unity stoichiometry of the reaction. This chapter also evaluates the follow-up chemistry leading to the formation of tribromide ions during the reaction. This was conducted using simulations

by Mr. Haotian Chen and it was confirmed that the formation of tribromide ion occurs when the concentration of reactant (Br^-) is more than 0.1 M. Using the determined formal potential in Chapter 6 the electrochemical rate constant of Br_2/Br^- redox couple was obtained at bare glassy carbon (GC) electrode and at single b-MWCNTs (using 'nano-impacts') by combining experimental data with simulations. It was observed that b-MWCNTs were only moderately electrocatalytic compared to a bare GC electrode.

In Chapter 7 the redox kinetics of VO_2^+/VO^{2+} redox couple was studied at b-MWCNTs and was compared to the kinetics at bare GC. Interestingly we found that b-MWCNTs were positively catalytic towards the oxidative reaction and '*negatively catalytic*' towards the reduction reaction as concluded from 'nano-impacts' experiment. The asymmetry is explained in terms of the multistep nature of the electrode reaction and the relative sequence of electron transfer and chemical steps.

The high surface area of CNTs can facilitate the adsorption of the electroactive species which makes it difficult to unambiguously distinguish between thin-layer effects and the adsorption using cyclic voltammetry alone since the peak current scales linearly with scan rate in both cases. Therefore, in chapter 8 we distinguish these phenomena using complementary 'nano-impact' studies where the oxidation of 4-hexyltresorcinol was used as a proof of concept. It was concluded in that case that the oxidation reaction was diffusion and not adsorption controlled.

Glossary

Greek Symbols

Symbol	Meaning	Units
$\bar{\mu}_i$	Electrochemical potential of species *i*	J mol^{-1}
$\emptyset_M$	Electrical potential of the metallic electrode	V
$\emptyset_S$	Electrical potential of the solution	V
Γ_{max}	Maximum surface coverage	mol cm^{-2}
γ_i	Activity coefficient of species *i*	Dimensionless
μ_i	Chemical potential of species *i*	J mol^{-1}
$\emptyset$	Electrode potential	V
α	Transfer coefficient (oxidation reaction)	Dimensionless
β	Transfer coefficient (reduction reaction)	Dimensionless
η	Overpotential	Dimensionless
v	Scan rate	V s^{-1}
ρ	Density	g m^{-3}
Γ	Surface coverage	mol cm^{-2}

Roman Symbols

Symbol	Meaning	Units
$[A]_{bulk}$	Bulk concentration	M
$[\ ]^0$	Standard concentration	mol dm^{-3}
a_i	Activity of the species *i*	mol dm^{-3}
a_i^0	Standard activity of species *i*	mol dm^{-3}
A_{ox}	Oxidation reaction frequency factor (1st order)	s^{-1}
A_{red}	Reduction reaction frequency factor (1st order)	s^{-1}
c_i	Concentration of species *i*	Dimensionless
$E^0_{f,\mathrm{eff}}$	Effective formal potential	V
E_f^0	Formal potential	V
I_{lim}	Limiting current	A
I_{ox}	Oxidative current	A
I_{red}	Reductive current	A
$k_{(ox)}$	Rate constant for oxidation reaction	cm s^{-1}
$k_{(red)}$	Rate constant for reduction reaction	cm s^{-1}
k_0	Standard electrochemical rate constant	cm s^{-1}
N_A	Avogadro constant	mol^{-1}
P^0	Standard pressure	N m^{-2}
S_A	Surface area of the molecule	m^{-2}
$[i]$	Concentration of species i	mol dm^{-3}
$-\Delta G_0^{\ddagger}$	Standard Gibbs energy of activation	J mol^{-1}
$-\Delta G_{ox}^{\ddagger}$	Oxidative Gibbs energy of activation	J mol^{-1}

$-\Delta G_{red}^{\ddagger}$	Reductive Gibbs energy of activation	J mol^{-1}
Ar	Area of electrode	cm^2
D	Diffusion coefficient	cm^2 s^{-1}
E	Electrode potential	V
E^0	Standard electrode potential	V
F	The Faraday constant	C mol^{-1}
I_p	Peak current	A
I_{ss}	Steady state current	A
j	Surface flux	mol cm^{-2} s^{-1}
k_b	Backward rate constant in equilibrium	Variable
K_{eq}	Equilibrium constant	Variable
k_f	Forward rate constant in equilibrium	Variable
l	Length	m
m	Number of protons	Dimensionless
n	Number of electrons	Dimensionless
Q	Charge	C
R	The gas constant	J K^{-1} mol^{-1}
T	Temperature	K
Zi	Charge of species *i*	Dimensionless
ΔE	Peak potential separation	V
R_e	Radius of the electrode	cm
δ	Diffusion layer thickness	cm

Abbreviations

Abbreviation	Meaning
LUMO	Lowest Unoccupied Molecular Orbital
HOMO	Highest Occupied Molecular Orbital
SHE	Standard Hydrogen Electrode
SCE	Saturated Calomel Electrode
IUPAC	International Union of Pure and Applied Chemistry
EDL	Electrical Double Layer
IHP	Inner Helmholtz Plane
OHP	Outer Helmholtz Plane
WE	Working Electrode
RE	Reference Electrode
CE	Counter Electrode
NP	Nanoparticles
b-MWCNTs	Bamboo-Like Multiwalled Carbon Nanotubes
EDAX	Energy Dispersive X – Ray Analysis
TEM	Transmission Electron Microscopy
CV	Cyclic Voltammetry
SEM	Scanning Electron Microscopy
GC	Glassy Carbon
PME	Particle Modified Electrodes
CNTs	Carbon Nanotubes
HER	Hydrogen Evolution Reaction
ORR	Oxygen Reduction Reaction
NHE	Normal Hydrogen Electrode

RS	Randles–Ševčík
BRR	Reduction of Bromine
BOR	Oxidation of Bromide
CCW	Clean Carbon Wire
RFB	Redox Flow Battery
VRFB	All-Vanadium RFB
LAF	Largest Area Face
IAF	Intermediate Area Face
SAF	Smallest Area Face
HR	4-Hexylresorcinol

Chapter 1
Introduction to Electrochemistry

Electrochemistry is a branch of chemistry that defines the relationship between chemical reactions and electricity and the interconversion of chemical and electrical energy. This chapter introduces the fundamental concepts in electrochemistry by providing a description of electrochemical equilibrium, electrode kinetics, mass transport of the electrolyte, the electrochemical cell and electrochemical techniques.

1.1 Electrochemical Equilibrium

The electrochemical equilibrium is achieved in electrochemical systems at the interface between an electronic conductor (electrode) and an ionic conductor (electrolyte) through transfer of charge across the phases. Herein, when an electrode (metal) is immersed in an electrolyte (solution) with redox species A and B, it undergoes a simple heterogeneous one-electron transfer at the electrode/electrolyte interface as given in Eq. (1.1) [1, 2]:

$$A(aq) + e^{-}(metal) \leftrightharpoons B(aq) \qquad (1.1)$$

where the redox species 'B (aq)' gets oxidised and 'A (aq)' gets reduced in the solution phase by losing and accepting electrons from the metal electrode. An equilibrium is established when the rate at which 'B (aq)' loses electrons to the electrode (metal) is balanced by the rate at which the electrons are released from the electrode to 'A (aq)'. Regardless of the position of equilibrium since the reaction involves the transfer of a charged particle, the electron, between the two phases charge separation arises at the interface and a potential difference is established [3]. The formation of the electrode potential is understood in terms of the pertinent energy levels of the redox species A and B in the potential determining equilibrium as shown in Figure 1.1. The electronic structure of electrode (metal) has conduction bands with free moving electrons. The energy levels

of the delocalised electrons in these conduction bands form an effective continuum of levels where the electrons are filled up to an energy maximum called the Fermi level. In contrast, the electronic energy levels of the solution phase are discrete and are described ~~thermodynamically~~ as the lowest unoccupied molecular orbital (LUMO) of '*A*' which gains an electron to form '*B*'.

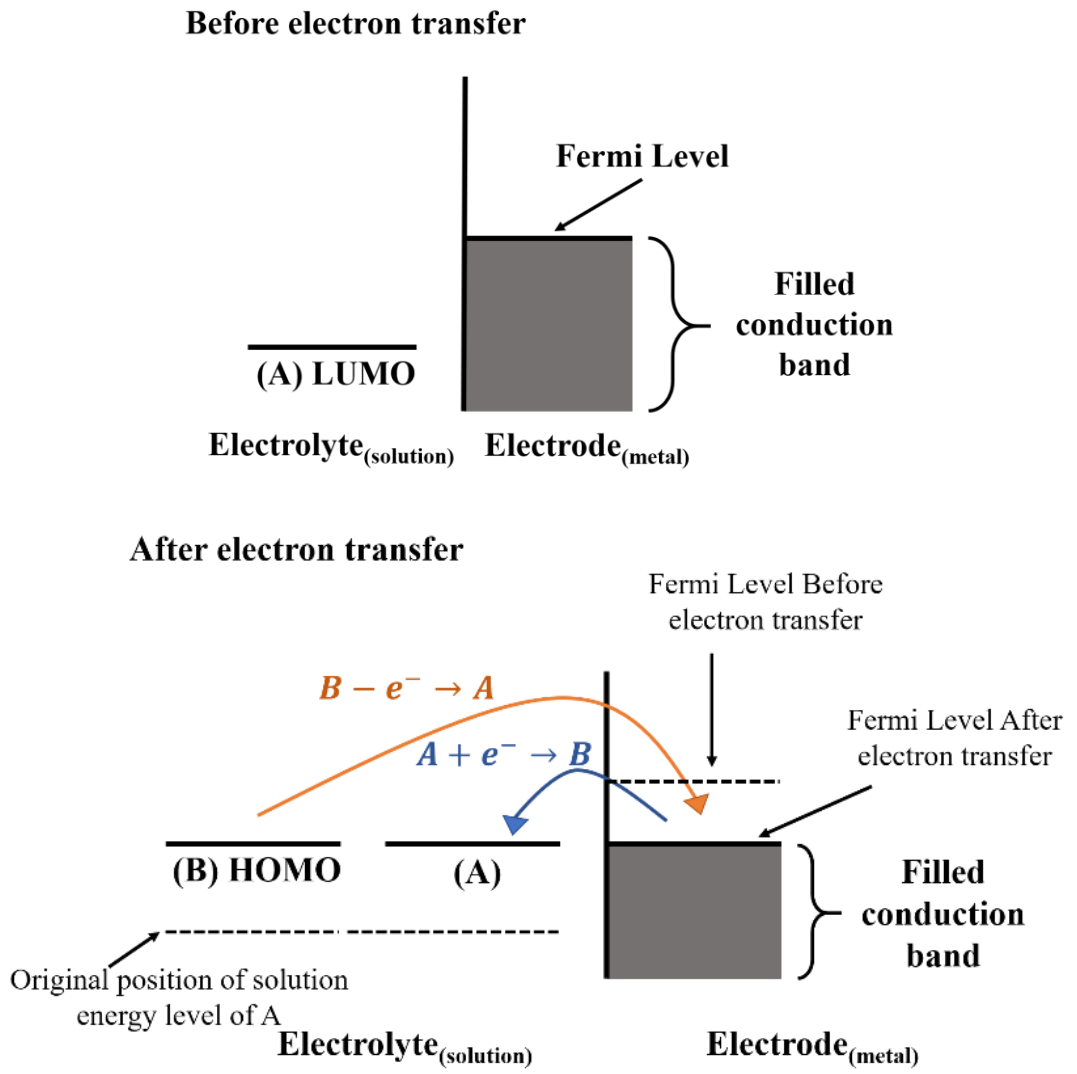


Figure 1.1 Graphic showing energy levels of electrode (metal) and electrolyte (solution) before and after the electron transfer process.

As shown in Figure 1.1 prior to the electron transfer, the Fermi level is higher than that of LUMO of 'A', hence the energetically favourable transfer of electrons from the Fermi level to LUMO of 'A' leads to the formation of 'B'. As a result of the electron transfer

the Fermi level lowers the energy where positive charge builds up on the electrode and the negative charge in the electrolyte raises its energy levels notably the highest occupied molecular orbital (HOMO) in B. When the energy levels approach equality electrons are transferred from the HOMO of 'B' to the Fermi level, thus reforming 'A' from 'B'. A dynamic equilibrium is attained when the rate at which the electrons leave the Fermi level of the electrode and reduce 'A' is equal to the rate at which electrons add to the electrode from 'B' which gets oxidised and no further net charge is observed. The charge separation between the electrode/electrolyte interface is reflected in the formation of electrode potential [1].

While a chemical equilibrium depends on the chemical potentials of the reactants and the products, an electrochemical equilibrium is controlled by the balance between chemical and electrical energies due to the transfer of charged particles across electrode/electrolyte interface. Accordingly, we consider the electrochemical potential (J mol^{-1}), $\bar{\mu}_i$ of species *i*,

$$\bar{\mu}_i = \mu_i + Z_i F\emptyset \tag{1.2}$$

where μ_i is the chemical potential of *i*, Z_i is the molecular charge of *i*, *F* is the Faraday constant (96,485 C mol^{-1}) and $\emptyset$ is the potential of electrode ($\emptyset_M$) or electrolyte ($\emptyset_S$) where the species *i* is found. In Eq. (1.2) the first term denotes the chemical potential, μ_i, and the second term, $Z_i F\emptyset$, defines the electrical energy of species *i*. Under constant temperature and pressure a balance is achieved between the electrochemical potentials of reactants and products is observed at electrochemical equilibrium [4].

Considering the electrochemical reaction in Eq. (1.1) at equilibrium,

$$\bar{\mu}_A + \bar{\mu}_{e^-} = \bar{\mu}_B \tag{1.3}$$

with Eq. (1.2) we get,

$$(\mu_A + Z_A F\emptyset_S) + (\mu_{e^-} - F\emptyset_M) = [\mu_B + (Z_A - 1)F\emptyset_S] \quad (1.4)$$

rearranging Eq. (1.4) gives,

$$F(\emptyset_S - \emptyset_M) = \mu_B - \mu_A - \mu_{e^-} \quad (1.5)$$

The chemical potential, μ_i for species *i* is expressed as [5],

$$\mu_i = \mu_i^0 + RTln\left(\frac{c_i}{[\ ]^0}\right) \quad (1.6)$$

where, μ_i^0 is the standard chemical potential, *R* is the gas constant (J K^{-1} mol^{-1}), *T* is the temperature (K), c_i is the concentration of species *i* in electrolyte and $[\ ]^0$ is the standard concentration (l mol dm^{-3}), measured under ideally dilute conditions at 1 bar pressure.

Substituting the chemical potential terms in Eq. (1.5) with Eq. (1.6) gives,

$$\mu_A = \mu_A^0 + RTln\left(\frac{c_A}{[\ ]^0}\right) \quad (1.7)$$

$$\mu_B = \mu_B^0 + RTln\left(\frac{c_B}{[\ ]^0}\right) \quad (1.8)$$

thus,

$$\emptyset_M - \emptyset_S = \frac{\Delta\mu^0}{F} + \frac{RT}{F} ln\left(\frac{c_A}{c_B}\right) \quad (1.9)$$

where,

$$\Delta\mu^0 = \mu_A^0 + \mu_{e^-} - \mu_B^0 \quad (1.10)$$

$\Delta\mu^0$ is a constant under given temperature and pressure.

Eq. (1.9) is the Nernst equation for a single electrode/electrolyte interface.

Note that the Eqs. (1.7) and (1.8) are for the chemical potentials of species in an electrolyte (solution) hence the standard concentration ($[\ ]^0$, l mol dm^{-3}) is used but for reactions involving gases like H_2, a standard pressure (P^0, $\sim 10^5$ N m^{-2}) is used. In case

of pure solid and liquid compounds, the term denoting concentration or pressure is eliminated and the chemical potentials are similar to the standard potential of the material.

While Eq. (1.9) is limited to its use for ideal solutions only, to accommodate the non-ideality under realistic conditions the concentration term is modified by an activity coefficient (γ).

$$a_i = \gamma_i c_i \tag{1.11}$$

where, a_i is the activity of the species i. Under ideally dilute conditions the activity coefficient is ~1 in which case the activity equals the concentration.

Therefore, Eq. (1.9) becomes,

$$\emptyset_M - \emptyset_S = \frac{\Delta\mu^0}{F} + \frac{RT}{F} ln\left(\frac{\gamma_a c_a}{\gamma_b c_b}\right) \tag{1.12}$$

Now, Eq. (1.12) is the Nernst equation for electrochemical equilibrium in non-ideal solutions.

However, the measurement of an absolute value of $\emptyset_M - \emptyset_S$ from a single electrode/electrolyte interface is not realistically possible hence a second electrode for instance a standard hydrogen electrode (SHE) or saturated calomel electrode (SCE) is introduced to the electrochemical system and described as a reference electrode[6]. The electrode at which the process of interest occurs is the working electrode. A constant interfacial potential drop is experienced at the surface of the reference electrode if the chemical species, for example H_2 and H^+ in the case of a hydrogen electrode are maintained at a constant pressure and concentration. The potential difference, E (V) between both the electrodes is measured (in equilibrium electrochemistry) or controlled (in voltammetry, as described below). The measured potential difference for a two-electrode system is given by [5],

$$E = \lim_{I \to 0}\left[(\emptyset_M - \emptyset_S)_{test} + IR - (\emptyset_M - \emptyset_S)_{reference}\right] \quad (1.13)$$

$$E = (\emptyset_M - \emptyset_S)_{test} + (\emptyset_M - \emptyset_S)_{reference} \quad (1.14)$$

where, 'R' is the resistivity of the electrolyte solution and the term 'IR' defines the potential drop in the solution phase between the two electrodes. Note that this term is negligible since current 'I' is tiny if appropriate instrumentation is used as in equilibrium electrochemistry where a digital voltmeter (or historically a potentiometer) is employed.

With the electrode potentials referenced against a common reference electrode, the Nernst equation for a two-electrode system is given as[7],

$$E = E^0 + \frac{RT}{F} ln\left(\frac{a_A^0}{a_B^0}\right) \quad (1.15)$$

where, E is the electrode potential measured against the reference electrode, and E^0 is the standard electrode potential of the redox couple A/B also against the same reference electrode. Note that the value of the activity is usually unknown since this is controlled not only by the involved species in the potential determining equilibrium but also by other electrolyte species around the working electrode. Thus, Eq. (1.15) is modified to a more generic, practical form by introducing a formal potential.

Hence, Eq. (1.15) is rewritten as,

$$E = E^0 + \frac{RT}{F} ln\left(\frac{\gamma_A c_A}{\gamma_B c_B}\right) = E^0 + \frac{RT}{F} ln\left(\frac{\gamma_A}{\gamma_B}\right) + \frac{RT}{F} ln\left(\frac{c_A}{c_B}\right) \quad (1.16)$$

This equation is simplified by defining the formal potential of the redox couple A/B as,

$$E_f^0 = E^0 + \frac{RT}{F} ln\left(\frac{\gamma_A}{\gamma_B}\right) \quad (1.17)$$

so,

$$E = E_f^0 + \frac{RT}{F} ln\left(\frac{c_A}{c_B}\right) \tag{1.18}$$

This form of the Nernst equation is widely adopted by the experimentalists in general for describing the change in electrode potential with respect to the species concentration in the solution. Note that this is only applicable to an electrochemical system in a dynamic equilibrium.

Since, the variation of pH in aqueous electrochemical reactions is inevitable, the Nernst equation is correspondingly adjusted for a general one-electron oxidation process,

$$A = B + mH^+ + e^- \tag{1.19}$$

From Eq. (1.19),

$$E = E_f^0(A/B) + \frac{RT}{F} ln\left(\frac{[B][H^+]^m}{[A]}\right) \tag{1.20}$$

$$E = E_f^0(A/B) + \frac{RT}{F} ln\left(\frac{[B]}{[A]}\right) + \frac{mRT}{F} ln[H^+] \tag{1.21}$$

where, $E_f^0(A/B)$ is the formal potential involving the activity coefficients of the species A and B, [A], [B], and $[H^+]$ are the concentrations of A, B and H^+ respectively and m is the number of protons transferred during the electrochemical reaction.

According to the IUPAC the pH is given by

$$pH = -log_{10}[\gamma_{H^+} H^+] \tag{1.22}$$

where, γ_{H^+} is the activity coefficient of proton.

thus, Eq. (1.22) becomes[8],

$$E = E_f^0(A/B) + \frac{RT}{F} ln\left(\frac{[B]}{[A]}\right) - 2.303\frac{mRT}{F} pH \tag{1.23}$$

From an experimental point of view, for a buffered media the electrochemical equilibrium can de denoted as

$$A \leftrightharpoons B + e^- \tag{1.24}$$

Thus, the *effective* formal potential $E^0_{f,\text{eff}}$ for the reaction in Eq. (1.25) is

$$E^0_{f,\text{eff}}(A/B) = E^0_f(A/B) \; - \; 2.303\frac{mRT}{F}pH \tag{1.25}$$

Hence,

$$E = E^0_{f,\text{eff}}(A/B) + \frac{RT}{F}ln\left(\frac{B}{A}\right) \tag{1.26}$$

1.2 Electrode Kinetics

In the previous section we discussed the thermodynamics necessary to describe the electrochemical equilibrium characterised by the *Nernst equation* wherein the equilibrium is under fast electrode kinetics. To quantitatively study the evolution of various species at the electrode/electrolyte interface in terms of their rate of chemical change via the interfacial charge transfer process (electrolysis) the kinetics of the electrode must be elucidated. In this section, a model of the electrode kinetics underpinning the classical concepts of current and potential interpretations will be discussed.

1.2.1. Butler – Volmer Theory: One electron transfer

Let us consider an electrochemical equilibrium for a one-electron transfer reaction[9]

$$A(aq) + e^-(metal) \underset{k_{(ox)}}{\overset{k_{(red)}}{\leftrightharpoons}} B(aq) \tag{1.27}$$

where, the $k_{(red)}$and $k_{(ox)}$ are electron transfer rate constants describing the reduction and oxidation reactions respectively. The electron transfer process at the electrode to A(aq) occurs via quantum mechanical tunnelling. Therefore, A(aq) must be located within *ca.* 10 – 20 Å of the electrode surface otherwise the rate of tunnelling, which

reduces with increase in the distance of separation, becomes prohibitively small. Hence, A(aq) must diffuse form the bulk solution to this critical distance before electron tunnelling can efficiently occur.

This electron transfer generates electrical current, I through the electrode and is given as,

$$I = FAj \tag{1.28}$$

where, F is the Faraday's constant, A (cm^2) is the area of the electrode and j (mol cm^{-2} s^{-1}) is the flux of the reactant undergoing electrolysis.

The net rate law for the electrochemical equilibrium in Eq. (1.27) is written as,

$$j = j_{red} - j_{ox} = k_{red}[A]_0 - k_{ox}[B]_0 \tag{1.29}$$

where, $[A]_0$ and $[B]_0$ are the concentrations of A (aq) and B(aq) at the electrode surface which typically differ from those in bulk solution.

The generic expression for the rate constants $k_{(red)}$and $k_{(ox)}$ is deduced from the Arrhenius equation[10] which is given by,

$$k^0 = A_{red}exp\left(\frac{-\Delta G_0^{\ddagger}}{RT}\right) = A_{ox}exp\left(\frac{-\Delta G_0^{\ddagger}}{RT}\right) \tag{1.30}$$

$$k_{red} = A_{red}exp\left(\frac{-\Delta G_{(red)}^{\ddagger}}{RT}\right) \tag{1.31}$$

$$k_{ox} = A_{ox}exp\left(\frac{-\Delta G_{(ox)}^{\ddagger}}{RT}\right) \tag{1.32}$$

where, k^0, $k_{(red)}$ and $k_{(ox)}$ are the standard, reductive and oxidative rate constants respectively. A_{red} and A_{ox} are the pre-exponential factors. Note that entropic effects are included in $-\Delta G_0^{\ddagger}$, not the pre-exponential term. $-\Delta G_0^{\ddagger}$, $-\Delta G_{(red)}^{\ddagger}$ and $-\Delta G_{(ox)}^{\ddagger}$ (J mol^{-1}), are the standard Gibbs energy of the reaction and the, reductive and oxidative Gibbs activation energy. The latter two quantities are also known as 'energy barriers'. Figure

1.2 schematically represents the Gibbs energy profile varying with the reaction coordinate. The reaction coordinate begins with the reactants at its lowest energy to products via the transition state, ‡[11], which is the point of maximum energy[12, 13].

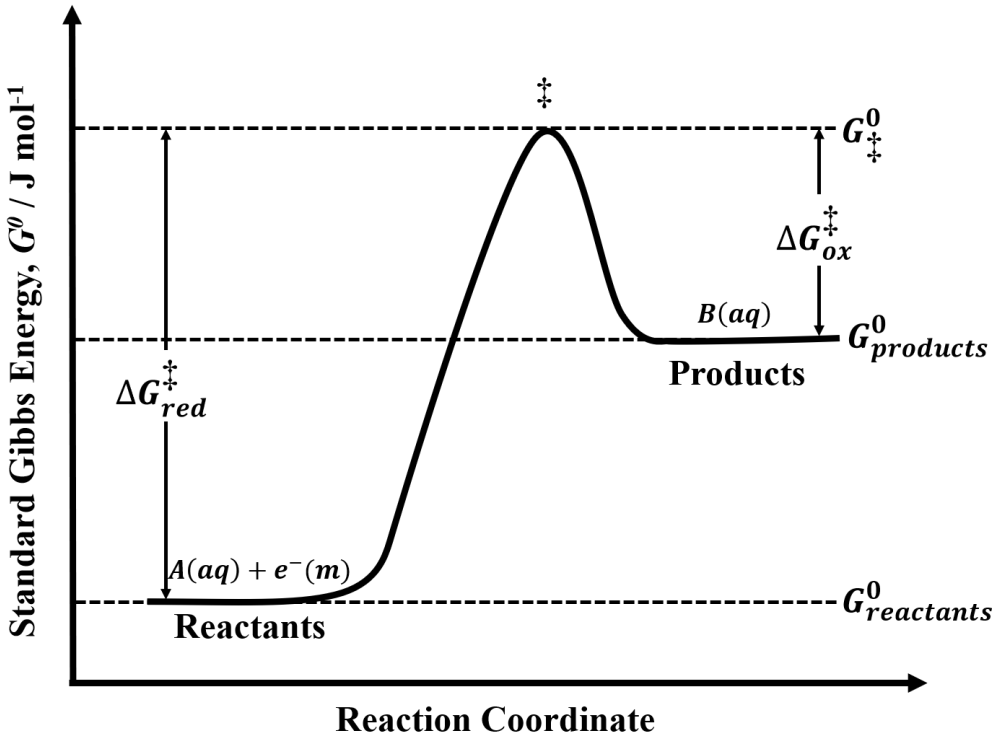


Figure 1.2 A reaction profile for simple one-electron transfer electrode process.

As mentioned earlier in section 1.1, the difference of the electrochemical energy of the reactants and products is related to the potential difference at the interface. Hence, the activation energy in an electrochemical reaction is similarly expressed as a function of applied interfacial potential and the formal potential, E_f^0. The change in electrode potential from its formal potential, E_f^0 to E is given by ΔE and the corresponding change in the energy of the Fermi level of the electrode is given by $F\Delta E = -F(E - E_f^0)$. Accordingly, the energy profile for a simple one-electron transfer either moves up or down when a negative or positive ΔE is applied respectively.

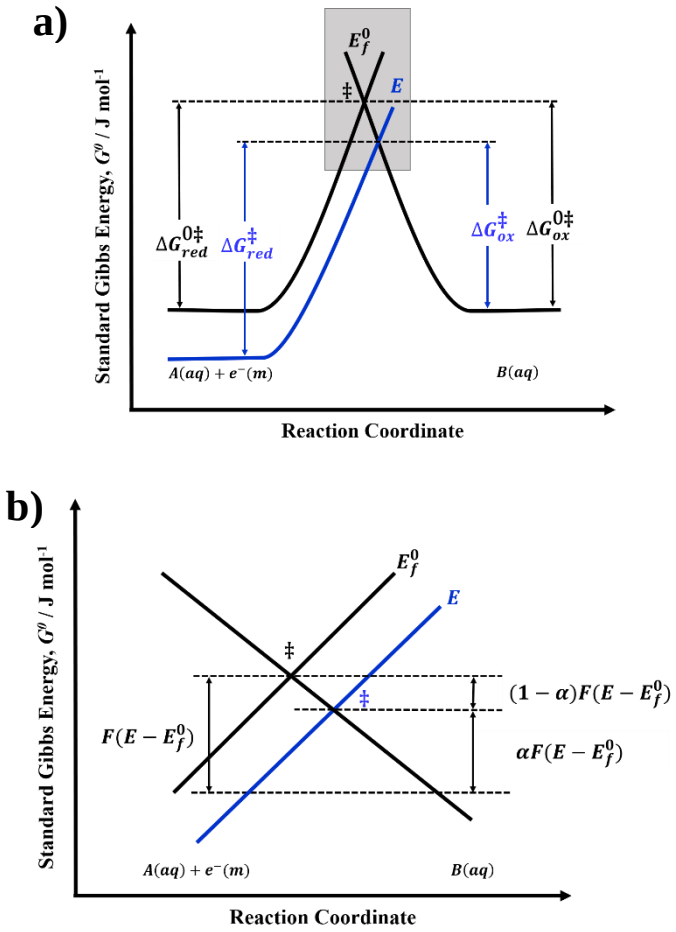


Figure 1.3 a) Effect of potential change on the standard Gibbs energy for a one-electron transfer reaction, and b) enlarged picture of the grey box in Figure 1.3a).

In Figure 1.3, the effect of change in the potential from formal potential to a more positive electrode potential, E is shown. As in Figure 1.3b) The energy barrier for $B(aq)$ decreases by $(1-\alpha)F(E-E_f^0)$. The fraction $(1-\alpha)$ can be written as β where α and β are the transfer coefficients ranging from zero to unity. Similarly, the cathodic energy barrier increases by a factor of $\alpha F(E-E_f^0)$[14]. Therefore, at constant temperature and pressure the Gibbs energy of activation for oxidation and reduction reaction is given by,

$$\Delta G_{red}^{‡} = \Delta G_0^{‡} + \alpha F\left(E - E_f^0\right) \tag{1.33}$$

$$\Delta G_{ox}^{‡} = \Delta G_0^{‡} - \beta F\left(E - E_f^0\right) \tag{1.34}$$

where, E and E_f^0 are the applied and formal potential respectively. α and β are the cathodic and anodic transfer coefficients respectively.

For a one – electron transfer reaction the value of the transfer coefficients ranges from 0 to 1 and sum as follows

$$\alpha + \beta = 1 \tag{1.35}$$

Note that, if α is close to 0 then the transition state for a reduction is *reactant – like*, but, if it approaches 1 then the transition state is *product – like*. However, in most cases,

$$\alpha \sim \beta \sim 0.5 \tag{1.36}$$

which suggests that the transition state lies intermediate in its electrical behaviour between the reactants and products.

Eqs. (1.30 – 1.34) can be rearranged as,

$$k_{red} = k^0 exp\left(-\frac{\alpha F\left(E - E_f^0\right)}{RT}\right) \tag{1.37}$$

$$k_{ox} = k^0 exp\left(\frac{\beta F\left(E - E_f^0\right)}{RT}\right) \tag{1.38}$$

where, $\left(E - E_f^0\right)$ is denoted as the overpotential (η) of the redox reaction, which relates the applied potential at the working electrode to the formal potential.

Further substituting Eq. (1.37) and (1.38) to the rate law in Eq. (1.29) gives,

$$j = k^0[A]_0 exp\left(-\frac{\alpha F\left(E - E_f^0\right)}{RT}\right) - k^0[B]_0 exp\left(\frac{\beta F\left(E - E_f^0\right)}{RT}\right) \tag{1.39}$$

This *flux – potential* relation is the Butler – Volmer equation[15]. From this equation, the Tafel law can be derived accordingly.

If the reduction reaction in Eq. (1.27) is faster than the reverse oxidation reaction, then the latter is negligible and hence the flux, *j*, can be approximately expressed as

$$j = k^0[A]_0 exp\left(-\frac{\alpha F\left(E - E_f^0\right)}{RT}\right) \tag{1.40}$$

Similarly, for the oxidation reaction,

$$j = k^0[B]_0 exp\left(\frac{\beta F\left(E - E_f^0\right)}{RT}\right) \tag{1.41}$$

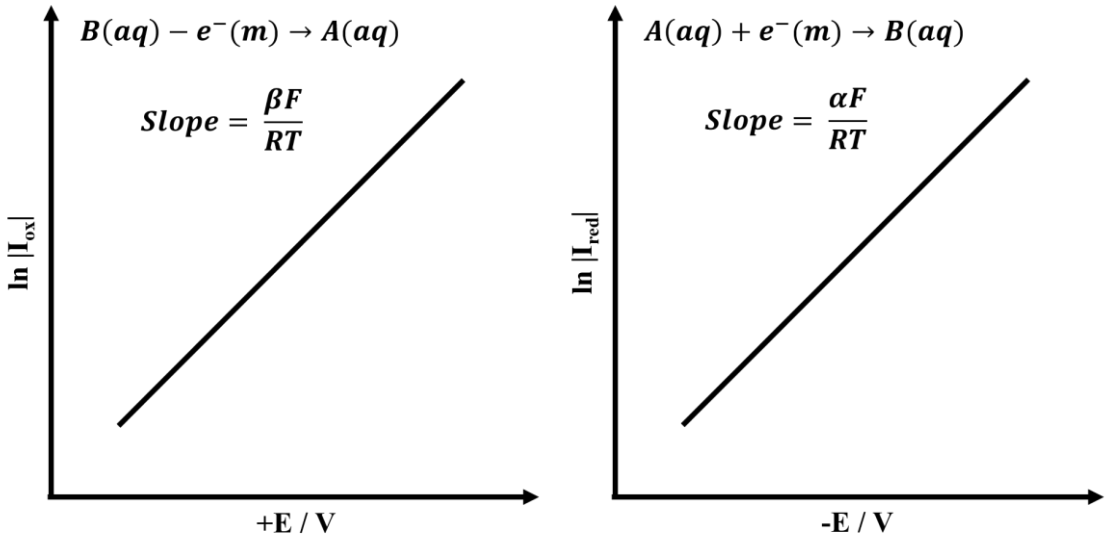


Figure 1.4 Tafel plots

If, concentrations of $[A]_0$ and $[B]_0$ near to the working electrode and in the bulk solution are similar then,

$$\ln|I_{red}| = -\frac{\alpha FE}{RT} + constant \tag{1.42}$$

$$\ln|I_{ox}| = \frac{\beta FE}{RT} + constant \tag{1.43}$$

where, I_{red} and I_{ox} are the reduction and oxidation currents respectively. Plots of $ln|I_{ox/red}|$ versus *E* is known as the Tafel plots as shown in Figure 1.4,[16] which, from their slopes, provide information on the magnitude of the transfer coefficients.

1.2.2. Multistep Electron Transfer Processes

Consider an electrochemical reduction of *A* to *C* via a two – electron transfer reaction at the electrode

$$A(aq) + e^{-}(metal) \leftrightharpoons B(aq) \tag{1.44}$$

$$B(aq) + e^{-}(metal) \leftrightharpoons C(aq) \tag{1.45}$$

Accordingly, either the first step or the second step can be the rate determining step.

From the Eqs. (1.37) and (1.38) the rate constants as applied for each step in Eqs. (1.44) and (1.45).

The fluxes j_A and j_B are given by

$$j_A = -k^0_{A/B} exp\left[\frac{-\alpha_1 F}{RT}\left(E - E^0_f(A/B)\right)\right][A]_0 + k^0_{A/B} exp\left[\frac{\beta_1 F}{RT}\left(E - E^0_f(A/B)\right)\right][B]_0 \tag{1.46}$$

$$j_B = k^0_{A/B} exp\left[\frac{-\alpha_1 F}{RT}\left(E - E^0_f(A/B)\right)\right][A]_0 - k^0_{A/B} exp\left[\frac{\beta_1 F}{RT}\left(E - E^0_f(A/B)\right)\right][B]_0 + k^0_{B/C} exp\left[\frac{\beta_2 F}{RT}\left(E - E^0_f(B/C)\right)\right][C]_0 - k^0_{B/C} exp\left[\frac{\alpha_2 F}{RT}\left(E - E^0_f(B/C)\right)\right][B]_0 \tag{1.47}$$

$$j_C = + k^0_{B/C} exp\left[\frac{-\alpha_2 F}{RT}\left(E - E^0_f(B/C)\right)\right][B]_0 - k^0_{B/C} exp\left[\frac{\beta_2 F}{RT}\left(E - E^0_f(B/C)\right)\right][C]_0 \tag{1.48}$$

where, α_1 and β_1 relate to one-electron reduction in Eq. (1.44), while α_2 and β_2 relate to Eq. (1.45).

The following two limiting cases are considered for two-step reduction reactions.

Case 1. The first one-electron transfer reduction is the rate determining step,

$$A(aq) + e^{-}(metal) \xrightarrow{slow} B(aq) \tag{1.49}$$

$$B(aq) + e^{-}(metal) \xrightarrow{fast} C(aq) \tag{1.50}$$

here, the concentration of *B* is tiny, hence the flux *j* is,

$$j_A = k^0_{A/B} exp\left[-\frac{\alpha_1 F}{RT}\left(E - E^0_f(A/B)\right)\right][A_0] \tag{1.51}$$

According to Eq. (1.42) the Tafel analysis is described as,

$$\ln|I_{red}| = -\frac{\alpha_1 FE}{RT} + constant \tag{1.52}$$

Similarly, for a two-step oxidation process where the first step is the rate determining step,

$$Z(aq) - e^{-}(metal) \xrightarrow{slow} Y(aq) \tag{1.53}$$

$$Y(aq) - e^{-}(metal) \xrightarrow{fast} X(aq) \tag{1.54}$$

The Tafel analysis gives,

$$\ln|I_{ox}| = +\frac{\beta_1 FE}{RT} + constant \tag{1.55}$$

where, β_1 is the transfer coefficient of *Y/Z* couple.

Case 2. In this case the electron transfer in the second step is the rate determining and the first step establishes a pre-equilibrium.

$$A(aq) + e^{-}(metal) \leftrightharpoons B(aq) \tag{1.56}$$

$$B(aq) + e^{-}(metal) \xrightarrow{slow} C(aq) \tag{1.57}$$

For this,

$$I_{red} = FA(j_A + j_B) = -FAj_C \tag{1.58}$$

where, *A* is the area of the electrode, hence under Tafel conditions the oxidation of *C(aq)* is neglected which gives,

$$j_C = -k^0_{B/C} exp\left[\frac{-\alpha_2 F}{RT}\left(E - E^0_f(B/C)\right)\right][B_0] \tag{1.59}$$

Noting that Eq. (1.56) describes a pre-equilibrium,

$$\frac{[B]^0}{[A]^0} = exp\left[\frac{-F}{RT}\left(E - E^0(A/B)\right)\right] \tag{1.60}$$

Hence Eq. (1.52) becomes,

$$j_C = -k^0_{B/C} exp\left[\frac{-\alpha_2 F}{RT}\left(E - E^0_f(B/C)\right)\right] exp\left[\frac{-F}{RT}\left(E - E^0(A/B)\right)\right][A]^0 \tag{1.61}$$

Hence,

$$\ln|I_{red}| = -\frac{(1+\alpha_2)FE}{RT} + constant \tag{1.62}$$

If we assume that

$$\alpha_1 \sim \beta_1 \sim \alpha_2 \sim \beta_2 \sim 0.5 \tag{1.63}$$

Then an observed transfer coefficient of *ca.* 0.5 indicates the transfer of the first electron is the rate determining as in *case 1*. In contrast a transfer coefficient of *ca.* 1.5 shows *case 2* predominates where the second electron transfer is the rate determining. Figure 1.5 shows the reaction profiles for both the cases.

Likewise, for a two-step oxidation involving a pre-equilibrium for *Y/Z* couple followed by a rate degerming step as given,

$$Z(aq) - e^-(metal) \leftrightharpoons Y(aq) \tag{1.64}$$

$$Y(aq) - e^-(metal) \xrightarrow{slow} X(aq) \tag{1.65}$$

The Tafel analysis gives,

$$\ln|I_{ox}| = +\frac{(1+\beta_1)FE}{RT} + constant \tag{1.66}$$

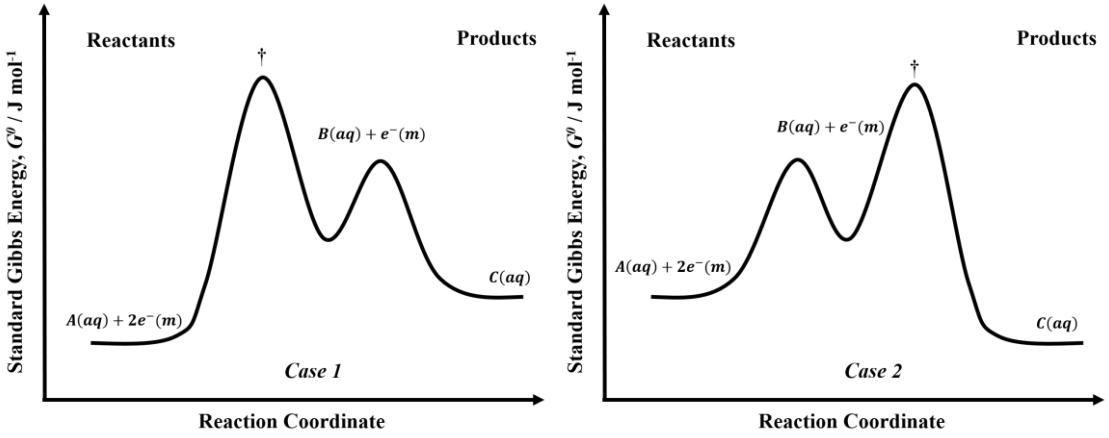


Figure 1.5 Reaction profiles for two-electron transfer.

In general, Tafel slopes can be used to identify the rate determining step in a multistep reaction.

1.3 Mass Transport

In the previous section we have discussed the kinetics related to charge transfer occurring at the electrode/electrolyte interface resulting in the depletion of the concentration of analyte near the electrode. This facilitates movement of reactants from bulk solution towards the electrode whilst the build-up of the products encourages their diffusion away from the electrode, such a phenomenon is known as mass transport. This section discusses the three main types of mass transport namely diffusion, convection and migration associated with the mass transport of the electroactive species[17].

1.3.1 Diffusion

Diffusion is defined as the net movement of species from higher concentration to lower concentration, in other words down a concentration gradient. According to Fick's 1st law of diffusion,

$$j = -D\frac{\partial c}{\partial x} \tag{1.67}$$

where, j/mol cm^{-2} s^{-1} is the flux corresponding to number of moles of the species passing through a unit area in unit time, D/cm^2 s^{-1} is the diffusion coefficient and $\frac{\partial c}{\partial x}$ is the local concentration gradient at x. Note that the negative sign implies the flow of flux down the concentration gradient.

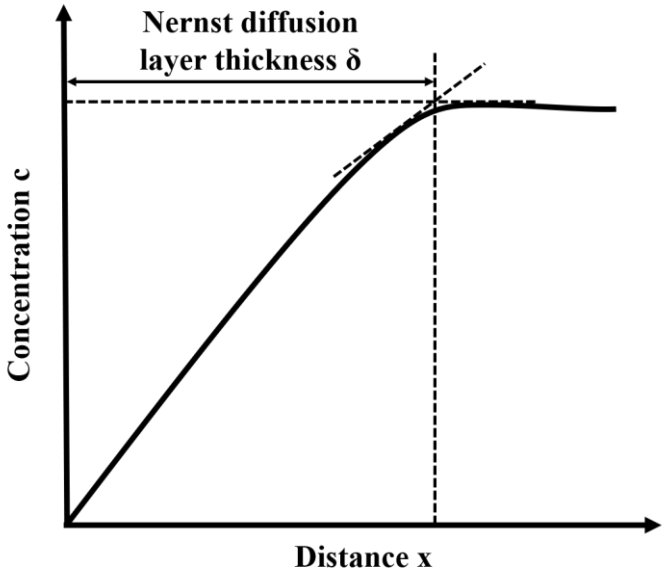


Figure 1.6 One-dimensional Nernst diffusion layer.

Figure 1.6 schematically represents the concentration of reactant plotted against the distance from the electrode during an electrochemical process. The *Nernst diffusion layer* is indicated in the figure which denotes the zone of depletion of reactants near the electrode surface.

While Fick's 1st law describes the flux through a plane, Fick's 2nd law considers the variation of concentration with respect to time at a point x, which is defined by,

$$\frac{\partial c}{\partial t} = D\frac{\partial^2 c}{\partial x^2} \tag{1.68}$$

where, ∂t is the time interval for diffusion[18].

Eq. (1.68) is given in one-dimension. For three-dimensions it becomes[6],

$$\frac{\partial c}{\partial t} = D\left(\frac{\partial^2 c}{\partial x^2} + \frac{\partial^2 c}{\partial y^2} + \frac{\partial^2 c}{\partial z^2}\right) \tag{1.69}$$

where, *x, y and z* are Cartesian coordinates.

For cylindrical coordinates, (*r, ϕ, z),*

$$\frac{\partial c}{\partial t} = D\left(\frac{\partial^2 c}{\partial r^2} + \frac{1}{r}\frac{\partial c}{\partial r} + \frac{\partial^2 c}{\partial z^2}\right) \tag{1.70}$$

where, *r* is the radial coordinate. Note that for a system with cylindrical symmetry, there is no dependence on the angle ϕ.

The Eq. (1.67) defining Fick's 1st law was complemented by Einstein and Von Smoluckowskii describing the random motion of molecules. The diffusion coefficient, *D* provides the measure of root mean square of distance, $\langle x^2 \rangle$ displaced at a time, *t*, which is given by,

$$\sqrt{\langle x^2 \rangle} = \sqrt{2Dt} \tag{1.71}$$

Accordingly, in a three-dimension Eq. (1.71) becomes

$$\sqrt{\langle x^2 \rangle + \langle y^2 \rangle + \langle z^2 \rangle} = \sqrt{6Dt} \tag{1.72}$$

1.3.2 Convection

Convection is the transport of species under mechanical forces and can be of two forms; natural and forced[19, 20]. Natural convection is due to density/thermal gradients resulting in movement of species from denser to less denser regions. This occurs near the working and/or counter electrode during the reactant depletion and product formation. Thermal convection is caused by imperfections of the thermostatting in the bulk solution or by the exo/endothermicity of the electrode reaction. This affects the reproducibility of the

experiments hence to avoid such variations the measurement time of voltammetric experiments is set to be relatively short, usually no more than a few seconds. Forced convection originates from the mechanical agitation like rotation of the electrode, solution stirring, gas bubbling. This forced convection alters the rate of mass transport assisting well-defined quantitative analysis for instance as in the use of forced convection in rotating disc electrode experiments[21].

1.3.3 Migration

Migration is the transport of charged species due to generation of an electric field resulting for example from the potential drop at the electrode/electrolyte interface[22] as described in section 1.1. The migratory flux $j_{m,i}$, for species i, at point x is expressed as,

$$j_{m,i}(x) = -\frac{z_i F}{RT} D_i c_i \frac{\partial \phi(x)}{\partial x} \tag{1.73}$$

where, z_i is the charge of species i, D_i is the diffusion coefficient, c_i is the concentration and $\frac{\partial \phi(x)}{\partial x}$/V m^{-1} is the electric ~~potential/~~field.

While the total flux in the bulk solution is described by Eq. (1.73), near the electrode, the flux j_i is due to mixed mass transport of diffusion and migration. The direction of the diffusional flux $j_{d,i}$ and the migratory flux $j_{m,i}$ can be same or opposite depending on the charge of i and the direction of the electric field. Figure 1.7 gives a schematic representation of three different possibilities where species *i* be positively, negatively or neutrally charged[23]. The migratory and diffusional fluxes are in same direction for reduction of cation or oxidation of anion, but, in opposite directions for oxidation of cation or reduction of anion.

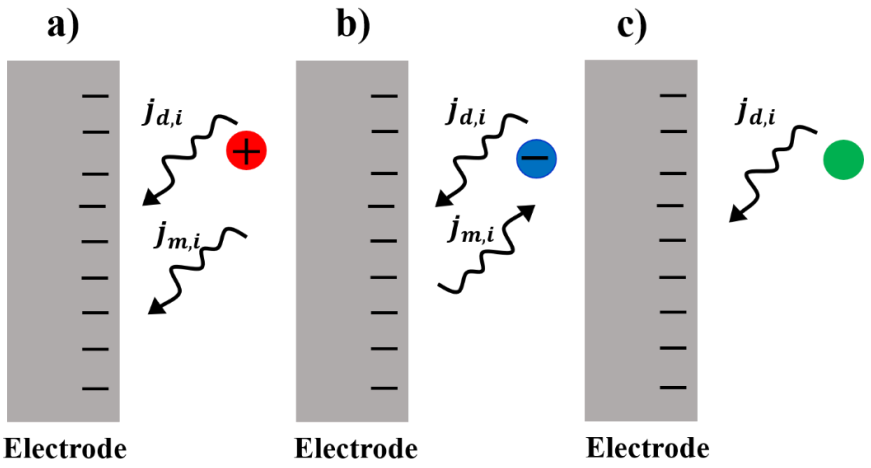


Figure 1.7 Reduction reaction with different contributions of migratory flux; a) positively charged species, b) negatively charged species, and c) uncharged species.

The electrochemical systems are significantly affected by migration effects, hence to eliminate this a large concentration of the supporting electrolyte is employed to restrict the electrical field in bulk solution and to reduce the ohmic drop [24, 25]. Under increased conductivity the interfacial potential drop is confined to a small region to the electrode giving rise to an *electrical double layer* (EDL) to a distance of *ca.* 10-20 Å from the electrode for electrolyte concentrations above *ca*. 0.1 M [26]. As schematically represented in Figure 1.8, a positively charged electrode surface adsorbs anions and dipolar solvent molecules through migration of such ions from bulk solution towards the electrode driven by electrostatic forces. The layer where the decay of the potential is rapid corresponds to these specifically adsorbed species and is known as the *Inner Helmholtz Plane, IHP* and the layer where non-specific adsorption of species occurs is called the *Outer Helmholtz Plane, OHP*. Beyond the OHP, is the diffuse layer where solvated ions are loosely electrostatically attracted towards the electrode surface and thus, thermal forces dominate over the electrostatic forces of attraction [27]. These layers form the EDL which maintains electrical neutrality at electrode/electrolyte interface. The change in potential across these layers show that the potential drop from metal/electrode to solution/electrolyte phase

within the Helmholtz layer has an appropriate size to match the required electron tunnelling distance for electrolyte concentrations above ca 0.1M. This potential drop is the driving force for any electrochemical reaction to proceed.

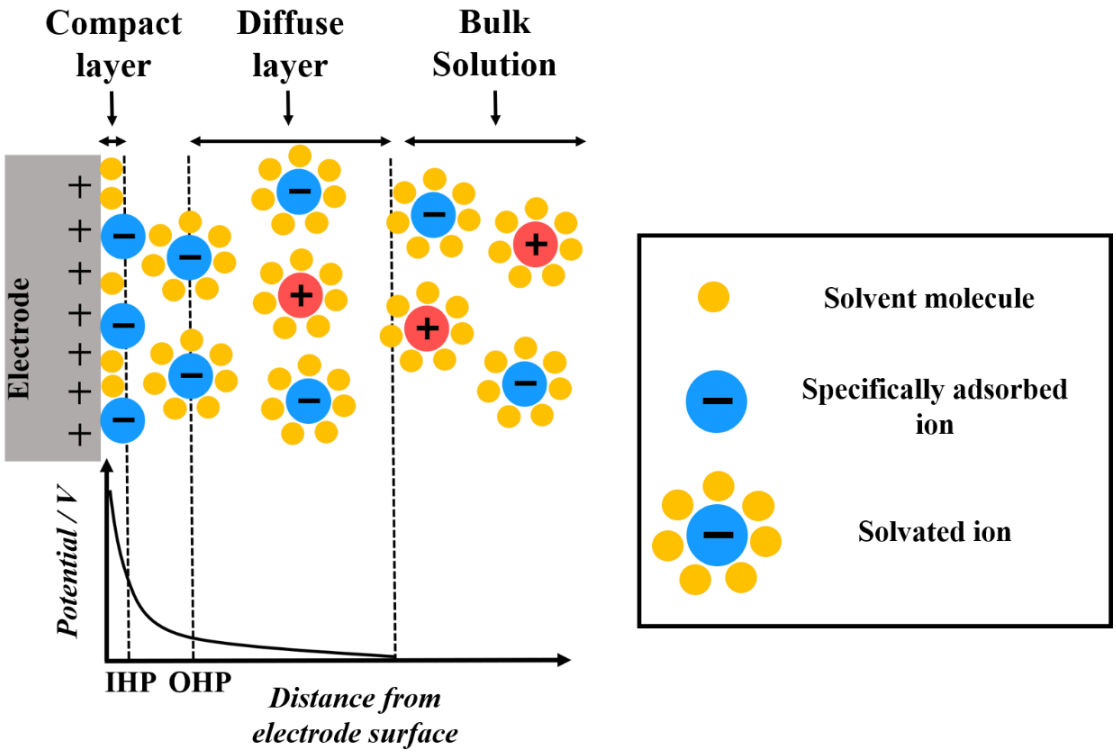


Figure 1.8 Model of electrical double layer regions where anions are specifically adsorbed at a positive electrode. The yellow, blue and red spheres represent solvated ions, anions and cations respectively.

1.4 Electrochemical Cells

The experimental evaluation of electrochemical systems is studied using a three-electrode system. A typical electrochemical cell comprises of a working electrode (WE) where the reaction of study occurs, a reference electrode (RE) that facilitates a stable measurement and control of the WE/electrolyte interface and a counter electrode (CE) through which the current passes to complete the circuit. The three-electrode cell is controlled using a potentiostat as shown in Figure 1.9. A constant potential, *E* is applied by the potentiostat between the WE and RE with negligible current flow through the later due to CE. The RE

provides a constant value of $(\phi_M - \phi_S)_{RE}$, so any changes in the applied potential, E is achieved in $(\phi_M - \phi_S)_{WE}$ of WE.

$$E = (\phi_M - \phi_S)_{WE} + IR - (\phi_M - \phi_S)_{RE} \quad (1.74)$$

where, IR is the potential/ohmic drop.

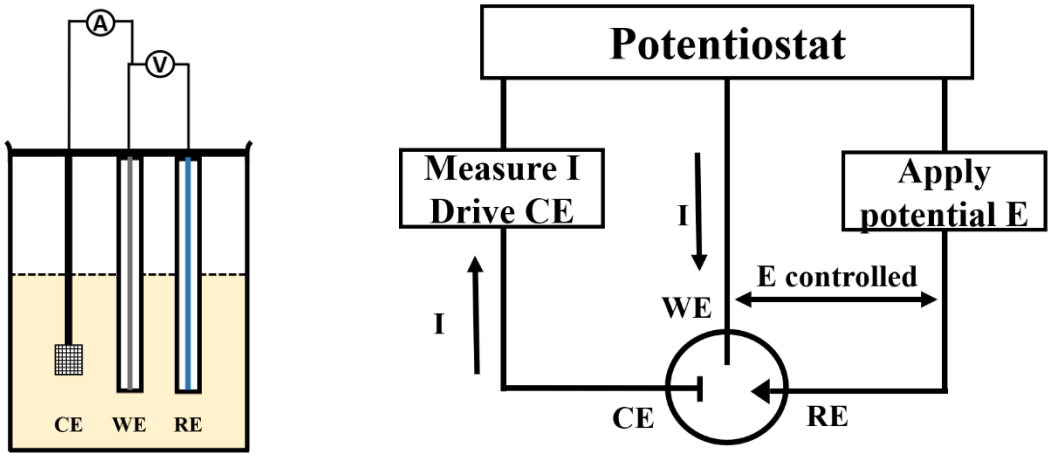


Figure 1.9 Schematic diagram of a three-electrode cell.

If IR is unknown then, $(\phi_M - \phi_S)_{WE}$ is also uncertain, to avoid such circumstances, the CE is required to pass same current as the WE. Note that the employed CE should be inert to the electrolyte studied to avoid any interference with the reaction under study. Commonly, graphite rod or platinum (Pt) wire/mesh is used.

A two-electrode system consisting only of WE and RE is applicable when the WE is a microelectrode since only very low current (~10^{-9} A) is passed[28, 29]. Thus, any change at RE and the IR term is negligible.

1.5 Electrochemical Techniques

This section elaborates three electrochemical techniques used to study the mechanisms, kinetics and thermodynamics of reactions at the electrode/electrolyte interface namely cyclic voltammetry, chronoamperometry and nano-impacts.

1.5.1 Cyclic Voltammetry

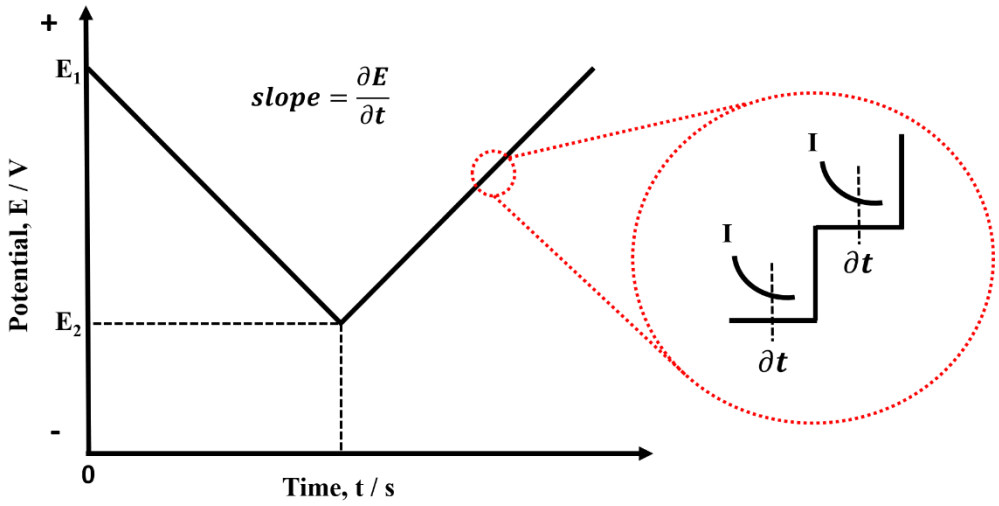


Figure 1.10 Potential-time profile of a cyclic voltammogram for a reduction reaction; the zoom-in picture shows the points in the potential steps at which the current is recorded.

The cyclic voltammetric technique is widely adapted among electrochemists to study the current response of any electrochemical reaction of interest. The potential of the working electrode is linearly swept within a potential range from say an initial potential, E_1, and to a reverse potential E_2 then swept back to E_1 at a constant scan rate, v (V s^{-1})[6, 30]. E_1 is usually selected so that there are no Faradaic currents observed in other words the current here is near-zero apart from non-Faradaic or capacitive current. At E_2 the reaction is usually fully driven where instantaneous electron transfer is observed after diffusion of the electroactive species to the electrode. At E_2 the scan is reversed to the initial potential E_1 thus completing a cycle. The linear ramp comprises in experimental practice multiple tiny potential steps or staircases imposed digitally as shown in Figure 1.10. The current is measured at each potential step, a plot of current against the applied potential is the cyclic voltammogram.

The shape of the voltammogram reflects the electrode kinetics, mass transport, and scan rate. Mass transport (diffusion) depends on the geometry of the working electrode (which will be discussed in Chapter 3), and the nature of the electroactive species.

1.5.2 Chronoamperometry

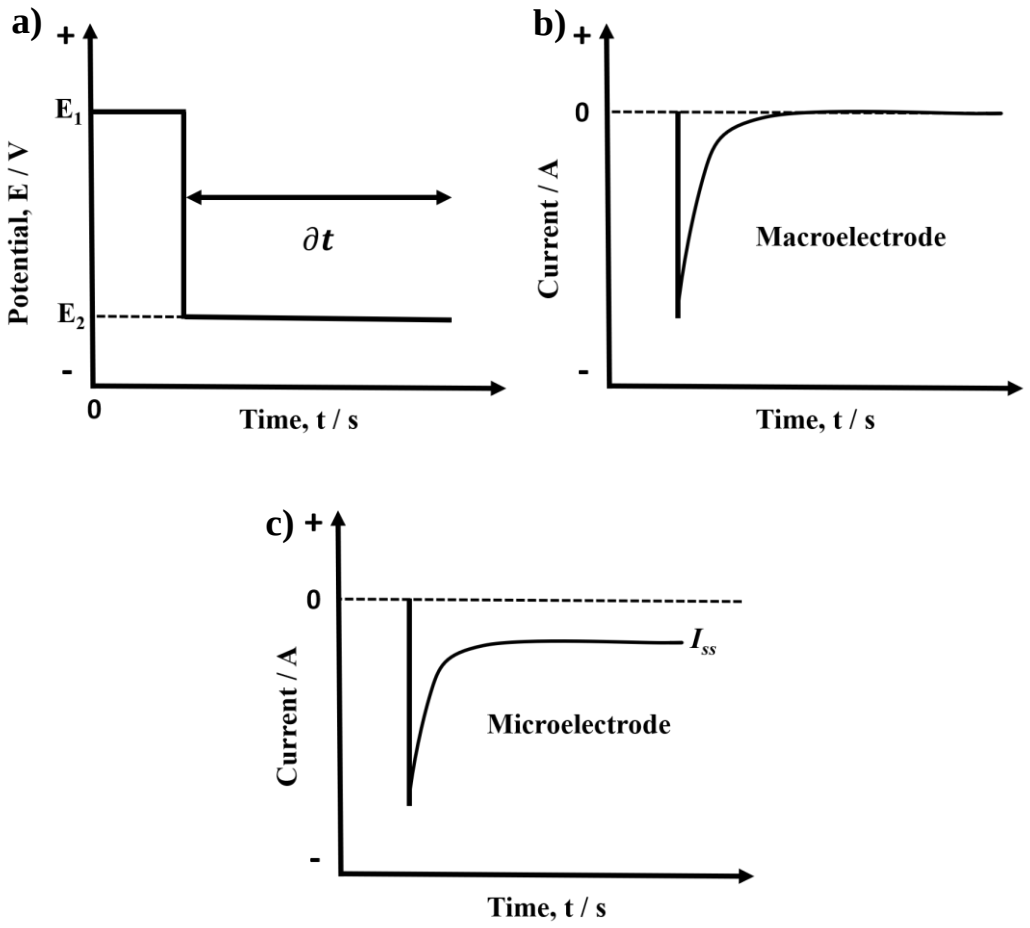


Figure 1.11 a) The potential – time profile for a single-step chronoamperometry. The corresponding chronoamperometric responses at b) macroelectrodes and c) microelectrodes.

Chronoamperometry is an electrochemical technique in which a constant potential is applied to the working electrode. The applied potential is instantaneously stepped from the initial potential E_1 where the current is typically nearly zero to a potential E_2 which provides sufficient overpotential for the reaction to occur so that the diffusing reactant towards the electrode is fully consumed. As shown in Figure 1.11 a large current is observed immediately after the step after which the current decays to zero (for

macroelectrodes experiencing linear diffusion) or a steady-state value (for microelectrodes experiencing convergent diffusion)[1]. This drastic decrease in current over a period of time is due to the consumption of the reactant at the vicinity of the electrode surface and the decay reflects the loss of electroactive material near the electrode as the diffusion layer enlarges with time.

1.5.3 Nano-Impacts

The recent rapid growth in the use of nanomaterials for a spectrum of applications especially in the field of electrocatalysis[31, 32], sensors[33], and drug delivery[34] is phenomenal. Nanomaterials are one-dimensional materials that range from 1 – 100 nm in size. Most of the reported electrochemical studies on nanomaterials are based on studies conducted on an ensemble of nanoparticles (NPs). The resulting measurements are thus an average of the large population of particles from which the intrinsic properties of the individual nanoparticles such as the size, morphology and catalytic ability are unpredictable due to agglomeration, and porosity effects. Hence, a technique to analyse the electrochemical properties of single NPs is highly essential.

'Nano-impacts' is an electrochemical technique used to analyse the characteristics of individual nanoparticles. In this technique by virtue of Brownian motion the NPs stochastically collide with the micro-sized working electrodes, where it can either get adsorbed, react or enhance a reaction catalytically[35-39]. Thus, there is a change in the electrode current on collision. The current responses can be from Faradaic or non-Faradaic processes. The Faradaic current response might result from either *direct* or *mediated* electron transfer processes. In a *direct* Faradaic impact as shown in Figure 1.12a, the electron transfer occurs between the NPs and the electrode where the colliding NPs may either get oxidised or reduced or dissolved[40-43].

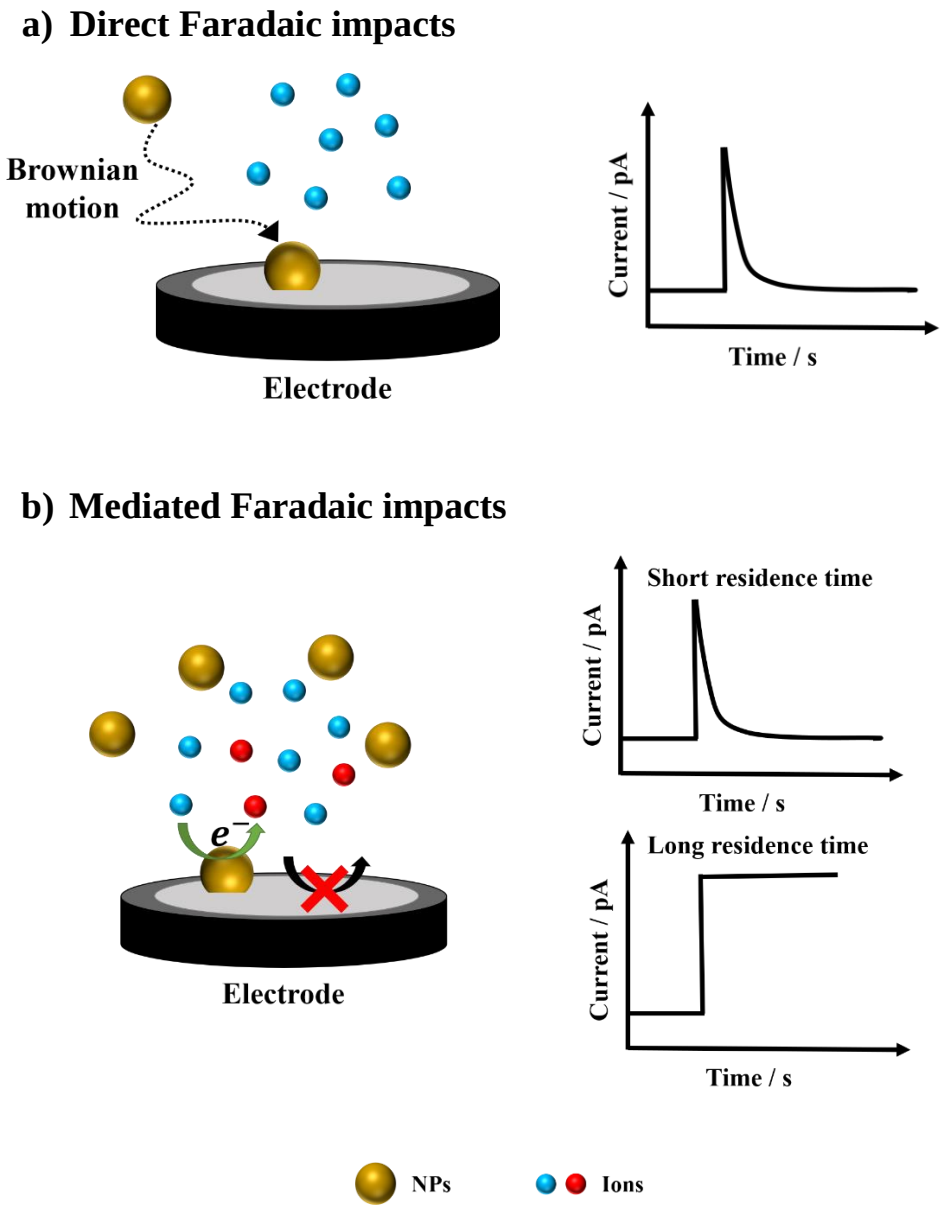


Figure 1.12 Schematic representation of a) direct Faradaic impacts and b) mediated Faradaic impacts along with their respective current – time transients.

In case of *mediated* Faradaic impacts as in Figure 1.12b, the redox couple is present in the solution. At an applied potential the reaction is unfavourable at the working electrode due to kinetic limitations whereas, ~~the~~ on collision of the NPs at the electrode it adopts the applied potential and the redox reaction takes place at the surface of the NPs leading to a spike or step in the current[44-46]. The current feature resembles that of either a spike

or a step depending on the time the NPs is in contact with the electrode. Note that for *mediated* Faradaic impacts the redox state of the NPs remains unaltered.

Non-Faradaic impacts include capacitive impacts which can be due to displacement of charge from the electrode/electrolyte interface specifically the EDL or due to charging of the NPs itself. Overall electrical neutrality is maintained by the electrons either leaving or entering the electrode as a result of changes in the ionic distribution at the interface. The observed capacitive impacts are used to estimate the potential of zero charge[47-49].

Note that the nano-impacts experiments of all types are usually conducted at micro-electrodes in order to reduce the capacitance of the interface so that the charging does not mask short lived collision events and to provide a rapid response time. Similarly, the potentiostat used needs to be selected with the response time in mind and carefully checked to ensure that the full charge is recorded during an impact event especially if quantitative data is sought.

References

1. Compton, R. G.; Banks, C. E., *Understanding Voltammetry, 3rd Edition* **2018**, 1-439.
2. Richard, G.; Sanders, C.; Giles, H., *Electrode Potentials*. Oxford University Press: 1996.
3. Rieger, P. H., *Electrochemistry*. Springer Science & Business Media: 1993.
4. Butler, J. A. V., The thermodynamics of the surfaces of solution. *Procedings of Royal Society London* **1932,** *135* (827), 348-375.
5. Arevalo, A.; Pastor, G., Verification of the Nernst Equation and Determination of a Standard Electrode Potential. *J Chem Educ* **1985,** *62* (10), 882-884.
6. Bard, A. J.; Faulkner, L. R., *Electrochemical Methods: Fundamentals and Applications*. **1983,** *20* (1), 91-92.
7. Vidal-Iglesias, F. J.; Solla-Gullon, J.; Rodes, A.; Herrero, E.; Aldaz, A., Understanding the Nernst Equation and Other Electrochemical Concepts: An Easy Experimental Approach for Students. *J Chem Educ* **2012,** *89* (7), 936-939.
8. Walczak, M. M.; Dryer, D. A.; Jacobson, D. D.; Foss, M. G.; Flynn, N. T., pH-dependent redox couple: Illustrating the Nernst equation using cyclic voltammetry. *J Chem Educ* **1997,** *74* (10), 1195-1197.
9. Gardiner, W. C., *Rates and mechanisms of chemical reactions*. W.A. Benjamin: New York, 1969.
10. Albery, W. J., *Electrode kinetics*. Oxford University Press, USA: 1975; Vol. 14.
11. Guidelli, R.; Compton, R. G.; Feliu, J. M.; Gileadi, E.; Lipkowski, J.; Schmickler, W.; Trasatti, S. J. P.; Chemistry, A., Defining the transfer coefficient in electrochemistry: An assessment (IUPAC Technical Report). **2014,** *86* (2), 245-258.
12. Johnston, H. S., *Gas phase reaction rate theory*. Ronald Press Co.: New York, 1966.
13. Laidler, K. J., Citation Classic - the Theory of Rate-Processes - the Kinetics of Chemical-Reactions, Viscosity, Diffusion and Electrochemical Phenomena. *Cc/Phys Chem Earth* **1988,** (46), 16-16.
14. Eyring, H. L. S. H. L. S. M., *Basic chemical kinetics*. Wiley: New York, 1980.
15. Butler, J. A. V., Studies in heterogeneous equilibria. Part II - The kinetic interpretation of the nernst theory of electromotive force. *T Faraday Soc* **1924,** *19* (3), 0729-0733.
16. Tafel, J., Über die Polarisation bei kathodischer Wasserstoffentwicklung, Zeitschrift für Physikalische Chemie. **1905,** *50U* (1), 641-712.
17. Agar, J. N., Diffusion and Convection at Electrodes. *Discuss Faraday Soc* **1947,** *1*, 26-37.
18. Fick, A., V. On liquid diffusion. *The London, Edinburgh, Dublin Philosophical Magazine, Journal of Science* **1855,** *10* (63), 30-39.

19. Novev, J. K.; Compton, R. G., Natural convection effects in electrochemical systems. *Curr Opin Electroche* **2018,** *7*, 118-129.

20. Rubio-Garcia, J.; Kucernak, A.; Charleson, A., Direct visualization of reactant transport in forced convection electrochemical cells and its application to redox flow batteries. *Electrochemistry Communications* **2018,** *93*, 128-132.

21. Montenegro, I.; Queirós, M. A.; Daschbach, J. L., *Microelectrodes: theory and applications*. Springer Science & Business Media: 2012; Vol. 197.

22. Belding, S. R.; Limon-Petersen, J. G.; Dickinson, E. J. F.; Compton, R. G., Cyclic Voltammetry in the Absence of Excess Supporting Electrolyte Offers Extra Kinetic and Mechanistic Insights: Comproportionation of Anthraquinone and the Anthraquinone Dianion in Acetonitrile. *Angew Chem Int Edit* **2010,** *49* (48), 9242-9245.

23. Pletcher, D., *A first course in electrode processes*. Royal Society of Chemistry: 2019.

24. Ngamchuea, K.; Batchelor-McAuley, C.; Compton, R. G., Anodic stripping voltammetry of silver in the absence of electrolytes: Theory and experiment. *J Electroanal Chem* **2018,** *830*, 122-130.

25. Toh, H. S.; Batchelor-McAuley, C.; Tschulik, K.; Uhlemann, M.; Crossley, A.; Compton, R. G., The anodic stripping voltammetry of nanoparticles: electrochemical evidence for the surface agglomeration of silver nanoparticles. *Nanoscale* **2013,** *5* (11), 4884-4893.

26. Dickinson, E. J. F.; Limon-Petersen, J. G.; Rees, N. V.; Compton, R. G., How Much Supporting Electrolyte Is Required to Make a Cyclic Voltammetry Experiment Quantitatively "Diffusional"? A Theoretical and Experimental Investigation. *J Phys Chem C* **2009,** *113* (25), 11157-11171.

27. Luck, J.; Latz, A., Modeling of the electrochemical double layer and its impact on intercalation reactions. *Phys Chem Chem Phys* **2018,** *20* (44), 27804-27821.

28. Rogers, E. I.; Streeter, I.; Aldous, L.; Hardacre, C.; Compton, R. G., Electrode kinetics and mechanism of iodine reduction in the room-temperature ionic liquid [C_4mim][NTf_2]. *J Phys Chem C* **2008,** *112* (29), 10976-10981.

29. Fleischmann, M.; Lasserre, F.; Robinson, J.; Swan, D., The Application of Microelectrodes to the Study of Homogeneous Processes Coupled to Electrode-Reactions .1. $E_{c'}$ and C_e Reactions. *J Electroanal Chem* **1984,** *177* (1-2), 97-114.

30. Nicholson, R. S.; Shain, I., Theory of Stationary Electrode Polarography for a Chemical Reaction Coupled between 2 Charge Transfers. *Analytical Chemistry* **1965,** *37* (2), 178.

31. Kang, Y. J.; Yang, P. D.; Markovic, N. M.; Stamenkovic, V. R., Shaping electrocatalysis through tailored nanomaterials. *Nano Today* **2016,** *11* (5), 587-600.

32. Jarju, J. J.; Figueiredo, M. C.; Kolen'ko, Y. V., Chapter 8 - Electrocatalysis using nanomaterials. In *Frontiers of Nanoscience*, Wain, A. J.; Dickinson, E. J. F., Eds. Elsevier: 2021; Vol. 18, pp 343-420.

33. Kour, R.; Arya, S.; Young, S. J.; Gupta, V.; Bandhoria, P.; Khosla, A., Review-Recent Advances in Carbon Nanomaterials as Electrochemical Biosensors. *J Electrochem Soc* **2020,** *167* (3).

34. Wen, A. M.; Steinmetz, N. F., Design of virus-based nanomaterials for medicine, biotechnology, and energy. *Chem Soc Rev* **2016,** *45* (15), 4074-4126.

35. Cheng, W.; Compton, R. G., Electrochemical detection of nanoparticles by 'nano-impact' methods. *Trac-Trend Anal Chem* **2014,** *58*, 79-89.

36. Mirkin, M. V.; Sun, T.; Yu, Y.; Zhou, M., Electrochemistry at One Nanoparticle. *Accounts Chem Res* **2016,** *49* (10), 2328-2335.

37. Wang, Y. X.; Shan, X. N.; Tao, N. J., Emerging tools for studying single entity electrochemistry. *Faraday Discuss* **2016,** *193*, 9-39.

38. Batchelor-McAuley, C.; Katelhon, E.; Barnes, E. O.; Compton, R. G.; Laborda, E.; Molina, A., Recent Advances in Voltammetry. *Chemistryopen* **2015,** *4* (3), 224-260.

39. Pumera, M., Impact Electrochemistry: Measuring Individual Nanoparticles. *ACS Nano* **2014,** *8* (8), 7555-7558.

40. Zhou, Y. G.; Rees, N. V.; Compton, R. G., The Electrochemical Detection and Characterization of Silver Nanoparticles in Aqueous Solution. *Angew Chem Int Edit* **2011,** *50* (18), 4219-4221.

41. Rees, N. V.; Zhou, Y. G.; Compton, R. G., The Aggregation of Silver Nanoparticles in Aqueous Solution Investigated via Anodic Particle Coulometry. *Chemphyschem* **2011,** *12* (9), 1645-1647.

42. Qiu, D. F.; Wang, S.; Zheng, Y. Q.; Deng, Z. X., One at a time: counting single-nanoparticle/electrode collisions for accurate particle sizing by overcoming the instability of gold nanoparticles under electrolytic conditions. *Nanotechnology* **2013,** *24* (50).

43. Zhou, Y. G.; Haddou, B.; Rees, N. V.; Compton, R. G., The charge transfer kinetics of the oxidation of silver and nickel nanoparticles via particle-electrode impact electrochemistry. *Phys Chem Chem Phys* **2012,** *14* (41), 14354-14357.

44. Xiao, X. Y.; Bard, A. J., Observing single nanoparticle collisions at an ultramicroelectrode by electrocatalytic amplification. *Journal of the American Chemical Society* **2007,** *129* (31), 9610-+.

45. Xiao, X. Y.; Fan, F. R. F.; Zhou, J. P.; Bard, A. J., Current Transients in Single Nanoparticle Collision Events. *Journal of the American Chemical Society* **2008,** *130* (49), 16669-16677.

46. Ahn, H. S.; Bard, A. J., Single-Nanoparticle Collision Events: Tunneling Electron Transfer on a Titanium Dioxide Passivated n-Silicon Electrode. *Angew Chem Int Edit* **2015,** *54* (46), 13753-13757.

47. Banks, C. E.; Rees, N. V.; Compton, R. G., Sonoelectrochemistry Understood via Nanosecond Voltammetry: Sono-emulsions and the Measurement of the Potential of Zero Charge of a Solid Electrode. *The Journal of Physical Chemistry B* **2002,** *106* (23), 5810-5813.

48. Rees, N. V.; Banks, C. E.; Compton, R. G., Ultrafast chronoamperometry of acoustically agitated solid particulate suspensions: Nonfaradaic and faradaic processes at a polycrystalline gold electrode. *J Phys Chem B* **2004,** *108* (48), 18391-18394.

49. Poon, J.; Batchelor-McAuley, C.; Tschulik, K.; Compton, R. G., Single graphene nanoplatelets: capacitance, potential of zero charge and diffusion coefficient. *Chem Sci* **2015,** *6* (5), 2869-2876.

Chapter 2

Experimental

This chapter outlines the chemical reagents used, along with the experimental methodologies and instrumentation adopted in the work presented in this thesis. Specific descriptions of the experiments can be found in relevant experimental sections of Chapters 3 – 8.

2.1 Chemicals and Reagents

All the chemicals and reagents listed in Table 2.1 used were purchased commercially and used without any further purification. The solutions were prepared using deionised water (Millipore, UK) with a resistivity of 18.2 MΩ cm at 298 K.

Table 2.1 List of chemicals, reagents and materials used in this thesis.

Chemical Name	Formula	Purity	Supplier
Sodium bromide	NaBr	99%	Sigma-Aldrich[1]
Nitric acid	HNO_3	65 – 70%	Fischer Scientific[2]
Acetone	C_3H_6O	99.50%	Merck[3]
Bromine	Br_2	99.99%	Merck[4]
Bromine water	Br_2	30%	HACH[5]
Vandadyl sulphate	$VOSO_4$	99.99%	Merck[6]
Vanadium pentoxide	V_2O_5	99.60%	Merck[7]
4-Hexylresorcinol	$C_{12}H_{18}O_2$	98%	Merck[8]
Bamboo-like multiwalled carbon nanotubes	/	/	NanoLab, Inc.,[9]

2.1.1 Bamboo-like Multiwalled Carbon Nanotubes

Bamboo-like multiwalled carbon nanotubes (b-MWCNTs) were purchased and used without any further purifications from NanoLab Inc., Massachusetts, USA. The length, diameter and specific surface area of the b-MWCNTs were 5-20 μm, 30(±10) nm and 200 $m^2 g^{-1}$ respectively as reported by the manufacturer [9]. Likewise, a transmission electron microscopy image (TEM) and atomic elemental composition data measured by energy dispersive X – ray analysis (EDAX) from the manufacturer is given in Figure 2.1 and Table 2.2 respectively.

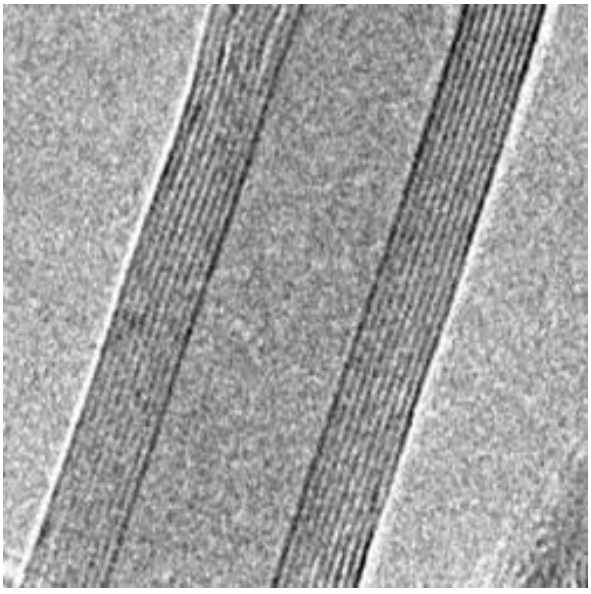


Figure 2.1 TEM image of b-MWCNTs provided by the manufacturer showing 9 concentric walls and a clear inner channel with10 nm of inner diameter.

Table 2.2 EDAX data of bamboo - like multiwalled carbon nanotubes giving the elemental atomic percentage.

Element	Weight %	Atomic %
Carbon	98.92	99.75
Sulfur	0.14	0.05
Iron	0.94	0.20

2.2Cyclic Voltammetry Experiments

Cyclic voltammetry (CV) studies were conducted using a three-electrode cell comprising of a working electrode, a reference electrode (saturated calomel, SCE; BASI Ltd., Japan; +0.241 V vs SHE) and a counter electrode (graphite rod) in a μAutolab II potentiostat (Metrohm – Autolab BV, Netherlands). All the experiments were carried out in a Faraday cage at 298 K. The voltammetry studies were controlled by General Purpose Electrochemical System (GPES) software. The different working electrodes used were a platinum (Pt) macrodisc electrode (1.5 mm in diameter, Sigma-Aldrich Ltd., UK), a glassy carbon electrode (3 mm in diameter, BASI Ltd., Japan), a platinum (Pt) microdisc electrode (5 μm in diameter, Sigma-Aldrich Ltd., UK), and an in-house made microwire carbon fibre electrode (7 μm in diameter and *ca.* 1 mm in length). Different working electrodes were used in different chapters and will be mentioned in the respective experimental section of each chapter.

2.3 Preparation of Macro/Micro-disc Electrodes

Prior to all the electrochemical experiments the electrodes were polished sequentially with 1.00 μm, 0.30 μm and 0.05 μm alumina slurries (Buehler, Micropolish II, Germany) unless otherwise specified. Electrodes were then washed with deionised water, sonicated for 10 s and then dried with N_2 prior to all the CV experiments. Details regarding the drop-cast experiments are detailed in the relevant chapters.

2.4 Fabrication of Microwire Carbon Fibre Electrodes

'Nano-impact' experiments were made with selected fixed potentials applied to the working electrode. A carbon microwire electrode of diameter 7 μm and length 1 mm (Goodfellow, Cambridge Ltd., UK) was employed as working electrode in a three-

electrode cell. Fabrication of the micro wire electrode was done as reported in the literature [10]. In brief, the carbon wire is attached to a conducting wire using a silver epoxy adhesive. After drying in the oven for 15 – 20 mins at 60°C, the wire was adhered into a plastic pipette such that the carbon fibre is protruded out of the tip. The pipette tip was then sealed using cyanoacrylate adhesive, dried overnight and used for experiments. Finally, the dried carbon fibre electrode was cut to a length of *ca.* 1 mm length. The nano-impact experiments were controlled by NOVA 2.1.5 software.

2.5 Optical Microscopy Imaging

Optical microscope images were made using a Zeiss Axio Examiner, A1 Epifluroscence microscope (Carl Zeiss Ltd., UK). 10x objective magnification (NA = 0.5, EC Plan – Neofluar) and a light source of LQ-HXP 120 V lamp were used. The emission filter was removed to obtain a surface – reflective equivalent, thus, the incident light was reflected by the electrode surface then tranmistted to the camera and the optical image of the opaque glassy carbon electrode was imaged. An ORCA – Flash 4.0 digital CMOS camera provided the images in 16-bit images with 4-megapixel resolution. The images were taken with help from Dr. Minjun Yang (Compton group).

2.6 Scanning Electron Microscopy Imaging

SEM imaging was carried out in a Zeiss Sigma 300 FEG – SEM at an accelerating voltage of 2.0 kV using samples drop-casted at glassy carbon slab. The images were taken by Dr. Minjun Yang (Compton group).

2.7 Simulation Software

The simulations mentioned in this thesis is carried out using DigiSim[11], a commercially available software unless otherwise specified.

References

1. Sodium bromide. https://www.sigmaaldrich.com/GB/en/product/sigald/310506.
2. Nitric acid. https://www.fishersci.co.uk/shop/products/nitric-acid-68-70-d-1-42-certified-ar-analysis-fisher-chemical/p-8015151.
3. Acetone 99.5. https://www.sigmaaldrich.com/GB/en/product/sigald/179124.
4. Bromine. https://www.sigmaaldrich.com/GB/en/product/aldrich/470864.
5. Bromine water 30g/L. https://www.hach.com/bromine-water-30-g-l-29-ml/product?id=7640196046.
6. Vanadium(IV) oxide sulfate hydrate. https://www.sigmaaldrich.com/GB/en/substance/vanadiumivoxidesulfatehydrate16300anhydrousbasis123334203.
7. Vanadium(V) oxide. https://www.sigmaaldrich.com/GB/en/substance/vanadiumvoxide181881314621.
8. 4-hexylresorcinol. https://www.sigmaaldrich.com/GB/en/product/aldrich/209465.
9. Nano-Lab Inc. Multiwalled carbon nanotubes. https://www.nano-lab.com/nanotubes-research-grade.html.
10. Ellison, J.; Batchelor-McAuley, C.; Tschulik, K.; Compton, R. G., The use of cylindrical micro-wire electrodes for nano-impact experiments; facilitating the sub-picomolar detection of single nanoparticles. *Sensor Actuat B-Chem* **2014,** *200,* 47-52.
11. BASi research products Digisim® Simulation Software For Cyclic Voltammetry. https://www.basinc.com/products/ec/digisim.

Chapter 3

Introduction to Carbon Nanotubes and Diffusion at Nanotube and Other Modified Electrodes

In this chapter the properties of carbon nanotubes (CNTs) and their application in a plethora of fields including sensing, energy conversion and storage technologies is discussed. CNTs are often deployed for electrochemical applications by drop-casting them over conductive substrate electrodes using cyclic voltammetry. Often these modified electrodes are formed of randomly distributed CNTs with can form multi-layers of significant porosity. This chapter discusses the mass transport of analyte species at such thick porous structures which underpins the experimental studies of the Br_2/Br^- and VO_2^+/VO^{2+} redox couples in subsequent chapters.

A part of this chapter has been published as a mini-review co-authored with Mr. Yifei Zhang in the journal Electrochemistry Communications[1].

3.1 Introduction

Carbon nanotubes (CNTs) emerged as a novel nanomaterial following their discovery in 1991 by Ijima[2, 3] and have subsequently received vast attention across a plethora of areas. The interest in and use of CNTs arise from properties such as high surface area, high electrical and thermal conductivity, chemical inertness in some applications and their surface defect rich geometry and ease of functionalisation due to surface groups such as carboxyl or quinone groups[4-6] which is an attractive feature for supporting heterogeneous catalysts like Pt, Pd[7-9]. The structure of CNTs takes the form of 'rolled-up' graphite sheets[10]. CNTs can be broadly classified into two principal types namely single-walled carbon nanotubes (SWCNTs) and multiwalled carbon nanotubes (MWCNTs). The

diameter of the CNTs range from a few to tens of nanometres and the lengths are generally in micrometres. The morphology of the MWCNTs depends on the synthetic route by which they are made. The two most important routes are chemical vapour deposition or the high voltage discharge arc method. Thus, MWCNTs can form as 'hollow-tubes', 'herringbone' or 'bamboo-like' structures as shown in Figure 3.1[10]. Similar to graphite the ends of the CNTs can be described as 'edge-plane-like' and the walls as 'basal-plane-like'. Hence, both 'herringbone' and 'bamboo-like' MWCNTs have huge numbers of 'edge-plane-like' sites that are thought to be responsible for the electrochemical properties[11-15].

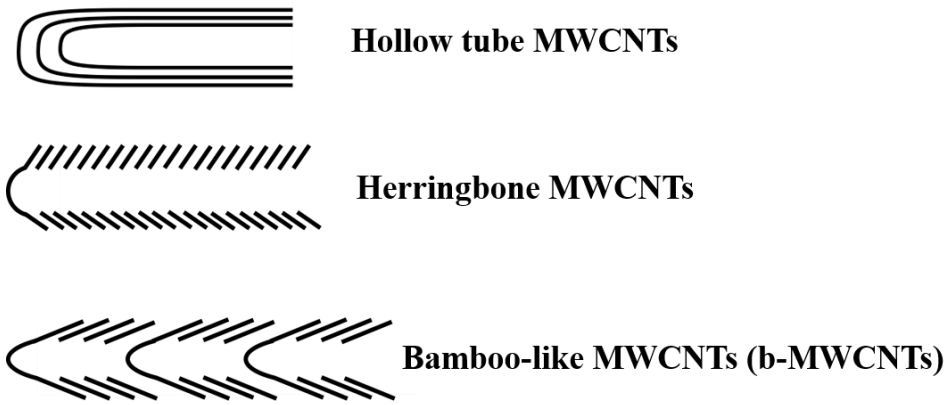


Figure 3.1 Schematic showing idealised different forms of MWCNTs

CNTs have found wide application for electrochemical sensing and electrocatalysis often in the form of modified electrodes CNTs composites are widely used for energy conversion and storage. A few examples where CNTs have been used effectively for electroanalysis are given in Table 3.1 and the applications in energy conversion are illustrated by the selected examples given in Table 3.2.

Table 3.1 Examples of CNTs modified electrodes in electroanalysis

CNTs modified electrode	Application / Technique used	Reference
Multiwalled carbon nanotubes (MWCNTs) modified glassy carbon (GC) electrodes	Detection of 2,4,6-trinitrotoluene via adsorptive stripping voltammetry.	[16]

GC modified with MWCNTs and ionic liquids	Detection of ciprofibrate using differential pulse voltammetry	[17]
MWCNTs modified screen printed electrodes	Detection of hesperidin using adsorptive stripping voltammetry.	[18]
MWCNTs modified GC electrode	Detection of hydrocholothiazide (HCT) and triamterene (TRT) using stripping voltammetry.	[19]
Au nanoparticles deposited CNTs modified GC electrode	Determination of As (III) using anodic stripping voltammetry	[20]
Functionalised MWCNTs modified GC electrode	Determination of paraquat using square-wave voltammetry	[21]

Table 3.2 Examples of CNTs composite electrodes in batteries and fuel cells

CNTs electrode composite	Application	Reference
MWCNTs/tin oxide (SnO_2) nanocomposite	Anode material in microbial fuel cell	[22]
Electrodeposited Pt-Ru and Pt-Ru-Ni nanoclusters on MWCNTs.	Electrocatalyst for oxygen reduction reaction (ORR) and methanol oxidation reaction (MOR)	[23]
Pd deposited MWCNTs	Anode material in direct formic acid fuel cell	[24]
Graphene oxide/MWCNTs nanocomposite	Electrocatalyst for vanadium redox flow battery	[25]
RuO_2 modified CNTs	Cathode in Li-O_2 wearable battery	[26]
Nitrogen doped CNTs	Cathode material for lithium-air batteries	[27]
Single-walled carbon nanotube (SWCNT) doped with nitrogen and phosphorous.	Bifunctional oxygen electrocatalyst	[28]

From Tables 3.1 and 3.2 it can be inferred that CNTs ensembles play a major role in electrocatalysis underpinning many different sensors, fuel cells and batteries. Electrodes

modified with CNTs are usually assumed to promote the electron transfer reactions of interest to the particular application. The fast, or otherwise, electron transfer kinetics of these modified electrodes is invariably analysed using the cyclic voltammetry technique. The criterion used is based on a reduced peak-to-peak separation of the redox peaks in a cyclic voltammogram as shown in Figure 3.2. The origin of this diagnostic has a basis in the well-developed theory of irreversible electron transfer kinetics within the Butler-Volmer (or Marcusian) framework at a planar electrode. The extent to which this is applicable to modified electrodes is critically discussed following the next section which explains the origin of the relationship between the peak-to-peak separation and the rate of electron transfer.

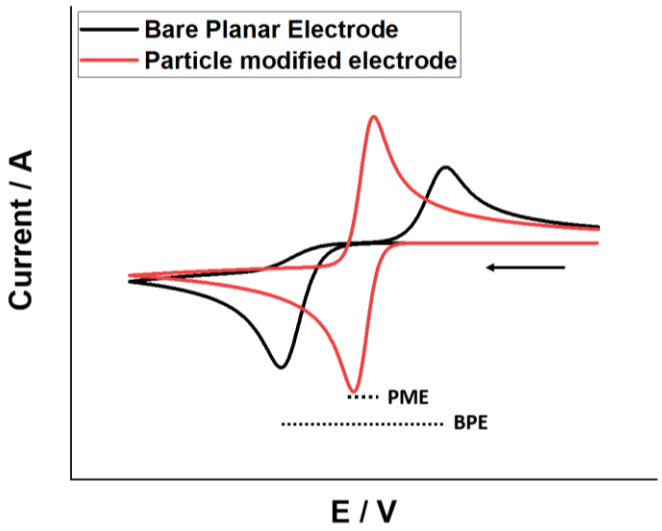


Figure 3.2 Representative cyclic voltammograms at a bare planar electrode (BPE) and at a particle modified electrode (PME) showing a reduced peak-to-peak separation for PME compared to BPE electrode which is often thought to indicate "electrocatalysis".

3.2 Theory: Diffusion at Planar and Modified Electrodes

This section discusses cyclic voltammetry at planar electrodes and the factors governing the peak-to-peak separation at planar macroelectrodes. Further the type of diffusion at planar electrode is explained and compared with the type of diffusion at particle modified

electrodes, especially carbon nanotube modified electrodes, with thick porous structures and its effect on the observed voltammetry.

3.2.1 Cyclic Voltammetry at Planar Electrodes

In chapter 1 we discussed that within the Butler-Volmer kinetic framework the rate of electron transfer is determined partly by the electrochemical rate constant k^0 as well as the electrode potential and the transfer coefficients. In simple terms the larger the rate constant the faster is the electrode kinetics and more "electrochemically reversible" is the electrochemical reaction or otherwise. The reversibility or irreversibility of the reaction is determined by the magnitude of the electrochemical rate constant relative to the prevailing rate of mass transport to the electrode. The rate of mass transport is crudely estimated using the mass transport coefficient m_T,

$$m_T = \frac{D}{\delta} \tag{3.1}$$

where δ is the diffusion layer thickness at a planar electrode undergoing a voltammetric scan and which depends approximately on the duration of the electrolysis time t by,

$$\delta \sim \sqrt{Dt} \tag{3.2}$$

where t is the time taken to scan the voltammogram across given potential and is given by,

$$\mathrm{t} \sim \frac{RT}{Fv} \tag{3.3}$$

where v is the scan rate in V per second. Eq. (3.2) assumes semi-infinite linear diffusion of the analyte to the planar electrode surface as shown in Figure 3.3. In such cases, the electrochemically active electrode area is uniformly accessible with the contributions from the electrode edge negligible since the size (radius) of the electrode is much greater

than the diffusion layer thickness. The term 'semi-infinite' implies that the expansion of the diffusion layer into the solution does not meet any boundaries or obstacles.

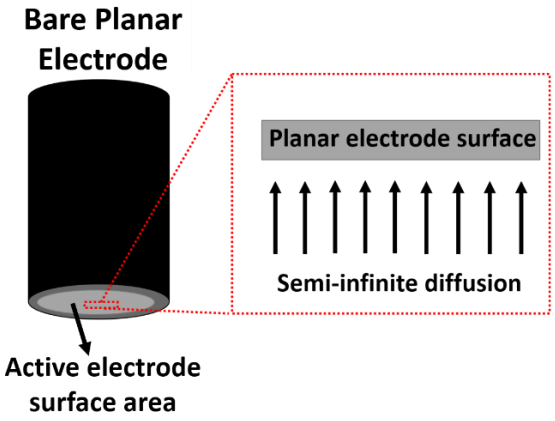


Figure 3.3 Schematic representation of semi-infinite diffusion at planar macroelectrodes.

Eq. (3.1) can be rewritten as

$$m_T \sim \sqrt{\frac{D}{(RT/Fv)}} \tag{3.4}$$

For a reversible reaction, the relationship between k^0 and m_T is given by,

$$k^0 \gg m_T \tag{3.5}$$

and for an irreversible reaction,

$$k^0 \ll m_T \tag{3.6}$$

The transition between the reversible and irreversible limits is followed by parameter Λ coined by Matsuda and Ayabe[29] and is defined by,

$$\Lambda = \frac{k^0}{\left(\frac{FDv}{RT}\right)^{1/2}} \tag{3.7}$$

According to Matsuda and Ayabe the following ranges were suggested for the three different classification at a stationary planar macroelectrodes:

i) Reversible

$$\Lambda \geq 15 \qquad k^0 \geq 0.3v^{1/2}\ cm\ s^{-1} \tag{3.8}$$

ii) Quasi-reversible

$$15 > \Lambda > 10^{-3} \qquad 0.3v^{1/2} > k^0 > 2 \times 10^{-5}\ v^{1/2}\ cm\ s^{-1} \tag{3.9}$$

iii) Irreversible

$$\Lambda \leq 10^{-3} \qquad k^0 \leq 2 \times 10^{-5}\ v^{1/2}\ cm\ s^{-1} \tag{3.10}$$

Note that here the numerical values were calculated for 298 K and assuming $\alpha \sim 0.5$[30].

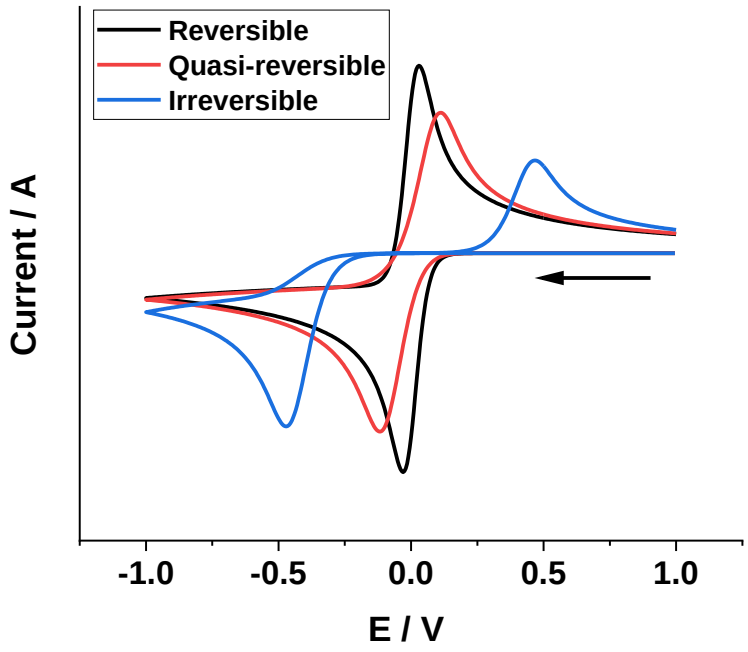


Figure 3.4 Schematic representation of reversible, quasi-reversible and irreversible cyclic voltammograms.

Figure 3.4 shows representative cyclic voltammograms for reversible, quasi-reversible and irreversible process. Here, for reversible voltammogram the separation between oxidative and reductive peak is less when compared to the quasi-reversible voltammogram and much less than the irreversible voltammograms. In addition, from the

fully irreversible to the fully reversible process there is a small increase in the peak current.

As discussed in Chapter 1 the thickness of the diffusion layer depends on the time taken to scan the voltammogram. The longer the time taken, the thicker is the diffusion layer, contrariwise, the faster the sweep rate the thinner is the diffusion layer. The voltammetric peak current reflects the maximum diffusive flux across the diffusion layer so the variation of the peak current I_p with voltage scan rate shows an increase with the scan rate. This is quantitatively described by the Randles-Ševčik equation for a simple one electron transfer for both reversible and irreversible processes as,

i) Reversible

$$I_p = 2.69 \times 10^5 AD^{1/2}[A]_{bulk}\upsilon^{1/2} \qquad at\ 298\ K \tag{3.11}$$

ii) Irreversible

$$I_p = 2.99 \times 10^5 \sqrt{\alpha} AD^{1/2}[A]_{bulk}\upsilon^{1/2} \quad at\ 298\ K \tag{3.12}$$

where α (for a reduction, or β for an oxidation reaction) is the transfer coefficient calculated from Tafel analysis as mentioned in Chapter 1, A is the active electrode surface area, D is the diffusion coefficient, $[A]_{bulk}$ is the concentration of the analyte species and υ is the scan rate.

The extent of the electrochemical reversibility is reflected in the peak-to-peak separation, ΔE_{pp} of the cyclic voltammograms and is given by

$$\Delta E_{pp} = |E_p(anodic) - E_p(cathodic)| \tag{3.13}$$

where E_p *(anodic)* and E_p *(cathodic)* are the peak potential of oxidative and reductive peaks respectively.

ΔE_{pp} changes at low scan rates, from reversible limit where, for a one electron process

$$\Delta E_{pp} = 2.218\frac{RT}{F} = 57\ mV\ (at\ 298\ K) \tag{3.14}$$

to high scan rates, the irreversible limit where, again for a one-electron process

$$\Delta E_{pp} = \frac{RT}{\alpha F}\ln \upsilon + constant \tag{3.15}$$

$$\Delta E_{pp} = \frac{59.4}{\alpha}\, log_{10}\, \upsilon + constant\ (at\ 298\ K)$$

Hence, to conclude in the reversible limit ΔE_{pp} is approximately 57 mV (at 298 K) and is independent of the scan rate, whereas under quasi and irreversible conditions ΔE_{pp} depends on the scan rate and the electrochemical rate constant. The peak-to-peak separation increases with scan rate but decreases with an increase in the rate constant. These conclusions however assume semi-infinite diffusion. In the next section we discuss voltammetry under thin layer conditions where the expansion of the diffusion layer during electrolysis is limited by the close proximity of a boundary to the electrode and which thus serves to spatially confine the diffusion layer.

3.2.2 Thin-Layer Voltammetry

Electrolysis of species in solution phase occurs under "thin-layer" conditions when the diffusion layer thickness ($\sim\sqrt{\pi Dt}$) reaches the boundary of the electrochemical cell. In such cases the current response of an electrochemically reversible process is more symmetrical than seen for semi-infinite diffusion as shown in Figure 3.5. Note the absence of the 'diffusional tail' seen for semi-infinite diffusion where the current decays $1/\sqrt{t}$ at potentials beyond the peak current.

For a reversible one electron transfer reaction ($A + e^- \rightarrow B$) under thin-layer the peak potential is similar to that of the formal potential $E_p = E_F^O$ and the peak current is given by,

$$I_p = \frac{F^2}{4RT} \upsilon AC \tag{3.16}$$

where υ is the scan rate, A is the area of the electrode and C is the concentration of analyte, A, assumed to be uniform in the thin layer prior to electrolysis where the initial concentration of B is zero. Note that in the limit of full thin-layer behaviour the concentrations of A and B remain uniform throughout the layer at all times at levels controlled by the electrode potential[31]. The peak-to-peak separation is independent of the scan rate and equal to zero since diffusional hysteresis is absent. The peak potentials correspond to the formal potential of the A/B couple.

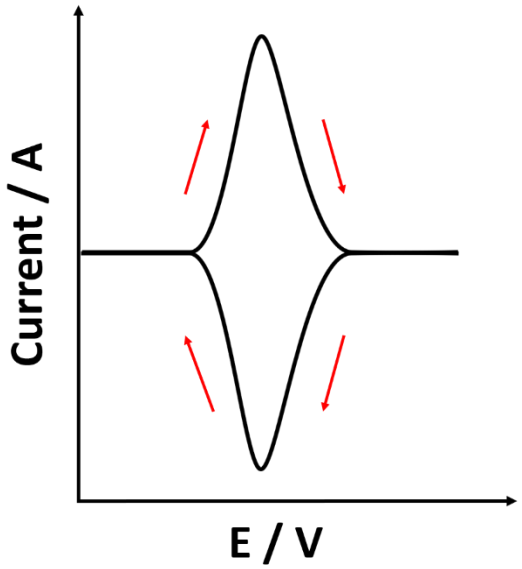


Figure 3.5 Representative cyclic voltammogram for a thin-layer cell showing symmetric redox peaks for an electrochemically reversible process.

In contrast, for a fully irreversible reductive electron transfer the peak potential, E_{pr} is given by,

$$E_{pr} = E_F^O + \frac{RT}{\alpha F} ln\left(\frac{RTk^o}{\alpha FA\upsilon}\right) \tag{3.17}$$

where E_F^O is the formal potential, A is the area of the cell, α is the transfer coefficient for a reduction reaction (to be replaced by β for an oxidation). Note that as the scan rate

increases, or the standard electrochemical rate constant decreases the reductive peak potential shifts to more negative values. The peak current for an irreversible reduction reaction, I_{pr} is,

$$I_{pr} = \frac{\alpha F^2}{2.718RT} \upsilon AC \tag{3.18}$$

Looking at both Eqs (3.16) and (3.18) it is noteworthy that in both the cases, the peak current is directly proportional to the scan rate (υ) unlike in semi-infinite diffusion where it is proportional to the square root of scan rate ($\upsilon^{1/2}$) as in Eq. (3.11) and (3.12). Note that though I_p is proportional to υ, the total charge under the i-E curve in Figure 3.5 is independent of υ as this corresponds to the complete electrolysis of all the analyte in the thin layer cell.

In general, if measurements of the peak potential are made as a function of scan rate the diffusional character ranging between the extreme limits of semi-infinite and thin-layer diffusion can be quantified by means of a log-log plot of the peak current against scan rate, the slope of which will lie between 0.5 and 1.0 corresponding to the two limits with intermediate values indicating a mixed character. Such plots are useful in the study of carbon nanotube modified electrodes which are next considered.

3.2.3 Diffusion at CNTs Modified Electrodes

The electrochemical behaviour of CNTs is usually studied by drop-casting them on a substrate electrode[32-34]. Figure 3.6 shows a schematic representation of the drop-cast technique. In this method, the CNTs are suspended in a solvent and a known volume of the aliquot is drop-casted over the substrate electrode and then dried before use. Such an electrode is denoted a CNTs modified electrode (CME).

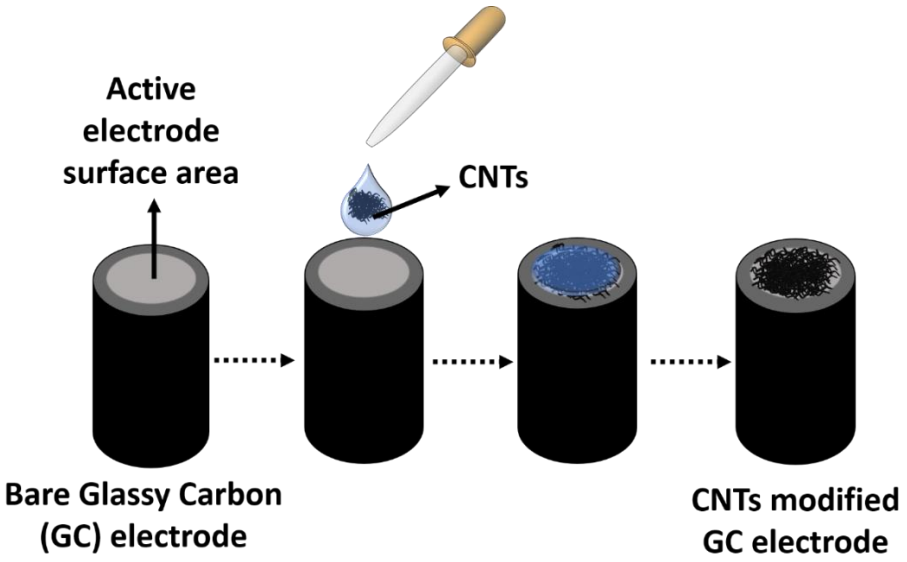


Figure 3.6 A schematic representation of drop-casting technique

Table 3.3 Examples of CNTs modified electrodes reported to show electrocatalytic behaviour.

Electrode	Reaction or species studied	Electrocatalytic w.r.t	Reference
MWCNTs modified GC	H_2O_2	GC	[35]
OCNTs modified GC	NADH oxidation	GC	[36]
MWCNT and SWCNT on GC	Catechol	GC	[37]
MWCNT and SWCNT on GC	ORR	GC	[38]
MWCNTs modified GC	Paracetamol	GC	[39]
SWCNTs on GC	Norepinephrine	GC	[40]
MWCNTs on GC	Nitric oxide	GC	[41]
MWCNTs on GC	H_2O_2	GC	[42]
MWCNTs on GC	Cysteine	GC	[43]
MWCNTs on GC	Hydrazine	GC	[44]

MWCNTs on GC	Vitamin D3 oxidation	GC	[45]
MWCNTs on GC	Dopamine	GC	[46]
MWCNTs on GC	Hydroquinone and Catechol	GC	[47]
MWCNTs on GC	Choline	GC	[48]
MWCNTs on GC	Ascorbic and uric acid	GC	[49]
MWCNTs on GC	Glucose oxidase	GC	[50]

MWCNTs, multiwalled carbon nanotubes, OCNTs, ordered carbon nanotubes, SWCNTs, single walled carbon nanotubes, GC, glassy carbon electrode, NADH, Nicotinamide adenine dinucleotide, ORR, oxygen reduction reaction

Typically, as exemplified in Table 3.3 'faster electrode kinetics' for a given redox reaction are reported at a CME than at the substrate electrode, often glassy carbon and so is generically interpreted as "electrocatalysis" by the nanotubes. This conclusion is drawn from the voltammogram by observing a decreased peak-to-peak separation of CME than the substrate electrode. However, such comparison is only valid if both the electrodes have similar mass transport regimes since the peak potential reflects a point of balance between the electrode kinetics and the rate of mass transport; the reduction may reflect a change in either or both of these quantities. Usually a CME is made with a thick layer of CNTs so that the redox reaction of interest occurs fully at the CNTs rather than at the underlying substrate electrode. For this a strong overlap of the diffusion layers of each CNT is required such that the coverage leads to of overall linear diffusion to the CME. According to Einstein's theory, for a voltammetric timescale t, the CNTs need to be within a distance of $\delta = (6Dt)^{1/2}$ from one another for a strong overlap[51] so that the

particles dominate the signal and not the substrate electrode. For instance, when $D = 10^{-5}$ cm^2 s^{-1}, for a timescale of few seconds, δ can be as large as *ca.* 100 microns. Thus, for a random distribution of particles at substrate electrode, a coverage of 10^5 particles cm^{-2} is required. Typically in experiments very much larger amounts of particles are deposited, as shown in Figure 3.7, covering the conductive area of the substrate electrode[52]. The effect of different coverages of CNTs modified electrodes on the cyclic voltammetry is discussed in detail in Chapter 4 for the Br_2/Br^- redox couple.

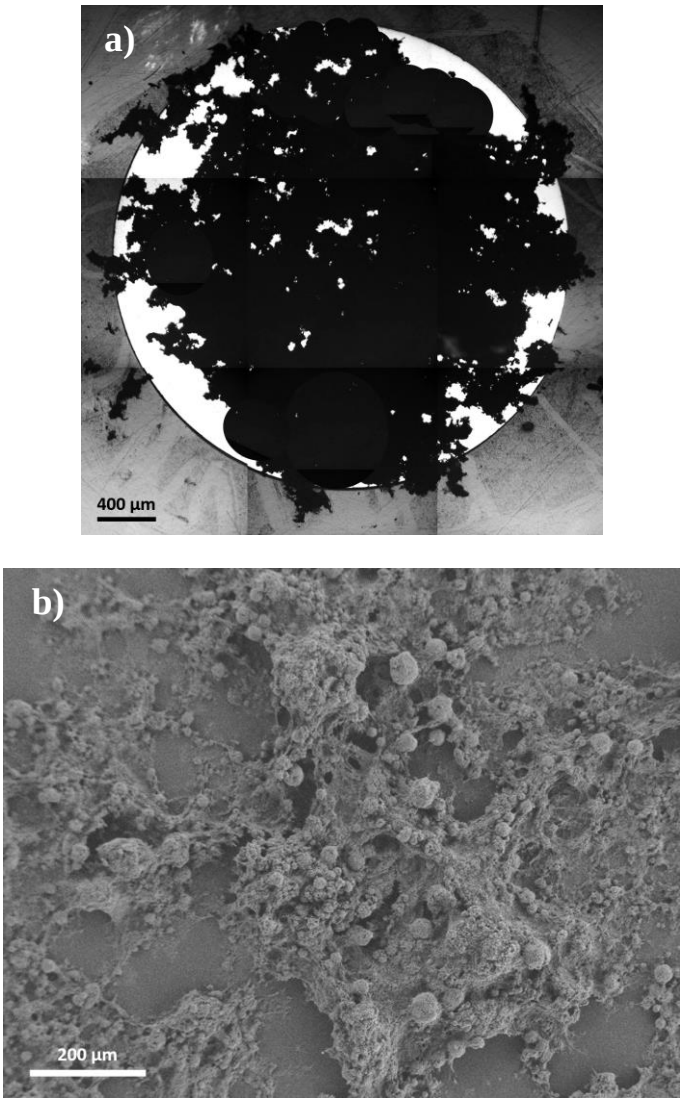


Figure 3.7 Images from optical microscope for a GC electrode with a geometric area 0.07 cm^2 which was drop-casted with 30 µg of CNTs, and) SEM images of CNTs drop-casted over carbon slab.

For most CMEs we can assume that the voltammetric signal arises exclusively from the CNTs and not the substrate electrode. The drop-casted CNTs on a substrate electrode usually exist as a thick porous layer where the nanotubes agglomerate and form pockets as implicit in the SEM images in Figure 3.7. It can be inferred that during the electrolysis process the modified electrode shows semi-infinite diffusion to the surface of the electrode. However, in the porous structure the electrolyte is trapped in CNTs pockets given that the average CNT to CNT separation is small compared to the distance diffused on the voltammetric timescale this resembles a thin-layer cell as discussed in the previous section[53-55]. Electrolysis within the film thus takes place under thin layer conditions. Under such circumstances, the peak potential shifts closer to the formal potential of the redox species than the peak potential measured under semi-infinite diffusion condition all other factors remaining constant[54].

In general (both reversible and irreversible reactions) voltammetry at a CME will show two signals for a single redox process. One signal arises from semi-infinite diffusion to the surface of the electrode mirroring that expected for an approximately flat non-porous surface and the other signal, observed nearer to the formal potential of the redox process of interest, that is to say with lower overpotential, is due to the electrolysis of reactant trapped in the porous structure displaying characteristics of 'thin-layer' voltammetry[56, 57]. Figure 3.8a shows a schematic representation of both semi-infinite diffusion to the CME surface and thin-layer electrolysis at the porous pockets and Figure 3.8b shows typical simulated voltammetry showing the splitting of peaks corresponding to the 'thin-layer' and semi-infinite diffusion peaks. The arrows in the figure show that as the amount of analyte in the porous layer increases the former peak increases relative to the latter peak. The simulated voltammogram is reproduced from reference[56].

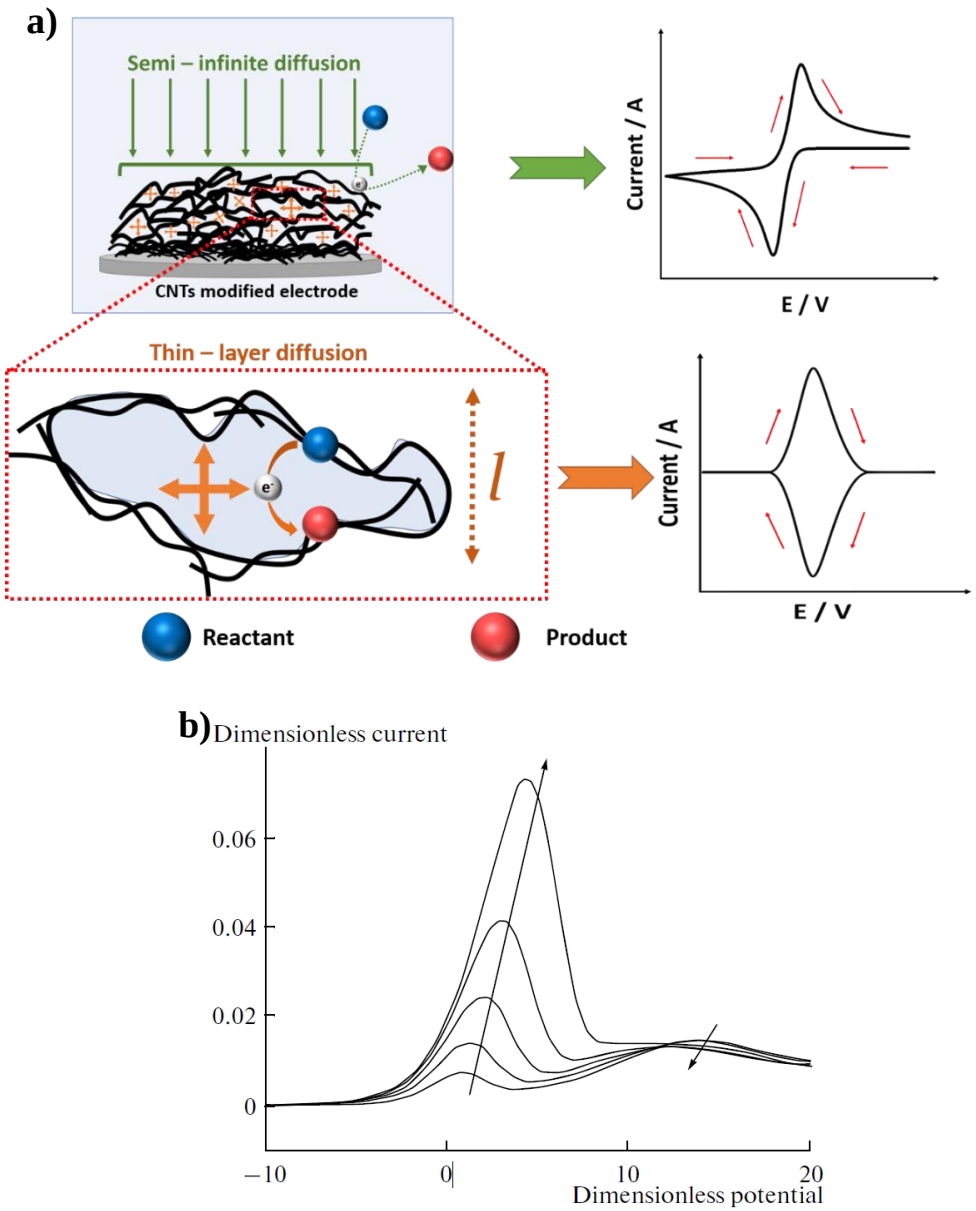


Figure 3.8 a) Schematic representation of semi-infinite diffusion at surface of CNTs (green arrows) and thin-layer diffusion (orange cross arrows) in the porous pockets formed by CNTs is shown along with their corresponding voltammetric signals and b) simulated voltammetry showing the two peaks seen for a single redox process arising from 'thin-layer' and semi-infinite diffusion. The arrows show an increase the peak current for thin-layer relative to that for semi-infinite diffusion as the amount of analyte in the porous layer increases. The figure is adapted from reference[56].

Note that the relative sizes of the two signals are controlled by the size of the porous layer of CNTs since the magnitude of the semi-infinite diffusion signal is essentially independent of this parameter whilst the charge passed in the thin layer signal scales with

the extent of the CNT layer. In extreme cases the latter dwarfs the former which can appear negligible. The interplay of semi-infinite diffusion and thin layer effects is generic to electrode modified with nanomaterials; a recent report indicated the presence of two signals for the oxidation of hydrazine at electrodes modified with palladium nanoparticles[58].

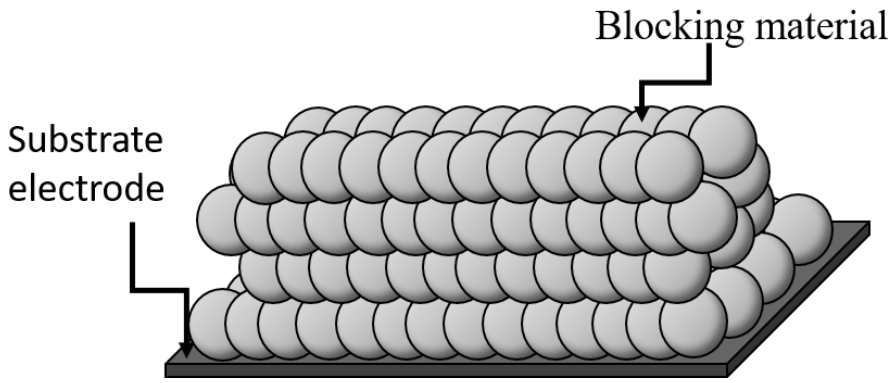


Figure 3.9 Schematic representation of substrate electrode partially blocked by non-conductive particles.

Given the complexity of the voltammetric response seen at CMEs it is interesting to briefly comment on the voltammetry observed when an electrode surface is partially 'blocked' by layers of inert (non-adsorbing, non-conducting) particles which simply serve to change the rate of diffusion of a redox species to the electrode surface, the spheres themselves playing no other role than to physically occupy space within the diffusion layer of the electrode so that electrolysis is exclusively constrained to take place at the electrode surface and not as with CMEs, within the porous layer. Figure 3.9 schematically illustrates the partially blocked electrode[59, 60].

Even for a fully electrochemically reversible reaction, due to the interplay of semi-infinite diffusion and thin-layer constraints inside the porous layers formed by the non-conductive nanoparticles the voltammetric signal is reduced in magnitude but importantly, the peak

to peak separation can increase or decrease relative to what is seen at the bare electrode even when the process is constrained to be fully Nernstian (reversible) in simulations! Such, results are intuitively interpreted as positive or negative catalysis. The exact responses depend on the voltage scan rate (in the case of linear sweep voltammetry), the number of monolayers of particles and the particle size[57, 59-61]. That such complexity in the voltammetric response is apparent even for the simplest possible case – that of a fully reversible process at a partially blocked electrode covered in a regular layered array of identically sized spheres – cautions against the drawing of firm conclusions in respect of 'electrocatalysis' using the cyclic voltammetry of CMEs or other particle modified electrodes alone. Thus, to understand the intrinsic catalytic property of nanoparticles, including CNTs, the 'nano-impact' technique is adopted where single nanoparticle is studied as discussed in Chapter 1. This method is used in Chapters 6 to 8 to assess CNTs as an electro-catalyst (or otherwise) for various redox couples.

3.3 Conclusions

To conclude, in this chapter we have discussed the complexity of interpreting cyclic voltammetric data for identifying the possible electro-catalytic behaviour of CNTs. Peak potentials and peak currents measured in isolation are likely to be ambiguous not least due to an uncertain mixture of semi-infinite diffusion and thin-layer effects at the surface and within the porous structure of CNTs layers respectively. The need to complement voltammetry with single entity measurements has been stressed, and this is reflected in the experimental approaches adopted in the following chapters.

References

1. Kumar, A. K. S.; Zhang, Y. F.; Li, D. L.; Compton, R. G., A mini-review: How reliable is the drop casting technique? *Electrochemistry Communications* **2020,** *121*, 106867.

2. Iijima, S., Helical Microtubules of Graphitic Carbon. *Nature* **1991,** *354* (6348), 56-58.

3. Iijima, S.; Ichihashi, T., Single-Shell Carbon Nanotubes of 1nm Diameter. *Nature* **1993,** *363* (6430), 603-605.

4. Li, X. T.; Hodson, H.; Batchelor-McAuley, C.; Shao, L. D.; Compton, R. G., Improving Formate and Methanol Fuels: Catalytic Activity of Single Pd Coated Carbon Nanotubes. *ACS Catal* **2016,** *6* (10), 7118-7124.

5. Ye, H. S.; Liu, X.; Cui, H. F.; Zhang, W. D.; Sheu, F. S.; Lim, T. M., Electrochemical oxidation of multi-walled carbon nanotubes and its application to electrochemical double layer capacitors. *Electrochemistry Communications* **2005,** *7* (3), 249-255.

6. Barathi, P.; Kumar, A. S., Facile Electrochemical Oxidation of Polyaromatic Hydrocarbons to Surface-Confined Redox-Active Quinone Species on a Multiwalled Carbon Nanotube Surface. *Chem-Eur J* **2013,** *19* (7), 2236-2241.

7. Terrones, M., Carbon nanotubes: synthesis and properties, electronic devices and other emerging applications. *Int Mater Rev* **2004,** *49* (6), 325-377.

8. Gooding, J. J., Nanostructuring electrodes with carbon nanotubes: A review on electrochemistry and applications for sensing. *Electrochim Acta* **2005,** *50* (15), 3049-3060.

9. Serp, P.; Corrias, M.; Kalck, P., Carbon nanotubes and nanofibers in catalysis. *Appl Catal a-Gen* **2003,** *253* (2), 337-358.

10. Banks, C. E.; Davies, T. J.; Wildgoose, G. G.; Compton, R. G., Electrocatalysis at graphite and carbon nanotube modified electrodes: edge-plane sites and tube ends are the reactive sites. *Chem Commun* **2005,** (7), 829-841.

11. Banks, C. E.; Moore, R. R.; Davies, T. J.; Compton, R. G., Investigation of modified basal plane pyrolytic graphite electrodes: definitive evidence for the electrocatalytic properties of the ends of carbon nanotubes. *Chem Commun* **2004,** (16), 1804-1805.

12. Moore, R. R.; Banks, C. E.; Compton, R. G., Basal plane pyrolytic graphite modified electrodes: Comparison of carbon nanotubes and graphite powder as electrocatalysts. *Analytical Chemistry* **2004,** *76* (10), 2677-2682.

13. Stuart, E. J. E.; Pumera, M., Nanographite Impurities of Single-Walled and Double-Walled Carbon Nanotubes Are Responsible for the Observed "Electrocatalytic" Effect towards the Reduction of Azo Groups. *Chem-Asian J* **2011,** *6* (3), 804-807.

14. Bom, D.; Andrews, R.; Jacques, D.; Anthony, J.; Chen, B. L.; Meier, M. S.; Selegue, J. P., Thermogravimetric analysis of the oxidation of multiwalled carbon nanotubes: Evidence for the role of defect sites in carbon nanotube chemistry. *Nano Letters* **2002,** *2* (6), 615-619.

15. Pumera, M.; Sasaki, T.; Iwai, H., Relationship between Carbon Nanotube Structure and Electrochemical Behavior: Heterogeneous Electron Transfer at Electrochemically Activated Carbon Nanotubes. *Chem-Asian J* **2008,** *3* (12), 2046-2055.

16. Wang, J.; Hocevar, S. B.; Ogorevc, B., Carbon nanotube-modified glassy carbon electrode for adsorptive stripping voltammetric detection of ultratrace levels of 2,4,6-trinitrotoluene. *Electrochemistry Communications* **2004,** *6* (2), 176-179.

17. Vicentini, F. C.; Ravanini, A. E.; Silva, T. A.; Janegitz, B. C.; Zucolotto, V.; Fatibello, O., A novel architecture based upon multi-walled carbon nanotubes and ionic liquid to improve the electroanalytical detection of ciprofibrate. *Analyst* **2014,** *139* (16), 3961-3967.

18. Sims, M. J.; Li, Q.; Kachoosangi, R. T.; Wildgoose, G. G.; Compton, R. G., Using multiwalled carbon nanotube modified electrodes for the adsorptive striping voltammetric determination of hesperidin. *Electrochim Acta* **2009,** *54* (22), 5030-5034.

19. Hudari, F. F.; Souza, J. C.; Zanoni, M. V. B., Adsorptive stripping voltammetry for simultaneous determination of hydrochlorothiazide and triamterene in hemodialysis samples using a multi-walled carbon nanotube-modified glassy carbon electrode. *Talanta* **2018,** *179*, 652-657.

20. Xiao, L.; Wildgoose, G. G.; Compton, R. G., Sensitive electrochemical detection of arsenic (III) using gold nanoparticle modified carbon nanotubes via anodic stripping voltammetry. *Anal Chim Acta* **2008,** *620* (1-2), 44-49.

21. Garcia, L. L. C.; Figueiredo, L. C. S.; Oliveira, G. G.; Fatibello, O.; Banks, C. E., Square-wave voltammetric determination of paraquat using a glassy carbon electrode modified with multiwalled carbon nanotubes within a dihexadecylhydrogenphosphate (DHP) film. *Sensor Actuat B-Chem* **2013,** *181*, 306-311.

22. Mehdinia, A.; Ziaei, E.; Jabbari, A., Multi-walled carbon nanotube/SnO2 nanocomposite: a novel anode material for microbial fuel cells. *Electrochim Acta* **2014,** *130*, 512-518.

23. Zhao, Y.; Fan, L. Z.; Ren, J. L.; Hong, B., Electrodeposition of Pt-Ru and Pt-Ru-Ni nanoclusters on multi-walled carbon nanotubes for direct methanol fuel cell. *Int J Hydrogen Energ* **2014,** *39* (9), 4544-4557.

24. Mazurkiewicz-Pawlicka, M.; Malolepszy, A.; Mikolajczuk-Zychora, A.; Mierzwa, B.; Borodzinski, A.; Stobinski, L., A simple method for enhancing the catalytic activity of Pd deposited on carbon nanotubes used in direct formic acid fuel cells. *Appl Surf Sci* **2019,** *476*, 806-814.

25. Han, P. X.; Yue, Y. H.; Liu, Z. H.; Xu, W.; Zhang, L. X.; Xu, H. X.; Dong, S. M.; Cui, G. L., Graphene oxide nanosheets/multi-walled carbon nanotubes hybrid as an excellent electrocatalytic material towards VO^{2+}/VO_2^{+} redox couples for vanadium redox flow batteries. *Energ Environ Sci* **2011,** *4* (11), 4710-4717.

26. Liu, T.; Xu, J. J.; Liu, Q. C.; Chang, Z. W.; Yin, Y. B.; Yang, X. Y.; Zhang, X. B., Ultrathin, Lightweight, and Wearable LiO_2 Battery with High Robustness and Gravimetric/Volumetric Energy Density. *Small* **2017,** *13* (6).

27. Li, Y. L.; Wang, J. J.; Li, X. F.; Liu, J.; Geng, D. S.; Yang, J. L.; Li, R. Y.; Sun, X. L., Nitrogen-doped carbon nanotubes as cathode for lithium-air batteries. *Electrochemistry Communications* **2011,** *13* (7), 668-672.

28. Li, J. C.; Hou, P. X.; Cheng, M.; Liu, C.; Cheng, H. M.; Shao, M. H., Carbon nanotube encapsulated in nitrogen and phosphorus co-doped carbon as a bifunctional electrocatalyst for oxygen reduction and evolution reactions. *Carbon* **2018,** *139*, 156-163.

29. Matsuda, H.; Ayabe, Y., Zur Theorie Der Randles-Sevcikschen Kathodenstrahl-Polarographie. *Z Elektrochem* **1955,** *59* (6), 494-503.

30. Compton, R. G.; Banks, C. E., *Understanding Voltammetry, 3rd Edition* **2018**, 1-439.

31. Hubbard, A. T., Study of the kinetics of electrochemical reactions by thin-layer voltammetry: I. theory. *Journal of Electroanalytical Chemistry and Interfacial Electrochemistry* **1969,** *22* (2), 165-174.

32. Zhou, Y. G.; Campbell, F. W.; Belding, S. R.; Compton, R. G., Nanoparticle modified electrodes: Surface coverage effects in voltammetry showing the transition from convergent to linear diffusion. The reduction of aqueous chromium (III) at silver nanoparticle modified electrodes. *Chem Phys Lett* **2010,** *497* (4-6), 200-204.

33. Wang, Y.; Ward, K. R.; Laborda, E.; Salter, C.; Crossley, A.; Jacobs, R. M. J.; Compton, R. G., A Joint Experimental and Computational Search for Authentic Nano-electrocatalytic Effects: Electrooxidation of Nitrite and L-Ascorbate on Gold Nanoparticle-Modified Glassy Carbon Electrodes. *Small* **2013,** *9* (3), 478-486.

34. Chaisiwamongkhol, K.; Ngamchuea, K.; Batchelor-McAuley, C.; Compton, R. G., Electrochemical detection and quantification of gingerol species in ginger (Zingiber officinale) using multiwalled carbon nanotube modified electrodes. *Analyst* **2016,** *141* (22), 6321-6328.

35. Zhao, G. C.; Yin, Z. Z.; Zhang, L.; Wei, X. W., Direct electrochemistry of cytochrome c on a multi-walled carbon nanotubes modified electrode and its electrocatalytic activity for the reduction of H2O2. *Electrochemistry Communications* **2005,** *7* (3), 256-260.

36. Chen, J.; Bao, J. C.; Cai, C. X.; Lu, T. H., Electrocatalytic oxidation of NADH at an ordered carbon nanotubes modified glassy carbon electrode. *Anal Chim Acta* **2004,** *516* (1-2), 29-34.

37. Xu, Z.; Chen, X.; Qu, X. H.; Dong, S. J., Electrocatalytic oxidation of catechol at multi-walled carbon nanotubes modified electrode. *Electroanal* **2004,** *16* (8), 684-687.

38. Kruusenberg, I.; Alexeyeva, N.; Tammeveski, K.; Kozlova, J.; Matisen, L.; Sammelselg, V.; Solla-Gullon, J.; Feliu, J. M., Effect of purification of carbon nanotubes on their

electrocatalytic properties for oxygen reduction in acid solution. *Carbon* **2011,** *49* (12), 4031-4039.

39. Hou, X. L.; Shen, G. J.; Meng, L.; Zhu, L.; Guo, M., Multi-walled carbon nanotubes modified glass carbon electrode and its electrocatalytic activity towards oxidation of paracetamol. *Russ J Electrochem* **2011,** *47* (11), 1262-1267.

40. Wang, J. X.; Li, M. X.; Shi, Z. J.; Li, N. Q.; Gu, Z. N., Electrocatalytic oxidation of norepinephrine at a glassy carbon electrode modified with single wall carbon nanotubes. *Electroanal* **2002,** *14* (3), 225-230.

41. Wu, F. H.; Zhao, G. C.; Wei, X. W., Electrocatalytic oxidation of nitric oxide at multi-walled carbon nanotubes modified electrode. *Electrochemistry Communications* **2002,** *4* (9), 690-694.

42. Wang, J.; Musameh, M., Carbon nanotube/teflon composite electrochemical sensors and biosensors. *Analytical Chemistry* **2003,** *75* (9), 2075-2079.

43. Chen, X.; Yang, Y.; Ding, M. Y., Electrocatalytic oxidation and sensitive detection of cysteine at layer-by-layer assembled carbon nanotube-modified electrode. *Anal Chim Acta* **2006,** *557* (1-2), 52-56.

44. Kamyabi, M. A.; Narimani, O.; Monfared, H. H., Electrocatalytic oxidation of hydrazine using glassy carbon electrode modified with carbon nanotube and terpyridine manganese(II) complex. *J Electroanal Chem* **2010,** *644* (1), 67-73.

45. Ramaprabhu, S.; Fathima, T. K. S., Evaluating the origin of the electrocatalytic activity of multiwalled carbon nanotubes towards Vitamin D3 oxidation. *J Electroanal Chem* **2022,** *911*.

46. Yang, H. C.; Zhou, C. X.; An, J. J.; Yang, L. F.; Yang, Y. Y.; Liu, X. L., Ultra-fast synthesis of iron decorated multiwalled carbon nanotube composite materials: A sensitive electrochemical sensor for determining dopamine. *J Alloy Compd* **2022,** *897*.

47. Yang, M.; Guo, H.; Sun, L.; Wu, N.; Wang, M. Y.; Yang, F.; Zhang, T. T.; Zhang, J. Y.; Pan, Z. L.; Yang, W., Simultaneous electrochemical detection of hydroquinone and catechol using MWCNT-COOH/CTF-1 composite modified electrode. *Colloid Surface A* **2021,** *625*.

48. Uwaya, G. E.; Fayemi, O. E., Electrochemical detection of choline at f-MWCNT/Fe3O4 nanocomposite modified glassy carbon electrode. *Mater Res Express* **2021,** *8* (5).

49. Abellan-Llobregat, A.; Vidal, L.; Rodriguez-Amaro, R.; Canals, A.; Morallon, E., Evaluation of herringbone carbon nanotubes-modified electrodes for the simultaneous determination of ascorbic acid and uric acid. *Electrochim Acta* **2018,** *285*, 284-291.

50. Liu, Y. X.; Zhang, J.; Cheng, Y.; Jiang, S. P., Effect of Carbon Nanotubes on Direct Electron Transfer and Electrocatalytic Activity of Immobilized Glucose Oxidase. *ACS Omega* **2018,** *3* (1), 667-676.

51. Einstein, A. B., On the Motion of Small Particles Suspended in Liquids at Rest Required by the Molecular-Kinetic Theory of Heat *Ann Phys-Berlin* **1905**.

52. Eloul, S.; Compton, R. G., Voltammetric Sensitivity Enhancement by Using Preconcentration Adjacent to the Electrode: Simulation, Critical Evaluation, and Insights. *J Phys Chem C* **2014,** *118* (42), 24520-24532.

53. Streeter, I.; Wildgoose, G. G.; Shao, L. D.; Compton, R. G., Cyclic voltammetry on electrode surfaces covered with porous layers: An analysis of electron transfer kinetics at single-walled carbon nanotube modified electrodes. *Sensor Actuat B-Chem* **2008,** *133* (2), 462-466.

54. Henstridge, M. C.; Dickinson, E. J. F.; Aslanoglu, M.; Batchelor-McAuley, C.; Compton, R. G., Voltammetric selectivity conferred by the modification of electrodes using conductive porous layers or films: The oxidation of dopamine on glassy carbon electrodes modified with multiwalled carbon nanotubes. *Sensor Actuat B-Chem* **2010,** *145* (1), 417-427.

55. Keeley, G. P.; Lyons, M. E. G., The Effects of Thin Layer Diffusion at Glassy Carbon Electrodes Modified with Porous Films of Single-Walled Carbon Nanotubes. *Int J Electrochem Sc* **2009,** *4* (6), 794-809.

56. Henstridge, M. C.; Dickinson, E. J. F.; Compton, R. G., Mass transport to and within porous electrodes. Linear sweep voltammetry and the effects of pore size: The prediction of double peaks for a single electrode process. *Russ J Electrochem* **2012,** *48* (6), 629-635.

57. Katelhon, E.; Compton, R. G., Unscrambling illusionary catalysis in three-dimensional particle-modified electrodes: Reversible reactions at conducting particles. *Appl Mater Today* **2020,** *18*.

58. Miao, R. Y.; Yang, M. J.; Compton, R. G., The Electro-oxidation of Hydrazine with Palladium Nanoparticle Modified Electrodes: Dissecting Chemical and Physical Effects: Catalysis, Surface Roughness, or Porosity? *J Phys Chem Lett* **2021,** *12* (28), 6661-6666.

59. Chen, L. F.; Katelhon, E.; Compton, R. G., Unscrambling illusory inhibition and catalysis in nanoparticle electrochemistry: Experiment and theory. *Appl Mater Today* **2019,** *16*, 141-145.

60. Chen, L. F.; Katelhon, E.; Compton, R. G., Particle-modified electrodes: General mass transport theory, experimental validation, and the role of electrostatics. *Appl Mater Today* **2020,** *18*.

61. Katelhon, E.; Chen, L. F.; Compton, R. G., Nanoparticle electrocatalysis: Unscrambling illusory inhibition and catalysis. *Appl Mater Today* **2019,** *15*, 139-144.

Chapter 4

Surface Heterogeneity of Drop-Casted Electrode Surfaces: Impact on Voltammetry

This chapter investigates the morphology of electrodes modified by drop-casting layers of bamboo-like multiwalled carbon nanotubes (b-MWCNTs) and is shown to exhibit significant heterogeneity in the form of 'patchy' surfaces formed after the evaporation of the carrier solvent. The variation of the heterogeneity with the total average coverage is studied and the consequences for quantitative analytical voltammetry is assessed. Specifically, the oxidation of bromide in aqueous solution is examined at b-MWCNT modified glassy carbon (GC) electrodes. Significant deviations from the expected voltammetry were observed even for average coverages which correspond to much in excess of multiple monolayers of b-MWCNTs. The observed voltammetry is related to the observed porous structure and the use of such modified electrodes, without concomitant microscopic surface characterisation, is caveated.

This chapter has been published in the journal *ChemElectroChem*[1], and was co-authored with Mr. Yifei Zhang where he discusses on the coffee-ring effect observed in case of platinum (Pt) nanoparticles drop-casted electrode and its effect on voltammetric analysis.

4.1 Introduction

In the previous chapter we looked at the aim of modification and the creation of particle modified electrodes (PMEs) such as carbon nanotubes (CNTs) represents a popular approach to impart greater apparent electrocatalytic behaviour to the surface so that the oxidation or reduction of the target analyte occurs at lower potentials, and ideally with larger currents, than that seen at the 'naked' (or 'bare') electrode so minimising the impact

of otherwise interfering species and offering greater analytical sensitivity[2]. Such decreases of overpotential can result from a diversity of effects including changed interfacial electron transfer kinetics, altered mass transport and analyte adsorption effects. A typical schematic representation of the drop-cast technique adopted for modifying electrodes with CNTs is shown in Chapter 3, Figure 3.6.

The first of these effects is expected, since the sensitivity of electron transfer to the chemical and physical nature of the electrode is widely recognized especially in multi-step processes where high energy intermediates can adsorb and so stabilize on some surfaces. Both the hydrogen evolution reaction (HER)[3] and the oxygen reduction reaction (ORR)[4] are paradigm cases with extremes of behaviour noted. Implicit in the idea that the modified layer(s) might change the electron transfer kinetics is the requirement that the particles are electrically conductive and that the electron transfer with the analyte takes place at the particle-solution interface (as opposed to at the substrate electrode). The catalytic voltammetry signal is seen at lower overpotentials than the one seen at the substrate electrode and is such that much of the analyte diffuses to the electrode surface and is consumed at the particles before a voltammetric sweep reaches the potential required for reaction on the underlying electrode. Two controlling factors that govern the voltammetric response are the heterogeneity of the nanoparticle's distribution on the substrate electrode and the response due to the ~~any~~ thick porous layer of nanoparticles[5-7].

First, the diffusion regime can vary according to the coverage of the drop-cast. This heterogeneity of the modified electrode can be classified into four categories as shown in Figure 4.1. In *case 1* (Figure 4.1a), the active electrode and the substrate electrode are widely spaced hence individual diffusional layers are observed and measurements are made at short times (fast scan rates) leading to planar diffusion, this requires $\delta \ll R_e$ where R_e is the radius of the electrode and δ is the size of the diffusion layer. In *case 2* (Figure

4.1b) $\delta > R_e$, the electrodes are again widely spaced but a longer measurement time leads to non-planar diffusion. In *case 3* (Figure 4.1c), the diffusional layers of both the active electrode and the substrate electrode overlap as they are spaced closely to each other. For *case 4* (Figure 4.1d), the spacing between the electrodes are very small compared to that in *case 3* hence strong overlap of the diffusional layers occur wherein, the electrode produces voltammetry almost completely corresponding to that of an active surface with the same geometric area as the substrate electrode. Another controlling factor in modified electrodes is the extent of coverage of the nanotubes which can range from sub-monolayer to a thick, porous layer with tube-tube contacts likely limiting the overall conductivity [8]. As b-MWCNTs are conductive, in the presence of a conductive sub-monolayer, the electrode surface constitutes a 'spatially heterogeneous electrode'[9]. In this case the average interparticle separation controls the observed voltammetry as discussed above. On the other hand, for a thick porous layer of conductive particles the modified electrode can exhibit both semi-infinite diffusion of the analyte from the bulk solution to the surface of the porous layer and thin layer diffusion due to electrolytic discharge within the pores of the porous layer, these effects are discussed in detail in Chapter 3. A thin layer response is observed in some reported nanotube modified electrodes[5, 6, 10] where the voltammetric peak potentials shifted closer to the reversible formal potential of the irreversible redox couple targets.

The purpose of this work is to explore the aspects of the above limiting cases for b-MWCNTs modified GC electrode applied in the oxidation of aqueous bromine. We explore the extent to which drop-casting can result in reproducible surfaces and the extent to which spatial heterogeneity is induced on the drop-casted surface[11].

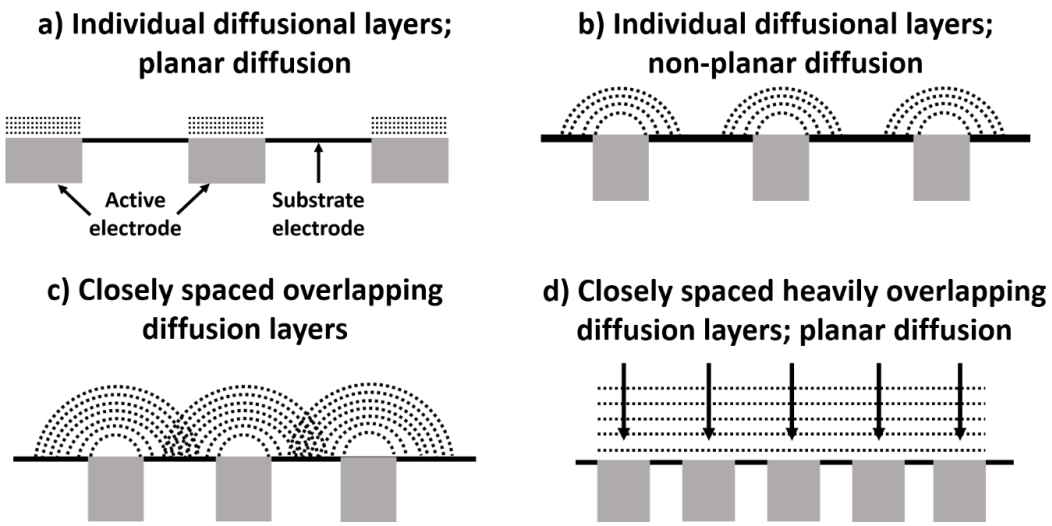


Figure 4.1 Schematic representation of four different cases of diffusion at active and substrate electrode

4.2 Experimental

All the chemicals are given in Chapter 2, Table 2.1. These were purchased commercially and used without any further purification. The details of the characterisation technique including optical microscopy and SEM are given in sections 2.4 and 2.5 respectively.

4.2.1 Preparation of Bare-GC Electrode and b-MWCNTs Modified GC Electrodes

First, the bare GC electrode was polished sequentially with 1.00 μm, 0.30 μm and 0.05 μm alumina slurries and then washed with deionised water, sonicated for 10 s, dried under N_2 flow and used as the working electrode. The diameter of the GC electrode was 0.30 cm with a geometric area of 0.07 cm^2.

For the b-MWCNTs modified GC working electrode, 1 mg of b-MWCNTs were dispersed in 1 mL of acetone by sonicating it for 10 minutes. An aliquot of 6 μL and 30 μL (containing 6 μg and 30 μg) of the b-MWCNTs dispersed solution was drop-casted over polished GC electrode. The modified GC electrode was dried under a constant gentle

nitrogen gas flow for 15 minutes and then used for the voltammetric experiments in a solution of 5 mM of NaBr with 0.1 M of HNO_3.

4.3 Results and Discussion

The electro-catalytic behaviour of drop-casted multiwalled carbon nanotube modified electrodes were investigated in the context of aqueous bromide oxidation. The electrode was modified as described in section 4.2.1. The b-MWCNTs drop-casted GC electrodes were investigated using cyclic voltammetry to study their possible electrocatalytic behaviour in respect of the oxidation of aqueous bromide to bromine.

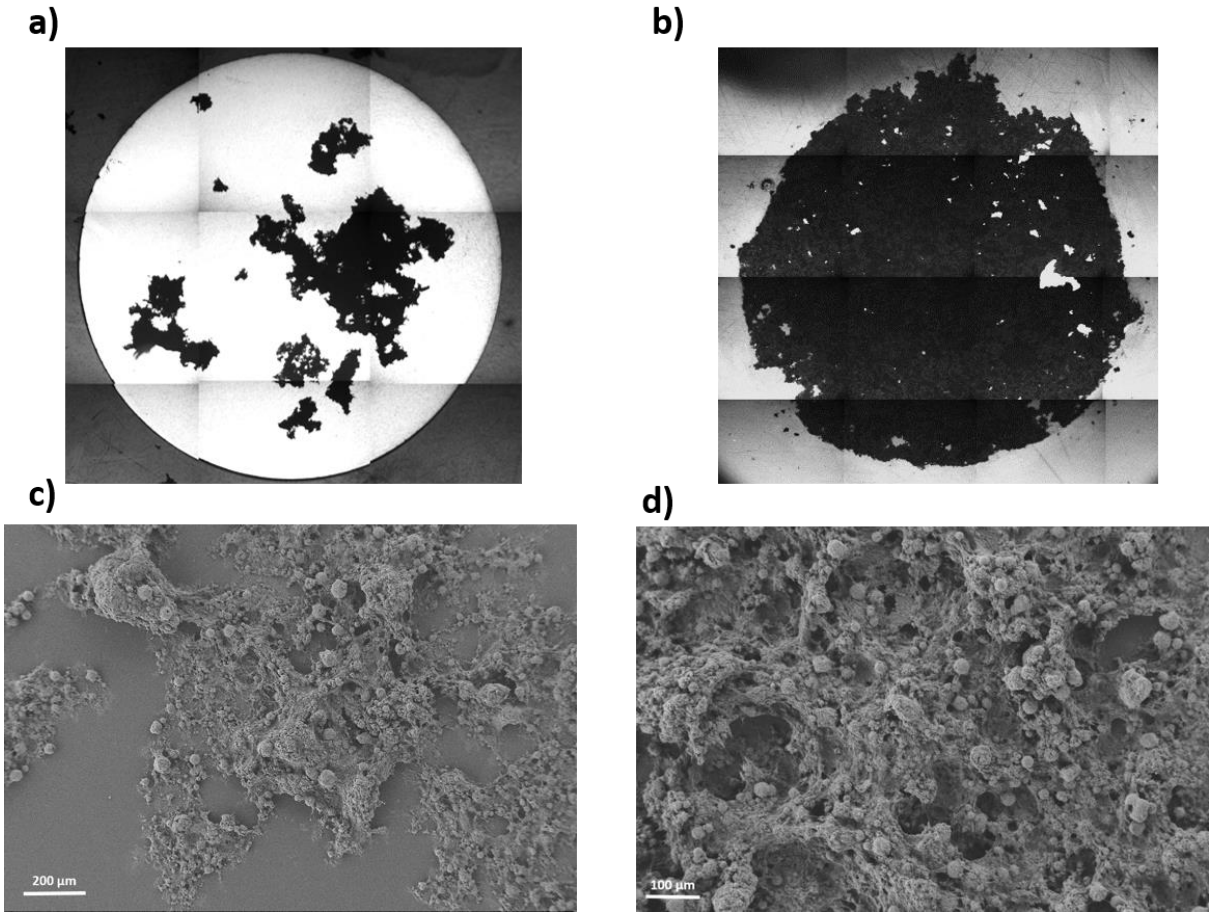


Figure 4.2 Images from optical microscope for a GC electrode with a geometric area 0.07 cm^2 which was drop-casted with a) 6 µg and b) 30 µg of b-MWCNTs; c) and d) SEM images of 6 µg b-MWCNTs drop-casted over carbon slab.

To characterize the deposition of the b-MWCNTs on the GC electrode, optical images were taken for the two PMEs and are shown in Figure 4.2 (the contrast lines observed are due to the stitching together of the individually taken images to form the full picture of a GC electrode). It was observed that the b-MWCNTs were deposited on the GC electrode for both 6 μg (Figure 4.3a) and 30 μg (Figure 4.3b) but depending on the volume of aliquots drop-casted, the active electrode area covered by the b-MWCNTs also varied. It is clear that a far from uniform deposit was created. For a drop-cast of 6 μg, the active electrode area covered by the b-MWCNTs was estimated to be *ca.* 20% and in the case of 30 μg it was *ca.* 98%.

However, in the latter case the deposit spread onto the insulation surrounding of the electrode; it is unclear to what extent the nanotubes in the latter area are in electrical contact with the substrate electrode. The extent to which the nanotubes aggregate and form multi-layered patches on the electrode is emphasized partly by the SEM images shown in Figure 4.2c and d. If it is assumed that a b-MWCNT is a cylinder (length 20 μm and diameter 30 ± 10 nm) when uniformly deposited with 6 μg of drop-cast in a close packed arrangement across the area of the electrode is calculated to have 25 layers (calculations are given in Appendix Section A4.1) of b-MWCNTs. Similarly, for 30 μg of drop-casted b-MWCNTs is estimated to be equivalent to 125 monolayers if it is spread over the whole geometric area of the GC electrode. However, as shown in Figure 4.2, the deposits are not spread out uniformly but form macroscopic patches on the GC electrode.

The presence of macroscopic bare patches of b-MWCNT modified electrodes is expected to influence the voltammetry observed at the electrode in the case of the low average coverages. In contrast the thicker layers formed at higher coverages may lack full electrical contact (both vertically and radially) throughout the film and can exhibit thin-layer rather than semi-infinite diffusional effects[5-7].

To investigate these effects voltammetry of the oxidation of bromide to bromine was next undertaken. 5 mM of NaBr was dissolved in 0.1 M of HNO_3 and was used as electrolyte for the investigation. The cyclic voltammogram as a function of scan rate is shown in Figure 4.3 for the bare GC electrode. The oxidative peak was found to be at +1.12 V vs. SCE (Figure 4.3 black line) which is comparable to the literature value (+ 1.08 V vs. SCE) [12]. The peak-to-peak separation was of the order of several hundred mVs and increased with scan rate which suggests that the oxidation of bromide at a GC electrode is fully electrochemically irreversible.

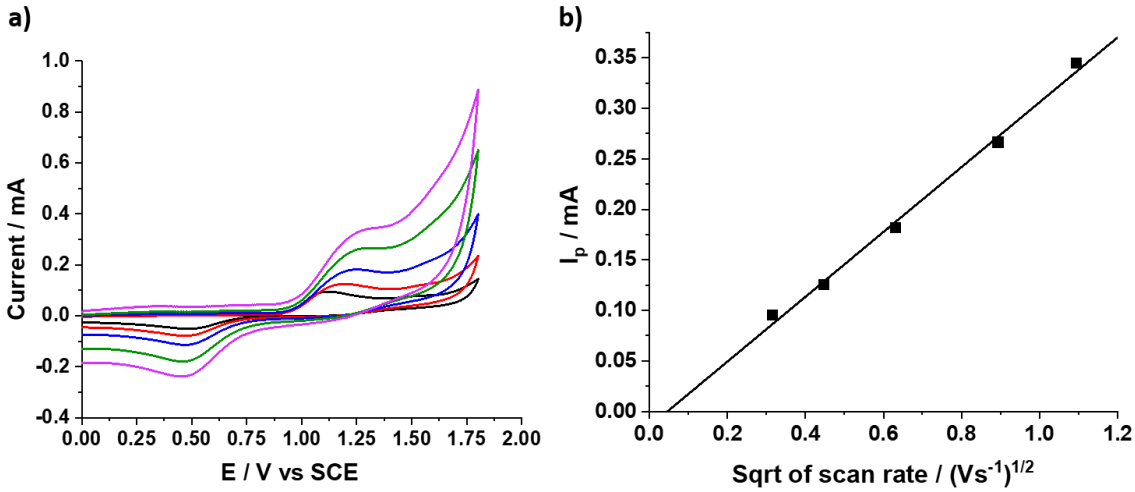


Figure 4.3 a) Voltammograms at a bare GC electrode in solution containing 5 mM NaBr with 0.1 M HNO_3 recorded as a function of scan rate (0.1 V s^{-1} (black line), 0.2 V s^{-1} (red line), 0.4 V s^{-1} (blue line), 0.8 V s^{-1} (green line), 1.2 V s^{-1} (magenta line); b) a plot of I_p versus square root of the scan rate.

A plot of peak current (I_p) versus square root of scan rate ($(V\ s^{-1})^{1/2}$) is given in Figure 4.3b, the linearity shows that I_p is proportional to the square root of scan rate suggesting a diffusion-controlled process. The Randles–Ševčík (R-S) equation for an irreversible one electron oxidation reaction was used to calculate the diffusion coefficient for the process using the measured transfer coefficient (β) of 0.43 from the Tafel slope analysis given in Appendix, Section A4.2. The R-S equation is, [13, 14],

$$I_p = 0.496\sqrt{n' + \beta}\, nFA[A]_{bulk}\sqrt{\frac{FvD}{RT}} \tag{4.1}$$

where n' is electrons transferred before the rate-determining step and n is the total number of electrons transferred, A is the geometric area of the electrode in m^2, β is the anodic transfer coefficient, $[A]_{bulk}$ is the bulk concentration of the analyte in mol m^{-3}, v is the scan rate in V s^{-1} and D is the diffusion coefficient in m^2 s^{-1}.

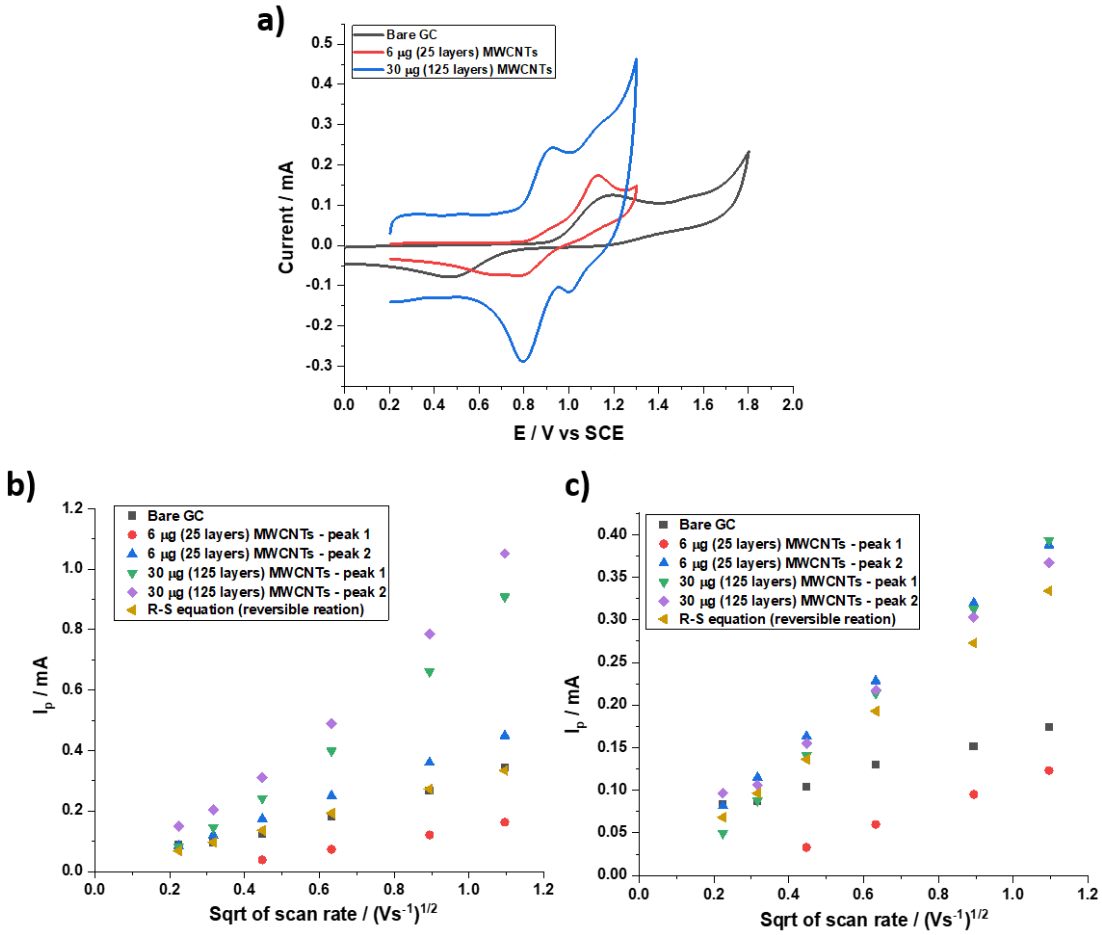


Figure 4.4 (a) Cyclic voltammograms of bare GC (black line), 6 µg drop-cast of b-MWCNTs (25 monolayers, red line), and 30 µg drop-cast of b-MWCNTs (125 monolayers, blue line), at a scan rate of 0.2 V s^{-1}. Plots of peak current I_p vs square root of scan rate (b) before and (c) after background subtraction. The analysed solution was 5 mM NaBr in 0.1 M HNO_3.

Inferring a value of n'= 0 from the Tafel analysis and putting n = 1 for the oxidation of a bromide anions, the diffusion coefficient was found to be 2.1 ± 0.1 × 10^{-9} m^2 s^{-1}. This

matches well with the literature value[15]. This value for the diffusion coefficient was independently checked using a platinum macro-electrode which gives reversible voltammetry under similar conditions (see Appendix Section A4.3).

The voltammetry for the bromide oxidation was then investigated on b-MWCNT-modified GC electrodes. The obtained voltammograms for the bare GC electrode, 25 monolayers drop-cast (6 μg) and 125 monolayers drop-cast (30 μg) at a scan rate of 0.2 V s^{-1} are shown in Figure 4.4a. The plot of peak current (I_p) vs square root of scan rate shows the comparison between the peak currents of bare GC, 25 monolayers (6 μg), 125 monolayers (30 μg) and the estimated peak current using R-S equation for a reversible one electron transfer process. Figure 4.5a shows the raw data without any background subtraction and Figure 4.5b is the voltammograms after background subtraction for all the experimental voltammograms obtained.

In the case of the lower coverage of nanotubes where the microscopy reported above shows a heterogeneous surface comprised of bare patches of electrodes and patches of heavily agglomerated nanotubes, it can be seen that the peak potentials of both the oxidative and reductive features shift closer together in comparison to the bare electrode. For the higher coverage both peaks have shifted much closer together and the voltammetric response (Figure 4.4a) is apparently more reversible although a very significant background current is observed as a result of capacitive charging as evidenced by the currents flowing in the potential range 0.2 – 0.6 V vs SCE.

The voltammograms as a function of scan rate for the b-MWCNTs deposited GC electrode is shown in Figure 4.5 (a and c are voltammograms before background subtraction; b and d are respective voltammograms after background subtraction).

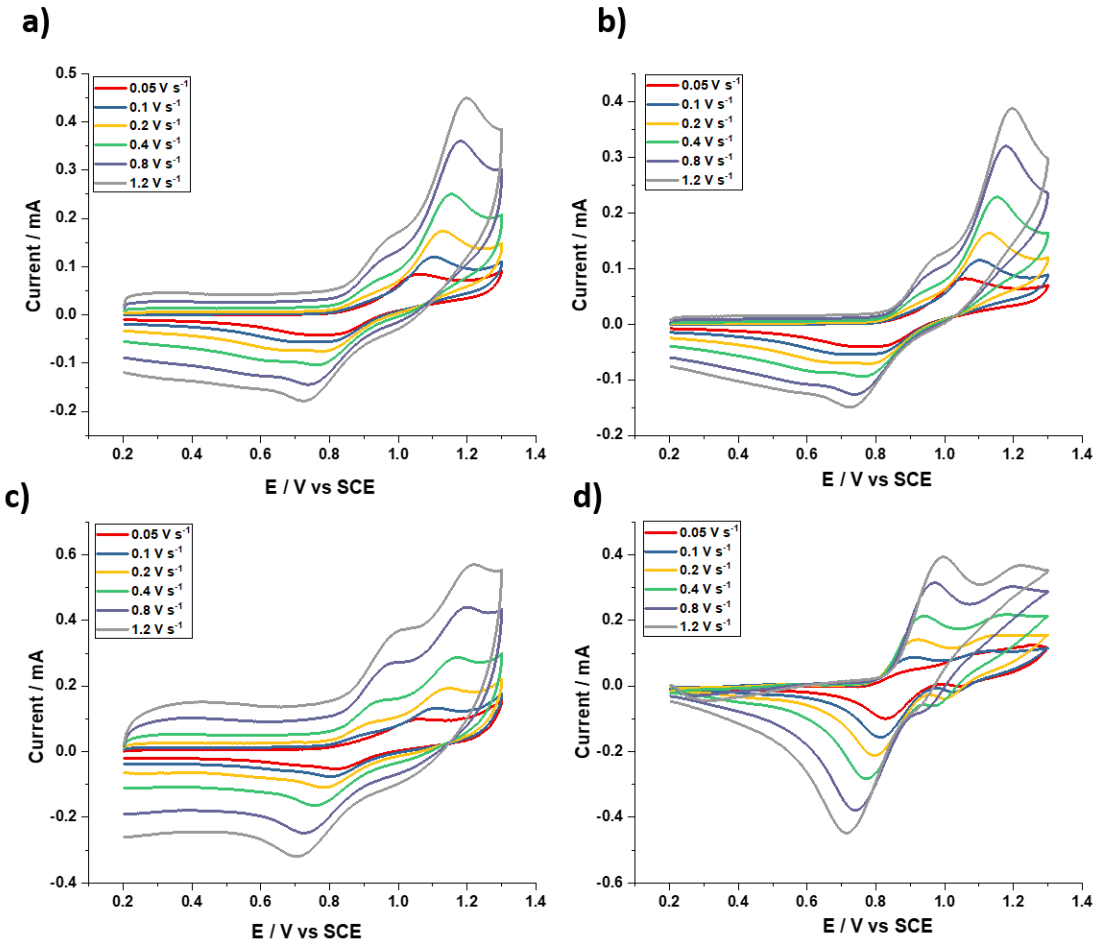


Figure 4.5 Cyclic voltammograms on a 6 µg of b-MWCNTs modified GC electrode (a) before background subtraction (b) after background subtraction and 30 µg of MWCNTs (c) before background subtraction (d) after background subtraction (0.05 V s^{-1}, red line ; 0.1 V s^{-1}, blue line; 0.2 V s^{-1}, yellow line; 0.4 V s^{-1}, green line; 0.8 V s^{-1}, navy line; 1.2 V s^{-1}, grey line). The analysed solution was 5 mM NaBr in 0.1 M HNO_3.

The current-potential response for 0.1 M HNO_3 was obtained and was used as background to subtract the capacitive charging from the actual voltammogram obtained for bromide oxidation and is shown in Figures 4.5b and c. The latter (30 µg) indicates a much greater electrode-electrolyte interfacial area as compared to the bare electrode and shows that the patches of agglomerates are likely highly porous. Interestingly the low coverage voltammogram (Figures 4.5a and b) shows a pre-wave of electroactivity at the potentials at which the bromide oxidation is seen for the higher coverage. Accordingly, the response is that of a mixed surface – bare patches of GC and porous patches of agglomerated

particles was observed. The change in the apparent electrochemical reversibility of the bromide oxidation in the presence of the b-MWCNTs might at first sight signal 'electrocatalysis' because of the increased apparent reversibility. However, the effect is equally consistent with the expected 'thin-layer' like voltammetry expected for porous layers. The b-MWCNTs exhibit a complicated mass transport behaviour which mostly is a combination of thin-layer and semi-infinite diffusion[6]. Figure 4.6 shows a logarithmic plot of peak current vs scan rate before (Figure 4.6a) and after (Figure 4.6b) background correction.

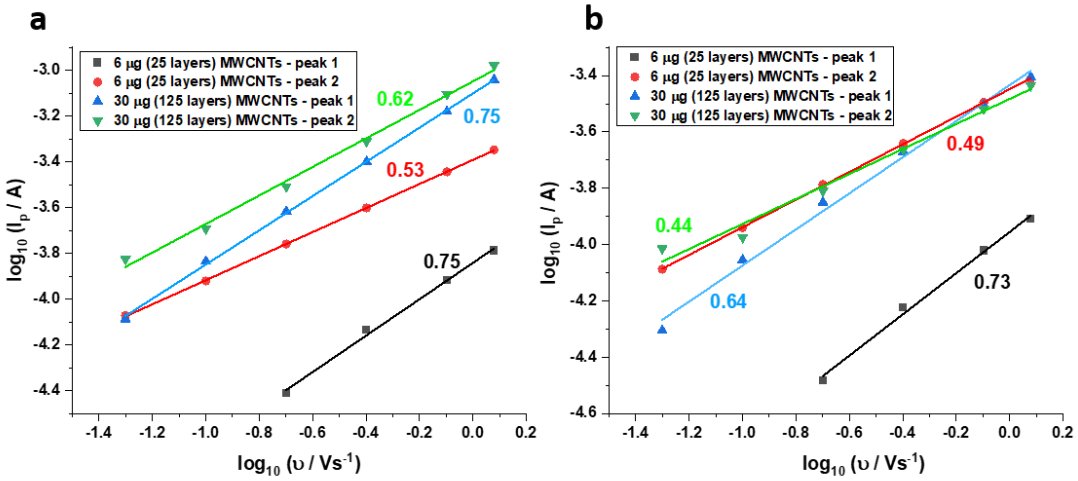


Figure 4.6 The logarithmic plot of peak current (I_p) vs scan rate; a) before background subtraction with gradients of 0.75 for 6 µg of b-MWCNTs - peak 1 (black line), 0.53 for 6 µg b-MWCNTs - peak 2 (red line), 0.75 for 30 µg b-MWCNTs - peak 1(blue line), 0.62 for 30 µg b-MWCNTs - peak 2 (green line); b) after background subtraction with gradients of 0.73 for 6 µg b-MWCNTs - peak 1 (black line), 0.49 for 6 µg b-MWCNTs - peak 2 (red line), 0.64 for 30 µg b-MWCNTs - peak 1 (blue line), 0.44 for 30 µg b-MWCNTs - peak 2 (green line).

The gradient value for each linear plot was found to deviate from 0.5, which corresponds to semi-infinite diffusion and the value of 1 which is expected for thin layer diffusion and/or adsorbed species[6]. This indicates that a mixed mass transport regime is observed with a combination of first thin-layer diffusion (or an adsorptive response) observed in the interior of the b-MWCNTs layer and second semi-infinite diffusion to the surface of

the layer [5]. The high surface area of the b-MWCNTs can facilitate the adsorption of the electroactive species which makes it difficult to unambiguously distinguish between thin-layer effects and the adsorption effects[7]. This general issue is explored further in Chapter 8.

4.4 Conclusions

Drop-casting method is widely used to modify electrodes with particles for electroanalysis. Often the creation of a random distribution of particles is assumed and this can be encouraged by electrochemical responses which are not inconsistent with the presumed surface morphology. However, it is clear that drop-casts which are far from ideal can be formed with b-MWCNTs forming patchy surfaces with exposed areas of bare electrode. Such surface modification gives plausible voltammetric responses making it to distinguish between thin-layer effects or adsorption effects and it is evident that complementary microscopic imaging must be conducted in parallel with the electrochemistry in order to avoid erroneous conclusions both qualitative and quantitative.

Appendix

Section A4.1 Calculation for Predicting the Number of Monolayers of b-MWCNTs Drop-Casted at GC Electrode

To estimate the number of monolayers at the glassy carbon (GC) electrode for 30 μg of drop-cast we assume a closed pack arrangement of the b-MWCNTs laid uniformly across the whole GC surface (area of GC electrode is 7.07 x 10^{-2} cm^2). The diameter of the b-MWCNTs is 30 nm, length is 6 – 20 μm and density is 1.4 g cm^{-3} (these values were sourced from the manufacturer).

Volume of single b-MWCNT (cylindrical geometry);

$$Volume = \pi r^2 l$$

where r is the radius of the b-MWCNT and l is the length of the b-MWCNT. Hence volume of single b-MWCNT is calculated to be 4.24 x 10^{-15} cm^3.

To find out the mass of single b-MWCNTs

$$Mass = Density \times Volume\ of\ single\ b-MWCNT$$

Thus, the mass of single b-MWCNT is 5.94 x 10^{-15} g.

1 mg of b-MWCNTs was dispersed in 1 mL of acetone for the drop-cast experiment, hence 30 μL of drop-cast will contain 3.00 x 10^{-5} g of b-MWCNTs. Therefore, number of b-MWCNTs present in 30 μL drop-cast is found to be 5.00 x 10^9.

Assuming the b-MWCNTs contact at the GC surface to be rectangular when arranged in a closed pack manner, the area covered by unit b-MWCNT is 1.80 × 10^{-9} cm^2. Hence, area covered by 5.00 x 10^9 b-MWCNTs is 9.09 cm^2. Now that we know the total area of both GC electrode and that of b-MWCNTs number of layers can be calculated as follows;

$$No.of\ monolayers\ of\ b-MWCNTs\ for\ 30\ \mu L\ drop\ cast$$

$$= \frac{Total\ area\ covered\ by\ b-MWCNTs}{Total\ surface\ area\ of\ GC\ electrode}$$

Thus, number of layers for 30 µL drop-cast on GC electrode is found to be 125 ± 5 monolayers.

Section A4.2 Tafel Analysis

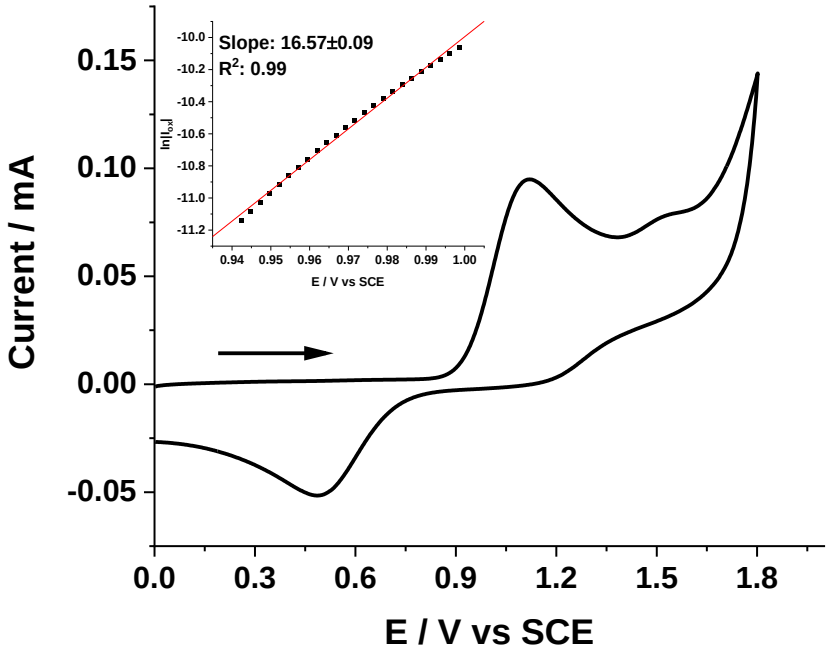


Figure A4.1 Cyclic voltammogram at bare GC electrode a) for oxidation of bromide in 5.00 (± 0.05) mM NaBr in 0.10 M HNO_3 at a scan rate of 0.1 V s^{-1}; Inset shows the Tafel plot with a slope of 16.57 (± 0.09) V^{-1} giving β of 0.45 (± 0.01).

In this section the transfer coefficient, β is calculated using Tafel analysis for the oxidation of bromide. β is calculated using the following expression (the method is explained in detail in Chapter 1, section 1.2),

$$\ln|I_{ox}| = \frac{\beta FE}{RT} + constant \qquad (4.2)$$

where, I_{ox} is the oxidative current. Note that the current range of 10 – 30% of the peak current was used to analyse in order to avoid the influence of mass transport [16].

Considering the oxidation of bromide at bare GC electrode in 5.00 (± 0.05) mM NaBr supported by 0.10 M HNO_3 a Tafel slope of 16.5 (± 0.1) V^{-1} was obtained from a plot of $\ln|I_{ox}|$ vs potential (E vs SCE), shown in the inlay of Figure S1 , inferred from the voltammetric response recorded at 0.1 Vs^{-1} (Figure S1). Further, β was calculated to be 0.43 (± 0.01) for bromide oxidation.

Section A4.3 Cyclic Voltammetry at Pt Macro-Disc Electrode to Evaluate the Diffusion Coefficient of Bromide.

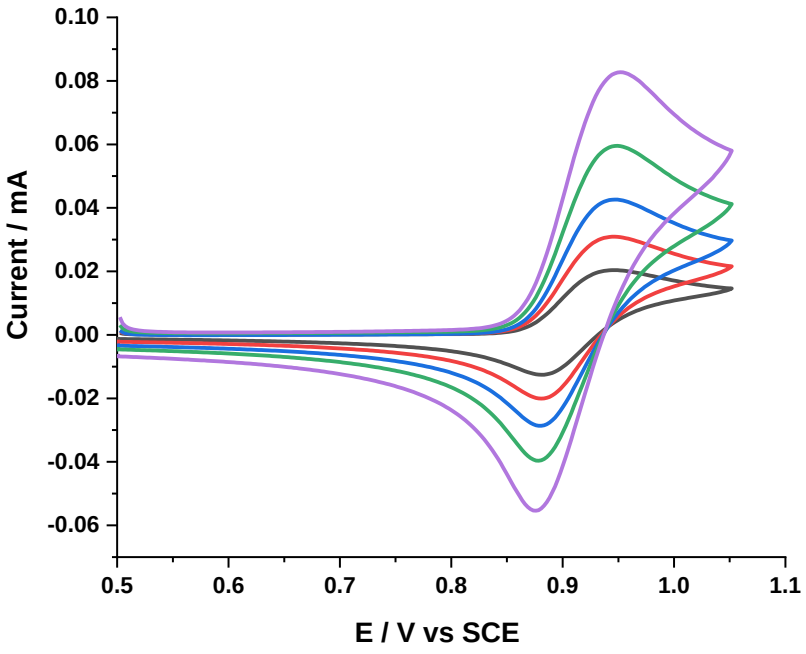


Figure A4.2 Voltammograms of Pt working electrode in 5mM NaBr in 0.1M HNO_3 solution recorded as a function of scan rate (20 mV s^{-1} (black line), 50 mV s^{-1} (red line), 100 mV s^{-1} (blue line), 200 mV s^{-1} (green line), 400 mV s^{-1} (magenta line).

A typical cyclic voltammetry experiment was conducted to calculate the diffusion coefficient for bromide to bromine oxidation under reversible conditions. A Pt working

electrode of diameter 1.5 mm was used in a solution containing 5.0 mM of NaBr and 0.1 M of HNO_3 as supporting electrolyte. Voltammogram as a function of scan rate is given in Figure A4.2. The diffusion coefficient is found to be ca. $2.280 \pm (0.002 \times 10^{-7}) \times 10^{-9}$ m^2 s^{-1} using relevant form of the Randles-Ševčik equation (Eq. 4.1) for non-unity stoichiometric reactions[17] and is comparable to the literature value of 2.08×10^{-9} m^2 s^{-1} [15].

References

1. Zhang, Y.; Selva Kumar, A. K.; Li, D.; Yang, M.; Compton, R. G., Nanoparticle- and Nanotube-Modified Electrodes: Response of Drop-Cast Surfaces. **2020,** *7* (22), 4614-4624.

2. Banks, C. E.; Davies, T. J.; Wildgoose, G. G.; Compton, R. G., Electrocatalysis at graphite and carbon nanotube modified electrodes: edge-plane sites and tube ends are the reactive sites. *Chem Commun* **2005,** (7), 829-841.

3. Zhao, G.; Rui, K.; Dou, S. X.; Sun, W., Heterostructures for Electrochemical Hydrogen Evolution Reaction: A Review. **2018,** *28* (43), 1803291.

4. Stacy, J.; Regmi, Y. N.; Leonard, B.; Fan, M., The recent progress and future of oxygen reduction reaction catalysis: A review. *Renewable and Sustainable Energy Reviews* **2017,** *69*, 401-414.

5. Streeter, I.; Wildgoose, G. G.; Shao, L. D.; Compton, R. G., Cyclic voltammetry on electrode surfaces covered with porous layers: An analysis of electron transfer kinetics at single-walled carbon nanotube modified electrodes. *Sensor Actuat B-Chem* **2008,** *133* (2), 462-466.

6. Sims, M. J.; Rees, N. V.; Dickinson, E. J. F.; Compton, R. G., Effects of thin-layer diffusion in the electrochemical detection of nicotine on basal plane pyrolytic graphite (BPPG) electrodes modified with layers of multi-walled carbon nanotubes (MWCNT-BPPG). *Sensor Actuat B-Chem* **2010,** *144* (1), 153-158.

7. Henstridge, M. C.; Dickinson, E. J. F.; Aslanoglu, M.; Batchelor-McAuley, C.; Compton, R. G., Voltammetric selectivity conferred by the modification of electrodes using conductive porous layers or films: The oxidation of dopamine on glassy carbon electrodes modified with multiwalled carbon nanotubes. *Sensor Actuat B-Chem* **2010,** *145* (1), 417-427.

8. Kätelhön, E.; Compton, R. G., Unscrambling illusionary catalysis in three-dimensional particle-modified electrodes: Reversible reactions at conducting particles. *Applied Materials Today* **2020,** *18*, 100514.

9. Davies, T. J.; Banks, C. E.; Compton, R. G., Voltammetry at spatially heterogeneous electrodes. *J Solid State Electr* **2005,** *9* (12), 797-808.

10. Sims, M. J.; Li, Q.; Kachoosangi, R. T.; Wildgoose, G. G.; Compton, R. G., Using multiwalled carbon nanotube modified electrodes for the adsorptive striping voltammetric determination of hesperidin. *Electrochim Acta* **2009,** *54* (22), 5030-5034.

11. Li, H.; Buesen, D.; Williams, R.; Henig, J.; Stapf, S.; Mukherjee, K.; Freier, E.; Lubitz, W.; Winkler, M.; Happe, T., Preventing the coffee-ring effect and aggregate sedimentation by in situ gelation of monodisperse materials. *Chemical science* **2018,** *9* (39), 7596-7605.

12. Haynes, W., the CRC Handbook of Chemistry and Physics 93rd Edition, 2012. *Chemical Rubber Company*.

13. Randles, J. E. B., A Cathode Ray Polarograph .2. The Current-Voltage Curves. *T Faraday Soc* **1948,** *44* (5), 327-&.

14. Compton, R. G.; Banks, C. E., *Understanding Voltammetry, 3rd Edition* **2018**, 1-439.

15. White, R. E.; Lorimer, S. E., A Model of the Bromine Bromide Electrode-Reaction at a Rotating-Disk Electrode. *J Electrochem Soc* **1983,** *130* (5), 1096-1103.

16. Li, D. L.; Lin, C. H.; Batchelor-McAuley, C.; Chen, L. F.; Compton, R. G., Tafel analysis in practice. *J Electroanal Chem* **2018,** *826*, 117-124.

17. Gómez-Gil, J. M.; Laborda, E.; Molina, A., General Explicit Mathematical Solution for the Voltammetry of Nonunity Stoichiometry Electrode Reactions: Diagnosis Criteria in Cyclic Voltammetry. *Analytical Chemistry* **2020,** *92* (5), 3728-3734.

Chapter 5

The Oxidation of Bromide at Pt Macro Electrode: Measurement of the Formal Potential of a Non-Unity Stoichiometric Electrode Reaction

The possible electrocatalysis of the Br_2/Br^- redox couple will be studied in the Chapter 6 at both ensemble and 'single' bamboo-like multiwalled carbon nanotubes (b-MWCNTs). In order to investigate the comparative electron transfer kinetics in the presence or absence of b-MWCNTs, as an essential preliminary it is essential to first know the formal potential, E_f^0 of the redox couple and second to explore if any follow-up chemistry exists on the voltammetric timescale. In the former case, the measurement using cyclic voltammetry at a macroelectrode necessitates establishing the correct form of the reversible *Randles-Ševčík* equation which reflects on the non-unity stoichiometry of the reaction. In the second case, it is necessary to identify any possible formation of the tribromide, Br_3^-.

In this chapter the cyclic voltammetry of the oxidation of bromide (Br^-) to bromine (Br_2) in aqueous solution is studied at a platinum (Pt) macro-electrode where a reversible electrode process is thought to occur. Also presented is a summary of the theory and associated simulation developed by Mr. Haotian Chen to address the analysis of the voltammetry to extract the two conclusions sought. This work has been published in the Journal of Electroanalytical Chemistry[1].

5.1 Introduction

The bromine/bromide (Br_2/Br^-) redox chemistry plays a crucial role in energy storage devices which include electrochemical capacitors[2] and many redox flow batteries notably zinc-bromine[3], vanadium-bromide[4], bromide-polysulphide[5], and organic (quinone-bromine[6]) batteries. The performance of the batteries is limited by the reaction kinetics of the Br_2/Br^- redox couple as they undergo multiple electron transfer processes, starting with

$$2Br^- - 2e^- \rightleftarrows Br_2 \tag{5.1}$$

They may possibly also involve the follow-up homogeneous chemical reaction accompanying the oxidation of Br^- where the formed Br_2 combines with the reactant Br^- reversibly to form Br_3^- ions[7],

$$Br_2 + Br^- \rightleftarrows Br_3^- \tag{5.2}$$

Hence, in the presence of large concentrations of Br^- the following limiting overall reaction is observed at the electrode,

$$3Br^- - 2e^- \underset{k_b}{\overset{k_f}{\rightleftarrows}} Br_3^- \tag{5.3}$$

$$K_{eq} = \frac{k_f}{k_b}$$

where K_{eq} is the equilibrium constant and k_f and k_b are the forward and backward rate constants respectively. K_{eq} is defined in terms of the concentrations of Br^-, Br_2 and Br_3^- as follows,

$$K_{eq} = \frac{[Br_3^-]}{[Br^-][Br_2]} \tag{5.4}$$

This reaction (Eq. (5.3)) has been studied extensively in both aqueous[8] and non-aqueous (nitrobenzene[9], acetonitrile and room temperature ionic liquids[10]) media. The K_{eq} and k_f

values for the formation of Br_3^- in aqueous media are reported as 17 M^{-1} and 1.5 × 10^9 M^{-1} s^{-1} at 25 °C [11]. The oxidation of bromide at Pt macro-electrodes is reported to be reversible in contrast to what is seen at carbon macro-electrodes[8, 12]. Hence, in this work the cyclic voltammetry of oxidation of bromine was conducted at the Pt macro-electrode to obtain reversible voltammograms which better allow the extraction of the formal potential and information about the possible formation of the tribromide anion. The obtained experimental results were compared with the simulations to obtain both the formal potential and the bulk concentration of Br^- required to form Br_3^-. The simulations were carried out by Mr. Haotian Chen.

5.2 Theory

At macro-electrodes, cyclic voltammetry yields qualitatively relevant information such as electrode reaction processes and pathways, as well as quantitative data such as equilibrium, rate and adsorption constants, and diffusion coefficients. For the simple one-electron oxidation process,

$$A - e^- \rightleftarrows B \tag{5.5}$$

the characterisation of electrochemically reversible voltammograms in terms of peak currents, and voltage scan rate dependency, is well known from the Randles-Ševčík equation[13],

$$I_p = 0.446nFA[A]_{bulk}\sqrt{\frac{nFvD}{RT}} \tag{5.6}$$

where *n* is the total number of electrons transferred (for a one-electron transfer it is 1), *A* is the geometric area of the electrode in m^2, $[A]_{bulk}$ is the bulk concentration of the analyte in mol m^{-3}, v is the scan rate in V s^{-1} and *D* is the diffusion coefficient in m^2 s^{-1}. Eq. (5.6) is widely adopted to interpret cyclic voltammetric results. However, it is critical

to understand that this only applies to electrode reactions with a unity stoichiometry. Hence for a reaction,

$$aA - ne^- \rightleftarrows bB \tag{5.7}$$

where $a = b$, Eq. (5.6) is valid, but when $a \neq b$ Eq. (5.6) no longer applies as stressed by Molina and her colleagues[14] who considered alternative forms of the equation for reactions with non-unity stoichiometry.

In the theory developed by Mr Haotian Chen for the Br_2/Br^- redox system the one-electron oxidation of a species *A* to *B* is considered to be electrochemically reversible and to be followed by a homogeneous chemical reaction of *A* with *B* to form *C*, where the mass-transport at the macro-electrode is diffusional. In the case of interest, $A = Br^-$, $B = Br_2$, and $C = Br_3^-$. Migration and convection effects are eliminated by using excess of supporting electrolyte[15] and running the voltammetry at a short enough timescale respectively[16, 17]. The overall reaction is,

$$2A \; - \; 2e^- \rightleftarrows B \tag{5.8}$$

$$B + A \underset{k_b}{\overset{k_f}{\rightleftarrows}} C \tag{5.9}$$

According to the Butler-Volmer theory, the electrode kinetics for reaction Eq. (5.8) is given by[18],

$$j = k_0 \exp\left[\frac{\beta F}{RT}\left(E - E_f^0\right)\right]\left(\frac{c_A(0,t)}{[A]^0}\right)^2 - k_0 \exp\left[-\frac{\alpha F}{RT}\left(E - E_f^0\right)\right]\left(\frac{c_B(0,t)}{[A]^0}\right) \tag{5.10}$$

where j is the net flux at the electrode surface, k_0 is the standard electrochemical rate constant, E_f^0 is the formal potential, $c_A(0,t)$ and $c_B(0,t)$ are the concentrations of species *A* and *B* on the electrode surface at time t. The F, R, and T are the Faraday Constant, the

Gas Constant and the absolute temperature respectively. The quantities α and β are the transfer coefficients. In most cases for a two-electron transfer reaction $\alpha + \beta = 2$ at potentials close to equilibrium.

Note that in Eq. (5.10) when the net flux, *j* is zero, the equation is reduced to the Nernst equation where $[\quad]^0$ is the standard concentration which is given by 1 M, therefore the Nernst equation is given as,

$$E = E_f^0(A/B) + \frac{RT}{F}\ln\left(\frac{\left(\frac{[B]}{[\quad]^0}\right)^{\frac{1}{2}}}{\frac{[A]}{[\quad]^0}}\right) \tag{5.11}$$

where *E* is the electrode potential and $E_f^0(A/B)$ is the formal potential of the *A/B* redox couple.

Nevertheless, if the standard concentration is the bulk concentration of bromide $[A]^0$, then the new formal potential, $E_f^{0\prime\prime}$ is introduced with a factor q,

$$q = \frac{[A]^0}{[\quad]^0} \tag{5.12}$$

Hence, the relationship between $E_f^{0\prime\prime}$ and standard state $[A]^0$ is given as,

$$E = E_f^{0\prime\prime}(A/B) + \frac{RT}{F}\ln\left(\frac{\left(\frac{[B]}{[A]^0}\right)^{\frac{1}{2}}}{\frac{[A]}{[A]^0}}\right) \tag{5.13}$$

$$= E_f^{0\prime\prime}(A/B) + \frac{RT}{F}\ln\left(\frac{\left(\frac{[B]}{q[\quad]^0}\right)^{\frac{1}{2}}}{\frac{[A]}{q[\quad]^0}}\right) \tag{5.14}$$

$$= E_f^{0''}\ (A/B) + \frac{RT}{F}\ln\left(\frac{\left(\frac{[B]}{[\ ]^0}\right)^{\frac{1}{2}}}{\frac{[A]}{[\ ]^0}}\right) + \frac{RT}{F}\ln\left(q^{\frac{1}{2}}\right) \tag{5.15}$$

$$E_f^0(A/B) = E_f^{0''}\ (A/B) + \frac{RT}{F}\ln\left(q^{\frac{1}{2}}\right) \tag{5.16}$$

Thus, the new formal potential $E_f^{0''}$ for *A/B* redox couple is,

$$E^{0''}_f(A/B) = E_f^0(A/B) - \frac{RT}{F}\ln\left(q^{\frac{1}{2}}\right) \tag{5.17}$$

This result emphasises that the *apparent* formal potentials observed in cyclic voltammetry will be dependent on the concentration of *A* (Br^-) used.

5.3 Simulations

Simulations were carried out by Mr. Haotian Chen using a home written C++ program with *std::thread* for parallel computing on Intel Core i7 CPU and the corresponding plots were plotted with Python Matplotlib.

Mr Chen[1] solved, via numerical simulation, the diffusion equations for *A*, *B* and *C* subject to Eqs. (5.10) and (5.11) as boundary conditions to predict the cyclic voltammograms observed for different values of the rate constants in Eq. (5.8) and for different bulk concentrations of *A* assuming zero bulk concentrations of *B* and *C*. The results from simulations were used to analyse the experimental voltammetric data discussed later in this chapter.

The simulations were carried out to analyse the influence of the bulk concentration of Br^- for the formation of Br_3^-. For this, simulations were carried out for the following reaction mechanism,

$$2Br^- - 2e^- \rightleftarrows Br_2 \tag{5.18}$$

$$3Br^- - 2e^- \underset{k_b}{\overset{k_f}{\rightleftarrows}} Br_3^- \tag{5.19}$$

The forward and backward reaction rate constants (k_f and k_b respectively) of 1.5×10^9 M^{-1} s^{-1} and 5×10^7 s^{-1} were used as obtained from the literature at 25 °C[11]. An equilibrium constant K_{eq} of 17 M^{-1} as defined in Eq. (5.4) was used from the literature as well. The diffusion coefficients of Br^-, Br_2 and Br_3^- of 2.08×10^{-9} m^2 s^{-1} [7], 1.18×10^{-9} m^2 s^{-1} [19, 20]and 1.14×10^{-9} m^2 s^{-1} [7] at 25 °C were used. Note that here the diffusion coefficient values used were from literature in order to study the effect of bulk concentration on the appearance of Br_3^- peak. Later in the chapter, the diffusion coefficient of Br^- is determined experimentally.

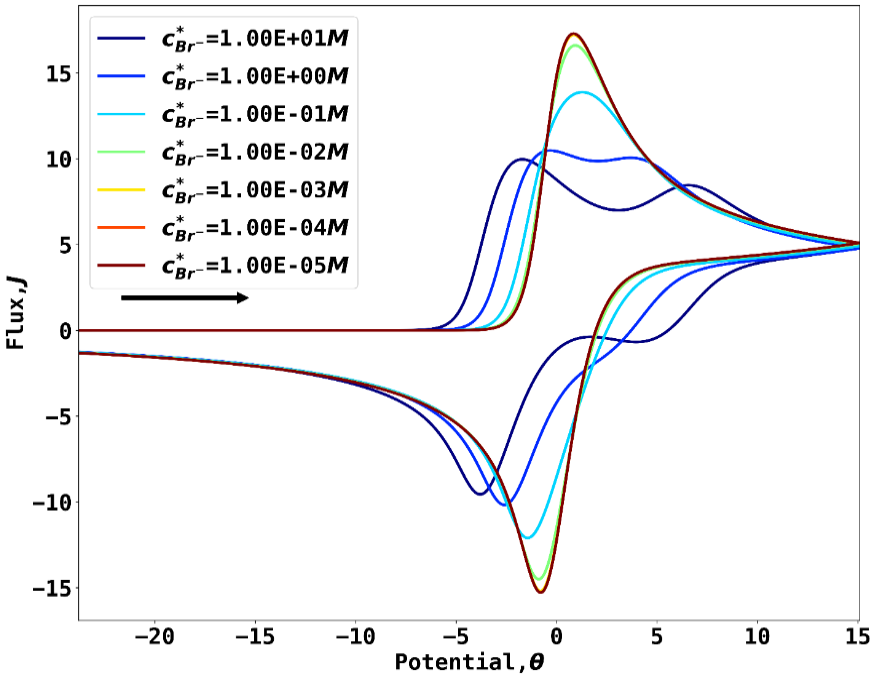


Figure 5.1 Voltammetry showing the effects of varying the bulk concentration of Br^- ($c^*_{Br^-}$) from 10^{-5} M to 10 M at scan rate of 100 $mV\ s^{-1}$. A second peak can be observed when $c^*_{Br^-}$ is larger than 0.1 M. The black arrow indicates the start and initial direction of potential sweep. (Simulated and plotted by Mr. Chen).

The cyclic voltammetry response was predicted for different bulk concentrations (10^{-5} M to 10 M) and is shown in Figure 5.1 at a scan rate of 100 mV s^{-1}. It was observed that

when the concentration of Br^- is lower than 0.1 M the voltammograms only showed a single peak corresponding to the oxidation of Br^- to form Br_2. However, on increasing the Br^- concentration above 0.1 M facilitates the formation of Br_3^- as in Eq. (5.19) thus, decreasing the peak flux of the first peak. This observation can be explained that at lower concentrations of Br^- insufficient Br_3^- is formed so as to be able to decompose to form the second peak. In summary, the second peak is only observed when the bulk concentration of Br^- is 0.1 M or above.

Next, experiments were conducted a Br^- bulk concentration of 5 mM which avoids the following homogeneous reaction as explained above to estimate the diffusion coefficients and the formal potential of Br_2/Br^- redox couple.

5.4 Experimental

All the chemicals used in this chapter are given in Chapter 2, Table 2.1 The chemicals were purchased commercially and used without any further purification.

5.4.1 Preparation of Pt Macro Electrodes

A platinum (Pt) macro electrode of diameter 1.5 mm and micro-electrode of diameter 10 μm was used after polishing with alumina slurries of progressively decreasing sizes of 1.00 μm, 0.30 μm and 0.05 μm. The electrodes were then washed with deionised water, sonicated for 10 s, dried under N_2 flow and used as working electrodes.

5.5 Results and Discussion

First steady-state voltammetry at a platinum (Pt) micro-disc electrode was used to measure the diffusion coefficient of bromide using a solution containing 5.0 mM of NaBr with 0.1 M of HNO_3. The radius of the Pt micro-disc electrode was calibrated to be $5.0 \pm 0.1\ \mu m$ using $1.0\ mM\ Ru(NH_3)_6Cl_3$[21]. The calibrated microelectrode was used to

record the bromide oxidation voltammetry under quasi steady-state conditions as shown in Figure 5.2 revealing a sigmoidal wave with a single wave potential of $0.65\ V$ (vs SCE). The limiting current was analysed using the following equation as given by Saito[22]

$$I = 4nF[c]Dr_e \tag{5.20}$$

where *n* is number of electrons transferred in the electrode process and assumed to have the value *n = 1* under microelectrode voltammetry conditions as no second wave was apparent, *F* is the Faraday constant, *[c]* is the bulk concentration of bromide, *D* is the diffusion coefficient of bromide and r_e is the radius of the micro-disc electrode.

From the above equation the diffusion coefficient of $2.10 \pm 0.02 \times 10^{-9}\ m^2 s^{-1}$ was obtained which compares favourably with the literature value of $2.08 \times 10^{-9}\ m^2 s^{-1}$ [23] obtained from conductivity measurements.

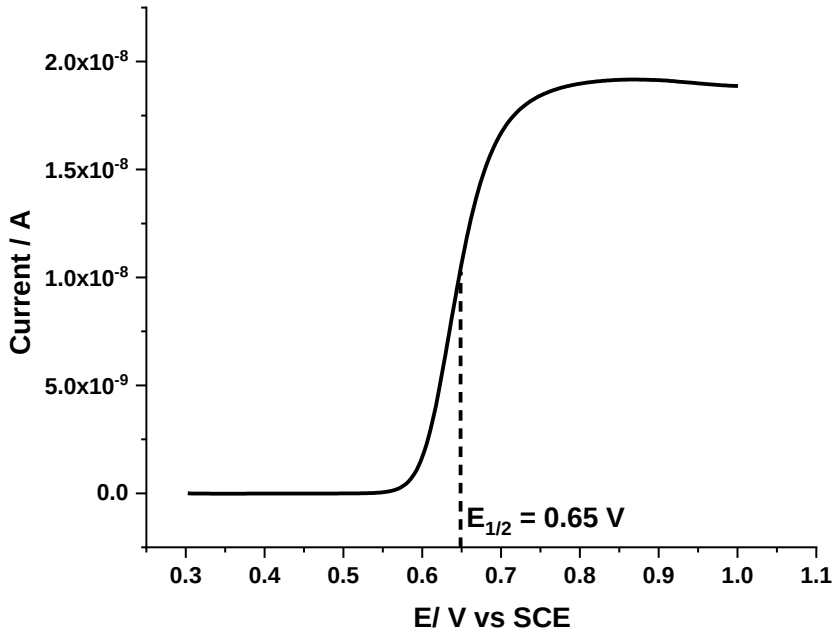


Figure 5.2 Quasi steady-state voltammogram of 5.0 mM of NaBr in 0.1 M HNO_3 at Pt micro-electrode of r = 5 μm and scan rate of $20\ mV\ s^{-1}$.

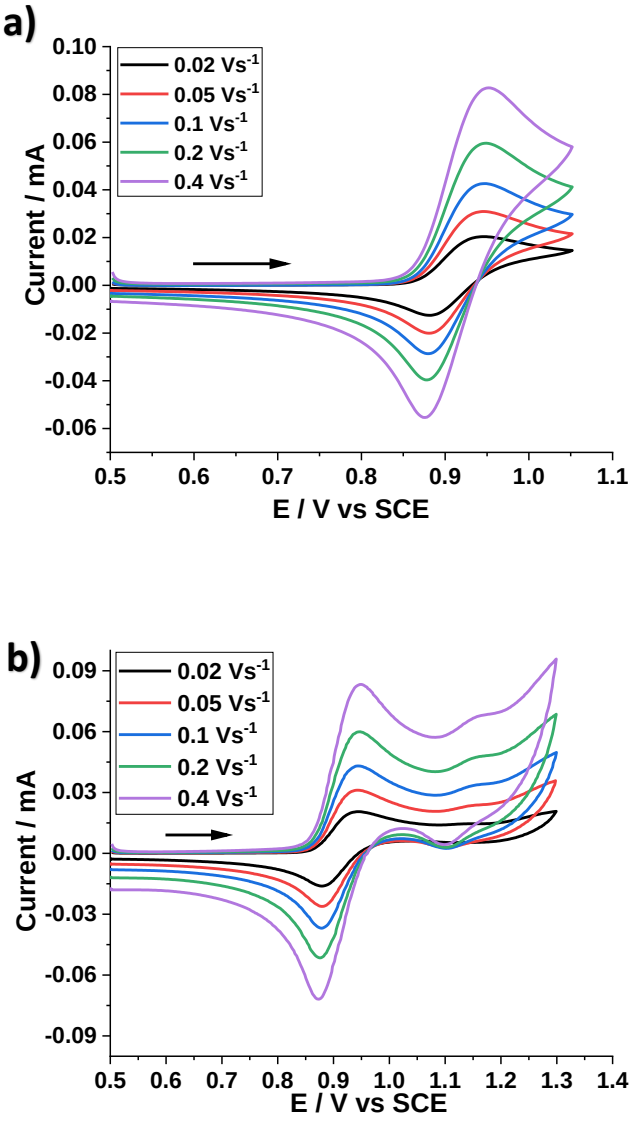


Figure 5.3 Cyclic voltammograms of 5.0 mM of NaBr in 0.1 M HNO_3 at Pt macro electrode of $r = 0.75\ mm$ as a function of scan rates. a) voltage scan ranges from 0.5 V to 1.05 V, b) voltage scan range from 0.5 V to 1.3 V. The black arrow indicates the start and initial direction of potential sweep.

Next cyclic voltammetry at a Pt macro-disc electrode (radius 0.75 mm; geometric area $1.8 \times 10^{-2}\ cm^2$) was conducted. Figure 5.3 shows the voltammetry of a 5.0 mM solution of NaBr in 0.1 M HNO_3 where the voltage scan range is from 0.5 V to 1.05 V (vs SCE) embracing the feature with a peak potential of 0.95 V (vs SCE) attributed to the reaction,

$$2Br^- - 2e^- \rightleftarrows Br_2$$

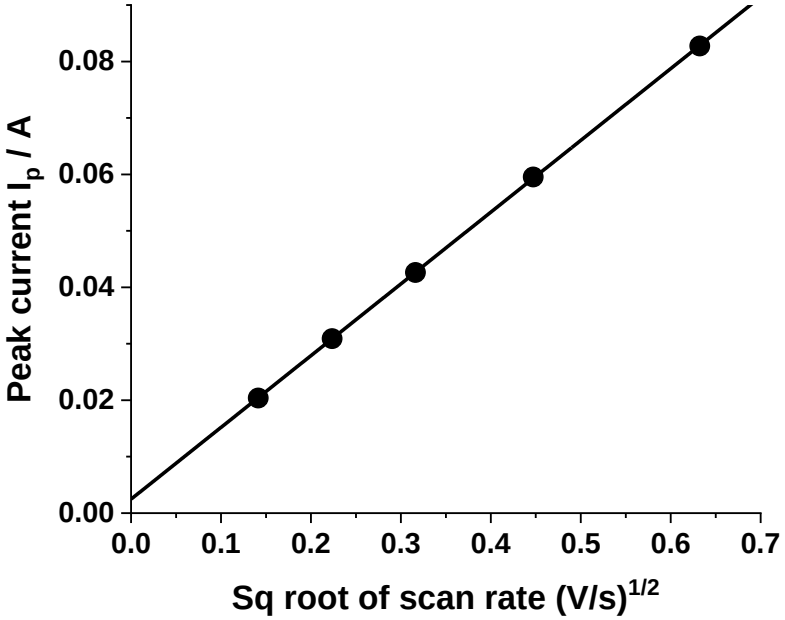


Figure 5.4 Plot of oxidative peak current (I_p) vs square root of scan rate for 5.0 mM of NaBr in 0.1 M HNO_3 at Pt macro electrode of $r = 0.75\ mm$.

Figure 5.4 shows that the peak current scales with the square root of the voltage scan rate as predicted. The linearity confirms a diffusion-controlled electrode process. The slope of the line in the inset has a value of $1.23 \times 10^{-4} \frac{A}{\sqrt{V/S}}$ after a small (<2%) baseline correction. This compares with a slope of $1.22 \times 10^{-4} \frac{A}{\sqrt{V/S}}$ predicted based on the simulations for the $Br_2/Br^-/Br_3^-$ system presented in the Appendix Section A5.1 using the measured diffusion coefficient for Br^- and optimising the diffusion coefficient for Br_2 for a value of 1.5×10^{-9} m^2 s^{-1}.

These simulations were made by Mr. Chen and good agreement is apparent. Note that the expected slope for a simple one-electron oxidation as in Eq. (5.5) on the basis of Randles-Ševčík equation is $1.08 \times 10^{-4} \frac{A}{\sqrt{V/S}}$ indicating the need for the stoichiometry of the Br_2/Br^- reaction is to be recognized. However, according to Molina's derivation[24] for

a two-electron transfer without a follow-up chemistry as in Eq. (5.8) is $1.21 \times 10^{-4} \frac{A}{\sqrt{V/S}}$). Although, the latter two calculated slopes assume the equality of the diffusion coefficients of Br^- and Br_2. The optimised value for the diffusion coefficient for bromine is higher than the value reported by Osipov et. al.[20] and widely cited in the secondary literature[19]. However, scrutiny of the original paper shows that the value was inferred from rotating disc measurements of the Br_2 electro-reduction in the presence of high concentrations for KBr such that, as shown above, the dominant species in solution would be the tribromide ion not bromine, Br_2. Bard estimated and used a value of 2.03×10^{-9} m^2 s^{-1} inferred from the Stokes-Einstein equation for the bromine diffusion coefficient[25].

The optimal value for the formal potential of the Br_2/Br^- redox couple found from simulation was found to be 0.913 V which is fully consistent with the reported standard potential of 0.8453 V vs SCE and for a bromide concentration of 5 mm as can be seen from Eq. (5.17) rewritten as,

$$E_f^{0''}\left(\frac{Br_2}{Br^-}\right) = E_f^0\left(\frac{Br_2}{Br^-}\right) - \frac{RT}{F}\ln\left(q^{\frac{1}{2}}\right) = \tag{5.21}$$

$$0.8453V - \frac{8.314\frac{J}{mol\cdot K} * 298K}{96485\frac{C}{mol}} * \ln\left(\sqrt{\frac{5mM}{1M}}\right) = 0.9133 \text{ V vs SCE}$$

Thus, the effective formal potential for the Br_2/Br^- couple was found to be 0.91 V vs SCE. The best fit simulated voltammograms using the optimised formal potential and diffusion coefficient are compared with the experimental voltammograms in Appendix FigureA5.1.

Interestingly, however, Figure 5.3b which shows the aqueous bromide oxidative voltammetry extended to more positive potentials, reveals a second wave with a peak potential of ca $1.2\,V$ (vs SCE). The origins of this second wave do not lie in the

dissociation of Br_3^- ions exclusively in the solution phase on the voltammetric timescale. This conclusion assumes the accuracy of the literature data for the formation and dissociation rate constants for Br_3^- are not in serious error. However, the above simulations and experiments show that negligible solution phase Br_3^- is formed at the Br^- concentrations used in the present study. Indeed, simulations show that a concentration of *ca*. 0.1 M of Br^- would be needed for sufficient Br_3^- ion to be generated for a second peak to be visible assuming all species are confined to the solution phase. At present the origins of the second feature are unclear but are likely to reside in the neglect of adsorbed species in the above model [26]. This is consistent with our observations that if Pt is replaced with glassy carbon as the electrode material no second peak is discernible except possibly at the very different potential of $+1.5\ V$(vs SCE) and obscured by solvent decomposition, an observation which hints at surface rather than solution chemistry operating. These results at GC electrode will be explained in next Chapter.

5.6 Conclusions

To conclude the oxidation of bromide to bromine with a non-unity stoichiometry was studied experimentally at Pt macro-disc with the help of simulation. The conditions under which the tribromide ion might be observed were identified whilst the role of surface adsorption in the case of Pt electrodes was noted along with the contrasting voltammetry between carbon and platinum electrodes. The simulations allowed for the non-unity stoichiometry of the reaction to be accounted for, which leads to a concentration dependence of the voltammetry even in the absence of tribromide formation and hence permitted inference of the formal potential of the Br_2/Br^- redox couple to be 0.91 V vs SCE.

Appendix

Section A5.1 Simulation

This section shows the cyclic voltammograms simulated using the best fit formal potential and are compared with the experimentally obtained cyclic voltammograms. These simulations were carried out by Mr. Haotian Chen.

The simulations were carried out for a simple one-electron transfer as follows,

$$\frac{1}{2}Br_2(l) + e^- \leftrightarrow Br^- \tag{5.20}$$

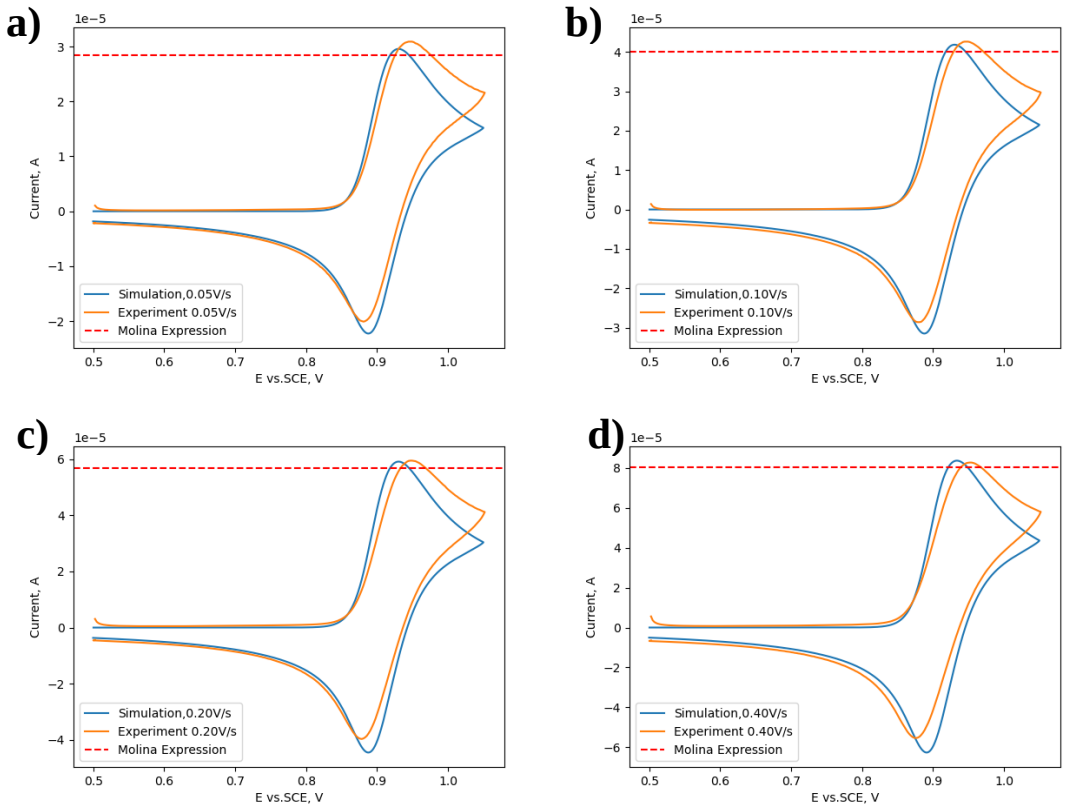


Figure A5.1 Simulated and experimental cyclic voltammograms at different scan rates, a) 50 mV s^{-1}, b) 100 mV s^{-1}, c) 200 mV s^{-1} and d) 400 mV s^{-1} (Simulated and plotted by Mr. Chen).

A formal potential of 0.91 V as inferred from Eq. (5.21), a diffusion coefficient of Br^- of 2.10 × 10^{-9} m^2 s^{-1} obtained from the micro-disk electrode as in Figure 5.2 and a diffusion coefficient of Br_2 of 1.5 × 10^{-9} m^2 s^{-1} (optimised for best fit) were used to run

the simulations for a bulk concentration of 5.0 mM at different scan rates as shown in Figure A5.1. The simulated plots are in good agreement with the experimental voltammograms.

Next, the peak currents versus square root of scan rate was plotted for the experimental, simulated and Molina's simulated voltammograms and are shown in Figure A5.2. The slope of the experiment line is $1.23 \times 10^{-4} \frac{A}{\sqrt{V/S}}$ which is in very good agreement with the slope value of the simulation $1.22 \times 10^{-4} \frac{A}{\sqrt{V/S}}$ and slope of $1.21 \times 10^{-4} \frac{A}{\sqrt{V/S}}$ expected from for Molina's equation. Note that Molina's equation considerers the diffusion coefficients of Br^- and Br_2 to be identical.

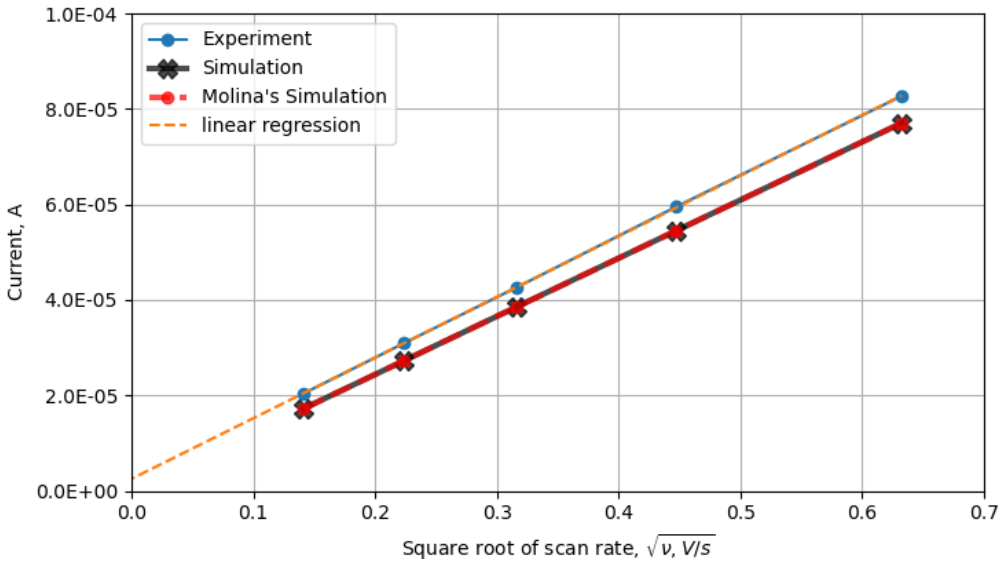


Figure A5.2 Plot of peak current versus sq. root of scan rate comparing the experimental and simulated plots together with the prediction of Molina's equation for the oxidation of Br^- of concentration of 5.0 mM (Simulated and plotted by Mr. Chen).

References

1. Chen, H. T.; Kumar, A. K. S.; Le, H. N.; Compton, R. G., Non-unity stoichiometric reversible electrode reactions. The effect of coupled kinetics and the oxidation of bromide. *J Electroanal Chem* **2020,** *876*.

2. Yamazaki, S.; Ito, T.; Yamagata, M.; Ishikawa, M., Non-aqueous electrochemical capacitor utilizing electrolytic redox reactions of bromide species in ionic liquid. *Electrochim Acta* **2012,** *86*, 294-297.

3. Archana, K. S.; Naresh, R. P.; Enale, H.; Rajendran, V.; Mohan, A. M. V.; Bhaskar, A.; Ragupathy, P.; Dixon, D., Effect of positive electrode modification on the performance of zinc-bromine redox flow batteries. *J Energy Storage* **2020,** *29*.

4. Vafiadis, H.; Skyllas-Kazacos, M., Evaluation of membranes for the novel vanadium bromine redox flow cell. *J Membrane Sci* **2006,** *279* (1-2), 394-402.

5. Zhou, H. T.; Zhang, H. M.; Zhao, P.; Yi, B. L., A comparative study of carbon felt and activated carbon based electrodes for sodium polysulfide/bromine redox flow battery. *Electrochim Acta* **2006,** *51* (28), 6304-6312.

6. Chen, Q.; Eisenach, L.; Aziz, M. J., Cycling Analysis of a Quinone-Bromide Redox Flow Battery. *J Electrochem Soc* **2016,** *163* (1), A5057-A5063.

7. White, R. E.; Lorimer, S. E., A Model of the Bromine Bromide Electrode-Reaction at a Rotating-Disk Electrode. *J Electrochem Soc* **1983,** *130* (5), 1096-1103.

8. Xu, J.; Georgescu, N. S.; Scherson, D. A., The Oxidation of Bromide on Platinum Electrodes in Aqueous Acidic Solutions: Electrochemical and In Situ Spectroscopic Studies. *J Electrochem Soc* **2014,** *161* (6), H392-H398.

9. Chang, J. H.; Bennett, B.; Bard, A. J., Detection of an Unstable Intermediate in Br- Electro-oxidation to Br^{3-} on a Platinum Electrode in Nitrobenzene by Scanning Electrochemical Microscopy. *Electrochim Acta* **2017,** *238*, 74-80.

10. Allen, G. D.; Buzzeo, M. C.; Villagran, C.; Hardacre, C.; Compton, R. G., A mechanistic study of the electro-oxidation of bromide in acetonitrile and the room temperature ionic liquid, 1-butyl-3-methylimidazolium bis(trifluoromethylsulfonyl)imide at platinum electrodes. *J Electroanal Chem* **2005,** *575* (2), 311-320.

11. Ruasse, M. F.; Aubard, J.; Galland, B.; Adenier, A., Kinetic-Study of the Fast Halogen Trihalide Ion Equilibria in Protic Media by the Raman-Laser Temperature-Jump Technique - a Non-Diffusion-Controlled Ion Molecule Reaction. *J Phys Chem-Us* **1986,** *90* (18), 4382-4388.

12. Mastragostino, M.; Gramellini, C., Kinetic-Study of the Electrochemical Processes of the Bromine Bromide Aqueous System on Vitreous Carbon Electrodes. *Electrochim Acta* **1985,** *30* (3), 373-380.

13. Ševčík, A., Oscillographic polarography with periodical triangular voltage. *Collection of Czechoslovak Chemical Communications* **1948,** *13*, 349-377.

14. Gomez-Gil, J. M.; Laborda, E.; Molina, A., General Explicit Mathematical Solution for the Voltammetry of Nonunity Stoichiometry Electrode Reactions: Diagnosis Criteria in Cyclic Voltammetry. *Analytical Chemistry* **2020,** *92* (5), 3728-3734.

15. Compton, R. G.; Banks, C. E., *Understanding Voltammetry, 3rd Edition* **2018**, 1-439.

16. Compton, R. G.; Laborda, E.; Ward, K. R., *Understanding Voltammetry: Simulation of Electrode Processes* **2014**, 1-24.

17. Novev, J. K.; Compton, R. G., Natural convection effects in electrochemical systems. *Curr Opin Electroche* **2018,** *7*, 118-129.

18. Butler, J. A. V., Studies in heterogeneous equilibria. Part II - The kinetic interpretation of the nernst theory of electromotive force. *T Faraday Soc* **1924,** *19* (3), 0729-0733.

19. Cussler, E. L., *Diffusion: Mass Transfer in Fluid Systems*. Cambridge University Press: 1997.

20. O. R. Osipov, M. A. N., Yu. M. Povarov and P. D. Lukovtsev, *Electrokhimiya* **1972,** *8*, 327.

21. Wang, Y.; Limon-Petersen, J. G.; Compton, R. G., Measurement of the diffusion coefficients of $[Ru(NH_3)_6]^{3+}$ and $[Ru(NH_3)_6]^{2+}$ in aqueous solution using microelectrode double potential step chronoamperometry. *Journal of Electroanalytical Chemistry* **2011,** *652* (1-2), 13-17.

22. SAITO, Y., A theoretical study on the diffusion current at the stationary electrodes of circular and narrow band types. *Review of Polarography* **1968,** *15* (6), 177-187.

23. White, R. E.; Lorimer, S., A model of the bromine/bromide electrode reaction at a rotating disk electrode. *Journal of the Electrochemical Society* **1983,** *130* (5), 1096.

24. Gomez-Gil, J. M.; Laborda, E.; Molina, A., General Explicit Mathematical Solution for the Voltammetry of Nonunity Stoichiometry Electrode Reactions: Diagnosis Criteria in Cyclic Voltammetry. *Anal Chem* **2020,** *92* (5), 3728-3734.

25. Chang, L.; Bard, A. J., Electrochemical Characterization of Bromine Reduction to Tribromide in Individual Nitrobenzene-in-Water Emulsion Droplets. *J Electrochem Soc* **2020,** *167* (6).

26. Xu, J.; Georgescu, N. S.; Scherson, D. A., The oxidation of bromide on platinum electrodes in aqueous acidic solutions: electrochemical and in situ spectroscopic studies. *Journal of The Electrochemical Society* **2014,** *161* (6), H392.

Chapter 6

Do Carbon Nanotubes Catalyse Bromine/Bromide Redox Chemistry ?

In the previous chapter the formal potential of Br_2/Br^- redox couple was derived using modified Nernst equation for non-unity stoichiometric reaction and the follow-up chemistry of the homogenous chemical reactions for the formation of tribromide (Br_3^-) ions providing a basis for the work in this chapter where the redox chemistry of both the bromide oxidation and bromine reduction reactions are studied at *single* bamboo-like multiwalled carbon nanotubes (b-MWCNTs) allowing inference of the electron transfer kinetics of the Br_2/Br^- redox couple, widely used in batteries. The nanotubes are shown to be mildly catalytic compared to a glassy carbon surface. Conventional voltammetry on porous ensembles of b-MWCNTs suggests that under such conditions thin-layer diffusion within the porous layers of the drop-casted b-MWCNTs layer is coupled with semi-infinite diffusion to the electrode surface giving rise to mixed transport regime which masks the true catalytic response.

The work in this chapter has been published in the journal *Chemical Science*[1].

6.1 Introduction

In Chapter 5 the formal potential of Br_2/Br^- redox couple which is a cathode reaction in zinc-bromine redox flow batteries[2] was calculated using the correct form of *Randles-Ševčík* equation reflecting the non-unity stoichiometric nature of the reaction[3]. The performance of batteries is generically limited by the thermodynamics and kinetics of the redox couples comprising the battery where fast ('reversible') electron transfer is

essential. In many cases, including the Br_2/Br^- couple the electrode reaction involves more than one electron as given in the stoichiometric reaction,

$$2Br^- - 2e^- \quad \rightleftarrows \quad Br_2 \tag{6.1}$$

with, at high bromide concentrations, the possibility of the follow up chemical reaction[3]

$$Br_2 + Br^- \quad \rightleftarrows \quad Br_3^- \tag{6.2}$$

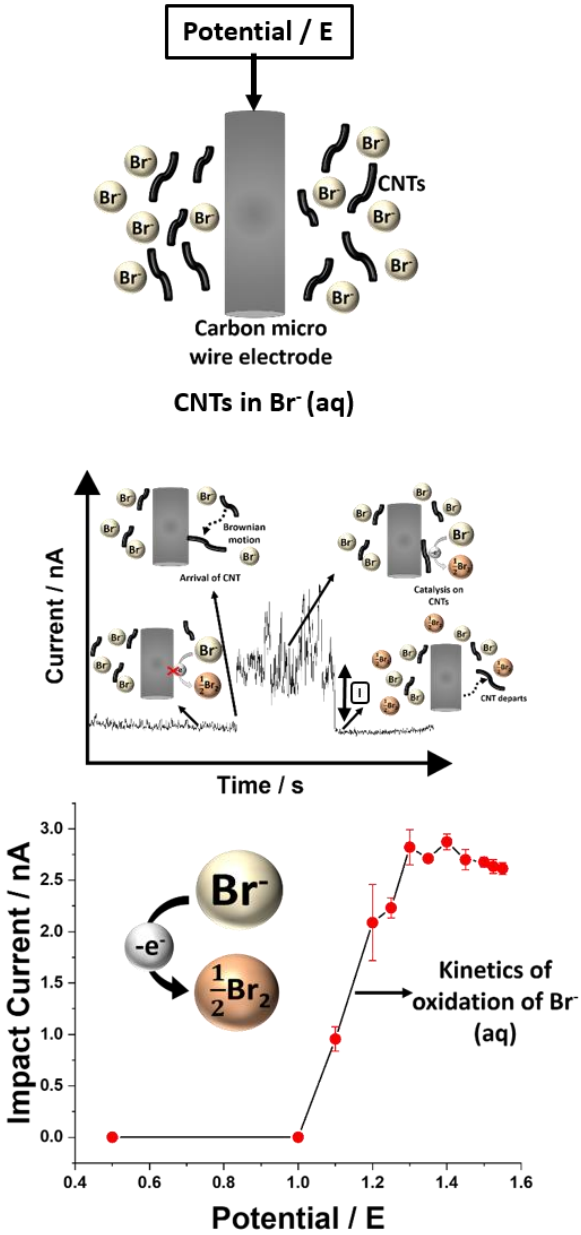


Figure 6.1 Schematic representation of 'nano-impact' electrochemistry on a carbon micro wire electrode for the oxidation of aqueous bromide from which the kinetics of the BOR are inferred. Analogous reductive experiments allow the inference of the kinetics of the BRR.

Since electrons are usually transferred sequentially this implies that the mechanism is multistep with any of the individual mechanistic steps in principle being rate limiting. For this reason, catalysts are commonly required to enhance the electrode kinetics at otherwise favourable electrode materials. One type of catalyst which has seen wide usage, including for the Br_2/Br^- couple[4, 5] are carbon nanotubes (CNTs) with suggested advantages as highlighted in Chapter 3[6]. The deployment of CNTs as a porous composite presents a further level of complexity to the electrode reaction beyond its multistep character because of the ill-defined mass transport within the porous layer. In particular ascertaining the intrinsic electron transfer kinetics and hence level of catalysis, if any, is essentially impossible since these are masked in the voltammetric response by diffusional mass transport effects[7-10]. Specifically, the transport within the porous structure of CNTs layers is dominated by thin-layer, and other[11, 12] effects which give the illusion of electrochemical reversibility. In order to unscramble possible electro-catalysis of the bromine/bromide couple a different approach is needed.

In the following we study both the electro-oxidation of bromide (BOR) and the electro-reduction of bromine (BRR) at *single* b-MWCNTs via 'nano-impact' (aka 'single entity') electrochemistry'[13-16] in aqueous solution. In this approach a microwire electrode at a fixed potential is inserted in a suspension of b-MWCNTs in the solution of interest. From time-to-time a single b-MWCNT impacts the electrode, adopts the potential of the latter for the duration of the impact which in the case of b-MWCNTs can vary from 1 - 100 of seconds[17-19] and sustained catalytic currents flow if the oxidation/reduction of interest is faster at the nanotube in comparison with the microwire electrode. The catalytic currents are studied as a function of potential revealing the electron transfer kinetics. Figure 6.1 shows the concept of the experiment.

6.2 Experimental

The chemicals used in this chapter are listed in Chapter 2, Table 2.1. The chemicals were purchased commercially and used without any further purification.

6.2.1 Preparation of Electrodes for Cyclic Voltammetry Studies

i) Pristine GC working electrode

Electro-oxidation of bromide (BOR) and reduction of bromine (BRR) were conducted in solutions of either 5.00 ± 0.05 mM NaBr in 0.10 M HNO_3 or 5.00 ± 0.06 mM bromine in 0.10 M HNO_3. A pristine glassy carbon (GC) electrode of diameter 0.30 cm and area 0.07 cm^2 was used as the working electrode after thorough cleaning using alumina powder (Buehler, Micropolish II) of nominal sizes 1 μm, 0.3 μm and 0.05 μm in an decending order on lapping pads. The electrode was further sonicated (Fisher Scientific FB15050 ultrasonic) in ultrapure water for 10 s to remove any residual alumina powder. The electrode was then dried under N_2 before experiments.

ii) b-MWCNTs modified GC working electrode

1 mg of b-MWCNTs in 1 mL of acetone was dispersed by sonicating it for 10 mins. 30 μL (30 μg of b-MWCNTs) from the dispersed solution was drop-casted on a clean pristine GC and dried under constant N_2 flow. Voltammetry was then conducted to study both BOR and BRR at the b-MWCNTs drop-casted GC.

6.2.2 Nano-Impacts at Carbon Microwire Electrode – Chronoamperometry Studies

An in-house fabricated carbon microwire electrode was used for these experiments. The detailed fabrication method is explained in Chapter 2, Section 2.4. For both BOR and BRR studies, the dispersed b-MWCNTs solution was obtained by adding 1 mg of b-MWCNTs in 1 mL of ultrapure water and then sonicated for 15 mins. In a

chronoamperometry experiment, 50 µL each of the dispersed b-MWCNTs solution was added to 5.00 ± 0.05 mM of NaBr in 0.10 M HNO_3 for observing impacts corresponding to BOR and 5.00 ± 0.06 mM of bromine in 0.10 M HNO_3 to observe impacts for BRR (1.10×10^{-15} M of dispersed b-MWCNTs).

6.3 Results and Discussion

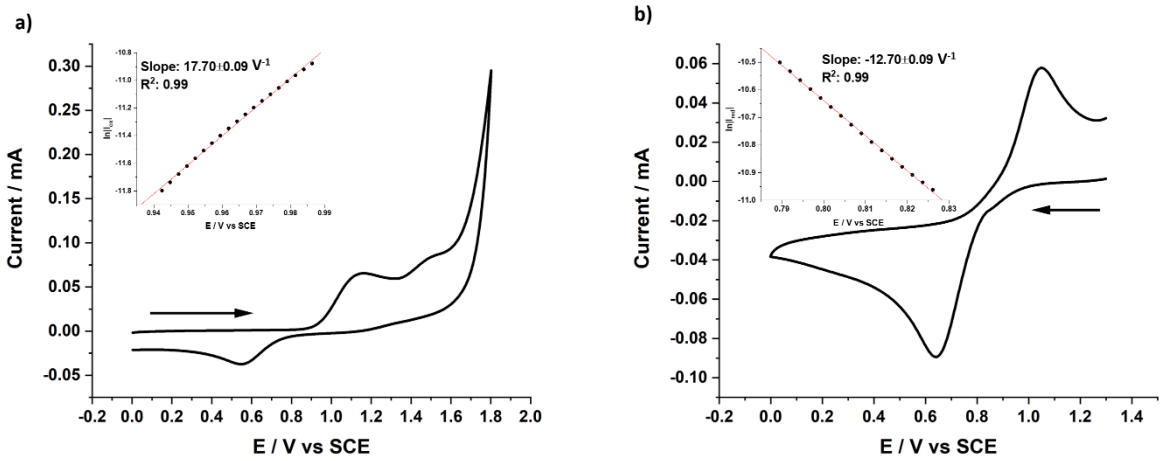


Figure 6.2 Cyclic voltammogram at pristine GC electrode a) for BOR in 5.00 (± 0.05) mM NaBr in 0.10 M HNO_3 at a scan rate of 0.05 Vs^{-1}; Inset shows the Tafel plot with a slope of 17.70 (± 0.09) V^{-1} giving β of 0.45 (± 0.01), b) for BRR 5.00 (± 0.06) mM Bromine in 0.10 M HNO_3 at a scan rate of 0.05 V s^{-1}; Inset shows Tafel plot with a slope of -12.70 (± 0.09) V^{-1} giving α of 0.33 (± 0.01). In both the cases 10% - 30% of the current range of the forward wave was used.

The BOR and BRR were studied first, voltammetrically at an unmodified glassy carbon (GC) electrode as shown in Figure 6.2 using 5.0 mM solutions of either NaBr or Br_2 in 0.1 M HNO_3. The cyclic voltammograms obtained showed that the Br_2/Br^- redox reaction at GC electrode is completely electrochemically irreversible. The midpoint potential was in the range 0.81 to 0.83 V versus saturated calomel electrode (SCE) corresponding to the scan rates 0.05 V s^{-1} to 0.8 V s^{-1} approximately consistent with the literature values for the Br_2/Br^- couple at carbon electrodes[20]. The formal potential calculated in Chapter 5 at Pt macro electrode for reversible Br_2/Br^- redox reaction is 0.91 V vs SCE. The deviation of the mid-point potential from the formal potential reflects

partly the non-unity stoichiometry, partly the inequality of the diffusion coefficients of bromine and bromide and partly the fact that the full electrochemical irreversibility coupled with the different transfer coefficients for the anodic and cathodic process which causes the two peaks to shift differently with scan rate so that the mid-point potential is itself scan rate dependent. The latter is discussed below.

The voltammograms were analysed to give transfer coefficients of 0.45 ± 0.01 and 0.33 ± 0.01 using the equations $\beta = \frac{RT}{F}\frac{\partial \ln |I_{ox}|}{\partial E}$ and $\alpha = \frac{RT}{F}\frac{\partial \ln |I_{red}|}{\partial E}$ (Figure 6.2, insets) for BOR and BRR respectively. Note that in both the cases a current range of 10% - 30% of the peak current was used for analysis to avoid the influence of mass transport[21]. Figure 6.3 shows the Tafel slopes of BRR and BOR at a scan rate of 0.05 V s^{-1}. The intersection of the Tafel plots reveal the equilibrium potential of Br_2/Br^- redox couple at 0.92 V vs SCE which is in very good agreement with the formal potential calculated in Chapter 5.

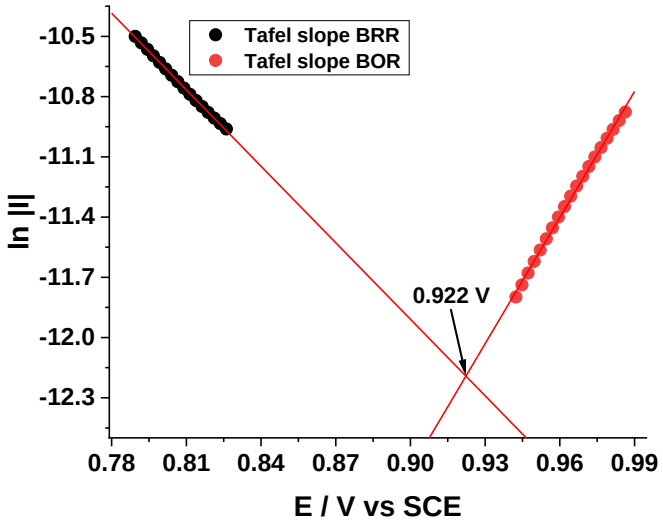


Figure 6.3 Tafel plots of BRR (black circles) and BOR (red circles) at a scan rate of 0.05 V s^{-1} whose intersection gives the equilibrium potential of 0.92 V vs SCE for Br_2/Br^- redox couple.

Further, a plot of peak current versus square root of scan rate for both the reaction is given in Figure 6.4. The linearity of the plot infer that both the processes are diffusional. The

diffusion coefficients D_{Br^-} and D_{Br_2} were calculated to be 2.05 (± 0.04) x 10^{-5} cm^2 s^{-1} and 1.50 (± 0.04) x 10^{-5} cm^2 s^{-1} using the Randles–Ševčík equation for an irreversible reaction. These values are also consistent with those reported in Chapter 5 where the former was confirmed from the experiment at Pt micro-disc electrode and the latter from the simulations.

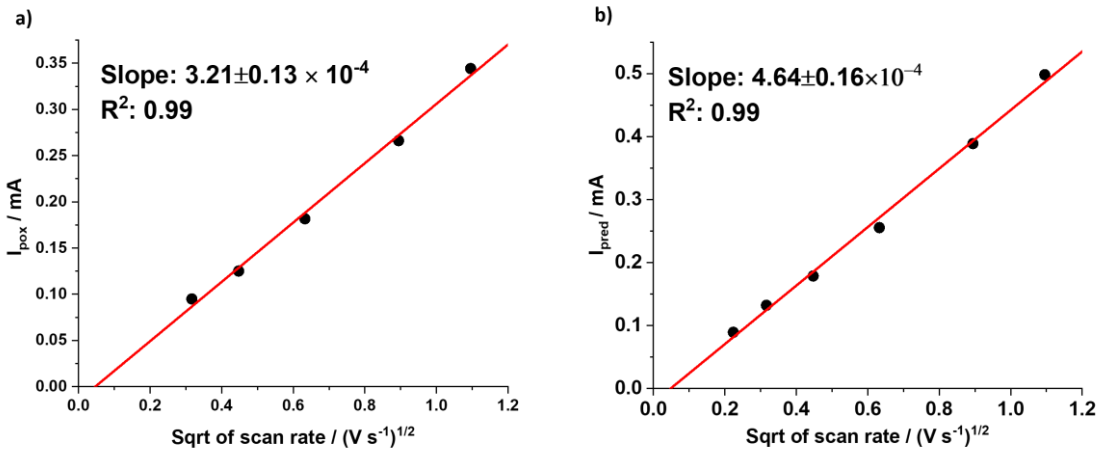


Figure 6.4 a) Plot of oxidative peak current (I_{pox}) vs square root of scan rate for 5.00 (± 0.05) mM NaBr in 0.10 M HNO_3 and D_{Br^-} 2.05 (± 0.04) x 10^{-5} cm^2 s^{-1} b) plot of I_{pred} vs square root of scan rate for 5.00 (± 0.06) mM Bromine in 0.10 M HNO_3 and D_{Br_2} 1.50 (± 0.04) x 10^{-5} cm^2 s^{-1}.

Next the electrodes were modified with 30 µg of b-MWCNTs consisting of ca. 125 monolayers (the calculation is given in Chapter 4, Appendix, Section A4.1) of b-MWCNTs assuming they are closely packed across the area of the GC electrode, and the resulting voltammograms are shown in Figure 6.5 (red lines) compared with the voltammograms at bare GC electrode (black lines). Note that, in reality the b-MWCNTs are likely arranged randomly and a much greater thickness is expected. The mid-point potential of 0.88 V vs SCE was obtained as an average of all the mid-point potentials at different scan rates. This value again slightly deviates from the calculated formal potential in Chapter 5 owing to the quasi-reversibility of the signal allied to the different oxidative and reductive transfer coefficients, as discussed above, and to the differences in the diffusion coefficients. In comparison with the unmodified electrode enhanced currents

are seen for the Br_2/Br^- couple which partly reflects the enhanced capacitance of the interface reflecting in turn the large surface area of the deposited nanotubes (*ca.* 60 - 120 cm^2). Larger signals are also seen indicating a thin layer contribution from material occluded within the porous layer which also leads to the *apparently* quasi-reversible shape of the voltammograms obtained for both reactions.

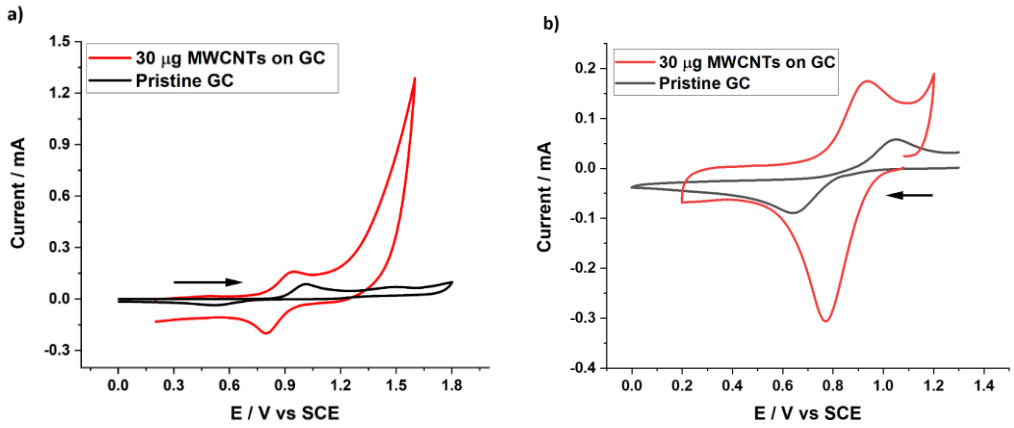


Figure 6.5 Cyclic voltammograms at pristine GC (black line) and 30 µg b-MWCNTs drop-casted on GC (red line) at a scan rate of 0.05 V s^{-1} a) for bromide oxidation reaction (BOR) in 5.0 mM NaBr in 0.1 M HNO_3, b) for bromine reduction reaction (BRR) in 5.0 mM Bromine in 0.1 M HNO_3.

As discussed in Chapter 3 CNT modified electrodes can exhibit both semi-infinite diffusion at the surface of the modified electrode and thin-layer diffusion within the electrolyte trapped in the porous layers with the latter resembling a thin-layer cell. The contribution of the different regimes of mass transport can be characterised by means of a log-log plot of peak current (I_p) versus scan rate (ν) with a slope of unity corresponding to thin-layer electrolysis and a slope of 0.5 to semi-infinite diffusion. An intermediate value often indicates a mixed regime as is thought to operate for b-MWCNTs modified electrodes[8, 10]. A log-log plot of (I_p) vs (ν) showed a gradient value of 0.68 (± 0.01) and 0.66 (± 0.03) for BOR and BRR as shown in Figure 6.6 suggesting a mixed mass transport regime[8, 10] with a combination of semi-infinite diffusion and thin layer behaviour. The transition from fully irreversible to *apparent* quasi-reversible character is sometimes

confused with electro-catalysis attributed to the CNTs rather than thin-layer diffusion[8-10, 22]. In order to ascertain the true catalytic response, single entity electrochemistry was measured to obtain the BOR and BRR responses at single b-MWCNTs.

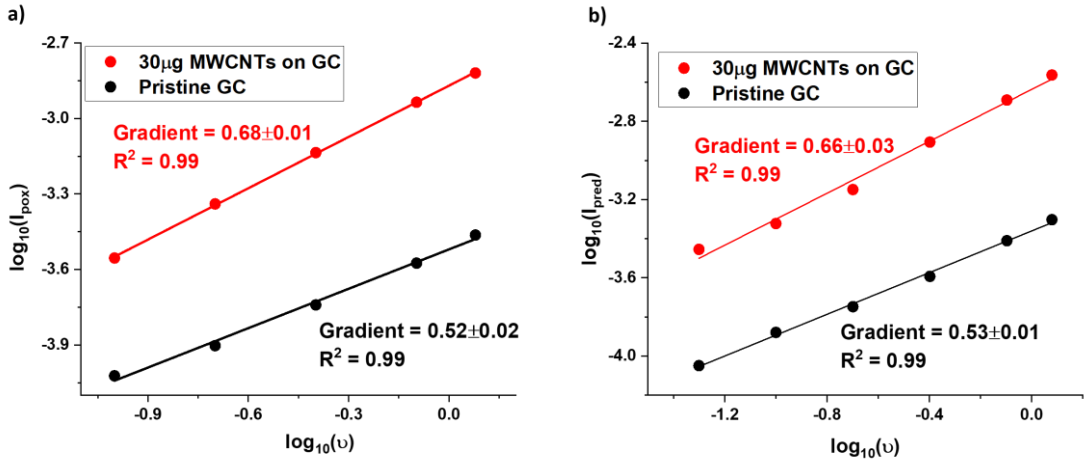


Figure 6.6 Plot of log I_p vs log ν a) for BOR at a GC modified with 30 μg of b-MWCNTs (red line) with a gradient value of 0.68 (± 0.01); and at a pristine GC (black line with a gradient value of 0.52 (± 0.02), b) for BRR at the b-MWCNTs modified GC (red line) with a gradient value of 0.66 (± 0.03) and at a pristine GC (black line with gradient value of 0.53 (± 0.01).

For single entity measurements, an in-house fabricated clean carbon wire (CWE, length 1 mm and diameter 7 μm) working electrode was used. The fabrication method is discussed in Chapter 2, Section 2.4. Chronoamperograms were first recorded at a constant applied potential of 1.3 V vs SCE and 0.2 V vs SCE for BOR and BRR respectively (5.0 mM solutions). These values were selected in the light of Figure 6.5 to provide a large overpotential for each reaction. Clear oxidative and reductive current steps were observed (Figure 6.7). These were ascribed due to the arrival of a single b-MWCNT at the electrode surface and the resulting catalytic electron transfer for the duration of the impact. No steps were observed in the absence of b-MWCNTs (Appendix, Figure A6.1). The average residence time of the b-MWCNT was 1.2 (± 0.5) seconds and the frequency of the collisions were 0.3 (± 0.1) impacts s^{-1}. The average impact current for the BOR at 1.3 V vs SCE was 2.8 (± 0.2) nA (65 impacts) and for the BRR at 0.2 V vs SCE to be 3.8 (± 0.1) nA (70 impacts). The impact currents were assumed to be entirely Faradaic since

control experiments in 0.1 M HNO_3 solution in the presence of 100 µg of b-MWCNTs (in the absence of Br^- and Br_2) showed no obvious impacts as shown in Figure 6.8.

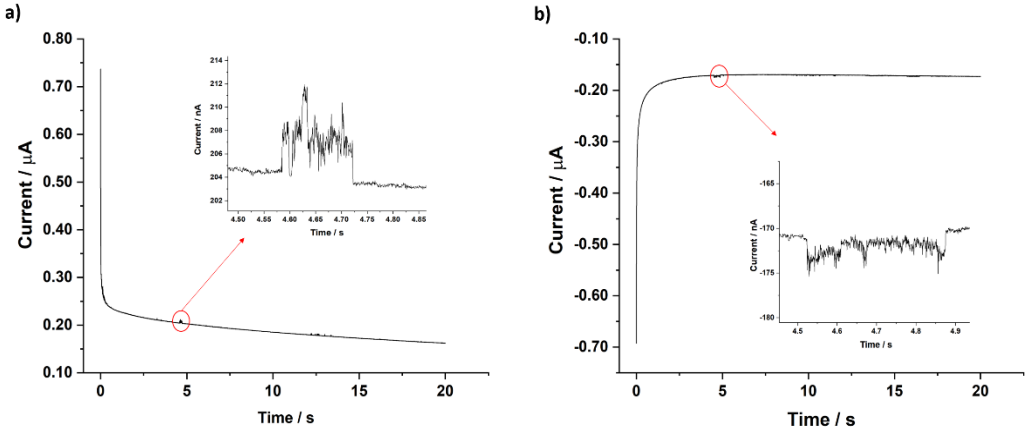


Figure 6.7 Chronoamperograms showing the impact step current a) for BOR in 5.0 mM NaBr in 0.1 M HNO_3 at 1.3 V vs SCE, b) for BRR in 5.0 mM Bromine in 0.1 M HNO_3 at 0.2 V vs SCE. Impacts observed at other potentials are shown in Appendix Section A6.2

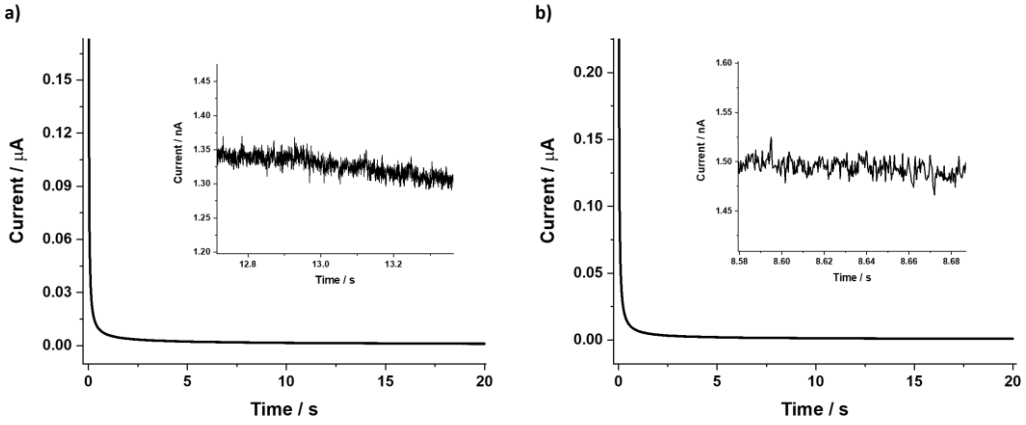


Figure 6.8 Chronoamperograms in 0.1 M HNO3 a) at 1.3 V vs SCE in the absence of MWCNTs b) at 1.3 V vs SCE in 100 µg of dispersed b-MWCNTs.

Further, single entity measurements were made over the potential range 1.10 V to 1.55 V vs SCE for BOR and 0.45 V to 0.10 V vs SCE for BRR using the same methodology as above. Impacts for both the BOR and BRR were observed at various potentials and analysed to obtain the average Faradaic current at each potential. The average impact step current in the two ranges was plotted against the applied potential (Figure 6.9).

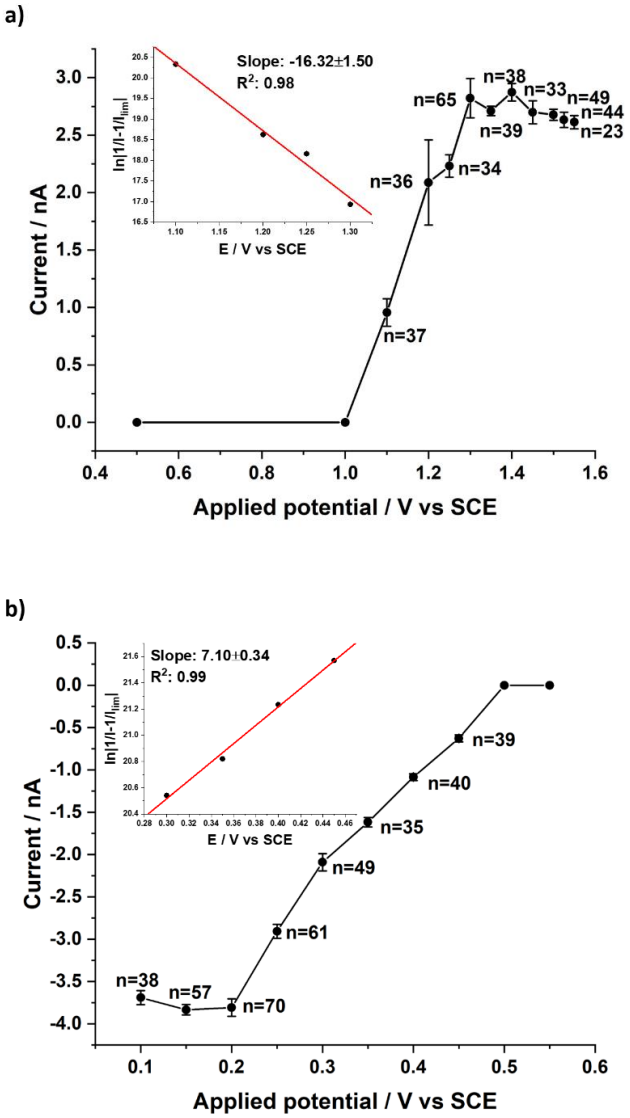


Figure 6.9 Average step currents observed as a function of applied potential a) for BOR in 5.0 mM NaBr in 0.1 M HNO_3 at, b) for BRR in 5.0 mM Bromine in 0.1 M HNO_3; inset in both the cases show mass transport corrected Tafel analyses.

Two sigmoidal curves were obtained reflecting the current – potential response for the either the bromide oxidation (BOR) or the bromine reduction (BRR) were seen. The curves reflect the average "voltammograms" (current-potential characteristics) for the Br_2/Br^- redox reaction at *single* carbon nanotubes. The shape of the two sigmoidal curves reflects the onset of electrolysis followed by a diffusion-controlled plateau at high over-

potentials[23]. Mass transport corrected Tafel analysis (Figure 6.9; insets) was conducted using the following equations[24],

$$\beta = \frac{RT}{F}\frac{\partial ln\left|\frac{1}{I_{ox}} - \frac{1}{I_{lim}}\right|}{\partial E} \tag{6.3}$$

$$\alpha = \frac{RT}{F}\frac{\partial ln\left|\frac{1}{I_{red}} - \frac{1}{I_{lim}}\right|}{\partial E} \tag{6.4}$$

where, I_{lim} is the limiting current.

A Tafel slope of -16.3 (± 1.5) V per decade was obtained for the BOR giving β of 0.42 (± 0.03). For the BRR slope of 7.1 (± 0.3) V per decade was obtained yielding α of 0.20 (± 0.01) as shown in Figure 6.9a and b insets).

Next, the length of the b-MWCNTs were calculated from the impact current obtained for both the BOR and the BRR assuming that the plateau currents in Figure 6.9 correspond to a diffusion controlled current. For this calculation, the b-MWCNT was considered to resemble a cylindrical electrode with length *l* and radius *r* following the approach to 'single-entity' studies of CNTs by Xiuting et., al.,[15, 23, 25] , the current for time *t* is given by Eq. (6.5)[26].

$$I_p = 2\pi nFDClf(\tau) \tag{6.5}$$

with,

$$f(\tau) = \frac{e^{-\sqrt{\pi\tau}/20}}{\sqrt{\pi\tau}} + \frac{1}{ln[(2e^{-\gamma}\tau)^{1/2} + e^{-5/3}]}$$

$$\tau = \frac{4Dt}{r^2}$$

where *D* is the diffusion coefficient, *C* is the analyte concentration, and *n* is the number of electrons.

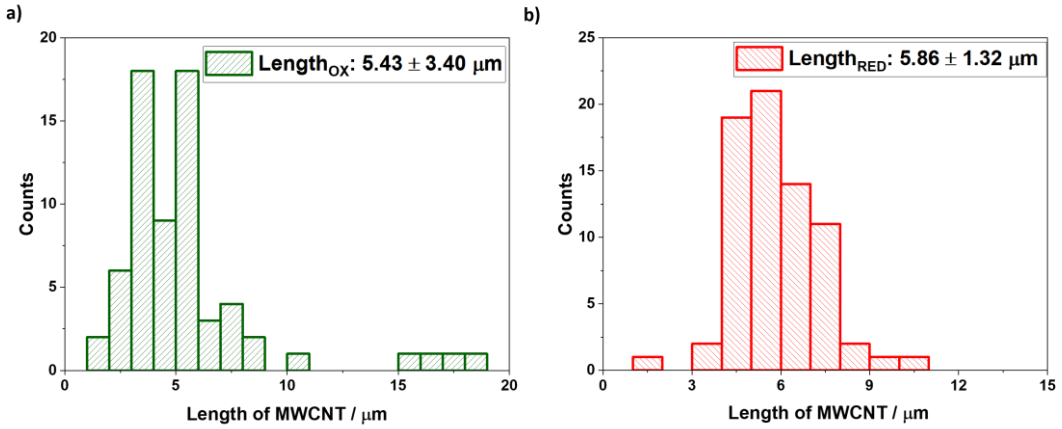


Figure 6.10 Histogram showing the length of b-MWCNTs calculated from observed impacts a) for BOR at 1.30 V vs SCE to be 5.43 (± 3.40) µm, b) for BRR at 0.20 V vs SCE to be 5.86 (± 1.32) µm.

The lengths were found to be 5.4 (± 3.4) µm (BOR) and 5.9 (± 1.3) µm (BRR) and are given in Figure 6.10. These values were compared with previously reported dark-field optical microscopy data and good agreement was observed with the literature value to be 5.3 (± 2.1) µm[27]. The observed consistency provides strong support for the choice of modelling the single entity voltammetry by analogy with that of a cylindrical electrode.

It is evident that the single entity measurements allow a clear analysis of the catalytic behaviour of the carbon nanotubes by providing a well-defined diffusional regime conducive to the extraction of the electrode kinetics of both the bromide oxidation and the bromine reduction process. In contrast electrodes formed by ensembles of carbon nanotubes in the form of a porous layer where the mixed transport regime is not amenable to ready modelling and the dissection of thin-layer effects from the measured voltammetry. The electron transfer kinetics for both the BOR and BRR at single b-MWCNTs was then obtained via full simulation of the two-single entity

'voltammograms' using the above measured diffusion coefficients and again treating the impacted b-MWCNT as a cylindrical electrode with uniform diffusional access and further assuming Butler – Volmer kinetics. The commercial software DigiSim was used for the simulations[28, 29]. The b-MWCNTs radius of 15 ± 5 nm was used as provided by the supplier and the length obtained from the impacts was employed. The formal potential of 0.91 V vs SCE was used as calculated in Chapter 5 at 298.15 K. The transfer coefficients β and α of 0.42 and 0.20 were used calculated from the mass transport corrected Tafel analyses of the impacts as in Figure 6.9; insets. Diffusion coefficients D_{Br^-} (2.05 x 10^{-5} cm^2 s^{-1}) and D_{Br_2} (1.50 x 10^{-5} cm^2 s^{-1}) were used as discussed above.

For BOR, a one electron transfer process was considered as given below,

$$Br^- - e^- \rightarrow \frac{1}{2}Br_2 \tag{6.6}$$

And for BRR the a two electron transfer process was modelled,

$$Br_2 + 2e^- \rightarrow 2Br^- \tag{6.7}$$

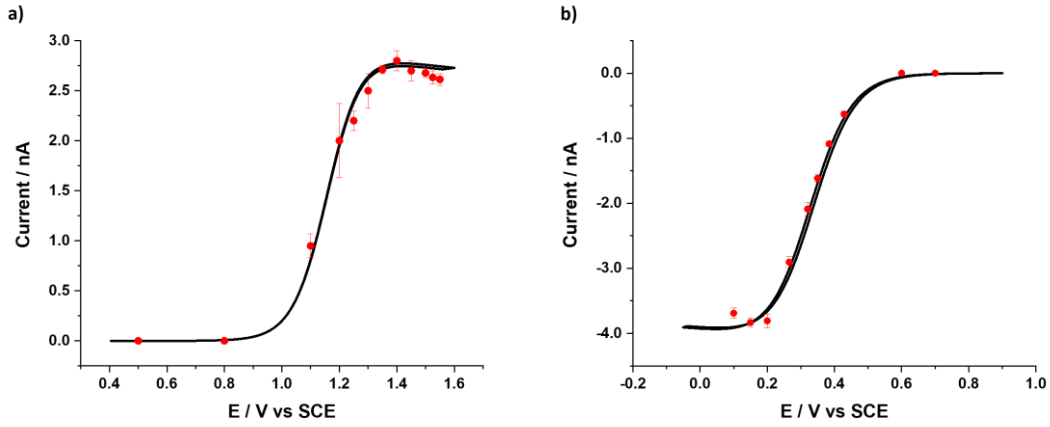


Figure 6.11 DIGISIM simulated curves (black line) for average impact currents obtained at different potentials (red circles) a) for BOR with rate constant (k_{BOR}) of 1.0 (± 0.1) x 10^{-3} cm s^{-1}; b) BRR with k_{BRR} of 5.0 (± 0.1) x 10^{-4} cm s^{-1}.

The bulk concentrations of both Br^- and Br_2 were 5.0 mM with other bulk concentrations set to zero at the beginning of the simulation. With all the parameters fixed, the only

unknown is the standard electrochemical rate constant *k*. The rate constants for both the BOR and the BRR were optimised to get the best fit for the voltammogram as shown in Figure 6.11. The standard electrochemical rate constants for each process, k_{BOR} and k_{BRR} were found to be 1.0 (± 0.1) x 10^{-3} cm s^{-1} and 5.0 (± 0.1) x 10^{-4} cm s^{-1} respectively.

Next, in order to compare the kinetics between b-MWCNTs and bare GC electrode the voltammograms at pristine GC were simulated. For this, the electrode geometry was considered to be planar with area of the electrode to be 7.07 x 10^{-2} cm^2. The transfer coefficients β and α were 0.45 and 0.33 for BOR and BRR respectively as in Figure 6.2. All the other parameters were as used similar to that used to simulate the impact voltammogram. In this way the rate constants at pristine GC for BOR and BRR were calculated to be 9.5 (± 0.1) x 10^{-5} cm s^{-1} and 2.0 (± 0.1) x 10^{-5} cm s^{-1} respectively (Figure 6.12) again referenced to the formal potential for the bromide/bromine couple of 0.91 V vs SCE.

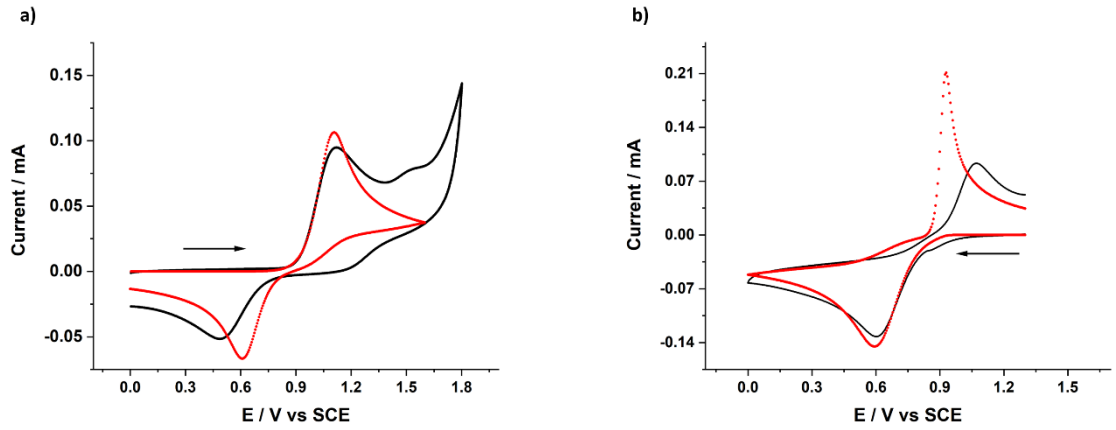


Figure 6.12 Overlay of DIGISIM simulated curves (red line) and experimental voltammograms at pristine GC (black line) a) for BOR with the standard electrochemical rate constant (k_{BOR}) 9.5 (± 0.1) x 10^{-5} cm s^{-1}, b) for BRR with standard electrochemical rate constant

The transfer coefficients and rate constants obtained from impacts were compared to the voltammograms obtained at pristine GC for BOR and BRR and are given in Table 6.1. It

is clearly evident that b-MWCNT shows some, albeit modestly, improved catalytic activity towards the Br_2/Br^- redox reaction when compared to pristine GC electrode.

Table 6.1 Transfer coefficients and rate constants for BOR in 5.0 mM NaBr in 0.1 M HNO_3 and BRR in 5.0 mM Bromine in 0.1 M HNO_3 obtained at Glassy Carbon macroelectrode GC, and single b-MWCNT impact current.

Analysed Parameter	Oxidation of Bromide	Reduction of Bromine
Transfer coefficient (GC)	$\beta = 0.45$	$\alpha = 0.33$
Transfer coefficient (Impact current)	$\beta = 0.42$	$\alpha = 0.20$
k_{BOR} / cm s^{-1} (GC)	9.5 (± 0.1) x 10^{-5}	2.0 (± 0.1) x 10^{-5}
k_{BRR}/ cm s^{-1} (Impact current)	1.0 (± 0.1) x 10^{-3}	5.0 (± 0.1) x 10^{-4}

6.4 Conclusions

In summary, the b-MWCNTs were studied for their catalytic behaviour towards the Br_2/Br^- redox couple. From the drop-cast experiment, the ensemble b-MWCNTs showed mixed mass transport behaviour complicating and precluding the elucidation of its catalytic behaviour. In contrast, nano-impact electrochemistry of b-MWCNTs shows the faster electrochemical rate constants compared to pristine GC. This confirms the catalytic activity of b-MWCNTs for Br_2/Br^- redox reaction but the values determined are insufficiently enhanced over glassy carbon as to leave considerable room for improvement via the use of alternative electrocatalysts to carbon nanotubes.

Appendix

Section A6.1 Chronoamperograms in the Absence of MWCNTs

Chronoamperograms were recorded in the absence of b-MWCNTs for BOR and BRR at 1.3 V vs SCE and 0.2 V vs SCE respectively. No Faradaic currents were observed.

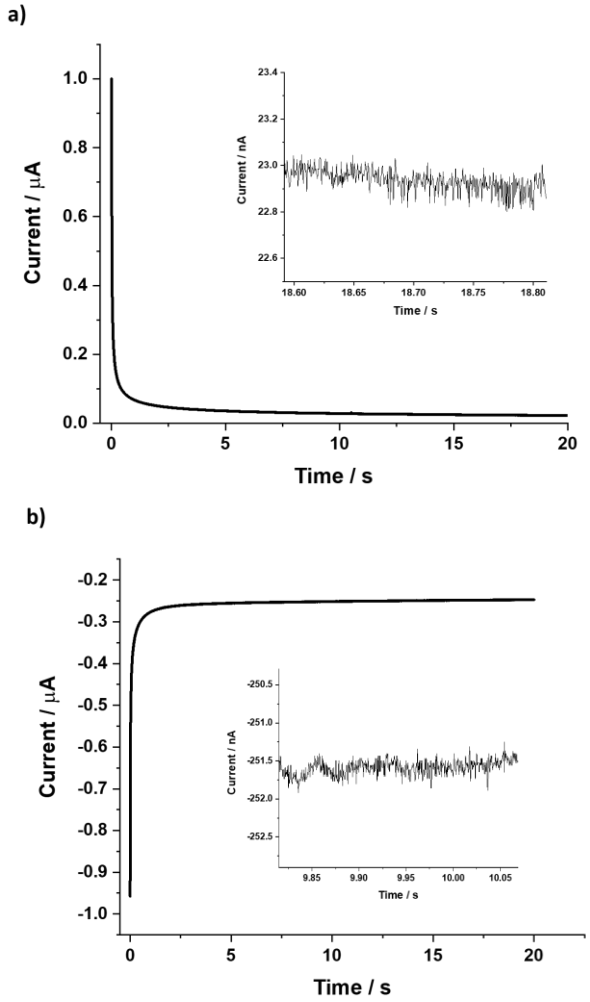


Figure A6.1 Chronoamperograms in the absence of b-MWCNTs a) BOR at 1.3 V vs SCE, b) BRR at 0.2 V vs SCE.

Section A6.2 Chronoamperograms Observed at Different Potentials for BOR and BRR

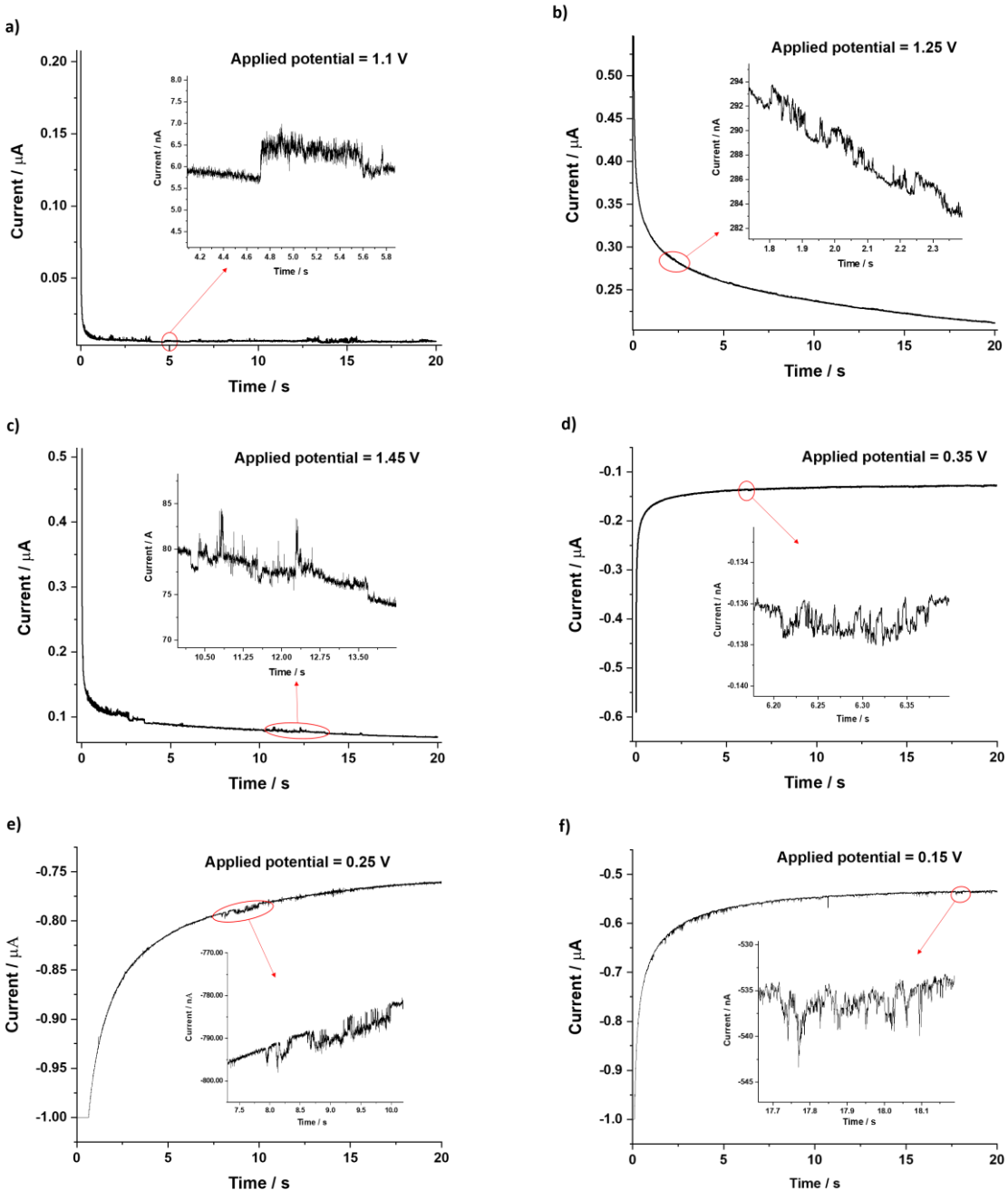


Figure A6.2 Chronoamperograms showing the impact step current for BOR in 5.0 mM NaBr in 0.1 M HNO_3 at a) 1.0 V , b) 1.25 V and c) 1.45 V and for BRR in 5.0 mM Bromine in 0.1 M HNO_3 at d) 0.35 V, e) 0.25 V and f) 0.15 V.

References

1. Kaliyaraj Selva Kumar, A.; Miao, R.; Li, D.; Compton, R. G., Do carbon nanotubes catalyse bromine/bromide redox chemistry? *Chem Sci* **2021,** *12* (32), 10878-10882.

2. Archana, K. S.; Naresh, R. P.; Enale, H.; Rajendran, V.; Mohan, A. M. V.; Bhaskar, A.; Ragupathy, P.; Dixon, D., Effect of positive electrode modification on the performance of zinc-bromine redox flow batteries. *J Energy Storage* **2020,** *29*.

3. Chen, H. T.; Kumar, A. K. S.; Le, H. N.; Compton, R. G., Non-unity stoichiometric reversible electrode reactions. The effect of coupled kinetics and the oxidation of bromide. *J Electroanal Chem* **2020,** *876*.

4. Jang, W. I.; Lee, J. W.; Baek, Y. M.; Park, O. O., Development of a PP/carbon/CNT composite electrode for the zinc/bromine redox flow battery. *Macromol Res* **2016,** *24* (3), 276-281.

5. Rui, X.; Parasuraman, A.; Liu, W.; Sim, D. H.; Hng, H. H.; Yan, Q.; Lim, T. M.; Skyllas-Kazacos, M., Functionalized single-walled carbon nanotubes with enhanced electrocatalytic activity for Br^-/Br^{3-} redox reactions in vanadium bromide redox flow batteries. *Carbon* **2013,** *64*, 464-471.

6. Yan, Y. B.; Miao, J. W.; Yang, Z. H.; Xiao, F. X.; Yang, H. B.; Liu, B.; Yang, Y. H., Carbon nanotube catalysts: recent advances in synthesis, characterization and applications. *Chem Soc Rev* **2015,** *44* (10), 3295-3346.

7. Cao, Q.; Shao, Z.; Hensley, D. K.; Lavrik, N. V.; Venton, B. J., Influence of Geometry on Thin Layer and Diffusion Processes at Carbon Electrodes. *Langmuir* **2021,** *37* (8), 2667-2676.

8. Streeter, I.; Wildgoose, G. G.; Shao, L. D.; Compton, R. G., Cyclic voltammetry on electrode surfaces covered with porous layers: An analysis of electron transfer kinetics at single-walled carbon nanotube modified electrodes. *Sensor Actuat B-Chem* **2008,** *133* (2), 462-466.

9. Sims, M. J.; Rees, N. V.; Dickinson, E. J. F.; Compton, R. G., Effects of thin-layer diffusion in the electrochemical detection of nicotine on basal plane pyrolytic graphite (BPPG) electrodes modified with layers of multi-walled carbon nanotubes (MWCNT-BPPG). *Sensor Actuat B-Chem* **2010,** *144* (1), 153-158.

10. Keeley, G. P.; Lyons, M. E. G., The Effects of Thin Layer Diffusion at Glassy Carbon Electrodes Modified with Porous Films of Single-Walled Carbon Nanotubes. *Int J Electrochem Sc* **2009,** *4* (6), 794-809.

11. Katelhon, E.; Compton, R. G., Unscrambling illusionary catalysis in three-dimensional particle-modified electrodes: Reversible reactions at conducting particles. *Appl Mater Today* **2020,** *18*.

12. Chen, L. F.; Katelhon, E.; Compton, R. G., Particle-modified electrodes: General mass transport theory, experimental validation, and the role of electrostatics. *Appl Mater Today* **2020,** *18*.

13. Sokolov, S. V.; Eloul, S.; Kätelhön, E.; Batchelor-McAuley, C.; Compton, R. G., Electrode–particle impacts: a users guide. *Phys Chem Chem Phys* **2017,** *19* (1), 28-43.

14. Cheng, W.; Compton, R. G., Electrochemical detection of nanoparticles by 'nano-impact' methods. *TrAC Trends in Analytical Chemistry* **2014,** *58*, 79-89.

15. Li, X. T.; Batchelor-McAuley, C.; Shao, L. D.; Sokolov, S. V.; Young, N. P.; Compton, R. G., Quantifying Single-Carbon Nanotube-Electrode Contact via the Nanoimpact Method. *J Phys Chem Lett* **2017,** *8* (2), 507-511.

16. Stevenson, K. J.; Tschulik, K., A materials driven approach for understanding single entity nano impact electrochemistry. *Curr Opin Electroche* **2017,** *6* (1), 38-45.

17. Li, X.; Batchelor-McAuley, C.; Whitby, S. A. I.; Tschulik, K.; Shao, L.; Compton, R. G., Single Nanoparticle Voltammetry: Contact Modulation of the Mediated Current. *Angew. Chem. Int. Ed.* **2016,** *55* (13), 4296-4299.

18. Li, X. T.; Hodson, H.; Batchelor-McAuley, C.; Shao, L. D.; Compton, R. G., Improving Formate and Methanol Fuels: Catalytic Activity of Single Pd Coated Carbon Nanotubes. *ACS Catal* **2016,** *6* (10), 7118-7124.

19. Li, X. T.; Batchelor-McAuley, C.; Tschulik, K.; Shao, L. D.; Compton, R. G., Ultra-small Palladium Nanoparticle Decorated Carbon Nanotubes: Conductivity and Reactivity. *Chemphyschem* **2015,** *16* (11), 2322-2325.

20. White, R. E.; Lorimer, S. E., A Model of the Bromine Bromide Electrode-Reaction at a Rotating-Disk Electrode. *J Electrochem Soc* **1983,** *130* (5), 1096-1103.

21. Li, D. L.; Lin, C. H.; Batchelor-McAuley, C.; Chen, L. F.; Compton, R. G., Tafel analysis in practice. *J Electroanal Chem* **2018,** *826*, 117-124.

22. Henstridge, M. C.; Dickinson, E. J. F.; Aslanoglu, M.; Batchelor-McAuley, C.; Compton, R. G., Voltammetric selectivity conferred by the modification of electrodes using conductive porous layers or films: The oxidation of dopamine on glassy carbon electrodes modified with multiwalled carbon nanotubes. *Sensor Actuat B-Chem* **2010,** *145* (1), 417-427.

23. Li, X. T.; Batchelor-McAuley, C.; Whitby, S. A. I.; Tschulik, K.; Shao, L. D.; Compton, R. G., Single Nanoparticle Voltammetry: Contact Modulation of the Mediated Current. *Angew Chem Int Edit* **2016,** *55* (13), 4296-4299.

24. Albery, W. J., Electrode Kinetics. *Philosophical Transactions of the Royal Society of London. Series A, Mathematical and Physical Sciences* **1981,** *302* (1468), 221-235.

25. Li, X. T.; Lin, C. H.; Batchelor-McAuley, C.; Laborda, E.; Shao, L. D.; Compton, R. G., New Insights into Fundamental Electron Transfer from Single Nanoparticle Voltammetry. *J Phys Chem Lett* **2016,** *7* (8), 1554-1558.

26. Ellison, J.; Batchelor-McAuley, C.; Tschulik, K.; Compton, R. G., The use of cylindrical micro-wire electrodes for nano-impact experiments; facilitating the sub-picomolar detection of single nanoparticles. *Sensor Actuat B-Chem* **2014,** *200,* 47-52.

27. Krittayavathananon, A.; Ngamchuea, K.; Li, X. T.; Batchelor-McAuley, C.; Katelhon, E.; Chaisiwamongkhol, K.; Sawangphruk, M.; Compton, R. G., Improving Single-Carbon-Nanotube-Electrode Contacts Using Molecular Electronics. *J Phys Chem Lett* **2017,** *8* (16), 3908-3911.

28. Bott, A. W.; Feldberg, S. W.; Rudolph, M. J. C. S., Fitting Experimental Cyclic Voltammetry Data with Theoretical Simulations Using DigiSim [R] 2.1. **1996,** *15,* 67-71.

29. BASi research products Digisim® Simulation Software For Cyclic Voltammetry. https://www.basinc.com/products/ec/digisim.

Chapter 7

Single Entity 'Nano-Catalysis': Carbon Nanotubes and the VO_2^+/VO^{2+} Redox Reaction

In the previous chapter we investigated the redox chemistry of bromide oxidation and bromine reduction at both ensemble and 'single' bamboo-like multi walled carbon nanotubes (b-MWCNTs) via cyclic voltammetry and 'nano-impacts'. In this chapter, we discuss the electrochemistry associated with another important redox flow battery (RFB), the all-vanadium RFB (VRFB). Cyclic voltammetry and single-entity electrochemistry are again used to evaluate the possible electrocatalysis of the VO_2^+/VO^{2+} electron transfer kinetics by means of b-MWCNTs particularly in comparison with the kinetics seen at carbon macro-electrodes. The individual nanotubes are shown to accelerate the reaction in the oxidative direction but to retard it in the reductive direction! The asymmetry is explained in terms of the multistep nature of the electrode reaction and the relative sequence of electron transfer and chemical steps. When an ensemble of nanotubes is drop-casted onto a glassy carbon electrode an electrochemically nearly reversible response is seen and understood in terms of the changed mass transport regime under which the reaction occurs.

This work has been published in the journal *ACS Catalysis*[1].

7.1 Introduction

In Chapter 6 we discussed the significance of RFBs as a potential energy storage technology and in particular we have studied the redox chemistry of oxidation of bromide and reduction of bromine at both ensemble and 'single' b-MWCNTs and compared its kinetics with bare carbon electrodes[2, 3]. Amidst all the available RFBs another much

studied is the vanadium redox flow battery (VRFB) developed by Skyllas-Kazacos et al., which is a good prospect for storing large – scale energy due to its efficiency and reliability[4]. The redox couples present in VRFB are the V^{3+}/V^{2+} (anolyte) and VO_2^+/VO^{2+} (catholyte) couples. Their respective redox reactions at the anode and cathode are as follows,

$$V^{2+} \rightleftharpoons V^{3+} + e^- \tag{7.1}$$

$$VO_2^+ + e^- + 2H^+ \rightleftharpoons VO^{2+} + H_2O \tag{7.2}$$

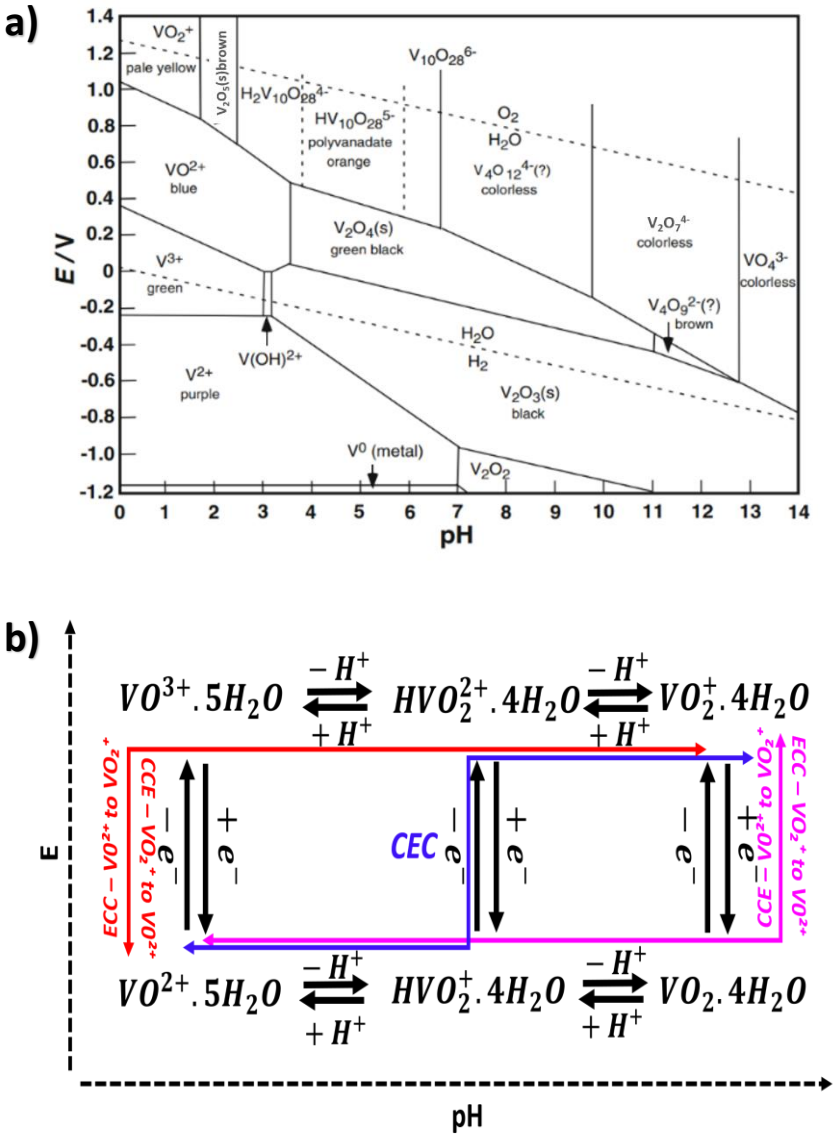


Figure 7.1 a) Pourbaix diagram for vanadium in aqueous solution at different pH versus potential referenced to the NHE. This figure is adapted from reference[5] with permission from Springer

Nature Publishers. b) Three mechanistic pathways for the VO_2^+/VO^{2+} redox couple. Please see main text for explanation. This scheme is adapted from data given in reference[6].

The Pourbaix diagram shown in Figure 7.1a shows the existence zones of the relevant species in terms of the potential vs NHE and pH. The standard electrode potentials for the redox couples 1 and 2 are -0.255 V and +1.000 V (vs NHE) respectively[7-9]. Redox couple in Eq. (7.1) involves a one electron transfer and the different oxidation states exist as various complexes in different acidic electrolytes[10], whilst redox couple in Eq. (7.2) involves electron and proton transfer as well as bond breaking. Both the redox couples show sluggish kinetics, and notably, fully electrochemically irreversible behaviour is seen on carbon macroelectrodes[11-13]. Predominantly, reports suggest that of the two redox couples, VO_2^+/VO^{2+} shows faster kinetics than V^{3+}/V^{2+} [11, 12, 14, 15] couple although there are conflicting reports[13, 16]. Sulphuric acid is the most commonly used solvent in VRFBs and leads to the formation of complexes of SO_4^{2-} or HSO_4^- such as $VO(SO_4)_2^{2-}$, $VOHSO_4^+$ at higher concentrations of the acid[16-18]. In strong non-complexing acids VO^{2+} exists as $[VO(H_2O)_5]^{2+}$ (blue oxovanadium ion) and VO_2^+ as cis-$[VO_2(H_2O)_4]^+$ (yellow dioxovanadium ion)[14, 19].

In respect of the VO_2^+/VO^{2+} redox couple, different possible multi-step mechanistic pathways for this reaction have been outlined by studying the current-voltage curves for the VO_2^+/VO^{2+} redox couple in perchloric acid and sulphuric acid at rotating disk graphite electrodes. These possible paths include *ECC*, *CEC* and *CCE* reactions where '*E*' stands for a one electron transfer and '*C*' represents chemical reaction, in this case one proton transfer and/or bond breaking or making. In Figure 7.1b the red arrow shows the *'ECC'* mechanism for the oxidation of VO^{2+} or *'CCE'* for the reduction of VO_2^+. The blue arrow shows the *'CEC'* mechanism for both oxidation of VO^{2+} and reduction of VO_2^+ and the pink arrow shows the *'CCE'* pathway for oxidation of VO^{2+} and *'ECC'* for reduction of

VO_2^+. In addition to the details in Figure 7.1b the complexes formed by the vanadium species with sulphate/bisulphate may add complexity[6]. The mechanistic pathways at carbon electrodes in acid as described above are dependent on both the electrode potential and the solution pH. In particular at more anodic (oxidation) and/or more cathodic (reduction) potentials the reaction is, in either direction, more likely to follow a *'ECC'* mechanism and hence is, for irreversible electron transfer, independent of pH. The reversible potential is, of course, dependent on pH as noted experimentally with the reversible potential shifting to more cathodic potentials with an increase in pH[6].

To accelerate the reaction kinetics of the VO_2^+/VO^{2+} redox reaction diverse electrocatalysts have been introduced and range from nanostructured carbon materials such as graphene[20], graphene oxides [21], and different types of carbon nanotubes (CNTs)[22, 23] to immobilising metal/metal oxide particles like Mn^{2+}, Pt^{4+}, Ir^{3+} [24]/ Mn_3O_4 [25], NiO [26], TiO_2 [27], Cr_2O_3 [28] on the electrode surface. In this study, we investigate if bamboo like multi-walled CNTs (b-MWCNTs) show catalysis[29] towards the VO_2^+/VO^{2+} redox reaction. The properties of CNTs have been discussed in detail in Chapter 3. In particular we make comparisons between measurements at nominally flat glassy carbon (GC) electrodes, with the same electrodes modified with b-MWCNTs and with *'single'* nanotubes using, for the latter, the approach of 'nano-impacts'[30, 31, 32, 33, 34]. The methodology has been discussed in Chapter 6.

In this way contrasts are drawn between the two different types of carbon (glassy carbon vs 'ensemble' and 'single' b-MWCNTs) and the three different transport regimes notably semi-infinite diffusion to a GC surface, a quasi-thin layer regime for material constrained within the porous layer of CNTs[29, 35, 36] and the highly efficient, convergent diffusion experienced at the single entity level where previously the diffusion to CNTs has, as discussed in the previous chapter, been characterised as akin to that to a cylinder of micro-

length and of nanoscale diameter[32]. Both the modes of transport and electro-catalysis are shown to influence the observed electrochemistry which in turn is thus sensitive to the different timescales employed.

7.2 Experimental

The chemicals used in this chapter are listed in Chapter 2, Table 2.1. They were purchased commercially and used as such without any purification.

7.2.1 Electrode Preparation for Cyclic Voltammetric Studies

i) Bare glassy carbon (GC) electrode

A bare GC electrode of area 7.07 x 10^{-2} cm^2 was used as the working electrode. Prior to use the GC electrode was polished sequentially with 1.00 μm, 0.30 μm and 0.05 μm alumina powder (Buehler, Micropolish II, Germany) unless otherwise specified below. Electrodes were then washed with deionised water and sonicated for 10 s then dried with N_2 prior to the CV experiments. First, the oxidation of the solvent, 1 M H_2SO_4 was studied followed by the oxidation of VO^{2+} and reduction of VO_2^+ 1 M H_2SO_4 in solution.

ii) b-MWCNTs modified GC electrode

A dispersion of b-MWCNTs was made in acetone 2.2 x 10^{-13} M (1 mg mL^{-1}), and sonicated for 20 mins. To study the oxidation of the b-MWCNTs, 2 μL of b-MWCNTs was drop-casted over GC electrode (after polishing as explained in section 2.2.1) and dried under steady N_2 flow and cyclic voltammetry was conducted in 1 M H_2SO_4. Next, to study the oxidation and reduction of VO^{2+} and VO_2^+ respectively, 20 μL of the b-MWCNTs dispersion was drop-casted on GC electrode. This b-MWCNTs drop-casted GC electrode was employed as working electrode to study the VO_2^+/VO^{2+} redox reaction in their respective solutions as described in the previous section. The voltammetric studies were conducted as mentioned in Chapter 2, section 2.2.

7.2.2 Microscopy Imaging

The instrumentation details of optical microscopy imaging and scanning electron microscopy are given in detail in Chapter 2, section 2.5 and 2.6 respectively.

7.2.3 'Nano-Impacts' Experiments on Single b-MWCNT – Chronoamperometric Studies

A carbon micro-wire electrode was used as the working electrode for these experiments. The electrode was fabricated as mentioned in Chapter 2, Section 2.4. The b-MWCNTs were dispersed in deionised water (2.2×10^{-13} M (1 mg mL^{-1})) and sonicated for 20 mins. For studying the impacts in the presence of the VO_2^+, VO^{2+} ions and in the absence of any vanadium ions (only 1 M H_2SO_4), 40 μL of the dispersed b-MWCNTs solution was added to the solution under study.

7.3 Results and discussion

This section is divided into several parts. First the electro - oxidation of b-MWCNTs in 1 M H_2SO_4 is explored using both cyclic voltammetry and, at the single particle level, 'nano-impacts'. The second part considers the oxidation in 5 mM VO^{2+} and reduction of 10 mM VO_2^+ with 1 M H_2SO_4 as supporting electrolyte at unmodified and b-MWCNTs modified GC electrodes and then at the single entity level through 'nano-impacts'. Finally, the electrochemical kinetics for the reactions were estimated by simulating the experimental results permitting inference of the catalytic effects (or otherwise) of the b-MWCNTs on the two electrode processes.

7.3.1 Oxidation of b-MWCNTs in 1 M H_2SO_4 at a Macro Bare and Modified GC Electrodes

The cyclic voltammograms recorded at both bare GC electrodes and GC electrodes modified with b-MWCNTs in 1 M H_2SO_4 are shown in Figure 7.2 for a scan rate of 50

mV s^{-1}. At unmodified GC electrodes only, solvent decomposition was observed at high positive potentials, whereas at b-MWCNTs modified GC electrodes an oxidative shoulder was seen at +1.8 V vs SCE and no reductive feature was seen in the anodic scan. However, a reductive feature was observed at -0.2 V vs SCE when the voltammetric scan was interrupted and the electrode potential was held at +1.8 V vs SCE for different time intervals (Figure 7.2b).

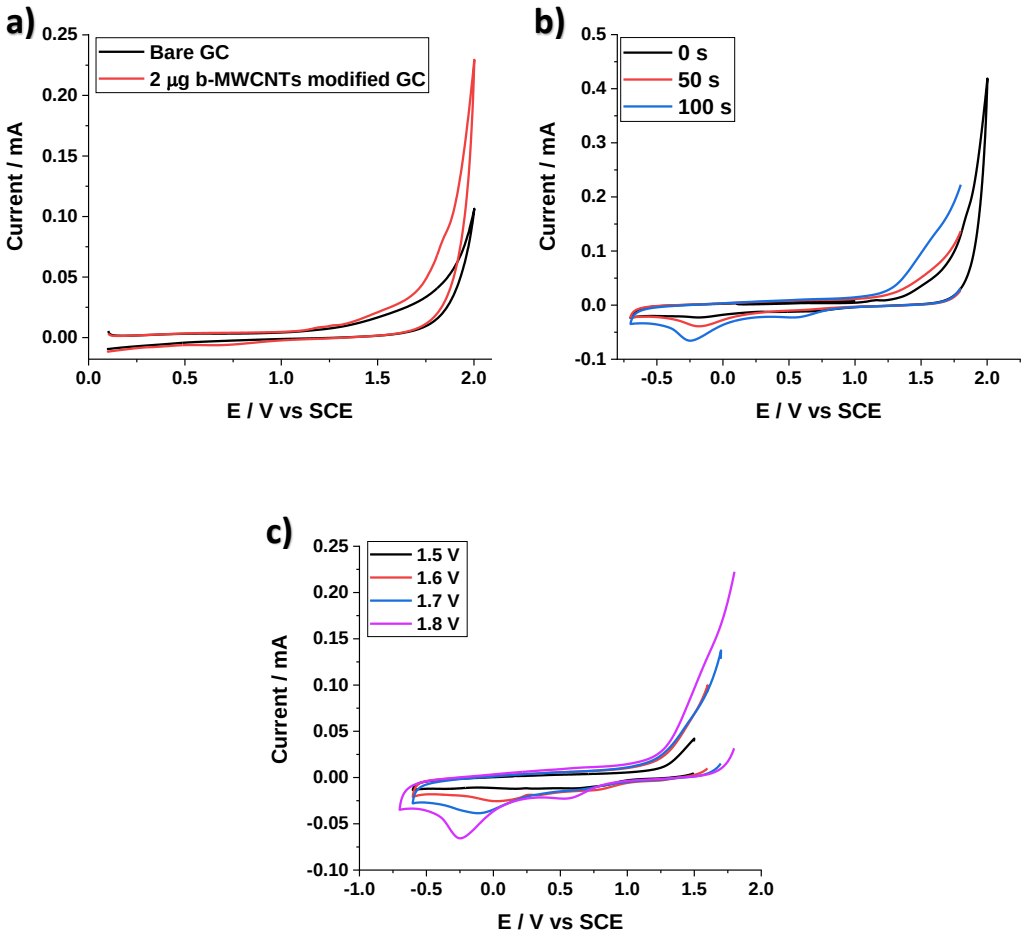


Figure 7.2 Cyclic voltammograms in 1 M H_2SO_4 at a scan rate of 50 mV s^{-1} a) at a bare GC electrode, black line and at a 2 µg b-MWCNTs modified GC electrode, red line; b) at 2 µg (in 2 µL of dispersion) b-MWCNTs modified GC electrode after oxidising at +1.8 V vs SCE at different time intervals (0s, black line; 50s, red line and 100s, blue line); c) at 2 µg (in 2 µL of dispersion) b-MWCNTs modified GC electrode after oxidising at at different potentials for 100s (+1.5 V vs SCE, black line; +1.6 V vs SCE, red line; +1.7 V vs SCE, blue line and +1.8 V vs SCE, magenta line)

The reductive feature at -0.2 V vs SCE is consistent with the reduction of surface quinone groups as reported elsewhere[37, 38] . We infer that the electro-oxidation of b-MWCNTs at potentials of +1.6 V vs SCE or above leads to the formation of quinone groups as seen in Figure 7.2c and likely other surface functional groups such as carboxyl, hydroxyl consistent with suggestions in the literature in respect of both chemical[39, 40] and electrochemical[37, 41] oxidation of b-MWCNTs.

However the magnitude of the charge seen in the reductive peaks is considerably lower than that passed during the electrolysis at +1.8 V vs SCE suggesting that the formation of the surface functionality is a side product accompanying the solvent oxidation. Note that the latter occurs at a lower potential on the b-MWCNTs modifed electrode than on the GC electrode indicating some possible electrocatalysis of the solvent oxidation by the b-MWCNTs possibly arising from the electrogenerated oxygen functionality although the role of ultra-trace metal impurities present in the nanotubes cannot be ruled out[42, 43].

7.3.2 Oxidative Electrochemistry of Single b-MWCNTs; 'Nano-Impacts'

Single entity electrochemistry was carried out for single b-MWCNTs impacting on a carbon wire electrode in 1 M H_2SO_4. First, current-time transients were recorded at fixed potentials in the absence of b-MWCNTs; no impact signals were observed (Figure 7.3a, black line). Then, second, 40 μL of b-MWCNTs dispersed in deionised water was added to the solution and the chosen potential was applied. The Brownian motion of the b-MWCNTs led to stochastic collisions with the carbon microwire electrode giving rise to current steps ('on' and 'off' related to the arrival and departure of single b-MWCNT at the carbon microwire electrode) in the chronoamperogram. Oxidative step currents were observed for potentials +0.6 V vs SCE and more positive. Figure 7.3a shows the oxidative step current at +1.2 V vs SCE depicting a clear step-up in current on the arrival of b-

MWCNT and a step-down in current showing the departure of a single b-MWCNT. The experiment was repeated to record the impact steps and average currents found as a function of potential is shown in Figure 7.3b. The onset of sustained oxidative currents during the impacts suggests that the b-MWCNTs undergo an electro-chemical oxidation reaction in the solvent 1 M H_2SO_4 (Note that in 0.1 M HNO_3 no such impact signals were observed under similar applied potentials as consistent with the reuslts in Chapter 6[44]. The electrochemical reaction causing the impact currents could be possibly either solvent oxidation or the oxidation of b-MWCNTs themselves. To further explore this, cyclic voltammetry experiments at bare GC electrodes and b-MWCNTs modified GC electrodes were conducted in 1 M H_2SO_4 (Figure 7.2a). The presence of b-MWCNTs on the electrode led to a shoulder on the solvent decomposition around +1.8 V vs SCE whilst the sustained solvent decomposition occurred at lower potentials on the b-MWCNTs modified electrodes as compared to the bare GC electrode. When voltammetric scans were paused at +1.8 V vs SCE for different periods of time leading to the observation of reductive signals at -0.2 V vs SCE (Figure 7.2b) on the following cathodic CV scans. These are assigned to the formation of quinone functional groups[37, 41] but the magnitude of charge seen in the quinone reduction peaks is very considerably lower than that passed in total during the electrolysis suggesting that the formation of the surface quinone functionality at +1.8 V vs SCE is a side reaction of the electrolysis and that solvent decomposition is the likely main process although the formation of other oxygen functionality, invisible in the CV, such as 'COOH' groups or 'OH' groups[37, 39-41] cannot be ruled out. Experiments were conducted in which voltammetric scans were paused at lower potentials than that of +1.8 V vs SCE showing that the onset potential for the reductive signals to appear was +1.6 V vs SCE (Figure 7.2c). The electrochemically induced functionality may contribute to the electrocatalysis of the solvent decomposition.

It is interesting that the potential for solvent decomposition and/or b-MWCNTs oxidation is around +0.7 V vs SCE in the single entity measurements but only occurs at much greater overpotentials at the b-MWCNTs modified macro electrode. We attribute this difference to the formation of a thin-layer of oxidised b-MWCNTs adjacent to the substrate GC electrode which if formed at the low potentials as seen in the single-entity experiment may inhibit charge injection into the drop-cast layer until the voltammetric sweep reaches much lower potentials.

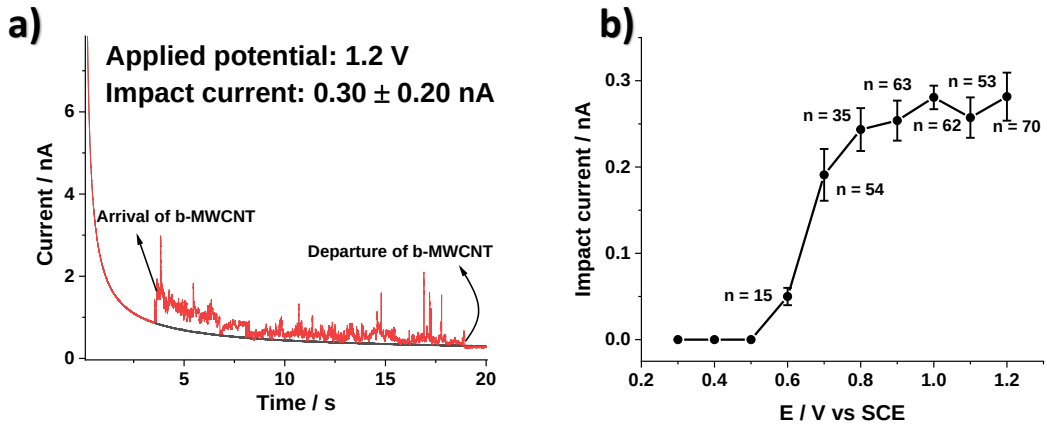


Figure 7.3 a) Current transients showing the oxidative impact currents at +1.2 V vs SCE at single b-MWCNTs in 1 M H_2SO_4, b) A plot of the average impact current vs applied potential (E vs SCE).

7.3.3 Cyclic Voltammetry of 5 mM VO^{2+} and 10 mM VO_2^+ at Bare GC Electrodes and at b-MWCNTs Modified GC Electrodes

A bare (unmodified) GC electrode was first used to study the electrochemical oxidation of 5.0 mM VO^{2+} and the reduction of 10.0 mM of VO_2^+ was investigated at a bare GC electrode. The shape of the reductive wave was sensitive to the surface preparation of the GC electrode as determined by the duration of polishing of the electrode and the size or sequence of the polishing grits used as reported and discussed in Appendix, section A7.1. In the following, we report the data reproducibly obtained using progressively smaller

polishing grits for the reduction of VO_2^+ noting that it is likely, given the surface sensitivity, that the reduction involves adsorbed intermediate species and/or involvement of surface functionality. The CV reveals an oxidative and reductive peak in corresponding solutions at +1.20 V and +0.30 V (vs SCE) at 25 mV s^{-1} and is shown in Figure 7.4a and b. The peak-to-peak separation between the oxidative and reductive peak was ~ 1 V which suggests that the reaction is electrochemically irreversible at carbon electrode surfaces. The peak potentials and irreversiblity of the electrode process at GC electrodes agrees well with the literature[12, 45].

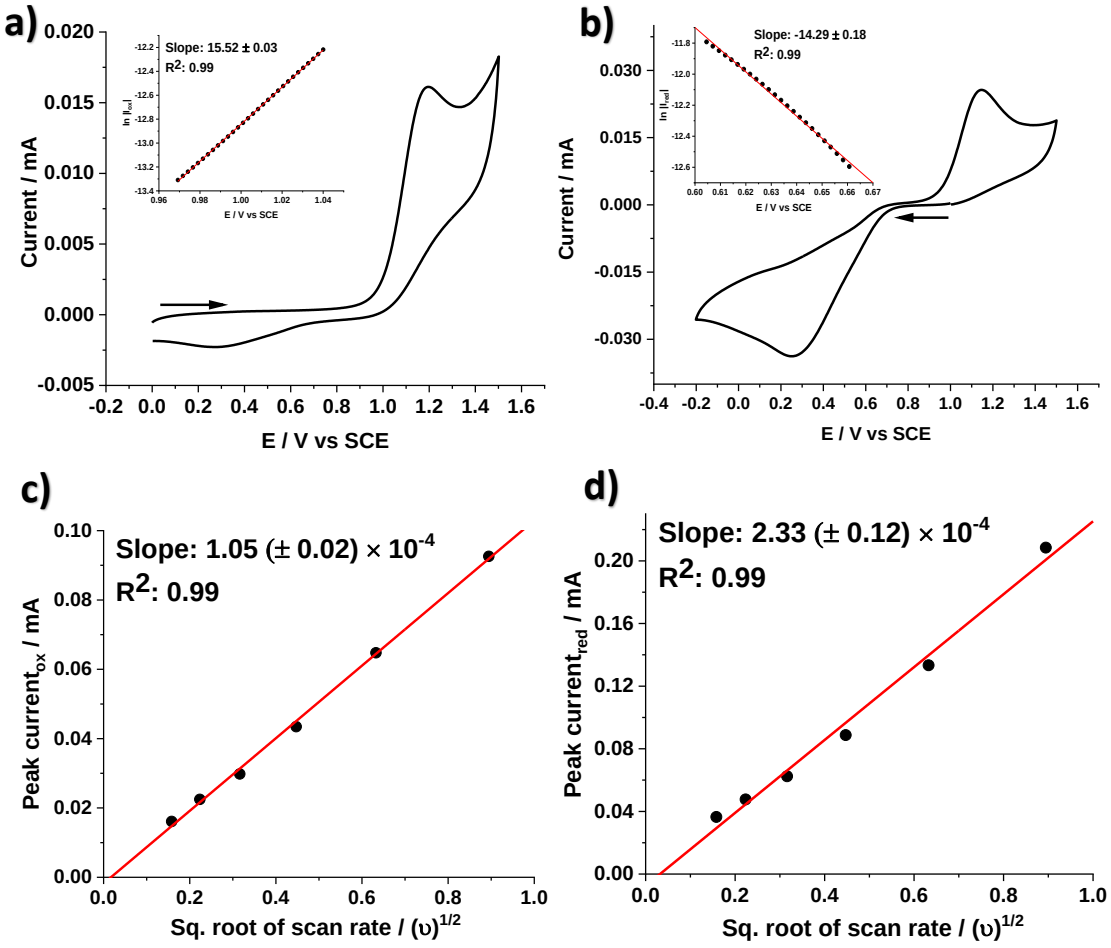


Figure 7.4 a) Cyclic voltammogram of 5 mM VO^{2+} in 1 M H_2SO_4 at bare GC electrode at a scan rate of 25 mV s^{-1}; inset: Tafel analysis with a slope of 15.52 (± 0.03) V per decade gives a transfer coefficient, β of 0.40 (± 0.01). b) Cyclic voltammogram of 10 mM VO_2^+ in 1 M H_2SO_4 at bare GC electrode at a scan rate of 25 mV s^{-1}; inset: Tafel analysis with a slope of -14.29 (± 0.17) V per decade gives a transfer coefficient, α of 0.37 (± 0.01); the current range of 10 – 30 % of the

respective peak current was used for the Tafel analyses. c) Plot of oxidative peak current versus square root of scan rate ($\nu^{1/2}$). d) Plot of reductive peak current versus square root of scan rate ($\nu^{1/2}$).

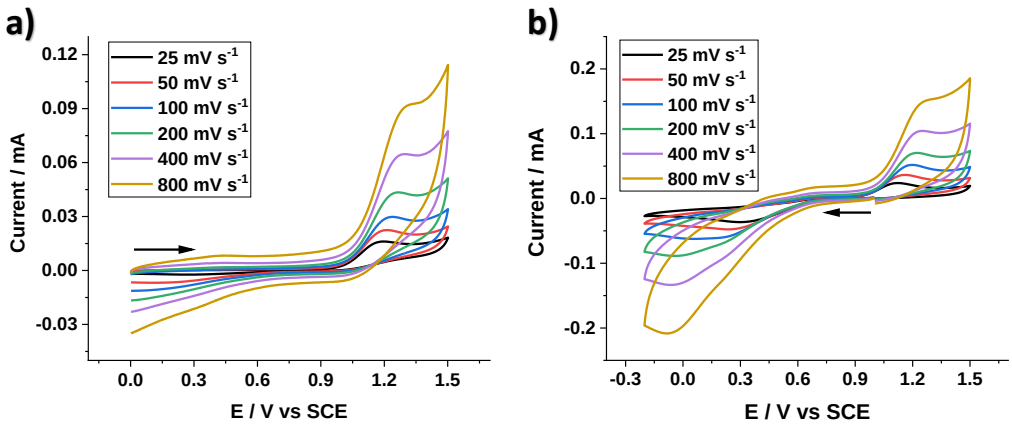


Figure 7.5 Cyclic voltammograms at a bare GC electrode as a function of scan rate for, a) oxidation of 5 mM VO^{2+} in 1 M H_2SO_4 and b) reduction of 10 mM VO_2^+ in 1 M H_2SO_4.

The transfer coefficients were calculated from Tafel analyses using the equations $\beta = \frac{RT}{F}\frac{\partial \ln|I_{ox}|}{\partial E}$ and $\alpha = \frac{RT}{F}\frac{\partial \ln|I_{red}|}{\partial E}$ as shown in Figure 7.4a and b insets. The Tafel plots were linear yielding transfer coefficients β and α, of 0.40 (± 0.01) and 0.37 (± 0.01) corresponding to a slope value of -14.29 (± 0.17) V per decade and 15.52 (± 0.03) V per decade for the oxidation and reduction reactions respectively. The values are in good agreement with those reported in the literature[45]. Here, in both the cases, a current range of 10% - 30% of the peak current was used for analysis to avoid the influence of mass transport[46]. The transfer coefficients in the range 0 to 1 suggest that the first electron transfer step is the rate determining step in each case whereas simple symmetric Marcus – Hush theory predicts a value of 0.5. The observed deviation from 0.5 signals the need for possible interpretation via asymmetric Marcus – Hush theory indicating weakening or bonding due to electron transfer. A plot of peak current versus square root of scan rate for oxidation of VO^{2+} and reduction of 10 mM of VO_2^+ is given in Figure 7.4c and d (see Appendix, Section A7.2 where the latter shows clear curvature if the peak current is

plotted against scan rate rather than the square root of scan rate). The linearity of the plot suggests that the reactions are diffusion controlled. The Randles-Ševčík equation for irreversible (one electron transfer was used to calculate the diffusion coefficient, $D_{VO^{2+}}$ was of 2.4 (± 0.1) x 10^{-6} cm^2 s^{-1} and $D_{VO_2^+}$ of 3.3 (± 0.1) x 10^{-6} cm^2s^{-1} were calculated (Figure 7.4c and d) from the Randles-Ševčík equation for irreversible electron transfer, this matches reasonably with the literature value of 2.1 x 10^{-6} cm^2 s^{-1} [47] and 2.8 x 10^{-6} cm^2s^{-1} respectively[48]. Cyclic voltammograms recorded as a function of scan rate is given in Figure 7.5.

Next, cyclic voltammetry on a b-MWCNTs modified GC electrode was carried out to study the electrocatalytic activity of b-MWCNTs towards the VO_2^+/VO^{2+} redox reaction. 20 μL of b-MWCNTs dispersed in acetone (2.2 x 10^{-13} M) was drop-casted on a polished GC electrode, then dried under a N_2 flow. The modified electrode was used as the working electrode in a three-electrode cell set-up to study both the oxidation of 5.0 mM VO^{2+} and the reduction of 10.0 mM VO_2^+ in 1 M H_2SO_4.

The cyclic voltammograms obtained for oxidation of 5.0 mM VO^{2+} and reduction of 10.0 mM of VO_2^+ at a scan rate of 25 mV s^{-1} at both bare GC and b-MWCNTs modified GC electrodes are shown in Figures 7.6a and b respectively. At the b-MWCNTs modified electrode, the oxidative and reductive peak potentials in their respective solutions were observed at +0.91 V and +0.72 V (vs SCE) with a peak-to-peak separation of ~ 200 mVs and a mid-point potential of *ca.* +0.81 V vs SCE for a scan rate of 25 mV s^{-1}. Cyclic voltammograms were recorded as a function of scan rate for the oxidation and reduction reactions and are shown in Figure 7.7. Logarithmic plots of the oxidative and reductive peak currents obtained in 5 mM VO^{2+} and 10 mM VO_2^+ respectively at both modified and unmodified GC electrode versus the logarithm of scan rate is given in Figure 7.6c and d.

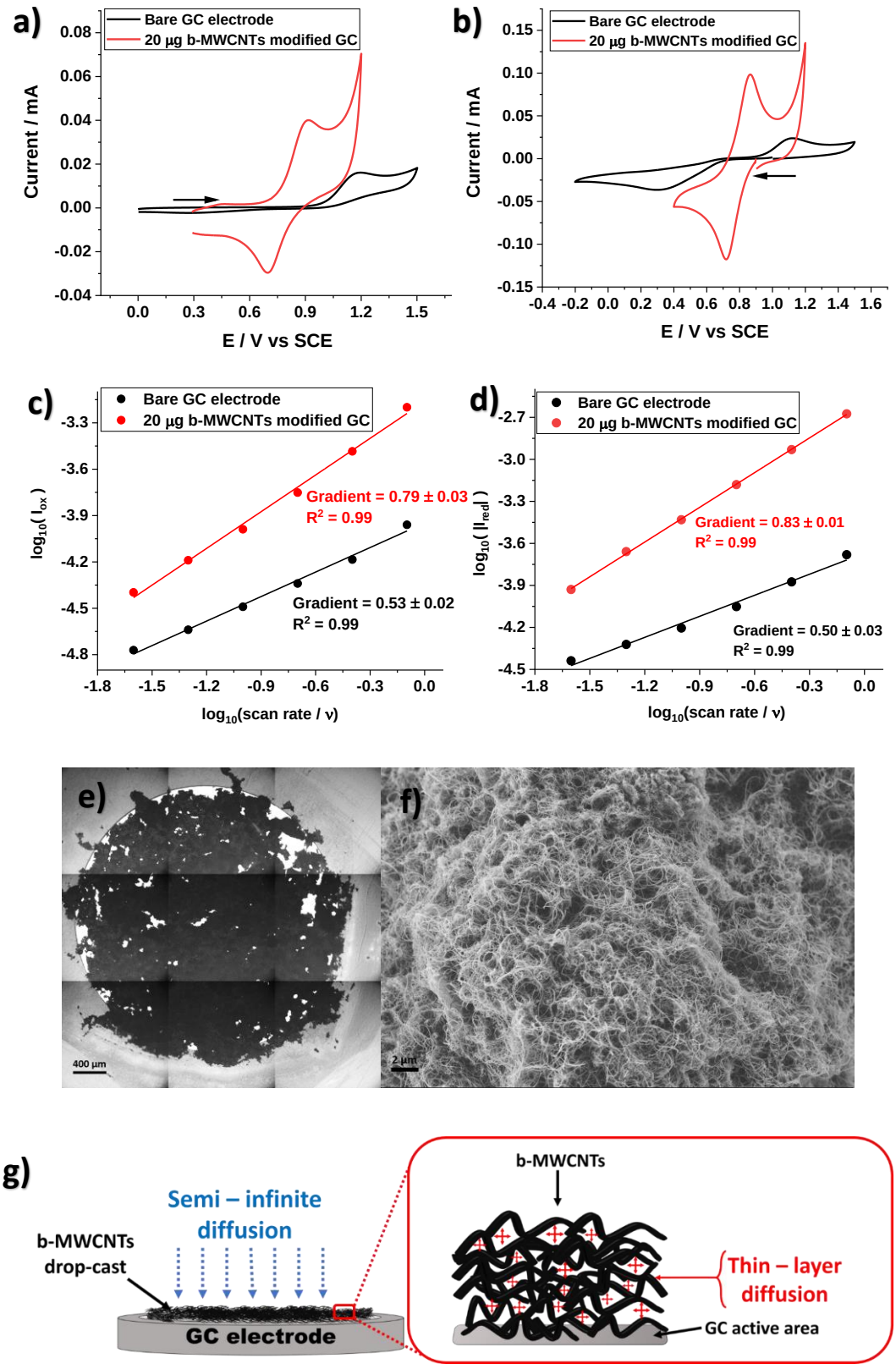


Figure 7.6 Cyclic voltammetry at bare GC electrode in black line/circles and 20 µg (20 µL of dispersion) of b-MWCNTs modified GC electrode in red line/circles, a) cyclic voltammograms of 5.0 mM VO^{2+} in 1 M H_2SO_4 at 25 mV s^{-1}, b) cyclic voltammograms of 10.0 mM VO_2^+ in 1 M H_2SO_4 at 25 mV s^{-1}, c) log-log plots of oxidative peak current (I_{ox}) versus scan rate (ν) in 5.0 mM

VO^{2+} in 1 M H_2SO_4, d) log-log plots of reductive peak current (I_{red}) versus scan rate (ν) in 10.0 mM VO_2^+ in 1 M H_2SO_4. e) Optical microscopy image of a b-MWCNTs modified GC electrode, f) a SEM image of b-MWCNTs showing the thick drop-casted porous layer and g) a schematic representation showing the *semi-infinite* diffusion at the b-MWCNTs surface and *thin-layer* diffusion in the porous structure (the arrows in red schematically show the *thin layer* diffusion *within* the porous layer which contrasts with the *semi-infinite* diffusion to the *surface* (blue arrows).

The gradients of the plots at bare GC electrode for oxidation in 5.0 mM VO^{2+} and reduction in 10.0 mM VO_2^+ are 0.53 (±0.02) and 0.50 (±0.03) respectively indicative of diffusional responses. In contrast at b-MWCNTs modified electrodes gradients of 0.79 (±0.03) and 0.83 (±0.01) for oxidation in 5.0 mM VO^{2+} and reduction in 10.0 mM VO_2^+ respectively were observed suggesting a significant component from thin layer diffusion to the response[35, 36].

It is seen that when compared with GC under similar conditions, the b-MWCNTs modified GC electrode shows larger peak currents and a reduced peak-to-peak separation for both the oxidation of VO^{2+} and the reduction of VO_2^+. At first sight this suggests possible electrocatalysis by the b-MWCNTs. However, mirroring the discussion in the previous chapter, the observations may rather likely reflect the change in diffusion from semi-infinite at the flat, unmodified electrode to a mass transport regime with a significant amount of thin layer diffusion resulting from voltammetric signal from analyte trapped within the thick porous agglomerates formed by the b-MWCNTs when drop-casted at the GC electrode[35, 36, 49]. The resulting thick porous layer is shown as an optical microscopy image over the full electrode surface in Figure 7.6e, with an SEM image shown in Figure 7.6f at much greater magnification. Clearly the drop-casted film traps solution containing analyte and since the b-MWCNTs are conductive the necessary conditions for thin-layer transport prevail. A schematic representation of the mass transport to and within b-MWCNTs film is shown in Figure 7.6g.

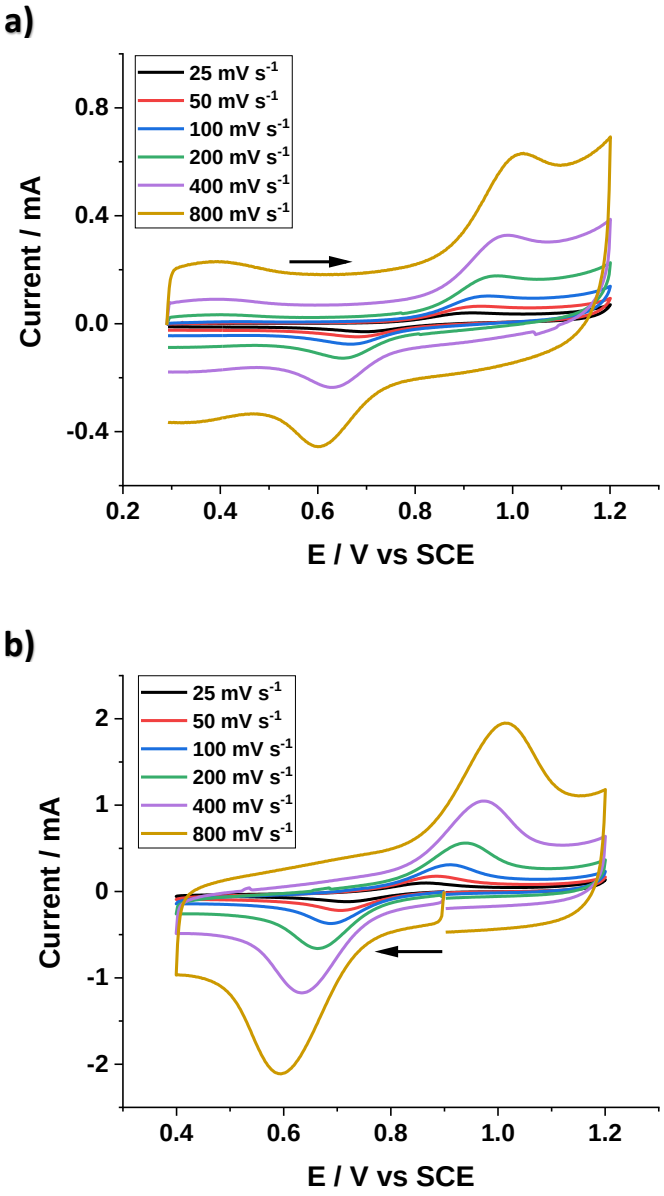


Figure 7.7 Cyclic voltammograms at a 20 µg (20 µL of dispersion) of b-MWCNTs modified GC electrode as a function of scan rate for, a) oxidation of 5 mM VO^{2+} in 1 M H_2SO_4 and b) reduction of 10 mM VO_2^+ in 1 M H_2SO_4.

7.3.4 'Nano-Impacts' of Single b-MWCNTs

In this section we investigate the possible electrocatalytic properties of 'single' b-MWCNTs as we have concluded from the previous section that an ensemble of b-MWCNTs shows complexity in determining the catalytic property due to mixed and difficult to quantify diffusion effects. 'Nano-impacts' experiments were conducted to reveal the voltammetric behaviour at single nanotubes for the VO_2^+/VO^{2+} redox reaction.

i) Nano-impacts and the oxidation of VO^{2+} at single b-MWCNTs

Nano-impact experiments were conducted on a solution of 5.0 mM VO^{2+} in 1.0 M H_2SO_4 containing a suspension of b-MWCNTs. The concentration of nanotubes was 4.0 μg mL^{-1} corresponding to 8.7 x 10^{-15} M. A carbon microwire electrode was held at fixed potentials in the range of +0.65 V to +1.30 V vs SCE. The chronoamperograms showed oxidative step currents as shown in Figure 7.8a where the applied potential was +1.20 V vs SCE and the sudden jumps in current correspond to the arrival or departure of a CNT as marked on the Figure 7.8a. At least 30 chronoamperograms were recorded at each potential to get a statistically meaningful number of distinctive current steps. Figure 7.8b shows the plot of average impact current versus the applied potential. A sigmoidal curve with two waves was observed representing the current-potential characteristics at single b-MWCNTs. The first wave with a half-wave potential of +0.65 V vs SCE corresponds to that seen in Figure 7.3b as confirmed by further impact experiments made in 10.0 mM of VO^{2+}. Each impact current step lasted for a few tens to hundreds of seconds showing the residence time of the b-MWCNTs at the carbon microwire electrode as given in Figure 7.9a. Figure 7.9b shows that the average residence times were seen to be independent of the applied potential.

The average impact current versus applied potential for 10.0 mM VO^{2+} is shown in Figure 7.8c which shows the overlaid impact currents in 5.0 mM VO^{2+}, 10.0 mM VO^{2+}, and in 1 M H_2SO_4 (with no vanadium species present). It shows that, the average impact current of the first wave doesn't change with an increase in VO^{2+} concentration whereas the second wave exhibits an increase in the impact current proportional to the concentration of VO^{2+}.

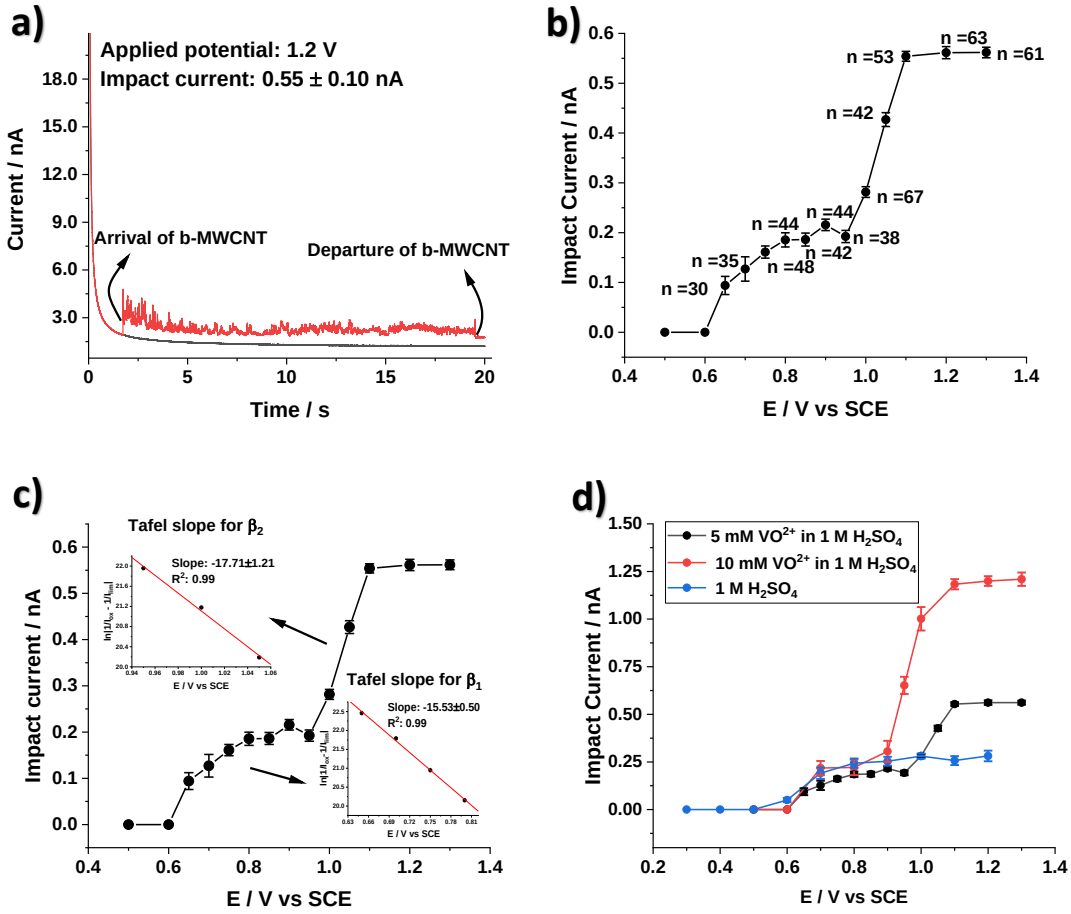


Figure 7.8 a) Chronoamperogram in 5.0 mM VO^{2+} showing an oxidative impact step current at +1.20 V vs SCE of applied potential, b) plot of average impact current vs applied potential (E vs SCE) in 5 mM VO^{2+}, c) mass transport corrected Tafel analyses for the two representative waves giving β_1 of 0.40 (±0.01) and β_2 of 0.45 (±0.03), d) average impact current vs applied potential (E vs SCE) in 5.0 mM VO^{2+} (black circles) and 10.0 mM VO^{2+} (red circles) and 1 M H_2SO_4 (blue circles).

The magnitude of the current for the first wave matches well with the impact current obtained in 1 M H_2SO_4 consistent with probable solvent oxidation as discussed above. Mass-transport corrected Tafel analyses was employed to calculate the transfer coefficient, β for the two waves in 5.0 mM VO^{2+} (Figure 7.8d) considering the high potential plateau of each wave to be the 'limiting current' of the voltammogram. The transfer coefficients β_1 corresponding to wave 1 was calculated to be 0.40 (± 0.01) and β_2 corresponding to wave 2 is 0.45 (± 0.03). Figure 7.8b shows a diffusion limited plateau

for the oxidation of VO^{2+} at high potentials. The limiting currents after subtraction of the contribution from the solvent oxidation in the first wave were analysed assuming the b-MWCNT is a cylindrical electrode[32]. Thus, $D_{vo^{2+}}$ of 2.3 (± 0.2) x 10^{-6} cm^2 s^{-1} for 5 mM VO^{2+} and 2.8 (± 0.1) x 10^{-6} cm^2 s^{-1} for 10 mM VO^{2+} was obtained, hence the $D_{vo^{2+}}$ was averaged to be 2.6 (± 0.2) x 10^{-6} cm^2 s^{-1}. This value matches well with the diffusion coefficient obtained for VO^{2+} at a bare GC electrode (i.e. 2.4 (± 0.1) x 10^{-6} cm^2 s^{-1}).

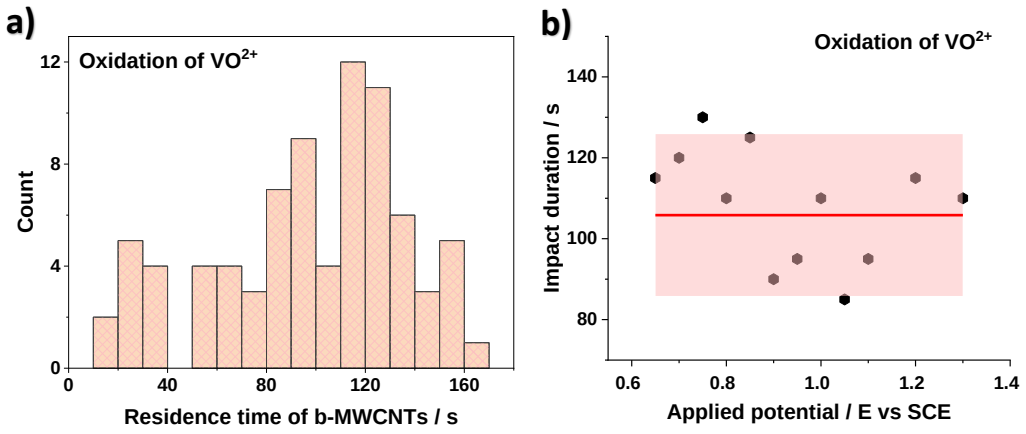


Figure 7.9 Histogram showing frequency of residence time of b-MWCNTs at carbon micro wire electrode during 'nano-impact' experiments a) for oxidation of 5.0 mM VO^{2+}, b) plot of average residence time of b-MWCNTs at different applied potentials, the red vertical line shows the overall average residence time at all potentials and the solid background shows the error bar for the overall residence time.

ii) 'Nano-impacts' and the reduction of VO_2^+ at single b-MWCNTs

Chronoamperograms were recorded in the absence of VO_2^+ ions in 1 M H_2SO_4; no reductive impact currents were observed in the potential range of -0.1 V vs SCE to -0.3 V vs SCE as seen in Figure 7.10. This observation excludes the possibility of any solvent reduction. Further, reduction of VO_2^+ at single b-MWCNTs was carried out in 10.0 mM VO_2^+ in 1 M H_2SO_4. Current-time transients were recorded at a constant applied potential ranging from -0.05 to -0.35 V vs SCE. Reductive Faradaic current steps were observed on stochastic collision of b-MWCNT with the carbon microwire working electrode for

potentials greater than -0.05 V vs SCE. Figure 7.11a shows a typical reductive step current at -0.30 V vs SCE with a step-up current on arrival of the b-MWCNT and a step-down current after *ca.* 12 seconds. The average residence time of the b-MWCNTs at the carbon microwire electrode was again independent of the applied potential as shown in Figure 7.12a and the frequency of residence time is given in Figure 7.12b. The average impact current at each applied potential was calculated from at least 30 impact events,

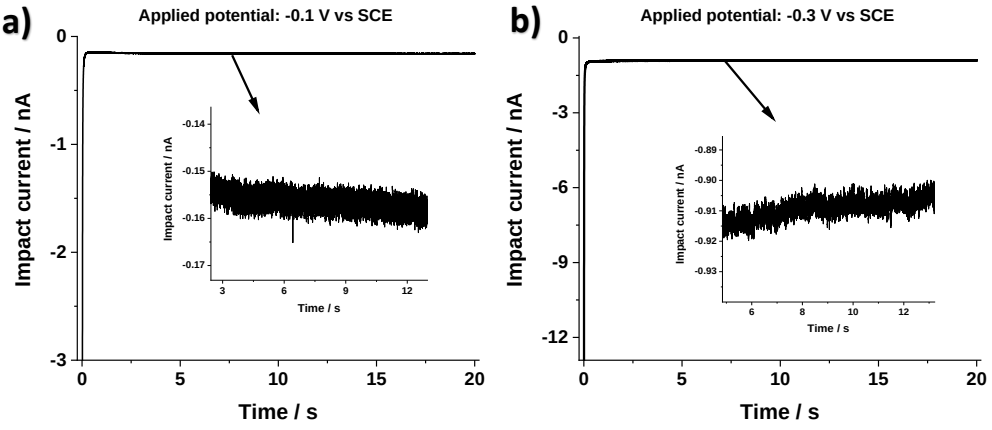


Figure 7.10 Chronoamperograms observed in 1 M H_2SO_4 by dispersing b-MWCNTs in the solution at applied potentials of a) -0.1 V vs SCE and b) -0.3 V vs SCE; the inset shows magnified chronoamperogram confirming the absence of any impacts.

Figure 7.11b shows the plot of average impact current versus applied potential and reveals a sigmoidal curve with two reductive waves depicting the possibility of two reductive reactions occurring at the b-MWCNT. Mass transport corrected Tafel analysis gave transfer coefficients α_1 of 0.30 (±0.04) and α_2 of 0.41 (±0.04) for wave 1 and 2 respectively as shown in Figure 7.11c. Assuming the overall reaction comprising both reductive features to be diffusion controlled at extreme negative potentials, the diffusion coefficient, $D_{VO_2^+}$ was calculated to be 3.0 (± 0.1) x 10^{-6} cm^2 s^{-1} for the plateau observed in Figure 7.11b, on the same basis as used for the oxidative currents in the previous section and assuming a cylindrical electrode. This $D_{VO_2^+}$ value compares well with the $D_{VO_2^+}$ obtained at bare GC electrode, 3.3 (± 0.1) x 10^{-6} cm^2 s^{-1} and literature[47].

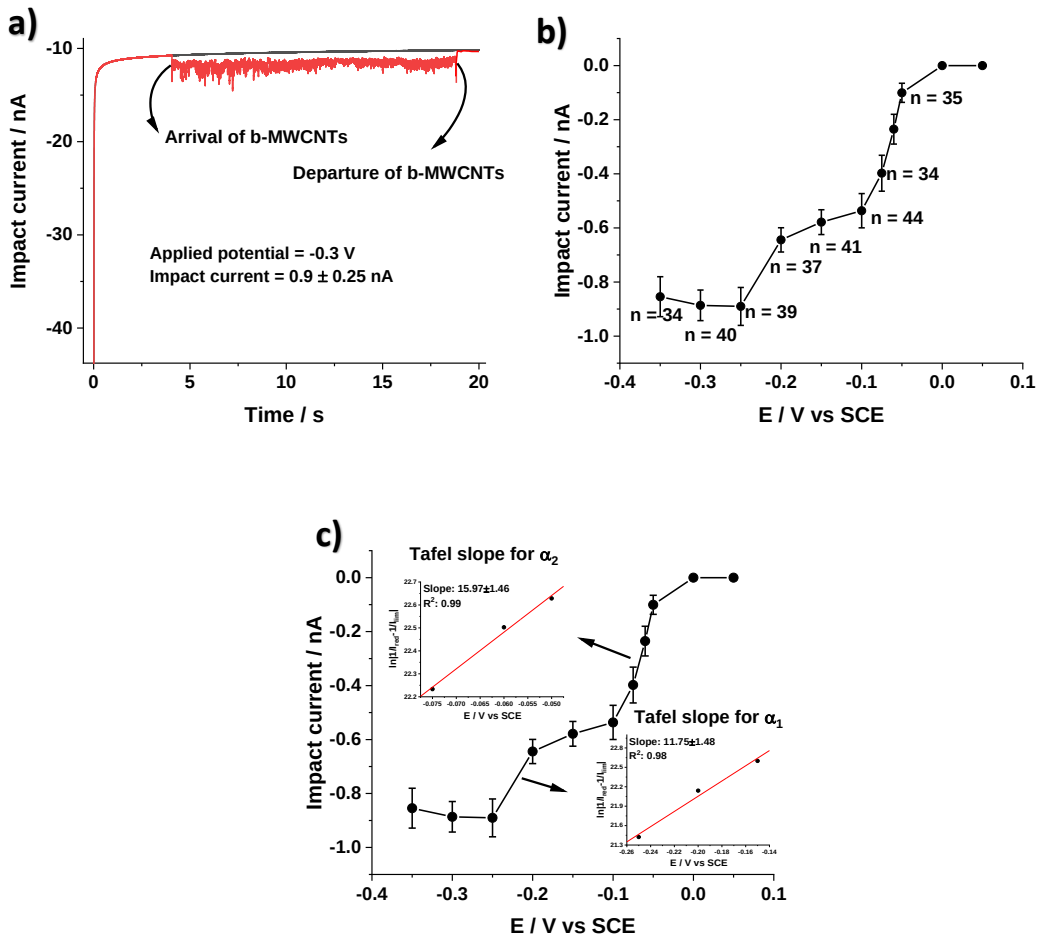


Figure 7.11 a) Chronoamperogram in 10.0 mM VO_2^+ showing reductive impact step current at -0.30 V vs SCE of applied potential, b) plot of average impact current vs applied potential (E vs SCE) in 10.0 mM VO_2^+, c) mass transport corrected Tafel analyses for the two representative waves giving α_1 of 0.30 (±0.04) and α_2 of 0.41 (±0.04).

The observation of the splitting of reductive wave under high mass transport conditions is consistent with the change of mechanism whereby a '*CEC'* process operates nearer the equilibrium potential[6] but that a change of mechanism to a process initiated by a one electron transfer becomes possible at more negative potentials. Under the high mass transport conditions, the timescale for the first '*C'* step of the '*CEC'* reaction is reduced and the current tends to be under kinetic control until higher reductive potentials, the full one electron process becomes possible with via the alternative '*ECC'* mechanism[6].

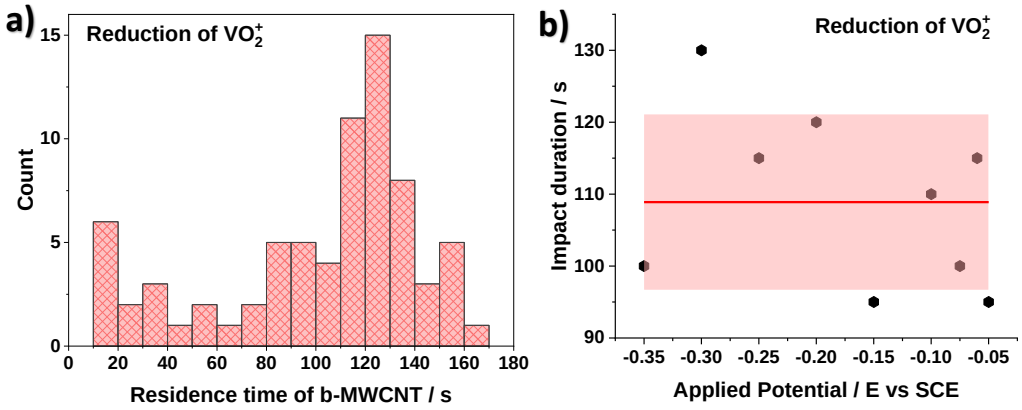


Figure 7.12 Histogram showing frequency of residence time of b-MWCNTs at carbon micro wire electrode during 'nano-impact' experiments a) reduction of 10.0 mM VO_2^+,b) plot of average residence time of b-MWCNTs at different applied potentials, the red vertical line shows the overall average residence time at all potentials and the solid background shows the error bar for the overall residence time.

7.3.5 Quantifying the Electrode Kinetics and Evaluating the Electrocatalysis of the VO_2^+/VO^{2+} Redox Couple

In this section we comparatively evaluate the electrochemical rate constants for the oxidation and reduction reactions at both bare GC electrodes and at single b-MWCNTs using the commercial DigiSim simulation software (Bioanalytical System Inc., USA) [50].

i) Electrode kinetics of the VO_2^+/VO^{2+} redox couple at a bare GC electrode

The cyclic voltammetry obtained at bare GC electrodes in 5 mM VO^{2+} with 1 M H_2SO_4 at 25 mV s^{-1} was modelled using commercial DigiSim software. As an initial approximation, the voltammogram was simulated as a simple one electron transfer ($A = B + e^-$) for a planar electrode geometry considering Butler – Volmer kinetics. The transfer coefficient, β of 0.40 and the diffusion coefficient $D_{VO^{2+}}$ of 2.3 (± 0.2) x 10^{-6} cm^2 s^{-1} were used as deduced from the experimental CV for the oxidation of VO^{2+}. Table 7.1 shows the standard and formal potentials of VO_2^+/VO^{2+} redox couple in different acidic media as reported in the literature.

Table 7.1 Standard potential and formal potential of VO_2^+/VO^{2+} in different acidic solutions

Standard potential	Formal potential
0.9996 V vs NHE (in 1 M $HClO_4$) [7, 9]	1.020 V vs NHE (in 1 M $HClO_4$) [7, 51]
	1.020 V vs NHE (in 1 M HCl) [7, 51]
	1.000 V vs NHE (in 1 M H_2SO_4) [7, 51]
	1.004 V vs NHE (in 1 M H_2SO_4) [52]
	1.103 V vs NHE (in 3 M H_2SO_4) [6]

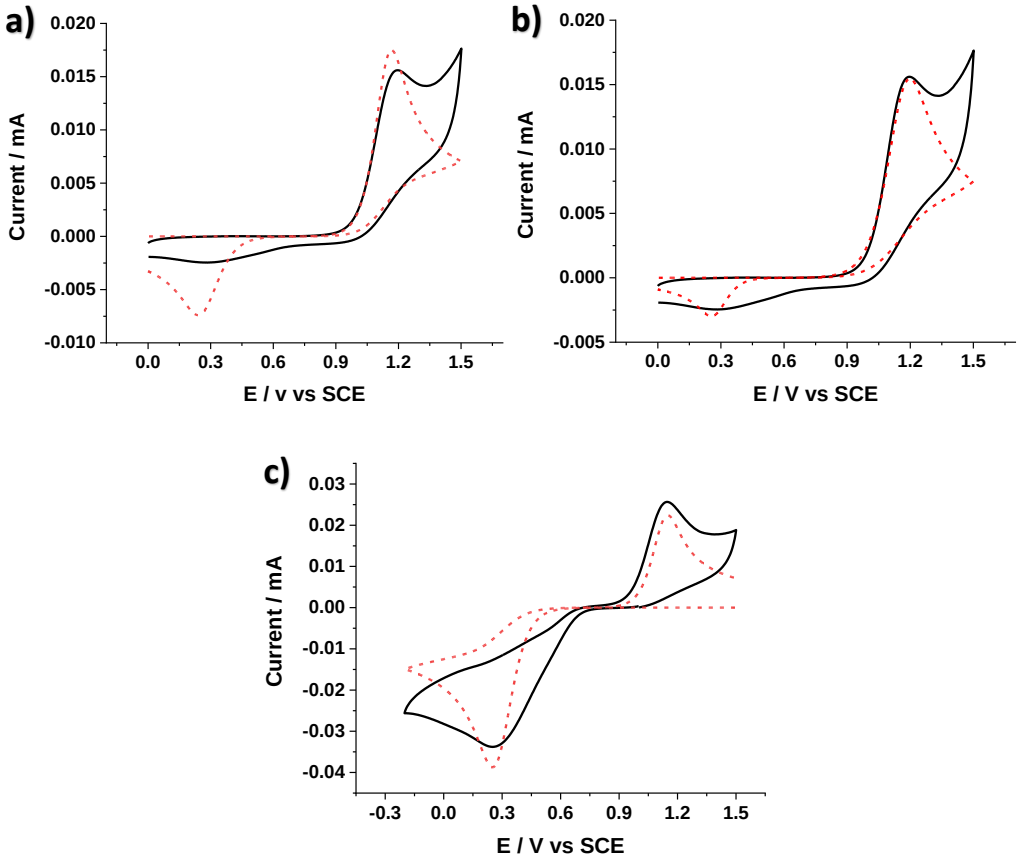


Figure 7.13 Cyclic voltammograms (black line) and DigiSim simulated curve (red dotted line) of a) 5.0 mM VO^{2+} in 1 M H_2SO_4 at bare GC electrode for β of 0.40 and k^0 of 4.0 (±0.2) x 10^{-7} cm s^{-1} at 25 mV s^{-1} for a simple one electron transfer; b) 5.0 mM VO^{2+} in 1 M H_2SO_4 at bare GC electrode for β of 0.40 and k^0 of 4.0 (±0.2) x 10^{-7} cm s^{-1} at 25 mV s^{-1} for a three step *'ECC'* reaction mechanism with the rate and equilibrium constants adjusted for optimal but not unique fit (see text). c) 10.0 mM VO_2^+ in 1 M H_2SO_4 at bare GC electrode for α of 0.60 and k^0 of 4.0 (±0.2) x 10^{-7} cm s^{-1} at 25 mV s^{-1} for a simple one electron transfer.

The formal potential, E^0 of +0.76 V vs SCE was used for the simulation corresponding to the literature in 1.0 M H_2SO_4. Hence, the only unknown parameter in the simulation is the standard electrochemical rate constant k^0 which was optimised to fit the experimental oxidative peak of the CV resulting in a value of k^0 of 4.0 (±0.2) x 10^{-7} cm s^{-1}. The simulated curve is shown in Figure 7.13a, from which it is seen that the oxidative peak potential and current matches well with the experimental data whereas, in contrast, a too large reductive peak current is predicted for the simulated curve. Further the experimental reductive wave is much too broad in comparison with the expectations of the simulation. This shows that the reaction is more complex than a simple one electron transfer involving solution phase species. In particular, the wave broadening may reflect surface adsorption effects, the involvement of which are hinted at by the sensitivity of the wave to the electrode preparation methods as discussed in Appendix, section A7.1.

In addition, and as inferred above from both literature[6] and the 'nano-impact' experiments reported above coupled homogeneous chemistry may play a role as is next discussed. We note that a three step *'ECC'* mechanism as shown in Figure 7.1b has been previously proposed[6] for the VO_2^+/VO^{2+} redox reaction,

$$VO^{2+} \rightleftharpoons VO^{3+} + e^- \quad (7.3)$$

$$VO^{3+} + H_2O \rightleftharpoons HVO_2^{2+} + H^+ \quad (7.4)$$

$$HVO_2^{2+} \rightleftharpoons VO_2^+ + H^+ \quad (7.5)$$

Exploratory simulations were conducted using this mechanism with the electrochemical rate constant and the transfer coefficient relating to the first step, viz the VO^{2+}/VO^{3+} reaction. The reductive wave is fully electrochemically irreversible so the overpotential was arbitrarily referenced to the formal potential of the VO_2^+/VO^{2+} redox couple. A transfer coefficient of 0.40 for the oxidative wave and of 0.60 for the reductive wave were assumed so that $\alpha + \beta = 1$. By the addition of the homogeneous chemistry and adjusting

the equilibrium and rate constants the approximate size and potential of the reverse peak could be obtained (Figure 7.13b) but not the breadth of the peak. Given the number of fitting parameters a unique fit was impossible so the equilibrium and rate constants reported in the Table 7.2 and must be seen simply as modelling parameters with no likely physical reality. The breadth of the reductive peak was again tentatively attributed to the possible role of surface adsorption processes.

Table 7.2 Simulation parameters used for simulating the CV at bare GC electrode for a *'ECC'* reaction mechanism. Note that the equilibrium constants are arbitrary for the purpose of proof of concept and do not have physical meaning.

Parameter	Input value
Geometry	Planar
Area of the electrode (cm^2)	7.07×10^{-2}
C (mM)	5.0 (VO^{2+}) / 10.0 (VO_2^+)
E^0 (V vs SCE)	0.76
Transfer coefficient α / β	0.60 / 0.40
k_0 (cm/s)	4.0×10^{-7}
$D_{vo^{2+}}$ (cm^2/s)	2.4×10^{-6}
$D_{vo_2^+}$ (cm^2/s)	3.3×10^{-6}
$K_{eq[3]}$	1.0×10^{5}
$k_{f[3]}$	2.0×10^{-2}
$k_{b[3]}$	2.0×10^{-7}
$K_{eq[4]}$	1.0×10^{5}
$k_{f[4]}$	1.0×10^{-2}
$k_{b[4]}$	1.0×10^{-7}

Nevertheless, to verify the accuracy of the formal potential and the electrochemical rate constant, simulations were made of the cyclic voltammograms recorded in 10.0 mM VO_2^+ supported by 1 M H_2SO_4. The simulations assumed the same standard electrochemical rate constant k^0 of 4.0 (±0.2) x 10^{-7} cm s^{-1} as inferred from the above together with a

reductive transfer coefficient of 0.60 and the experimentally measured diffusion coefficient $D_{VO_2^+}$ of 3.3 (± 0.1) x 10^{-6} cm^2 s^{-1} inferred above from the Randles-Ševčík plots. Figure 7.13c shows the fit obtained which satisfactorily reproduces the observed reduction peak potential and peak current. The peak is again broadened, giving an apparently low transfer coefficient not inconsistent with some involvement of surface adsorption/desorption processes.

To conclude the analysis of the GC electrode data, a standard electrochemical rate constant k^0 of 4.0 (±0.2) x 10^{-7} cm s^{-1} was found to be the best fit for the VO_2^+/VO^{2+} redox reaction at a bare GC electrode surface with the following net rate law describing the electrode kinetics of the overall reaction in 1.0 M H_2SO_4.

$$VO^{2+} + H_2O \underset{k_c}{\overset{k_a}{\rightleftarrows}} VO_2^+ + e^- + 2H^+ \quad (7.6)$$

$$j = k_a[VO^{2+}] - k_c[VO_2^+] \quad (7.7)$$

where j is the flux (mol cm^{-2} s^{-1}), $k_a = k^0 e^{\left[\frac{\beta\left(E - E_f^0\right)}{RT}\right]}$, $k_c = k^0 e^{\left[\frac{-\alpha\left(E - E_f^0\right)}{RT}\right]}$, β is 0.40, α is 0.60 and k^0 is 4.0 (±0.2) x 10^{-7} cm s^{-1}. A formal potential E^o of +0.76 V vs SCE, was adopted for the redox couple VO_2^+/VO^{2+} in 1 M H_2SO_4 as explained above. The concentrations of H^+ and of H_2O are constant under the conditions investigated and subsumed within the rate constant and definition of the formal potential.

Note that by referencing the overpotential to the formal potential of the VO_2^+/VO^{2+} couple the rate constant and the transfer coefficients reflect effects due to coupled homogeneous chemistry as well as the characteristics of the one electron reaction interconverting VO^{2+} and VO_2^+. Thus, the effects of the rate constants and equilibrium constants describing the homogeneous chemistry are lumped into the reported standard electrochemical rate constant which is thus expected, for example and notably, to be pH dependent.

ii) Electrode kinetics of the VO_2^+/VO^{2+} redox couple at single b-MWCNTs via nano-impact experiments

We next analysed the VO_2^+/VO^{2+} redox reaction kinetics at single b-MWCNTs by simulating the current – potential response obtained from the 'nano-impacts' experiment using DigiSim simulation software[50]. Single b-MWCNTs were modelled as a cylindrical electrode with a length of 6.0 x 10^{-4} cm and a radius of 1.5 x 10^{-6} cm assuming Butler – Volmer kinetics. The simulation was carried out for a one electron transfer as in Eq (7.3) for a formal potential, E^o of +0.76 V vs SCE and diffusion coefficients $D_{vo^{2+}}$ of 2.3 (± 0.2) x 10^{-6} cm^2 s^{-1} and $D_{vo_2^+}$ of 3.3 (± 0.1) x 10^{-6} cm^2 s^{-1} inferred from simulation at bare GC electrodes as reported above. For oxidation of 5.0 mM VO^{2+} in 1 M H_2SO_4 the best fit parameters were a transfer coefficient, β_2 of 0.45 (consistent with the Tafel analysis given in Figure 7.8c) and a standard electrochemical rate constant, k^0 of 1.1 (±0.1) x 10^{-3} cm s^{-1}. The fit with experimental data is given in Figure 7.14a. Likewise, Figure 7.14b shows the simulated curve for the impact data obtained for oxidation of 10.0 mM VO^{2+} using similar parameters as in Table 7.3.

Table 7.3 Simulation parameters used to simulate the 'nano-impacts' data

Parameter	**Input value for oxidation of VO^{2+}**	**Input value for reduction of VO_2^+**
Geometry	Cylindrical	Cylindrical
Radius (r, cm)	1.50 x 10^{-6}	1.50 x 10^{-6}
Length (l, cm)	6.00 x 10^{-4}	6.00 x 10^{-4}
C (mM)	5.00, 10.00 (VO^{2+})	10.00 (VO_2^+)
E^0 (V vs SCE)	0.76	0.76
Transfer coefficient α / β	0.45	0.41
k_0 (cm/s)	1.1 x 10^{-3}	7.0 x 10^{-8}
$D_{vo^{2+}}$ (cm^2/s)	2.45 x 10^{-6}	2.45 x 10^{-6}
$D_{vo_2^+}$ (cm^2/s)	3.27 x 10^{-6}	3.27 x 10^{-6}

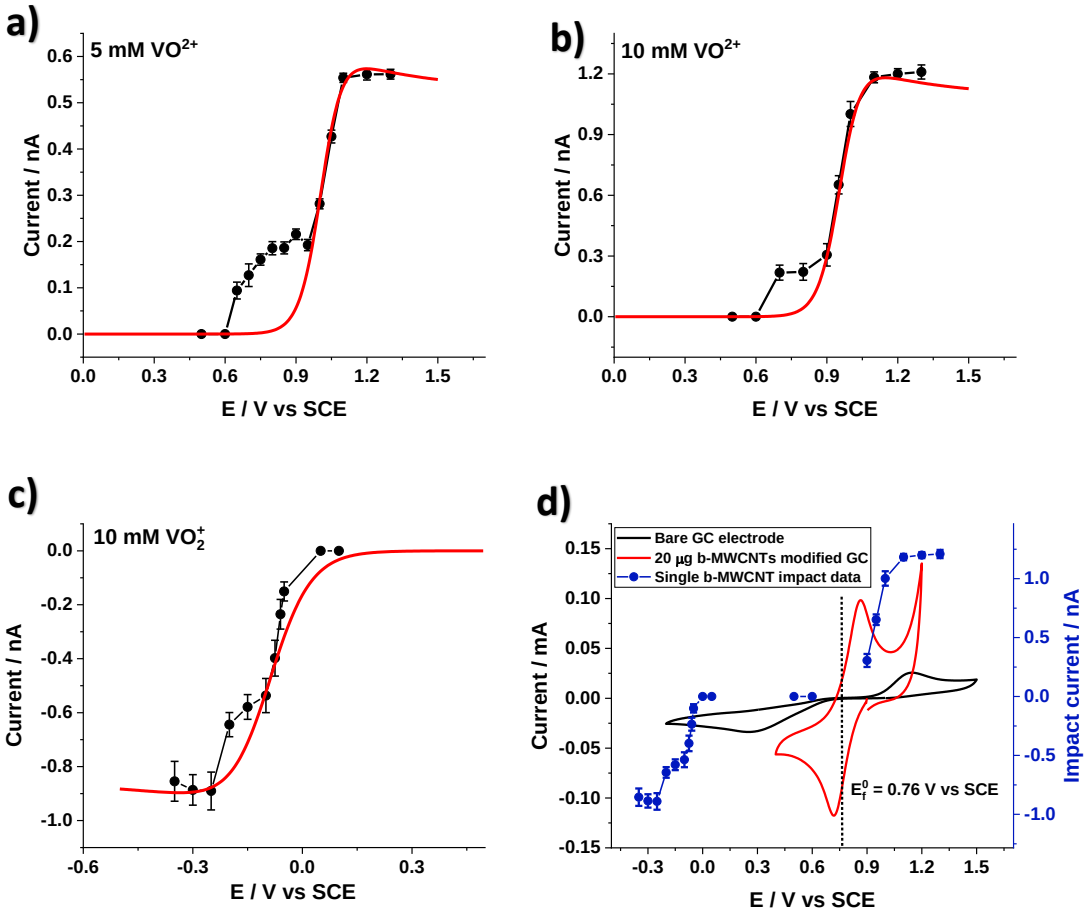


Figure 7.14 a) Impact data (black circles) of single b-MWCNTs and the corresponding DigiSim simulated curve (red line) for 5.0 mM VO^{2+} with β of 0.45 and k^0 of 1.1 (±0.1) x 10^{-3} cm s^{-1}; b) Impact data of single b-MWCNTs and fitted DigiSim simulated curve for 10.0 mM VO^{2+} with β of 0.45 and k^0 of 1.1 (±0.1) x 10^{-3} cm s^{-1}; c) Impact data of single b-MWCNTs and DigiSim simulated curve for 10.0 mM VO_2^+ with β of 0.41 and k^0 of 7.0 (±0.3) x 10^{-8} cm s^{-1} and d) Overlaid plot of cyclic voltammograms in 10.0 mM VO_2^+ at bare GC electrode (black line), 20 µg b-MWCNTs modified GC electrode (red line) and single b-MWCNTs impact data (in both 10.0 mM VO^{2+} and VO_2^+, blue circles), the vertical dotted line shows the formal potential of the VO_2^+/VO^{2+} redox couple.

Next, simulation was carried out for the reduction of 10.0 mM VO_2^+ giving a best fit for a transfer coefficient, α_2 of 0.41 (guided by the plot in Figure 7.11c) and a standard electrochemical rate constant k^0 of 7.0 (±0.3) x 10^{-8} cm s^{-1}, the parameters used for the simulation are given in Table 7.2. The fit is shown in Figure 7.14c which approximates the overall wave to a reasonable extent but fails to capture the split wave character

discussed above. Nevertheless, the approximate fitting serves to allow the assessment of the comparative catalytic responses as discussed in the following section but note that the rate constant reported for the reduction is extremely small since given the description of the reduction as an effective one electron process it includes the effects of the chemical reactions preceding the actual electron transfer event.

7.3.6 Evaluation of Carbon Nanotubes as Electrocatalysts for the VO_2^+/VO^{2+} Redox Couple

We next address the possible electrocatalysis of the VO_2^+/VO^{2+} redox couple by b-MWCNTs. Figure 7.14d summarises the electrochemical responses seen at a bare GC macroelectrode, at single nanotubes and from drop-casted ensembles of nanotubes. It is evident that at the GC electrode the response is that of a kinetically slow, highly electrochemically irreversible process with both the oxidative and reductive features appearing at large overpotentials compared to the formal potential of the couple (Figure 7.14d, dotted vertical line). The oxidative process is thought (see above) to be an '*ECC'* process, with the inverse sequence, '*CCE'*, applying to the reduction at lower reductive potentials. The low k^0 value signals intrinsically slow electrode kinetics at the single entity level and the kinetic limitations become visible as a result of the very high mass transport enjoyed by the single, isolated nanotubes which does not mask the kinetic limitations. In contrast when the electrode is modified with a layer of b-MWCNTs the voltammetric response is suggestive of a nearly electrochemically reversible redox couple. This most likely reflects the changed mass transport both within the porous b-MWCNTs layer and to the underlying electrode which much more nearly reflects thin layer (as opposed to semi-infinite) diffusive conditions. Thus, the electrode kinetics becomes fast relative to mass transport and approximately reversible behaviour is seen[49].

Table 7.4 Transfer coefficients and simulated standard electrochemical rate constants k^0 at a bare GC electrode and at single b-MWCNTs. Note that the rate constants are calculated assuming a formal potential of +0.76 V vs SCE

Reaction of study	Parameters analysed	Bare GC electrode	Single b-MWCNT
Oxidation in 5.0 / 10.0 mM VO^{2+} in 1 M H_2SO_4	Transfer coefficient, β	0.40	0.45
	Rate constant, k^0	4.0 (±0.2) x 10^{-7} cm s^{-1}	1.1 (±0.1) x 10^{-3} cm s^{-1}
Reduction in 10.0 mM VO_2^+ in 1 M H_2SO_4	Transfer coefficient, α	0.60	0.41
	Rate constant, k^0	4.0 (±0.2) x 10^{-7} cm s^{-1}	7.0 (±0.3) x 10^{-8} cm s^{-1}

Table 7.4 shows a comparison of the inferred standard electrochemical rate constants and transfer coefficients from the measurements at the GC electrode and from single entity data. For the oxidation both the rate constant and transfer coefficient changes markedly with the former being larger for the single b-MWCNT in comparison with GC whilst the small increase in transfer coefficient from 0.40 to 0.45 also facilitates faster electron transfer than seen on GC electrodes. Clearly individual nanotubes are catalytic towards the oxidation of VO^{2+}. In contrast for the reduction of VO_2^+ the two parameters indicate a marked slowing of the electrode process – an example of '*negative catalysis'*, thus making the overall redox reaction slow. The asymmetry in catalytic behaviour reflects the multistep nature of the process with rate determining electron transfer in the case of the oxidation whereas for the reduction the chemical steps which must precede electron transfer are discouraged by the fast mass transport regime seen at single nanotubes. Moreover, given this insight and the response seen for the drop-cast layers in Figure 7.14d

we infer that the catalysis apparent in the voltammetry of the drop-cast layer is illusory and that the apparent near reversible response in the case of the b-MWCNTs modified electrodes is attributable to the changed mass transport regime rather than an intrinsic catalysis.

7.4 Conclusions

We have investigated the possible *'nano-catalysis'* of the VO_2^+/VO^{2+} redox couple by b-MWCNTs and shown that in comparison to the electron transfer at a glassy carbon electrode. At b-MWCNTs the oxidative process is accelerated whereas the reductive process is retarded. Note that such a conclusion does not violate the principle of microscopic reversibility[53, 54] since the two reactions occur at different electrode potentials and have different transition states. Despite the retardation of the reduction, if an ensemble of nanotubes is used on the electrode surface the altered mass transport regime with effective thin layer diffusion replacing semi-infinite diffusion and hence the changing the voltammetric timescale, the impression of effective electrocatalysis is given since because of the confined diffusion the electrode response appears more electrochemically reversible. We thus recommend the more general use of single entity measurements in synergy with ensemble voltammetry to explore electrocatalysis noting that the complexity and slowness of mass transport within porous layers challenges conventional voltammetry and impedance spectroscopy.

Appendix

Section A7.1 The Effect of Electrode Preparation on the Reduction of 10 mM VO_2^+

This section reports the sensitivity of bare GC electrodes to different polishing methods in the reduction of VO_2^+ which is reflected on the shape of reductive wave seen in the voltammetry. Two different polishing methods were adopted for this study. In Method 1 the GC electrode was polished for 40 s with a single alumina powder of size 1.00 µm, 0.30 µm or 0.05 µm, then washed, sonicated for 10 s and dried with N_2. In Method 2 the GC electrode was polished sequentially for 120 s (40 s in each) with 1.00 µm, 0.30 µm and 0.05 µm alumina powders (Method 2), then washed, sonicated for 10 s, and dried. Different responses were seen; for Method 1 one reductive peak was observed at +0.30 V vs SCE at a scan rate of 25 mV s^{-1} as in Figure A7.1a, Method 1. But, for Method 2 two reductive peaks were observed as shown in Fig A7.1a, Method 2.

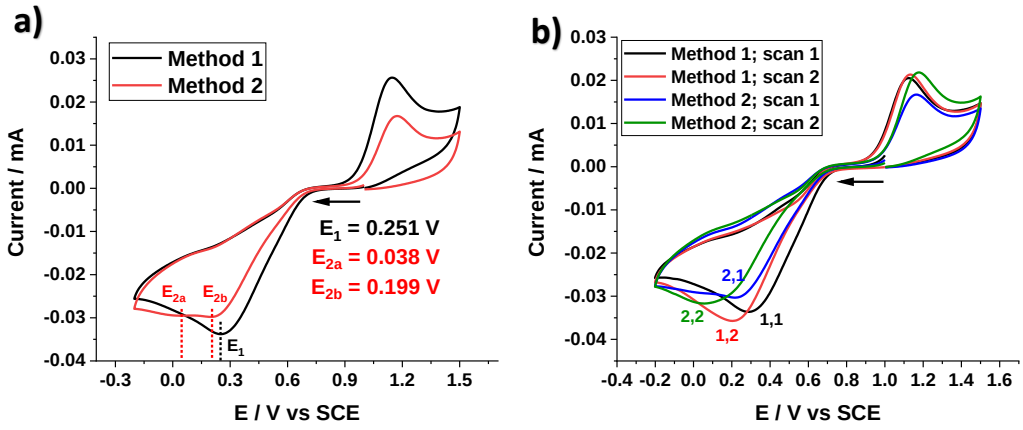


Figure A7.1 a) Cyclic voltammograms in 10.0 mM VO_2^+ in 1 M H_2SO_4 at bare GC electrode at a scan rate of 25 mV s^{-1}, method 1 (0.05 µm alumina powder); black line and method 2 (1.00 µm, 0.30 µm or 0.05 µm alumina powder); red line, b) Cyclic voltammograms of two consecutive scans after each method of polishing; black line, method 1 and scan 1, red line; method 1 and scan 2; blue line, method 2 and scan 1; blue line, method 2 and scan 2.

Consecutive CV scans (2nd scan) were recorded for both the methods and the reductive peak shifted to more negative potential compared to the first scan in both the cases, hence

the bare GC electrode was polished using Method 1 since no splitting of reductive wave was observed before every cyclic voltammetry experiment for the reduction reaction; this method of polishing ensured reproducible results. The change in the reductive wave can be tentatively attributed to surface roughness or adsorption effects[12, 47, 55] due to the prolonged polishing time for method 2 (120 s) over method 1 (40 s). No such phenomena was observed for the oxidation of VO^{2+}.

Section A7.2 Plot of Peak Current Versus Scan Rate at Bare GC Electrodes for the Voltammetry of Oxidation of VO^{2+} and Reduction of VO_2^+

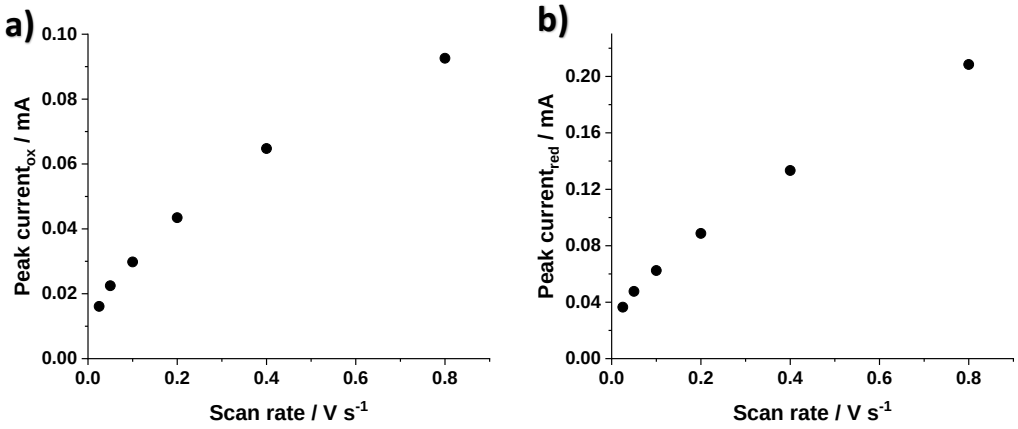


Figure A7.2 a) Plot of oxidative peak current versus scan rate in 5.0 mM VO^{2+} in 1 M H_2SO_4 at a bare GC electrode. b) Plot of reductive peak current versus scan rate in 10.0 mM VO_2^+ in 1 M H_2SO_4 at a bare GC electrode. The plot shows the non-linear behaviour in contrast to the plots in the main text of peak current against the square root of scan rate which are linear.

References

1. Kaliyaraj Selva Kumar, A.; Compton, R. G., Single-Entity "Nano-Catalysis": Carbon Nanotubes and the VO^{2+}/VO_2^+ Redox Reaction. *ACS Catal* **2022,** *12* (8), 4754-4764.
2. Tokuda, N.; Furuya, M.; Kikuoka, Y.; Tsutui, Y.; Kumamoto, T.; Kanno, T., Development of a Redox Flow (RF) Battery for energy storage. *Pcc-Osaka 2002: Proceedings of the Power Conversion Conference-Osaka 2002, Vols I - III* **2002**, 1144-1149.
3. Wu, M. C.; Zhao, T. S.; Jiang, H. R.; Zeng, Y. K.; Ren, Y. X., High-performance zinc bromine flow battery via improved design of electrolyte and electrode. *J Power Sources* **2017,** *355*, 62-68.
4. Skyllas-Kazacos, M.; Rychcik, M.; Robins, R. G.; Fane, A. G.; Green, M. A., New All-Vanadium Redox Flow Cell. *J Electrochem Soc* **1986,** *133* (5), 1057-1058.
5. Kanamori, K.; Tsuge, K., Inorganic Chemistry of Vanadium. In *Vanadium: Biochemical and Molecular Biological Approaches*, Michibata, H., Ed. Springer Netherlands: Dordrecht, 2012; pp 3-31.
6. Gattrell, M.; Park, J.; MacDougall, B.; Apte, J.; McCarthy, S.; Wu, C. W., Study of the mechanism of the vanadium 4+/5+redox reaction in acidic solutions. *J Electrochem Soc* **2004,** *151* (1), A123-A130.
7. Jordan, A. J. B. R. P. J., *Standard potentials in aqueous solution*. Routledge: 1985.
8. Coryell, C. D.; Yost, D. M., The reduction potential of vanadic acid to vanadyl ion in hydrochloric acid solutions. *Journal of the American Chemical Society* **1933,** *55*, 1909-1915.
9. Carpenter, J. E., The constitution of the pentavalent vanadium ion in acid solution. *Journal of the American Chemical Society* **1934,** *56* (7), 1847-1850.
10. Agarwal, H.; Florian, J.; Goldsmith, B. R.; Singh, N., V^{2+}/V^{3+} Redox Kinetics on Glassy Carbon in Acidic Electrolytes for Vanadium Redox Flow Batteries. *ACS Energy Lett* **2019,** *4* (10), 2368-2377.
11. Sum, E.; Skyllas-Kazacos, M., A Study of the V(II)/V(III) Redox Couple for Redox Flow Cell Applications. *J Power Sources* **1985,** *15* (2-3), 179-190.
12. Sum, E.; Rychcik, M.; Skyllas-Kazacos, M., Investigation of the V(V)/V(IV) System for Use in the Positive Half-Cell of a Redox Battery. *J Power Sources* **1985,** *16* (2), 85-95.
13. Wu, X. W.; Yamamura, T.; Ohta, S.; Zhang, Q. X.; Lv, F. C.; Liu, C. M.; Shirasaki, K.; Satoh, I.; Shikama, T.; Lu, D.; Liu, S. Q., Acceleration of the redox kinetics of VO^{2+}/VO_2^+ and V^{3+}/V^{2+} couples on carbon paper. *J Appl Electrochem* **2011,** *41* (10), 1183-1190.
14. Oriji, G.; Katayama, Y.; Miura, T., Investigation on V(IV)/V(V) species in a vanadium redox flow battery. *Electrochim Acta* **2004,** *49* (19), 3091-3095.

15. Aaron, D.; Sun, C. N.; Bright, M.; Papandrew, A. B.; Mench, M. M.; Zawodzinski, T. A., In Situ Kinetics Studies in All-Vanadium Redox Flow Batteries. *ECS Electrochem Lett* **2013,** *2* (3), A29-A31.

16. Kaneko, H.; Nozaki, K.; Wada, Y.; Aoki, T.; Negishi, A.; Kamimoto, M., Vanadium Redox Reactions and Carbon Electrodes for Vanadium Redox Flow Battery. *Electrochim Acta* **1991,** *36* (7), 1191-1196.

17. Kausar, N.; Howe, R.; Skyllas-Kazacos, M., Raman spectroscopy studies of concentrated vanadium redox battery positive electrolytes. *J Appl Electrochem* **2001,** *31* (12), 1327-1332.

18. Rahman, F.; Skyllas-Kazacos, M., Solubility of vanadyl sulfate in concentrated sulfuric acid solutions. *J Power Sources* **1998,** *72* (2), 105-110.

19. Cotton, F. A.; Wilkinson, G.; Murillo, C. A.; Bochmann, M.; Grimes, R., *Advanced inorganic chemistry*. Wiley New York: 1988; Vol. 6.

20. Park, M.; Jeon, I. Y.; Ryu, J.; Baek, J. B.; Cho, J., Exploration of the Effective Location of Surface Oxygen Defects in Graphene-Based Electrocatalysts for All-Vanadium Redox-Flow Batteries. *Adv Energy Mater* **2015,** *5* (5).

21. Li, W. Y.; Liu, J. G.; Yan, C. W., Reduced graphene oxide with tunable C/O ratio and its activity towards vanadium redox pairs for an all vanadium redox flow battery. *Carbon* **2013,** *55*, 313-320.

22. Li, C. C.; Xie, B. S.; Chen, J.; He, J. J.; He, Z. X., Enhancement of nitrogen and sulfur co-doping on the electrocatalytic properties of carbon nanotubes for VO^{2+}/VO_2^{+} redox reaction. *RSC Adv* **2017,** *7* (22), 13184-13190.

23. Zhu, H. Q.; Zhang, Y. M.; Yue, L.; Li, W. S.; Li, G. L.; Shu, D.; Chen, H. Y., Graphite-carbon nanotube composite electrodes for all vanadium redox flow battery. *J Power Sources* **2008,** *184* (2), 637-640.

24. Sun, B. T.; Skyllas-Kazacos, M., Chemical Modification and Electrochemical-Behavior of Graphite Fiber in Acidic Vanadium Solution. *Electrochim Acta* **1991,** *36* (3-4), 513-517.

25. Kim, K. J.; Park, M. S.; Kim, J. H.; Hwang, U.; Lee, N. J.; Jeong, G.; Kim, Y. J., Novel catalytic effects of Mn_3O_4 for all vanadium redox flow batteries. *Chem Commun* **2012,** *48* (44), 5455-5457.

26. Yun, N.; Park, J. J.; Park, O. O.; Lee, K. B.; Yang, J. H., Electrocatalytic effect of NiO nanoparticles evenly distributed on a graphite felt electrode for vanadium redox flow batteries. *Electrochim Acta* **2018,** *278*, 226-235.

27. Hou, B. X.; Cui, X. M.; Chen, Y. G., In situ TiO_2 decorated carbon paper as negative electrode for vanadium redox battery. *Solid State Ionics* **2018,** *325*, 148-156.

28. Xiang, Y.; Daoud, W. A., Cr_2O_3 modified graphite felt as a novel positive electrode for vanadium redox flow battery. *Electrochim Acta* **2018,** *290*, 176-184.

29. Keeley, G. P.; Lyons, M. E. G., The Effects of Thin Layer Diffusion at Glassy Carbon Electrodes Modified with Porous Films of Single-Walled Carbon Nanotubes. *Int J Electrochem Sc* **2009,** *4* (6), 794-809.

30. Sokolov, S. V.; Eloul, S.; Kätelhön, E.; Batchelor-McAuley, C.; Compton, R. G., Electrode–particle impacts: a users guide. *Phys Chem Chem Phys* **2017,** *19* (1), 28-43.

31. Li, X. T.; Batchelor-McAuley, C.; Tschulik, K.; Shao, L. D.; Compton, R. G., Ultra-small Palladium Nanoparticle Decorated Carbon Nanotubes: Conductivity and Reactivity. *Chemphyschem* **2015,** *16* (11), 2322-2325.

32. Li, X. T.; Batchelor-McAuley, C.; Whitby, S. A. I.; Tschulik, K.; Shao, L. D.; Compton, R. G., Single Nanoparticle Voltammetry: Contact Modulation of the Mediated Current. *Angew Chem Int Edit* **2016,** *55* (13), 4296-4299.

33. Zhou, Y. G.; Rees, N. V.; Compton, R. G., The Electrochemical Detection and Characterization of Silver Nanoparticles in Aqueous Solution. *Angew Chem Int Edit* **2011,** *50* (18), 4219-4221.

34. Miao, R. Y.; Chen, L. F.; Shao, L. D.; Zhang, B. S.; Compton, R. G., Electron Transfer to Decorated Graphene Oxide Particles. *Angew Chem Int Edit* **2019,** *58* (36), 12549-12552.

35. Streeter, I.; Wildgoose, G. G.; Shao, L. D.; Compton, R. G., Cyclic voltammetry on electrode surfaces covered with porous layers: An analysis of electron transfer kinetics at single-walled carbon nanotube modified electrodes. *Sensor Actuat B-Chem* **2008,** *133* (2), 462-466.

36. Sims, M. J.; Rees, N. V.; Dickinson, E. J. F.; Compton, R. G., Effects of thin-layer diffusion in the electrochemical detection of nicotine on basal plane pyrolytic graphite (BPPG) electrodes modified with layers of multi-walled carbon nanotubes (MWCNT-BPPG). *Sensor Actuat B-Chem* **2010,** *144* (1), 153-158.

37. Ye, H. S.; Liu, X.; Cui, H. F.; Zhang, W. D.; Sheu, F. S.; Lim, T. M., Electrochemical oxidation of multi-walled carbon nanotubes and its application to electrochemical double layer capacitors. *Electrochemistry Communications* **2005,** *7* (3), 249-255.

38. Barisci, J. N.; Wallace, G. G.; Baughman, R. H., Electrochemical studies of single-wall carbon nanotubes in aqueous solutions. *J Electroanal Chem* **2000,** *488* (2), 92-98.

39. Frackowiak, E.; Delpeux, S.; Jurewicz, K.; Szostak, K.; Cazorla-Amoros, D.; Beguin, F., Enhanced capacitance of carbon nanotubes through chemical activation. *Chem Phys Lett* **2002,** *361* (1-2), 35-41.

40. Datsyuk, V.; Kalyva, M.; Papagelis, K.; Parthenios, J.; Tasis, D.; Siokou, A.; Kallitsis, I.; Galiotis, C., Chemical oxidation of multiwalled carbon nanotubes. *Carbon* **2008,** *46* (6), 833-840.

41. Shao, Y. Y.; Yin, G. P.; Zhang, J.; Gao, Y. Z., Comparative investigation of the resistance to electrochemical oxidation of carbon black and carbon nanotubes in aqueous sulfuric acid solution. *Electrochim Acta* **2006,** *51* (26), 5853-5857.

42. Pumera, M., Carbon nanotubes contain residual metal catalyst nanoparticles even after washing with nitric acid at elevated temperature because these metal nanoparticles are sheathed by several graphene sheets. *Langmuir* **2007,** *23* (11), 6453-6458.

43. Pumera, M.; Iwai, H., Metallic Impurities within Residual Catalyst Metallic Nanoparticles Are in Some Cases Responsible for "Electrocatalytic" Effect of Carbon Nanotubes. *Chem-Asian J* **2009,** *4* (4), 554-560.

44. Kumar, A. K. S.; Miao, R. Y.; Li, D. L.; Compton, R. G., Do carbon nanotubes catalyse bromine/bromide redox chemistry? *Chem Sci* **2021,** *12* (32), 10878-10882.

45. Holland-Cunz, M. V.; Friedl, J.; Stimming, U., Anion effects on the redox kinetics of positive electrolyte of the all-vanadium redox flow battery. *J Electroanal Chem* **2018,** *819*, 306-311.

46. Li, D. L.; Lin, C. H.; Batchelor-McAuley, C.; Chen, L. F.; Compton, R. G., Tafel analysis in practice. *J Electroanal Chem* **2018,** *826*, 117-124.

47. Zhong, S.; Skyllas-Kazacos, M., Electrochemical-Behavior of Vanadium(V) Vanadium(IV) Redox Couple at Graphite-Electrodes. *J Power Sources* **1992,** *39* (1), 1-9.

48. Yamamura, T.; Watanabe, N.; Yano, T.; Shiokawa, Y., Electron-transfer kinetics of Np^{3+}/Np^{4+}, NpO_2^{+}/NpO_2^{2+}, V^{2+}/V^{3+}, and VO^{2+}/VO_2^{+} at carbon electrodes. *J Electrochem Soc* **2005,** *152* (4), A830-A836.

49. Henstridge, M. C.; Dickinson, E. J. F.; Aslanoglu, M.; Batchelor-McAuley, C.; Compton, R. G., Voltammetric selectivity conferred by the modification of electrodes using conductive porous layers or films: The oxidation of dopamine on glassy carbon electrodes modified with multiwalled carbon nanotubes. *Sensor Actuat B-Chem* **2010,** *145* (1), 417-427.

50. Rudolph, M., An Algorithm of General Application for the Digital-Simulation of Electrochemical Processes. *J Electroanal Chem* **1990,** *292* (1-2), 1-7.

51. Swift, E. H., *A System of Chemical Analysis (qualitative and semi-quantitative) for the Common Elements*. W.H Freeman and Company: San Francisco, 1940.

52. Pourbaix, M., Pourbaix,M - Atlas of Electrochemical Equilibria in Aqueous Solutions. *Anti-Corros* **1967,** *14* (2), 234.

53. Denbigh, K. G., *The Principles of Chemical Equilibrium: With Applications in Chemistry and Chemical Engineering*. 4 ed.; Cambridge University Press: Cambridge, 1981.

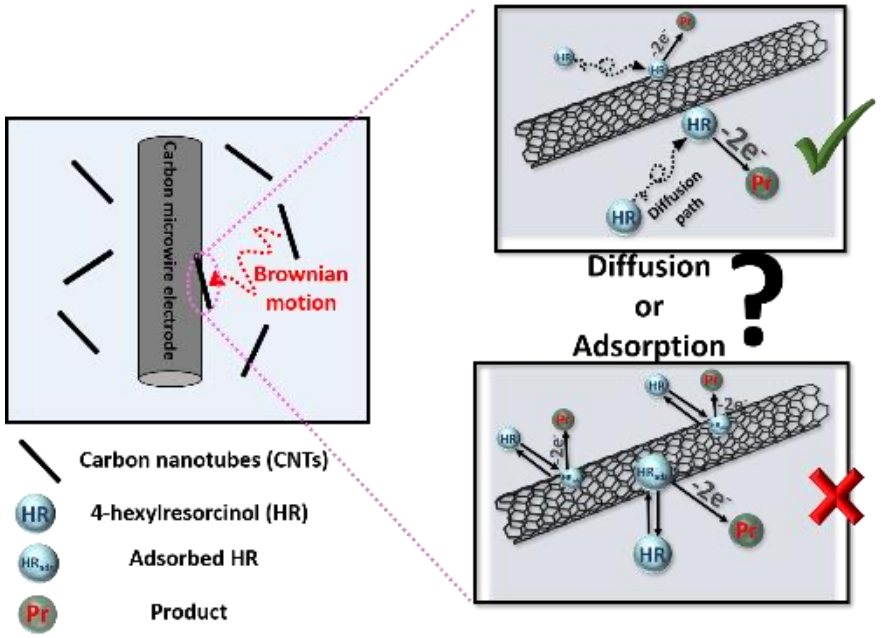
54. Albery, W. J., *Electrode kinetics*. Clarendon Press: 1975.

55. Lee, J.; Muya, J. T.; Chung, H.; Chan, J., Unraveling V(V)-V(IV)-V(III)-V(II) Redox Electrochemistry in Highly Concentrated Mixed Acidic Media for a Vanadium Redox Flow Battery: Origin of the Parasitic Hydrogen Evolution Reaction. *ACS Appl Mater Inter* **2019,** *11* (45), 42066-42077.

Chapter 8

Understanding Carbon Nanotube Voltammetry: Distinguishing Adsorptive and Thin Layer Effects via 'Single-Entity' Electrochemistry

In Chapter 4 we pointed out that cyclic voltammetry of ensembles of nanotube modified electrodes fails to distinguish between signals from electroactive material adsorbed on the tubes to those due to a thin-layer response of analyte material occluded in the pores of the ensemble.



Scheme 8.1 Schematic representation showing that the impact current is diffusion-controlled process rather than adsorption.

In this chapter we demonstrate that the distinction can be clearly made by combining cyclic voltammetry with single-entity measurements and provide proof of concept for the case of b-MWCNTs and the oxidation of 4-hexylresorcinol (HR), where the increased signals were seen at the modified electrode are concluded to arise from thin-layer

diffusion and not adsorptive effects. The physical insights are generic to porous, conductive composites.

This work has been published in the Journal of Physical Chemistry Letters[1].

8.1 Introduction

In the previous chapters we have looked at the important role played by electrodes made of composites of carbon nanotubes (CNTs) or of surfaces modified, for example, by drop-casting layers of CNTs. Specifically, the areas of electroanalysis and energy conversion benefit from the use of these deliberately designed interfaces as discussed in Chapter 3. Physically whether formed via drop-casting or some means of compression perhaps with the addition of a binding agents such as Nafion[2], the electroactive layer usually takes the form of a random aggregate of CNTs and displays a significant level of porosity, although carefully grown nanotube 'forests' confer greater order. Nevertheless, porosity is essential since it allows the access of electrolyte to the high internal surface area of the porous CNTs layer which is at least partly the cause of the apparent electrocatalysis often shown by such surface modifications[3].

Key to understanding the electrocatalytic responses of CNTs modified electrodes is deciphering their voltammetry which is the current response to an electrode potential ramp applied to the CNTs modified electrode. For the case of a flat, planar electrode this response is well understood and characterised by the Randles – Ševčík equations[4-7]. Here, the peak current reflects a compromise between an increasing rate of electron transfer and an ever-decreasing concentration of reactant local to the electrode as the potential is scanned, and scales directly with the square root of scan rate, signalling the role of diffusion in bringing fresh reactant to the surface[8]. In the case of electrodes modified with porous layer two peaks may be observed in the voltammetry. One again reflects semi –

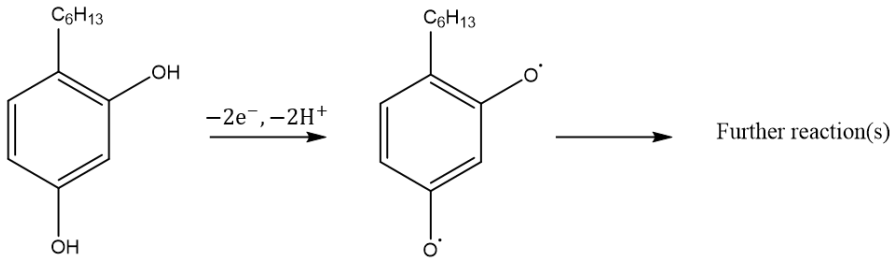
infinite diffusion to the exterior of the layer as for a flat non-porous surface, the other seen at lower over potential results from the electrolysis of reactant occluded within the porous layer which typically displays characteristics of 'thin – layer' diffusion[3, 9-14]. The latter has a peak current which scale more directly with scan rate signifying that the contents of the porous layer are more responsive to alteration of potential and hence are relatively more under thermodynamic control and the potential of the peak is closer to the formal potential of the redox couple so apparently 'catalysed'.

It is evident that the response of the peak current to the scan rate can be used to signal the presence of thin-layer diffusion within a CNTs layer. However, if an analyte is adsorbed on the surface of a flat non-porous electrode the voltammetric signal also scales directly with scan rate[15] again reflecting the absence of diffusion. This then poses a question that if a voltammetric signal is observed from a porous layer of CNTs which scales directly with scan rate, does it signify that there is thin-layer diffusion within the porous layer or is the analyte adsorbed on the surface of the CNTs rather than being occluded within the pores?

The problem of differentiating between the diffusional and adsorptive behaviour of CNTs layers is not only of fundamental importance in understanding the electrode reaction mechanism but also relevant for analytical understanding since CNTs modified electrodes are extensively used for adsorptive stripping analysis (see Chapter 3). In this application the CNTs are used to adsorptively pre – concentrate the analyte prior to being detected and quantified voltammetrically[16-18].

In the following we compare and contrast single-entity electrochemistry measurements with ensemble responses to make a clear distinction between adsorptive and thin-layer effects. Specifically, we consider the voltammetry of 4-hexylresorcinol at both the single

bamboo-like multiwalled carbon nanotubes (b-MWCNTs) and at drop-casted layers of b-MWCNTs. The oxidation of HR is thought[18] to be a two electron and two proton transfer process as given in Scheme 8.2.



Scheme 8.2 Electrochemical oxidation of 4-hexylresorcinol undergoing a two electron and two proton process [18].

8.2 Experimental

All the chemicals used in this chapter were purchased commercially. The details of these chemicals are given in Chapter 2, Table 2.1.

8.2.1 Preparation of Bare GC Electrode and b-MWCNTs Modified GC Electrode

A bare GC electrode of radius 0.15 cm and area 7.07 x 10^{-2} cm^2 was used as the working electrode. The GC electrode was polished sequentially with 1.0 μm, 0.3 μm and 0.05 μm alumina powder (Buehler, Micropolish II, Germany). Electrodes were then washed with deionised water and sonicated for 10 s then dried with N_2 prior to the CV experiments.

For b-MWCNTs modified electrode, a dispersion of b-MWCNTs was made in acetone of a concentration of 2.2 x 10^{-13} M (1 mg mL^{-1}), and sonicated for 20 mins. and dried under steady N_2 flow. 5, 7, 10 and 12 μg (70, 98, 140, 170 μg cm^{-2} in coverage respectively) of the above dispersion were drop-casted on the cleaned GC electrode and then dried under stable N_2 flow prior to the CV experiments.

The oxidation of HR was conducted at bare GC electrode and b-MWCNTs modified electrodes in 0.10 mM of HR supported by 0.05 M of Britton-Robinson Buffer solution of pH 1.5.

8.2.2 'Nano-Impact' Experiments at Single b-MWCNTs – Chronoamperometry Studies

The 'nano-impact' experiments were made at fixed potentials applied to the working electrode. A carbon micro-wire electrode of diameter 7 μm and length 1 mm was employed as the latter. Fabrication of the micro-wire electrode is described in Chapter 2, Section 2.4. The b-MWCNTs were dispersed in deionised water 2.2 x 10^{-13} M (1 mg mL^{-1}) and sonicated for 20 mins, then a known concentration was added to the solution of study for observing the impact siganls.

8.3 Results and Discussion

In this section we discussed the results obtained from cyclic voltammetry analysis for oxidation of HR at bare GC and b-MWCNTs modified GC. Further 'single-entity' analysis was conducted to distinguish if the reaction is diffusion controlled or otherwise.

8.3.1 Cyclic Voltammetric Analysis at Bare GC and b-MWCNTs Modified GC

First voltammetric investigations were conducted using 0.10 mM aqueous solutions of 4-hexylresorcinol (HR) with 0.05 M Britton-Robinson buffer solution (BRS) of pH 1.5. The cyclic voltammograms (CV) were recorded as a function of scan rate at a pristine glassy carbon (GC) electrode and are given in Figure 8.1a. A clear oxidative peak corresponding to the oxidation of HR was observed and no such voltammetric response was observed in the absence of HR as given in Figures 8.1b and c.

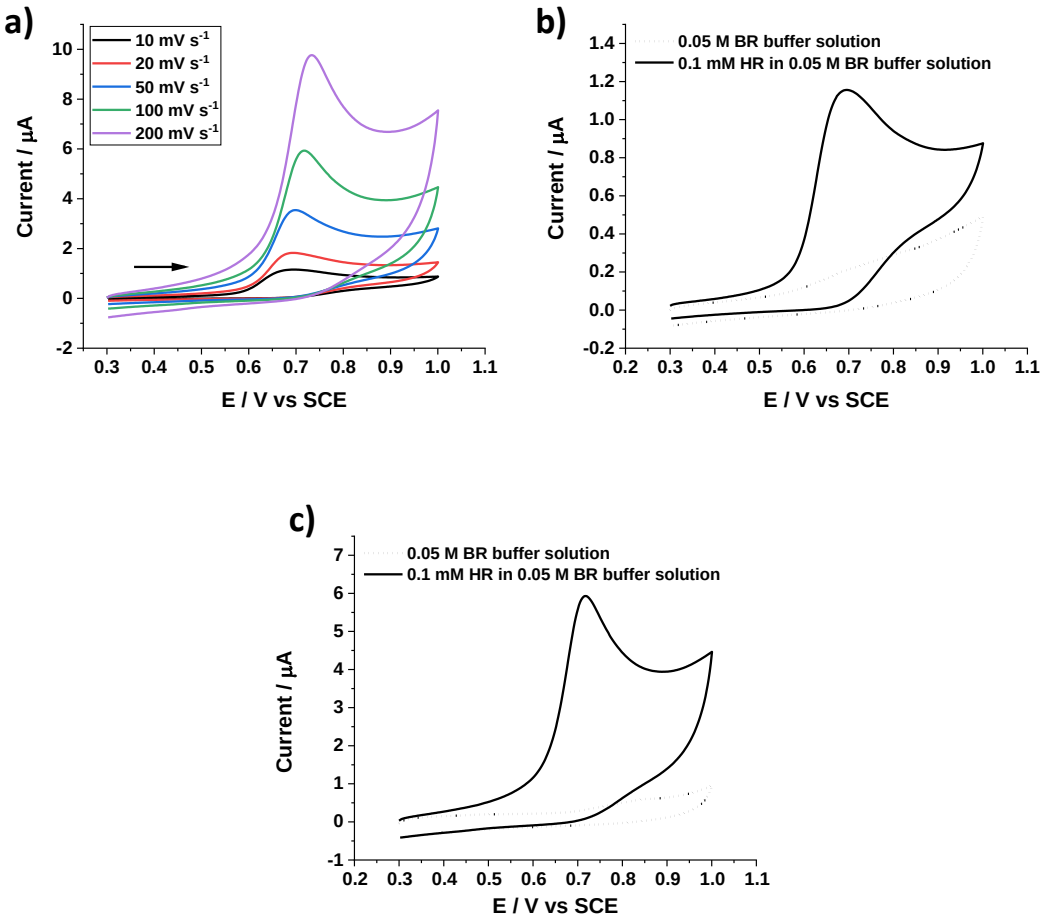


Figure 8.1 Cyclic voltammograms at a bare GC electrode a) in 0.10 mM hexylresorcinol with 0.05 M BR buffer solution as a function of scan rate, b) bare GC in 0.10 mM HR with 0.05 M BR buffer (solid line) and only BR buffer solution (dotted line) at scan rates 10 mV s^{-1} and c) 100 mV s^{-1}.

Further, cyclic voltammetry was conducted at drop-casted ensembles of b-MWCNTs of different coverages (70, 98, 140 and 170 µg cm^{-2} of b-MWCNTs on GC). The voltammograms recorded as a function of scan rate at different coverages respectively are given in Figure 8.2. The minimum number of layers of b-MWCNTs were estimated (calculations in Chapter 4 Appendix, Section A4.1) assuming that the nanotubes were arranged in a closed packing arrangement at the GC electrode surface similar to the previous chapters and were found to be 21, 30, 42 and 50 layers of b-MWCNTs for a drop-cast of 70, 98, 140 and 170 µg cm^{-2} respectively. Given the assumption made in

respect of packing these numbers are likely to be significant under-estimates since the layers will in reality likely be made of randomly oriented tubes. Moreover, in the absence of HR, no such voltammetric feature was observed as shown in Figure 8.3.

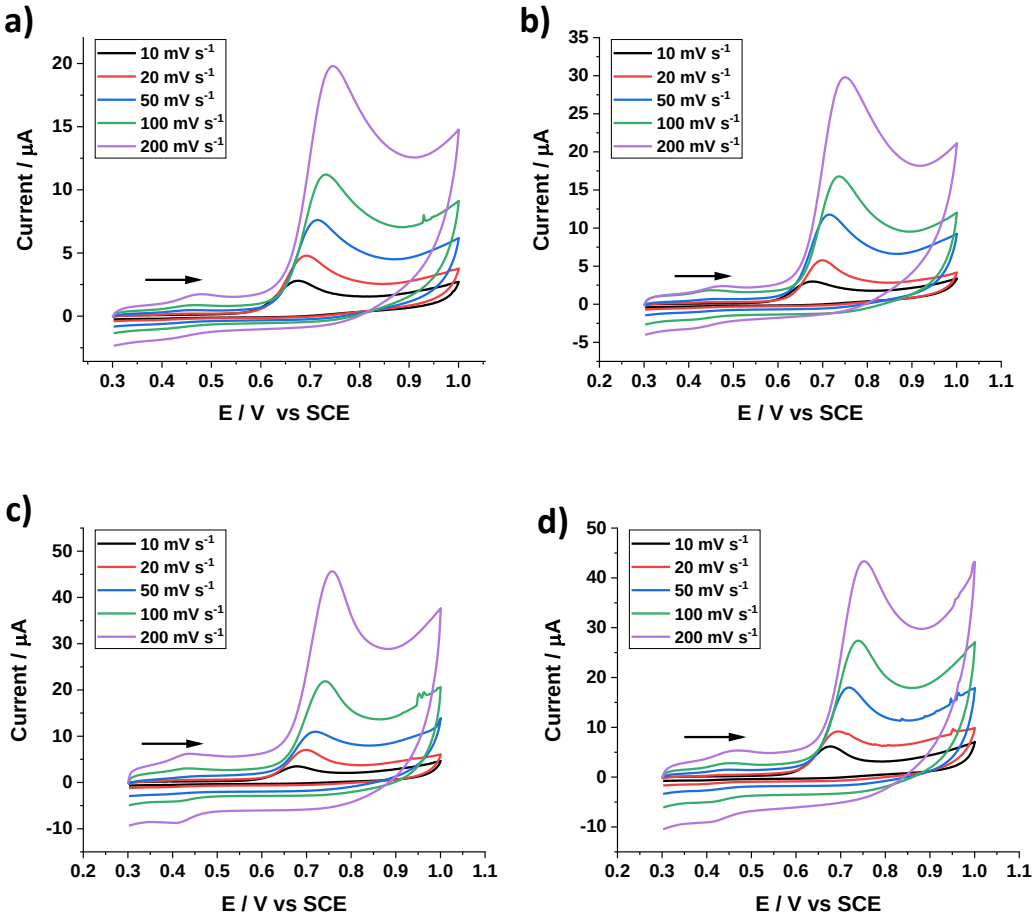


Figure 8.2 Cyclic voltammograms of 0.10 mM hexylresorcinol in 0.05 M BR buffer solution as a function of scan rate at a) 70 µg cm^{-2} of b-MWCNTs on GC, b) 98 µg cm^{-2} of b-MWCNTs on GC, c) 140 µg cm^{-2} of b-MWCNTs on GC and d) 170 µg cm^{-2} of b-MWCNTs on GC.

The overlaid voltammograms at bare GC and different coverages of b-MWCNTs drop-casted GC at a scan rate of 100 mV s^{-1} are shown in Figure 8.4, where a chemically irreversible oxidative peak was observed at *ca.* +0.74 V vs SCE, which matches well with the reported formal potential of oxidation of HR[18]. The plots of peak current versus scan rate and square root of scan rate are given in Figure 8.5. To assess the scan rate dependence of the peak current log-log plots were made as shown in Figure 8.6.

Approximately linear plots were observed, the slopes of which are given in Figure 8.6, where slope values between 0.5 and 1.0 were noted. A slope of 0.5 would correspond to a semi-infinite diffusional signal whilst a value of 1.0 corresponds to adsorptive or thin layer responses as discussed in Chapter 3.

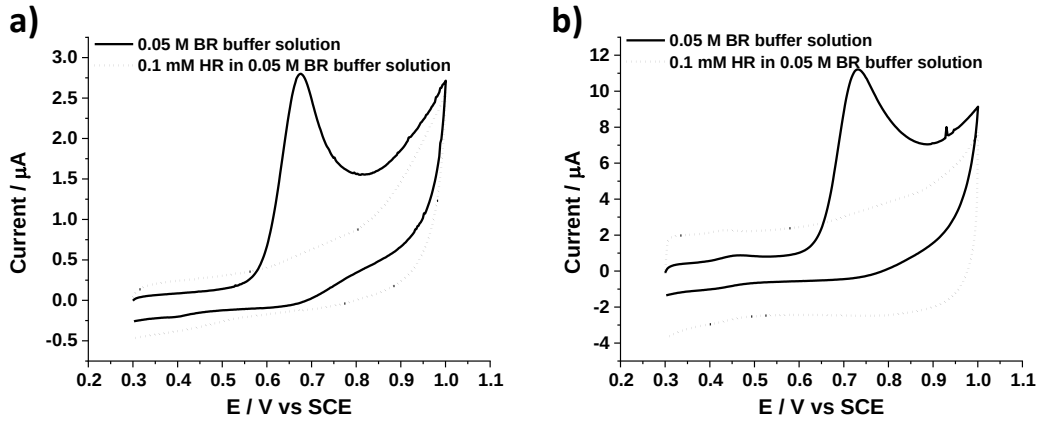


Figure 8.3 Cyclic voltammograms at 70 µg cm^{-2} of b-MWCNTs on GC electrode in 0.10 mM HR with 0.05 M BR buffer (solid line) and only BR buffer solution (dotted line) at scan rates a) 10 mV s^{-1} and b) 100 mV s^{-1}.

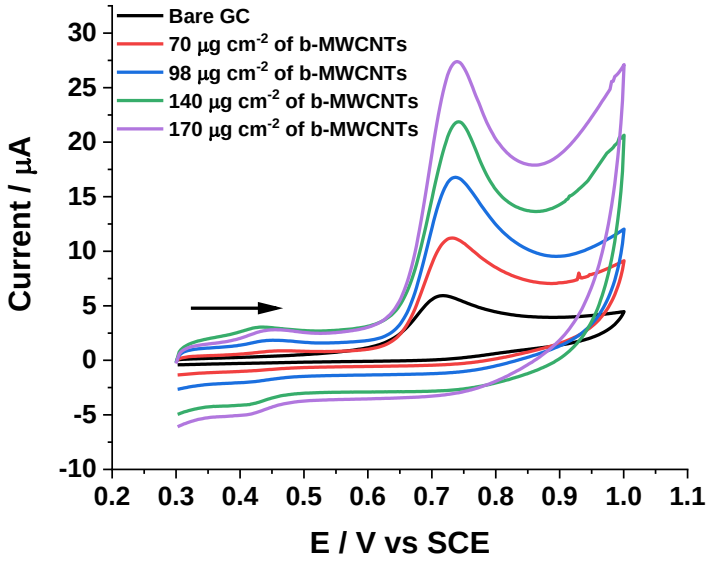


Figure 8.4 Cyclic voltammograms of 0.10 mM hexylresorcinol in 0.05 M BR buffer solution at bare GC electrode (black line), at variable drop-casted coverages of b-MWCNTs; 70 (red line),

98 (blue line), 140 (green line) and 170 (magenta line) μg cm^{-2} on a GC electrode (radius = 1.5 mm) at a scan rate of 100 mV s^{-1}.

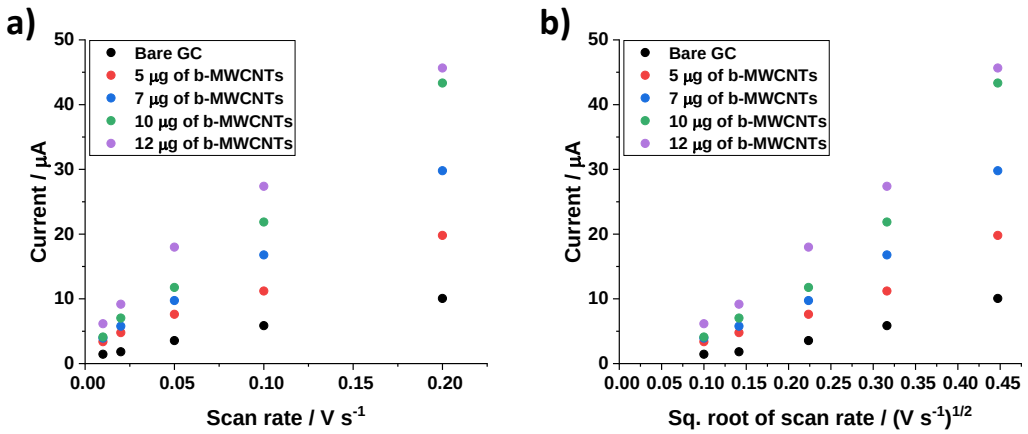


Figure 8.5 Bare GC electrode (black circles), 70 (red circles), 98 (blue circles), 140 (green circles) and 170 (magenta circles) μg cm^{-2} of b-MWCNTs on a GC electrode, in 0.10 mM hexylresorcinol with 0.05 M BR buffer solution. a) plot of peak current versus scan rate, b) plot of peak current versus square root of scan rate.

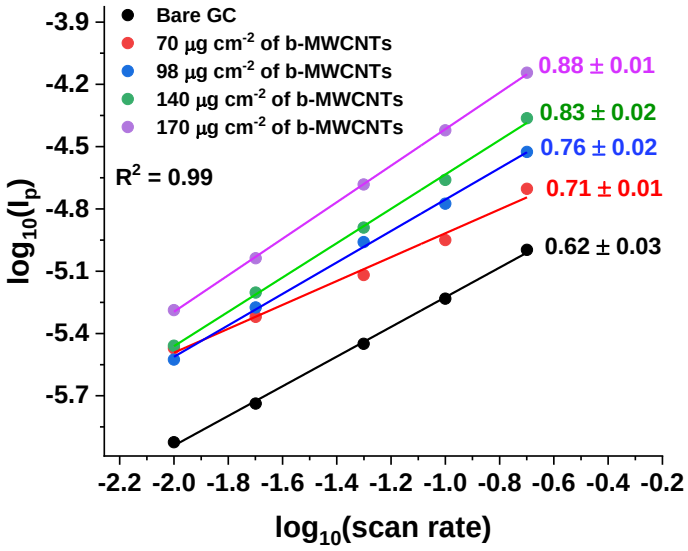


Figure 8.6 Plot of log peak current versus log scan rate in 0.10 mM hexylresorcinol with 0.05 M BR buffer solution at bare GC electrode (black circles), 70 (red circles), 98 (blue circles), 140 (green circles) and 170 (magenta circles) μg cm^{-2} of b-MWCNTs on a GC electrode.

It can be seen that as the coverage of b-MWCNTs increases the signals tends towards unity indicating a greater contribution from the porous b-MWCNT layer as would be

expected. It is evident that whilst the CV measurements emphasise the role of the porous layer they cannot in themselves distinguish between adsorptive and thin layer effects. Accordingly, we next turn to single entity electrochemistry measurements.

8.3.2 'Single-Entity' Electrochemical Study of b-MWCNTs

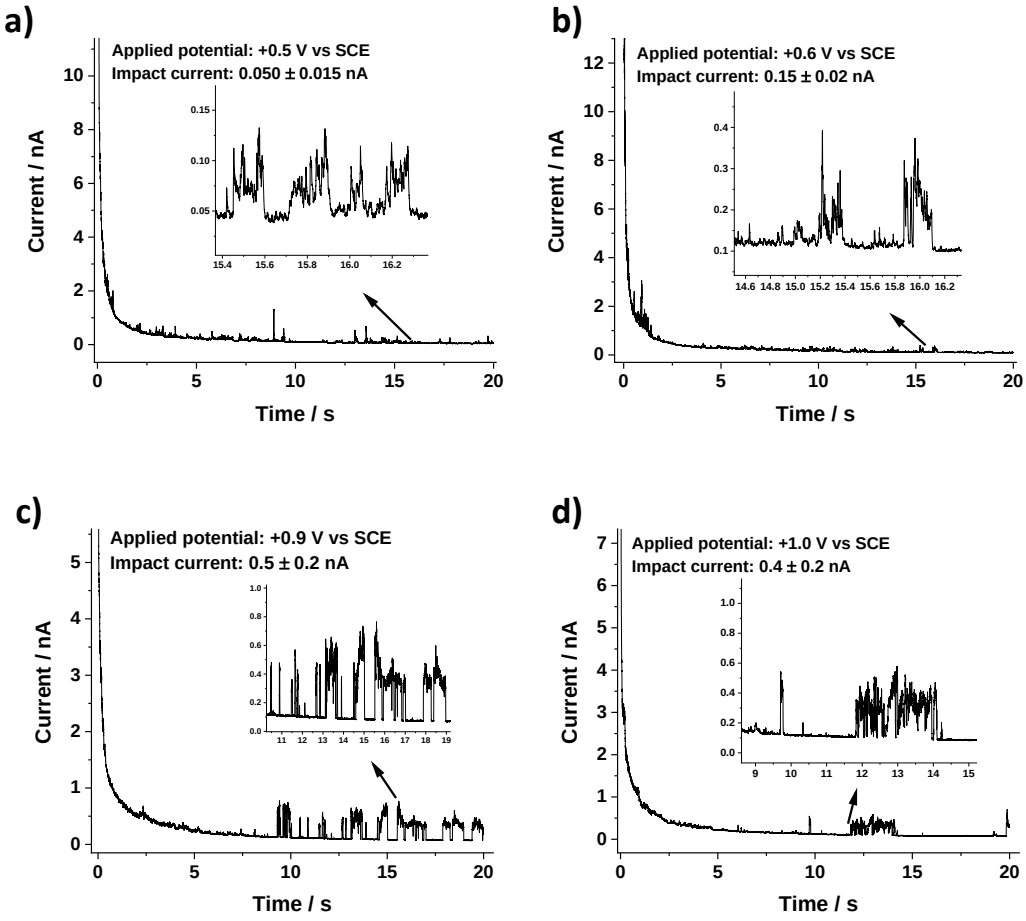


Figure 8.7 Chronoamperograms showing representative impact signals in 0.10 mM HR with 0.05 M BR solution at applied potentials of a) +0.5 V vs SCE, b) +0.6 V vs SCE, c) +0.9 V vs SCE and d) +1.0 V vs SCE.

Single-entity electrochemical analysis of b-MWCNTs in 0.10 mM HR with 0.05 M BRS was carried out to understand the voltammetry at single b-MWCNT levels without the complication of the uncertain mass-transport characteristics arising from layer porosity in the CV of drop-cast experiments as mentioned above. For this, chronoamperometric experiments were carried out at different fixed potentials using a carbon fibre microwire

electrode (7.0 μm in diameter, for fabrication method see Chapter 2). The selected potential was applied to the electrode with 1.3×10^{-14} M of b-MWCNTs dispersed in it. Impact signals were measured over the potential range +0.5 V to +1.0 V vs SCE. Figure 8.7 shows representative impacts measured in the presence of 0.10 mM HR where the sharp on-off features which correspond to the arrival and departure of the b-MWCNT from the surface of the electrode. During the period of the impact sustained Faradaic currents flow which are of an approximately constant value on top of which some random current fluctuations are evident and which arise from movement of the b-MWCNT at the interface modulating the electron transfer distance[19].

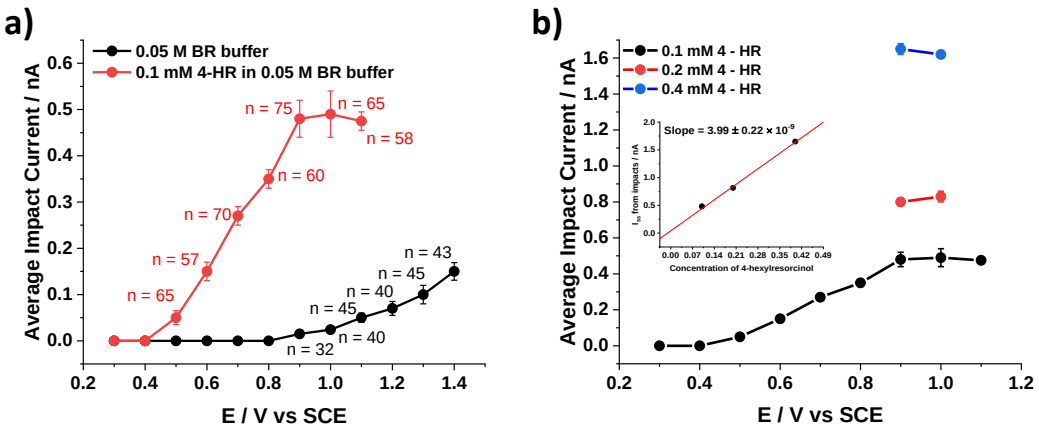


Figure 8.8 Plot of average impact current versus applied potential in b-MWCNTs dispersed a) in 0.10 mM 4 – HR in 0.05 M BR buffer solution (red circles) and 0.05 M BR buffer solution only (black circles) n is the number of impacts analysed at each applied potential, b) in 0.10 mM (black circles), 0.2 mM (red circles) and 0.4 mM (blue circles) of 4 – HR, in 0.05 M BRS.

The red line in Figure 8.8a shows how the average impact current varies with potential leading to a voltammogram-like dependence with a maximum current seen as a plateau at potentials above +0.9 V vs SCE. Comparison with Figure 8.1 suggests that the current likely arises from the oxidation of HR. The average impact duration was 1.2 s and the frequency of impacts 0.5 s^{-1}. Note that no impact signals were seen in the absence of b-MWCNTs as shown in Figure 8.9. In the absence of HR, but in the presence of the b-

MWCNTs tiny signals were observed and the average impact current is shown by the black circles in Figure 8.8a. Figure 8.10 shows typical impact signals seen in the absence of HR at +0.9 V to +1.4 V vs SCE. These were assigned to capacitive impacts consistent with the increase in capacitive currents at high positive potentials[20, 21] and also the oxidation of the b-MWCNTs themselves as discussed elsewhere[22]. The impact signals seen in the absence of HR are tiny in comparison with the Faradaic signals seen in the presence of HR hence attention was next turned to the further consideration of these signals.

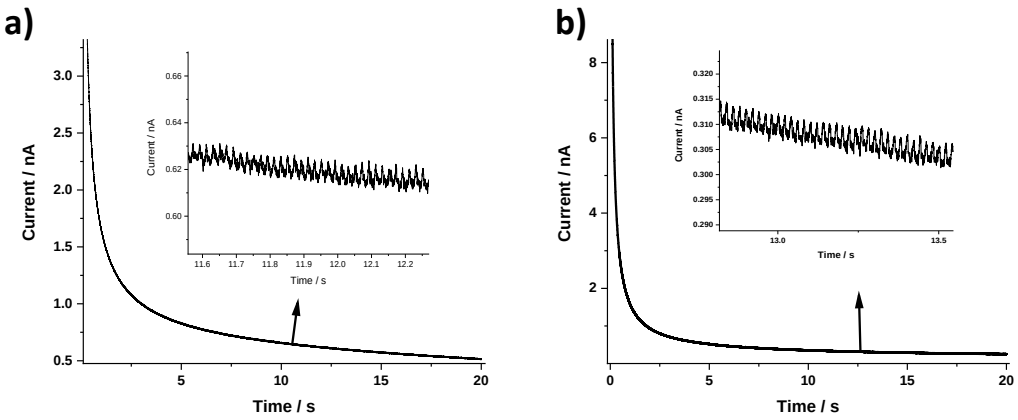


Figure 8.9 Chronoamperogram without b-MWCNTs at applied potential of +1.0 V vs SCE, a) only 0.05 M BR buffer solution and b) in 0.10 mM hexylresorcinol with 0.05 M BR buffer solution

Further experiments were conducted in which impact currents were measured as a function of potential using increased concentrations of HR of 0.20 and 0.40 mM, using potentials corresponding with the plateau current seen in Figure 8.8a for 0.10 mM HR. The data are shown in Figure 8.8b (red and blue circles for 0.20 and 0.40 mM respectively) showing that the current scales approximately linearly with concentration. This observation is consistent with two possible explanations; first the signals represent the oxidation of HR adsorbed on the b-MWCNT surface or, second, represent a diffusion-controlled oxidation of HR at the single b-MWCNT entity. The sustained currents

flowing throughout the duration of the impact suggest the latter. Further in the first case the average charge per impact was calculated for each of the three concentrations of HR studied and compared with that expected for the 2-electron oxidation on the basis of an estimated monolayer coverage of HR on a single CNT. The estimation of the latter and the comparison is discussed in the next section.

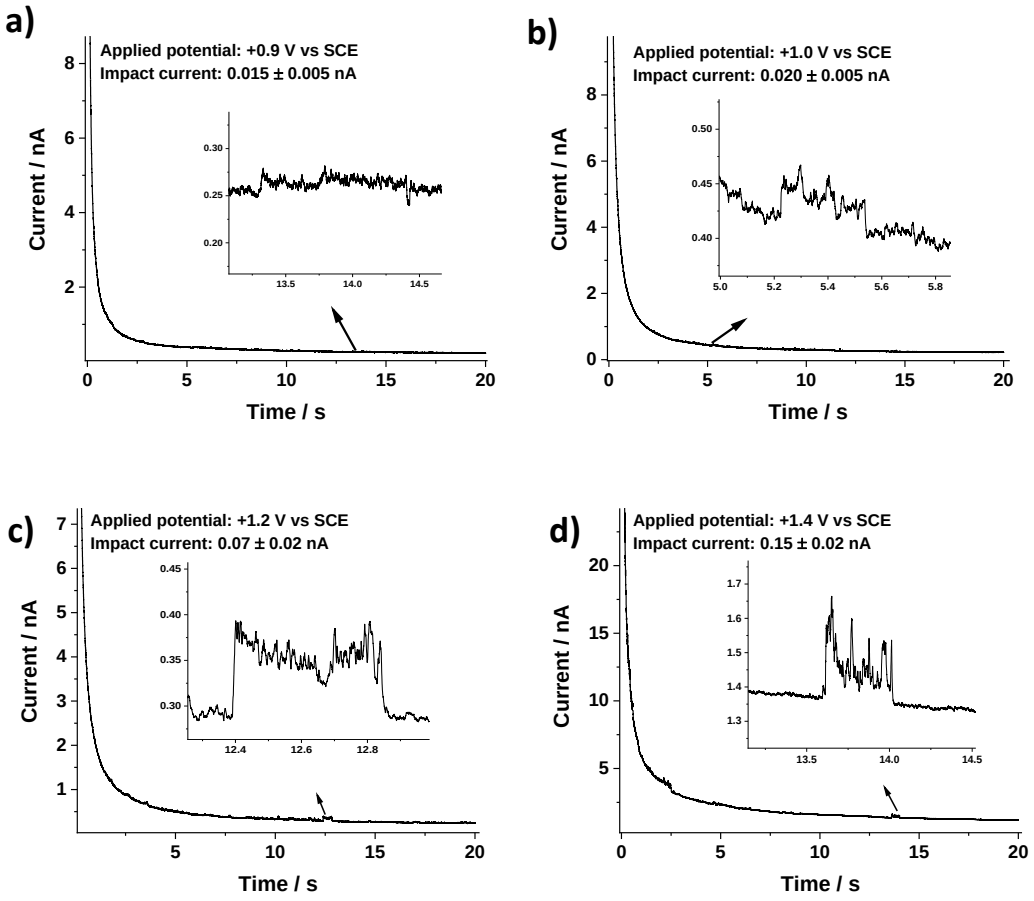


Figure 8.10 Chronoamperograms showing representative impact signals in only 0.05 M BR solution at applied potentials of a) +0.9 V vs SCE, b) +1.0 V vs SCE, c) +1.2 V vs SCE and d) +1.4 V vs SCE.

8.3.3 Interpreting Impact Signals as Adsorptive in Origin

To analyse if the impact currents obtained from the impacts of single b-MWCNTs were adsorptive or diffusional, first the assumption was made for the adsorption of HR onto the surface of single b-MWCNT. To estimate the number of monolayers of adsorption

three differently possible orientations of adsorptions were considered, flat, vertical and end oriented.

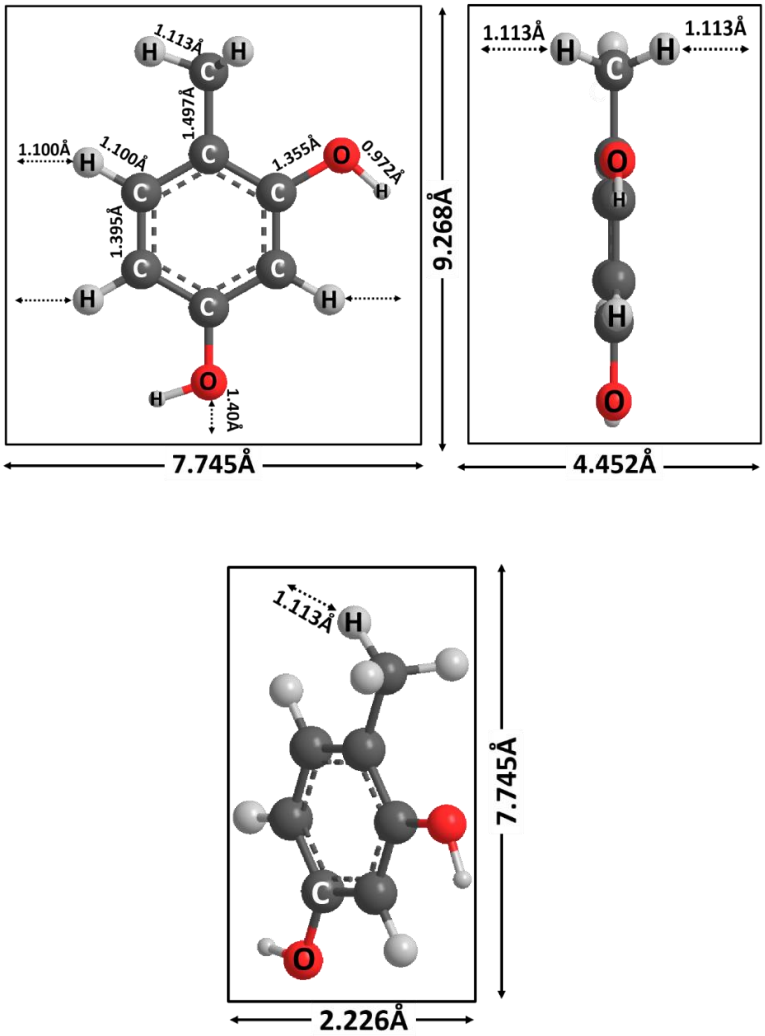


Figure 8.11 Rectangular box model of 4-hexylresorcinol showing three faces of the cuboid enclosing the molecule.

Then, the maximum surface coverages were calculated using the area of the molecule. Note that the bond lengths, bond angles and van der Waals radii were obtained from ChemDraw 3D software.

The maximum surface coverage, Γ_{max} is given by,

$$\Gamma_{max} = \frac{1}{N_A S_A} \tag{8.1}$$

where, N_A is the Avogadro constant and S_A is the surface area of the molecule.

The surface areas of the molecule were calculated by assuming three different possible orientations for adsorption on the surface of the b-MWCNTs, namely via each of the three faces of the rectangular box (cuboid) encompassing the molecule as shown in Figure 8.11.

Note that the dimensions of the cuboid containing the molecule is defined by the bond lengths and angles together with the van der Waal radii of the atoms at the extremities of the molecule.

The areas of the three faces were calculated to be as follows.

1) Flat face (largest area face, LAF): 7.18 (±0.04) x 10^{-15} cm^2
2) Vertical face (intermediate area face, IAF): 4.13 (±0.05) x 10^{-15} cm^2
3) End face (smallest area face, SAF): 1.45 (±0.11) x 10^{-15} cm^2

Thus, the coverages, Γ_{max}, were estimated assuming close packing of the cuboids, to be,

1) Flat face (Γ_{max} LAF): 2.31 (±0.12) x 10^{-10} mol cm^{-2}
2) Vertical face (Γ_{max} IAF): 4.02 (±0.13) x 10^{-10} mol cm^{-2}
3) End face (Γ_{max} SAF): 1.19 (±0.23) x 10^{-9} mol cm^{-2}

The charge passed from the oxidation of one monolayer of HR adsorbed on the surface of the b-MWCNTs can be calculated using the following equation,

$$\Gamma = \frac{Q}{nFA} \tag{8.2}$$

where, Γ is the surface coverage in mol cm^{-2}, Q is the charge calculated form the impact currents in C, n is the number of electrons, F is the Faraday constant in C mol^{-1} and A is the area of the single b-MWCNT.

Thus, the charge for each orientation is,

1) LAF: 3.78 (±0.02) x 10^{-13} C
2) IAF: 6.59 (±0.06) x 10^{-13} C
3) SAF: 1.95 (±0.09) x 10^{-12} C

The average charge calculated from the impact current in 0.10 mM, 0.20 mM and 0.40 mM of HR is 7.54 (±1.50) x 10^{-12} C, 1.52 (±1.35) x 10^{-11} C and 3.05 (±1.44) x 10^{-11} C respectively.

Hence the number of monolayers of HR adsorbed on the b-MWCNTs for each orientation is given in Table 8.1, assuming a close packed arrangement.

Table 8.1 No. of monolayers of HR adsorbed at single b-MWCNTs at various concentrations assuming the currents are due to adsorbed HR (but see text for refutation of this assumption)

Concentration / mM	**No. of monolayers**		
	Flat view	**Edge view**	**End view**
0.10	20 (±2)	11 (±3)	4 (±3.5)
0.20	40 (±2)	23 (±3)	8 (±3.5)
0.40	81 (±2)	46 (±3)	16 (±3.5)

It was found that if adsorption takes place then it must be multi-layer adsorption on the single b-MWCNT with as many as 4-20 layers observed depending on the orientation of HR at the b-MWCNT surface. These are implausibly large so the origin of the signals in adsorptive behaviour is discounted. Alternatively, the impact data was analysed on the assumption that the steady currents reflect diffusion-controlled oxidation of HR as is discussed in the section below.

8.3.4 Interpreting Impacts as Diffusion Controlled Faradaic Signals for 4-hexylresorcinol Oxidation

The impact signals were alternatively considered to be diffusion-controlled, hence the diffusion coefficient of HR was calculated from the impact data and compared with expectations based on literature values (Table 8.2).

Table 8.2 Diffusion coefficients of different quinones in aqueous solutions at 298 (±3) K. Note that the literature values were rounded to two significant figures.

Solution	Diffusion coefficient/ $cm^2\ s^{-1}$	Reference
1.0 mM hydroquinone in 1 M sulfuric acid	5.0×10^{-6}	[23]
0.5 mM anthraquinone-2-sulfonate in 0.1 M KOH	5.7×10^{-6}	[24]
5.0 mM p-benzoquinone in 0.5 M KCl	7.0×10^{-6}	[25]
1.0 mM 2,5-dihydroxy-1,4-benzoquinone in 1 M KOH	3.7×10^{-6}	[26]
1.0 mM 9,10-anthraquinone-2,7-disulfonic acid in 1 M H2SO4	4.4×10^{-6}	[27]
1.0 mM anthaquinone-2-sulfonate in 0.1 M NaOH and 0.1 M KCl	4.7×10^{-6}	[28]
1.0 mM anthraquinone-2,6-disulfonate in 0.1 M NaOH and 0.1 M KCl	5.2×10^{-6}	[28]

The magnitude of the diffusion coefficient, *D*, was estimated treating the single b-MWCNT as a cylindrical electrode as discussed in previous chapters[19, 29-32] using the known length *l*, radius *r* of the tube and assuming the oxidation is a 2-electron transfer process as in Scheme 8.2. The following equation is used to calculate the diffusion coefficient at cylindrical electrodes[33],

$$I_{ss} = 2\pi nFDClf(\tau) \qquad (8.3)$$

with,

$$f(\tau) = \frac{e^{-\sqrt{\pi\tau}/20}}{\sqrt{\pi\tau}} + \frac{1}{ln[(2e^{-\gamma}\tau)^{1/2} + e^{-5/3}]}$$

$$\tau = \frac{4Dt}{r^2}$$

where the value of γ = 0.5772, *D* is the diffusion coefficient, *C* is the analyte concentration, *n* is the number of electrons transferred during the oxidation of HR where, as shown in Scheme 8.2, (n = 2) , and *t* is the impact duration.

Figure 8.8b (inset) shows a plot of of I_{ss} versus concentration which was analysed according to Eq (8.3) In this way the diffusion coefficient of 4-hexylresorcinol was estimated to be 4.04 (± 2.26) x 10^{-6} cm^2 s^{-1} by assuming that the impact signals are diffusive. Comparison with literature values given in the Table 8.2 shows that this value is of a magnitude expected for quinones in aqueous solutions and suggests that this is a plausible interpretation of the impact signal data.

We infer that HR undergoes diffusional electro-oxidation at the b-MWCNTs when studied as single entities and hence infer that in the case of the CV of ensembles b-MWCNTs that the response reflects thin-layer diffusion, rather than adsorptive effects.

8.4 Conclusions

To conclude, the oxidation of HR was investigated at both ensemble and 'single' b-MWCNTs through voltammetric and 'nano-impacts' methods respectively. Voltammetric analysis of ensembles of b-MWCNTs were inconclusive in distinguishing between adsorptive and thin layer diffusive effect. However, single entity measurements clearly demonstrated diffusion-controlled electrochemistry at individual carbon nanotubes allowing the inference that the ensemble voltammetric response is that of thin layer diffusion from within the pores between the b-MWCNTs rather than resulting from adsorption onto the nanotubes. Last, we note that whilst this work was conducted on the b-MWCNTs the implications are generic to porous electrodes in general including the many used in energy conversion and chemical sensing based on nanoparticles.

References

1. Kaliyaraj Selva Kumar, A.; Compton, R. G., Understanding Carbon Nanotube Voltammetry: Distinguishing Adsorptive and Thin Layer Effects via "Single-Entity" Electrochemistry. *The Journal of Physical Chemistry Letters* **2022**, 5557-5562.
2. Wang, J.; Musameh, M.; Lin, Y. H., Solubilization of carbon nanotubes by Nafion toward the preparation of amperometric biosensors. *Journal of the American Chemical Society* **2003,** *125* (9), 2408-2409.
3. Sims, M. J.; Rees, N. V.; Dickinson, E. J. F.; Compton, R. G., Effects of thin-layer diffusion in the electrochemical detection of nicotine on basal plane pyrolytic graphite (BPPG) electrodes modified with layers of multi-walled carbon nanotubes (MWCNT-BPPG). *Sensor Actuat B-Chem* **2010,** *144* (1), 153-158.
4. Compton, R. G.; Banks, C. E., Understanding Voltammetry, 3rd Edition. *Understanding Voltammetry, 3rd Edition* **2018**, 1-439.
5. Randles, J. E. B., A Cathode Ray Polarograph .2. The Current-Voltage Curves. *T Faraday Soc* **1948,** *44* (5), 327-&.
6. Ševčík, A., Oscillographic polarography with periodical triangular voltage. *Collection of Czechoslovak Chemical Communications* **1948,** *13*, 349-377.
7. Nicholson, R. S.; Shain, I., Theory of Stationary Electrode Polarography - Single Scan Cyclic Methods Applied to Reversible Irreversible Kinetic Systems. *Analytical Chemistry* **1964,** *36* (4), 706-&.
8. Einstein, A., The motion of elements suspended in static liquids as claimed in the molecular kinetic theory of heat. *Ann Phys-Berlin* **1905,** *17* (8), 549-560.
9. Keeley, G. P.; Lyons, M. E. G., The Effects of Thin Layer Diffusion at Glassy Carbon Electrodes Modified with Porous Films of Single-Walled Carbon Nanotubes. *Int J Electrochem Sc* **2009,** *4* (6), 794-809.
10. Streeter, I.; Wildgoose, G. G.; Shao, L. D.; Compton, R. G., Cyclic voltammetry on electrode surfaces covered with porous layers: An analysis of electron transfer kinetics at single-walled carbon nanotube modified electrodes. *Sensor Actuat B-Chem* **2008,** *133* (2), 462-466.
11. Henstridge, M. C.; Dickinson, E. J. F.; Aslanoglu, M.; Batchelor-McAuley, C.; Compton, R. G., Voltammetric selectivity conferred by the modification of electrodes using conductive porous layers or films: The oxidation of dopamine on glassy carbon electrodes modified with multiwalled carbon nanotubes. *Sensor Actuat B-Chem* **2010,** *145* (1), 417-427.
12. Chen, L. F.; Katelhon, E.; Compton, R. G., Unscrambling illusory inhibition and catalysis in nanoparticle electrochemistry: Experiment and theory. *Appl Mater Today* **2019,** *16*, 141-145.

13. Chen, L. F.; Katelhon, E.; Compton, R. G., Particle-modified electrodes: General mass transport theory, experimental validation, and the role of electrostatics. *Appl Mater Today* **2020,** *18*.

14. Katelhon, E.; Chen, L. F.; Compton, R. G., Nanoparticle electrocatalysis: Unscrambling illusory inhibition and catalysis. *Appl Mater Today* **2019,** *15*, 139-144.

15. Li, Q.; Batchelor-McAuley, C.; Compton, R. G., Electrochemical Oxidation of Guanine: Electrode Reaction Mechanism and Tailoring Carbon Electrode Surfaces To Switch between Adsorptive and Diffusional Responses. *J Phys Chem B* **2010,** *114* (21), 7423-7428.

16. Kachoosangi, R. T.; Wildgoose, G. G.; Compton, R. G., Sensitive adsorptive stripping voltammetric determination of paracetamol at multiwalled carbon nanotube modified basal plane pyrolytic graphite electrode. *Anal Chim Acta* **2008,** *618* (1), 54-60.

17. Jin, G. P.; He, J. B.; Rui, Z. B.; Meng, F. S., Electrochemical behavior and adsorptive stripping voltammetric determination of quercetin at multi-wall carbon nanotubes-modified paraffin-impregnated graphite disk electrode. *Electrochim Acta* **2006,** *51* (21), 4341-4346.

18. Kachoosangi, R. T.; Wildgoose, G. G.; Compton, R. G., Adsorptive stripping voltammetric determination of 4-hexylresorcinol in pharmaceutical products using multiwalled carbon nanotube based electrodes. *Electroanal* **2008,** *20* (15), 1714-1718.

19. Li, X. T.; Batchelor-McAuley, C.; Whitby, S. A. I.; Tschulik, K.; Shao, L. D.; Compton, R. G., Single Nanoparticle Voltammetry: Contact Modulation of the Mediated Current. *Angew Chem Int Edit* **2016,** *55* (13), 4296-4299.

20. Poon, J.; Batchelor-McAuley, C.; Tschulik, K.; Compton, R. G., Single graphene nanoplatelets: capacitance, potential of zero charge and diffusion coefficient. *Chem Sci* **2015,** *6* (5), 2869-2876.

21. Sokolov, S. V.; Eloul, S.; Katelhon, E.; Batchelor-McAuley, C.; Compton, R. G., Electrode-particle impacts: a users guide. *Phys Chem Chem Phys* **2017,** *19* (1), 28-43.

22. Kaliyaraj Selva Kumar, A.; Compton, R. G., Single-Entity "Nano-Catalysis": Carbon Nanotubes and the VO2+/VO2+ Redox Reaction. *ACS Catal* **2022,** *12* (8), 4754-4764.

23. Yang, B.; Hoober-Burkhardt, L.; Wang, F.; Prakash, G. K. S.; Narayanan, S. R., An Inexpensive Aqueous Flow Battery for Large-Scale Electrical Energy Storage Based on Water-Soluble Organic Redox Couples. *J Electrochem Soc* **2014,** *161* (9), A1371-A1380.

24. Li, Q.; Batchelor-McAuley, C.; Lawrence, N. S.; Hartshorne, R. S.; Compton, R. G., Electrolyte tuning of electrode potentials: the one electron vs. two electron reduction of anthraquinone-2-sulfonate in aqueous media. *Chem Commun* **2011,** *47* (41), 11426-11428.

25. Tang, Y. H.; Wu, Y. R.; Wang, Z. H., Spectroelectrochemistry for electroreduction of p-benzoquinone in unbuffered aqueous solution. *J Electrochem Soc* **2001,** *148* (4), E133-E138.

26. Yang, Z. J.; Tong, L. C.; Tabor, D. P.; Beh, E. S.; Goulet, M. A.; De Porcellinis, D.; Aspuru-Guzik, A.; Gordon, R. G.; Aziz, M. J., Alkaline Benzoquinone Aqueous Flow Battery for Large-Scale Storage of Electrical Energy. *Adv Energy Mater* **2018,** *8* (8).

27. Wiberg, C.; Carney, T. J.; Brushett, F.; Ahlberg, E.; Wang, E. G., Dimerization of 9,10-anthraquinone-2,7-Disulfonic acid (AQDS). *Electrochim Acta* **2019,** *317*, 478-485.

28. Batchelor-McAuley, C.; Li, Q.; Dapin, S. M.; Compton, R. G., Voltammetric Characterization of DNA Intercalators across the Full pH Range: Anthraquinone-2,6-disulfonate and Anthraquinone-2-sulfonate. *J Phys Chem B* **2010,** *114* (11), 4094-4100.

29. Li, X. T.; Batchelor-McAuley, C.; Shao, L. D.; Sokolov, S. V.; Young, N. P.; Compton, R. G., Quantifying Single-Carbon Nanotube-Electrode Contact via the Nanoimpact Method. *J Phys Chem Lett* **2017,** *8* (2), 507-511.

30. Li, X. T.; Batchelor-McAuley, C.; Tschulik, K.; Shao, L. D.; Compton, R. G., Ultra-small Palladium Nanoparticle Decorated Carbon Nanotubes: Conductivity and Reactivity. *Chemphyschem* **2015,** *16* (11), 2322-2325.

31. Li, X. T.; Lin, C. H.; Batchelor-McAuley, C.; Laborda, E.; Shao, L. D.; Compton, R. G., New Insights into Fundamental Electron Transfer from Single Nanoparticle Voltammetry. *J Phys Chem Lett* **2016,** *7* (8), 1554-1558.

32. Li, X. T.; Hodson, H.; Batchelor-McAuley, C.; Shao, L. D.; Compton, R. G., Improving Formate and Methanol Fuels: Catalytic Activity of Single Pd Coated Carbon Nanotubes. *ACS Catal* **2016,** *6* (10), 7118-7124.

33. Ellison, J.; Batchelor-McAuley, C.; Tschulik, K.; Compton, R. G., The use of cylindrical micro-wire electrodes for nano-impact experiments; facilitating the sub-picomolar detection of single nanoparticles. *Sensor Actuat B-Chem* **2014,** *200*, 47-52.

Chapter 9

Conclusions

Carbon nanotubes (CNTs) have been suggested in the literature to be electrocatalytic for various electrode reactions relating to applications including sensing and energy devices. In this thesis we have investigated the catalytic behaviour of CNTs for the Br_2/Br^- and VO_2^+/VO^{2+} redox couples at both ensemble and as individual entity using cyclic voltammetry and 'nano-impacts' respectively and have compared the kinetics seen at CNTs to those at bare glassy carbon (GC) electrodes. Bamboo-like multiwalled carbon nanotubes (b-MWCNTs) were used in this work and the following conclusions were drawn.

b-MWCNTs modified GC electrodes made using the drop-cast technique were observed to form heterogeneously distributed surfaces of agglomerated CNTs. Depending on the amount of b-MWCNTs the distribution varied across the substrate electrode, especially at lower concentrations where the substrate electrode was exposed, leading to voltammetric waves corresponding to both the substrate and the b-MWCNTs. Hence when studying particle modified electrodes, it is recommended that complementary microscopic imaging be conducted in parallel with voltammetry to identify the distribution of b-MWCNTS and to aid the interpretation of the voltammetric data. Modification with large quantities of CNTs lead to the formation of thick porous layers of b-MWCNTs. Voltammetric analysis at such porous structures may show illusory catalytic results notably reduced overpotentials which in turn may be mis-understood for faster electrode kinetics but in reality, this is due to the peak arising from the analyte trapped within the porous layer having thin layer voltammetric characteristics with a peak potential closer to the formal potential. Thus, these surface modifications forming thick

porous layers of b-MWCNTs give voltammetric responses which are ambiguous to interpret in terms of the catalytic behaviour due to mixed mass transport effects. Hence, we have used and recommend 'nano-impact' measurements.

First, for the Br_2/Br^- redox couple before evaluating the electron transfer kinetics at b-MWCNTs and carbon substrate electrode, we clarified two important aspects. One is the formal potential of the redox couple and the other are the conditions under which the formation of tribromide ions takes place. For this, with the help of simulations conducted by Mr. Haotian Chen the formal potential was found to be +0.91 V vs SCE using the correct form of Randles-Ševčík equation corresponding to the non-unity stoichiometry of the redox reaction. Also, the conditions under which the tribromide ion might be observed in aqueous solution at 298 K were identified to require concentrations >0.1 M of bromide concentration. Using the obtained formal potential, the electrocatalytic behaviour of b-MWCNTs towards the redox couple was next investigated separately for oxidation of bromide and reduction of bromine. 'Nano-impacts' analysis revealed that b-MWCNTs showed faster electrochemical rate constants compared to that seen at a bare GC but are possibly not sufficiently enhanced for use in electrochemical applications.

Second, for the VO_2^+/VO^{2+} redox couple 'nano-impacts' measurements exposed interesting asymmetric catalysis at individual b-MWCNTs. The oxidative process was observed to be kinetically accelerated compared to a bare GC electrode while, the reductive process was negatively catalysed by the b-MWCNTs. The asymmetry was concluded to reflect to the multi-step nature of the electrochemical reaction mechanism.

Another ambiguity in analysing voltammetry at modified electrodes is to distinguish between thin-layer effects and adsorption effects, since for both the cases the peak current varies linearly with the scan rate. We have concluded that 'nano-impacts' analysis in

parallel with the cyclic voltammetry permits the sought distinction between adsorptive and thin-layer voltammetry. The oxidation of 4-hexylresorcinol was used for proof of concept and it was found that for this case, the reaction at single CNTs was diffusion controlled so that the voltammetry was thin layer and not adsorptive.

To summarise, this thesis concludes that if ensembles of CNTs are used to modified electrodes and studied using cyclic voltammetry, a reduced peak-to-peak separation is not necessarily indicative of electrocatalytic behaviour since this shift of both voltammetric peaks towards the formal potential can occur as a result of thin-layer diffusion within the pores and/or changed electron transfer kinetics. Hence, we recommend the use of single-entity electrochemistry in synergy with voltammetric analysis to explore the intrinsic electrocatalytic behaviour of nanoparticles and also to differentiate between the adsorptive and thin-layer effects.

Last, whilst this work was conducted exclusively on b-MWCNTs the implications are generic to electrodes modified with other nanoparticles that form porous layers including the many used in energy conversion and chemical sensing.